Quantum transport investigations of low-dimensional electron gases in $Al_xGa_{1-x}As$/GaAs- and Bi_2Se_3-based materials

Dissertation

zur Erlangung des akademischen Grades
doctor rerum naturalium
(Dr. rer. nat.)
im Fach Physik
Spezialisierung: Experimentalphysik

eingereicht an der
Mathematisch-Naturwissenschaftlichen Fakultät
der Humboldt-Universität zu Berlin

von
M. Sc. Christian Riha, geb. Feilcke

Präsidentin der Humboldt-Universität zu Berlin:
Prof. Dr.-Ing. Dr. Sabine Kunst

Dekan der Mathematisch-Naturwissenschaftlichen Fakultät:
Prof. Dr. Elmar Kulke

Gutachter/innen:

1. Prof. Dr. Saskia F. Fischer
2. Prof. Dr. Hartmut Buhmann
3. Prof. Dr. Thomas Schröder

Tag der mündlichen Prüfung: 11.12.2018

Abstract

The transport properties of an electron gas with reduced dimensionality are dominated by the electron's wave nature. This allows to observe various quantum effects, such as quantum interference.

In the first part of this thesis etched quantum rings and one-dimensional (1D) constrictions, based on $Al_xGa_{1-x}As/GaAs$ heterostructures, are investigated with respect to their transport properties. Thermal noise measurements in equilibrium show that the expectation value agrees with the noise spectra of all 1D constrictions but is exceeded by up to 60 % for the noise spectra of all quantum rings.

Noise measurements in thermal non-equilibrium reveal that the heat flow can be switched on and off for a quantum ring by a global top-gate. The measured magnetoresistance of the quantum rings shows oscillations that are attributed to the Aharonov-Bohm effect. The observability of these oscillations strongly depends on the cooling process of the sample and the oscillations show indications of a beating as well as phase rigidity.

In the second part of the thesis the surface states of exfoliated Bi_2Se_3 microflakes are studied. For microflakes that show a metallic temperature dependence of the resistance weak anti-localization is observed. This observation suggests that the magnetoresistance is a result of layered transport of 2D channels in the bulk rather than just the surface 2D channels. A microflake with semiconducting characteristics does not show indications of such a 2D layered transport and its magnetoresistance is considered to be carried by the 2D surface states only.

Kurzzusammenfassung

Die Transporteigenschaften eines Elektronengases mit reduzierter Dimensionalität werden von den Welleneigenschaften der Elektronen bestimmt. Dies ermöglicht es, verschiedene Quanteneffekte, wie Quanteninterferenz, zu beobachten.

Im ersten Teil dieser Arbeit werden geätzte Quantenringe und eindimensionale (1D) Verengungen, basierend auf $Al_xGa_{1-x}As$/GaAs-Heterostrukturen, hinsichtlich ihrer Transporteigenschaften untersucht. Messungen des thermischen Rauschens im Gleichgewichtszustand zeigen, dass der Erwartungswert mit den Rauschspektren aller 1D Verengungen übereinstimmt, jedoch um bis zu 60 % bei allen Quantenringen überschritten wird.

Rauschmessungen im thermischen Nichtgleichgewicht ergeben, dass der Wärmefluss in Quantenringen mithilfe einer globalen Steuerelektrode (Topgate) an- und ausgeschaltet werden kann. Die magnetische Widerstandsänderung der Quantenringe zeigt Oszillationen, die dem Aharonov-Bohm-Effekt zugeordnet werden. Die Beobachtbarkeit dieser Oszillationen hängt stark von dem Abkühlvorgang der Probe ab und die Oszillationen zeigen Hinweise auf ein Schwebungsmuster sowie auf Phasenstarre.

Im zweiten Teil der Arbeit werden die Oberflächenzustände von exfolierten Bi_2Se_3 Mikroflocken untersucht. Für Mikroflocken mit metallischen Temperaturabhängigkeiten des Widerstandes wurde schwache Anti-Lokalisierung beobachtet. Diese Beobachtung deutet darauf hin, dass sich die magnetische Widerstandsänderung weniger ausschließlich aus den 2D Oberflächenkanälen als vielmehr aus einem geschichtetem Transport von 2D Kanälen im Volumenkörper zusammensetzt. Eine Mikroflocke mit halbleitenden Eigenschaften zeigt keine Hinweise auf solch einen geschichteten 2D Transport und es wird angenommen, dass ihre magnetische Widerstandsänderung ausschließlich von den 2D Oberflächenzuständen verursacht wird.

Contents

List of Figures

List of Tables

List of Symbols

Symbol	Description	SI-Unit
$\vec{A}$	Vector potential	Vs/m
$\vec{B}$	Magnetic field	A/m
$\vec{B}_{\varphi}$	Phase coherence characteristic field	A/m
C_{Fit}	Electrical capacity from fit	F
D	Diffusion constant	m^2/s
D_{xD}	Density of states in x dimensions	-
d	Dimensionaility	-
E	Energy	J
E_{F}	Fermi energy	J
F	Enclosed area	m^2
f	Frequency	Hz
f_0	Fermi-distribution	-
G	Electrical conductance	S
g	Differential electrical conductance	S
$g_{\mathrm{x\text{-}y}}$	g from contact x to contact y	S
H	Hamiltonian	J
I	Current	A
I_{1D}	One-dimensional current	A
I_{h}	Heating current	A
I_{Osc}	Excitation current	A
$\vec{k}$	Wave vector	1/m
$\vec{k}_{\mathrm{F}}$	Fermi wave vector	1/m
l	Geometrical device length	m
l_{φ}	Phase coherence length	m
L_{T}	Thermal length	m
m_{e}^*	Effective mass (here isotrope)	kg
n_{2d}	Two-dimensional electron density	$1/\mathrm{m}^2$
$\dot{Q}$	Rate of heat flow	$\mathrm{kg\ m}^2/\mathrm{s}^3$
$\dot{Q}_{\mathrm{X\text{-}Y}}$	$\dot{Q}$ from reservoir X to reservoir Y	$\mathrm{kg\ m}^2/\mathrm{s}^3$
R	Electrical resistance	Ω
R_{amp}	Amplifier input resistance	Ω
R_{xx}	Auto-correlation function	-
R_{xy}	Cross-correlation function	-
S_{xy}	Cross-power spectral density	V^2/Hz
S_{I}	S_{xy} from current fluctuation	V^2/Hz
S_{V}	S_{xy} from voltage fluctuation	V^2/Hz
$S_{\mathrm{V,w}}$	White part of S_{V}	V^2/Hz
$S_{\mathrm{V,Th}}$	Theoretical value for $S_{\mathrm{V,w}}$	V^2/Hz

T	Temperature	K
T_{Bath}	Bath temperature	K
T_{C}	QPC-characteristic temperature	K
T_{e}	Electron temperature	K
$T_{\mathrm{e}}^{\mathrm{X}}$	T_{e} of the reservoir X	K
T_{L}	Lattice temperature	K
T_{amp}	Amplifier temperature	K
$T_{\alpha,\beta}$	Transmission probability	-
t	Time	s
V	Voltage	V
V_{G}	Gate voltage	V
V_{L}	Lattice potential	V
V_{SD}	Source-drain voltage	V
V_{Th}	Threshold gate voltage	V
V_{sig}	Signal voltage	V
V_{amp}	Amplified signal voltage	V
$\vec{v}$	velocity	m/s
$\vec{v}_{\mathrm{D}}$	Drift velocity	m/s
$\vec{v}_{\mathrm{F}}$	Fermi velocity	m/s
w	Geometrical device width	m
α,β	Electron modes	-
β	Exponent in Hooge relation	-
α_{HLN}	Test-Parameter of HLN-Model	-
ϵ_{n}	Energy of QPC mode	J
γ,γ'	Electron path	-
γ	Gate efficiency	-
λ_{F}	Fermi wavelength	m
μ_{e}	Electron mobility	m^2/Vs
μ_{s}	Chemical potential of source-contact	J
μ_{d}	Chemical potential of drain-contact	J
Φ_{el}	Electrostatic potential	V
Φ_{m}	Magnetic flux	Wb
φ	Electron phase	-
ρ	Electrical resistivity	Ω
σ	Electrical conductivity	S/m
ω_x, ω_y	Measure for QPC-quality	Hz
$\Psi_{\vec{k}}$	Electron wave function	-

Constant	**Description**	**Value**
e	Elementary charge	$1.60217662 \cdot 10^{-19}$ C
G_0	Conductance quantum	$7.7480917346 \cdot 10^{-5}$ S
h	Planck constant	$6.626070040 \cdot 10^{-34}$ Js
$\hbar$	Reduced Planck constant	$1.054571800 \cdot 10^{-34}$ Js
k_{B}	Boltzman constant	$1.38064852 \cdot 10^{-23}$ J/K
m_0	Electron rest mass	$9.10938356 \cdot 10^{-31}$ kg
R_{K}	Klitzing constant	25.8128075 kΩ
Φ_0	Magnetic flux quantum	$2.067833831 \cdot 10^{-15}$ Wb
π	Ludolphine number	3.14159265358978

List of Abbreviations

Short form	**Long from**
xD	x-dimensional
2DEG	Two-dimensinal electron gas
AB	Aharonov-Bohm
AC	Alternating current
ARPES	Angle-resolved photoemission spectroscopy
DC	Direct current
DOS	Density of states
EBL	Electron beam lithography
FFT	Fast Fourier transformation
HLN	Hikami-Larkin-Nagaoka
MBE	Molecular beam epitaxy
MOVPE	Metal-organic vapour deposition epitaxy
PSD	Power spectral density
PDF	Probability density function
QPC	Quantum point contact
RRR	Residual resistance ratio
SdH	Shubnikov-de Haas
SEM	Scanning electron microscope
SOC	Spin-orbit coupling
TRS	Time-reversal symmetry
UVL	Photolithography
WAL	Weak anti-localization
WL	Weak localization

Chapter 1

Introduction

At the beginning of the 19th century Thomas Young was the first who demonstrated the wave-like nature of light in an interference experiment [1], that is known as the double-slit experiment nowadays. In the subsequent century Max Planck's solution of the black body radiation problem, known as Planck's law, introduced the energy quantum of electromagnetic radiation. The idea of considering light as quantum enabled Einstein later to explain the photoelectric effect for which he was awarded the Nobel Prize in physics in 1921. The theory of light being a particle and a wave at the same time led to the wave-particle duality. The hypothesis of Louis-Victor de Broglie, which claims that this duality is a property of all matter, was made in 1924 and was later verified for electrons by the two independent experiments of Thomson and Davisson, which was awarded with the Nobel Prize in physics for all of them. Together with the works of various other physicists, such as Erwin Schrödinger [2], a new branch in physics, the quantum mechanics, was created as expressed in the Copenhagen interpretation in 1927 [3].

Quantum mechanics treats both, particles with and those without mass as waves whose position and momentum are described with a density probability function [4, 5]. This allows particles to interfere with each other and with themselves, as demonstrated for electrons in the Aharonov-Bohm effect [6], the weak localization (WL) effect [7, 8] and in the weak anti-localization (WAL) effect [9]. In addition, physical properties become quantized at low energy and atomic length scales. Examples for this are the possibility to reduce the dimensionality of an electron gas [10] and the observation of the quantization of the electrical conductance in one-dimensional electron gases [11, 12].

Modern epitaxy methods, such as the molecular beam epitaxy [13], enable the growth of single crystalline semiconductor layers with atomic precision. This allows the creation of III-V semiconductor heterostructures [14] that confine the spatial movement of electrons to two dimensions in the conducting channel and that serve as base for various electronic devices [15]. The usage of the binary compounds AlAs and GaAs has proven to result in the highest electron mobilities among III-V semiconductor heterostructures [16, 17] due to their lattice constants that deviate by less than 1% from each other. By electron beam lithography and subsequent nanopatterning of the channel the dimensionality can be further reduced to one dimension.

The two-dimensional electron gas that is provided at a semiconductor heterojunction was used by Klaus von Klitzing, who discovered the quantum Hall effect in 1980 [18]. The quantum Hall state represents a system where electrons propagate dissipa-

tionless along edge channels, whereas the bulk remains electrically non-conducting. The band structure of a quantum Hall state is closely related to the field of topological insulators [19, 20, 21, 22], where the electric current is carried exclusively by electrons that occupy the topologically non-trivial surface states. Due to the helical movement of the electrons in these edge states topological insulators are excellent candidates for the development of spintronics, i.e. spin-based electronics. Moreover, the realization of a solid-state quantum computer [23] is expected to be achievable by combining properties of topological insulators and superconductors.

The subject that deals with the above-mentioned quantum effects is referred to as mesoscopic physics and closes the gap between the macroscopic world, i.e. the bulk, and the microscopic world that deals with the atomic scale. One aim of mesoscopic physics is to use quantum effects in low-dimensional devices and circuits [24, 25, 26]. The realization of such quantum devices relies on the capability to detect and manipulate quantum states, such as the phase coherence length. This is a measure of the length over which an electron keeps its initial phase information and is therefore a crucial property for observing quantum interference.

In this thesis two material systems, $Al_xGa_{1-x}As/GaAs$ and Bi_2Se_3, are investigated with respect to their low-dimensional transport properties. Both systems allow to study the phase coherence of electrons. In the case of $Al_xGa_{1-x}As/GaAs$ this can be done by means of the Aharonov-Bohm effect and in the case of Bi_2Se_3 by WAL due to strong spin-orbit coupling. Both methods are based on the interference of electrons and require the measurement of the magnetoresistance. One question in this thesis is whether this interference can be studied in the absence of magnetic fields when the noise of the interferometer is studied. A further question concerns phase rigidity that is known to occur in symmetric devices. This effect describes the inability of electrons in a given system to change their phase by values other than 0 or π. It is tested whether the phase rigidity can also occur in an asymmetric device when the measurement setup is kept symmetric. Since the phase coherence of electrons is sensitive to temperature, the third question is how heat flow evolves in a network of 1D waveguides in the presence of a temperature gradient. The last question is motivated from recent evidences of layered 2D transport in a Bi_2Se_3 crystal [27]. It is studied whether similar evidences can be found in interference phenomena, such as WAL in Bi_2Se_3 microflakes. The outline of the thesis is as follows:

In the **2nd chapter** the physical concept of low-dimensional transport is introduced. Subsequently, the diffusive and the ballistic transport regime are studied together with their corresponding length scales. The Landauer-Büttiker formalism is outlined along with the one-dimensional ballistic transport and the model of the quantum point contact. After an introduction to the quantum Hall and Shubnikov-de Haas effect the main models of electrical noise, predominantly thermal noise, are presented. At the end of the chapter the underlying theory of the Aharonov-Bohm effect, the WL effect and the WAL effect is treated.

The **3rd chapter** deals with the properties of the two studied material systems and with the preparation of the samples that are used in this thesis. First, the functionality of $Al_xGa_{1-x}As/GaAs$ heterostructures is presented and explained. Second, the fabrication of the $Al_xGa_{1-x}As/GaAs$-based devices, processed at the Ruhr-Universität Bochum by the group of Prof. Dr. Andreas Wieck, Prof. Dr. Dirk Reuter and by Dr. Sven Buchholz, is explained. Subsequently, the concept of topo-

logical insulators is introduced and the exfoliation and lithographic processes of the investigated Bi_2Se_3 are shown.

Chapter 4 introduces the measurement setups that are used in this thesis. First, the cryogenic techniques are presented. Furthermore, the two-point and four-point measurement setups for the electrical characterization of the $Al_xGa_{1-x}As$/GaAs- and Bi_2Se_3-based devices are presented.

The electrical characterization of the $Al_xGa_{1-x}As$/GaAs-based devices is shown in **chapter 5**. This includes the determination of the effective mass by evaluating Shubnikov-de Haas oscillations, the measurement of the two-point quantized conductance as well as subband spectroscopy. In addition, a measurement method is presented that serves as alternative approach of the subband spectroscopy and improves the reliability of the deduced parameters.

The noise characterization of the $Al_xGa_{1-x}As$/GaAs-based devices is presented in **chapter 6**. The thermal noise is measured for 1D constrictions and quantum rings. The correlation of noise sources is taken into consideration in an attempt to explain a fraction of the thermal noise that exceeds the expectation value.

In **chapter 7** the heat flow in a quantum ring is investigated out of thermal equilibrium in terms of thermal noise measurements. This yields important information for interferometer devices since the phase coherence length depends on the temperature. A model that is based on the Wiedemann-Franz relation is presented and provides an explanation for the distribution of the heat flow in the quantum ring. At the end of the chapter results from wave packet simulations, performed by Dr. Christoph Kreisbeck and Dr. Tobias Kramer, are compared with the experimental findings.

In **chapter 8** interference experiments of the quantum rings are presented. Magnetoresistance oscillations, interpreted as Aharonov-Bohm oscillations, are found to highly depend on the cooling process of the device and are investigated with respect to their phase evolution in the presence of an electric field.

In **chapter 9** the results of the temperature-dependent resistance $R(T)$ and the magnetoresistance $R(\vec{B})$ of Bi_2Se_3 microflakes are presented. The microflakes show metallic $R(T)$ characteristics and a cusp in the magnetoresistance. The cusp can be attributed to WAL in terms of the Hikami-Larkin-Nagaoka model if the transport by layered parallel conducting 2D systems is considered. No signs of layered transport are found for a microflake with semiconducting $R(T)$ characteristics when evaluating its cusp in the magnetoresistance.

Chapter 10 gives a summary of the experimental results and the according interpretations. At the end of this chapter suggestions are given for further steps concerning the $Al_xGa_{1-x}As$/GaAs quantum rings and the Bi_2Se_3 microflakes.

Chapter 2

Properties and realization of low-dimensional electron systems

In this chapter the theoretical basics of some important aspects in mesoscopic physics will be introduced in a short version. This includes the properties of low-dimensional electron systems, characteristic length scales and transport regimes. The focus will lie on the ballistic transport regime, where the transport properties are dominated by the scattering at the sample boundaries rather than the scattering from impurities. Important quantum effects that result from ballistic transport are the quantization of the electrical conductance and the interference of electron waves in one-dimensional (1D) quantum rings. For a deeper insight into the following topics additional literature [28, 29, 30, 31, 32] is recommended.

2.1 Properties of low-dimensional electron gases

Electrons in a conductor can propagate in any spatial direction if no confining potentials V_c are present. The freedom of motion is connected to the availability and separation of the energy states that can be occupied by conduction electrons. Since an electron is a fermion, i.e. a particle with spin 1/2, the Pauli-principle prevents two electrons with the exact same set of quantum numbers to occupy the same energy state E. The time-independent Schrödinger equation describes the system for a state $\Psi_{\vec{k}}(\vec{r})$ with energy E, position vector $\vec{r} = (x, y, z)$ and wave vector $\vec{k} = (k_x, k_y, k_z)$ as

$$H\Psi_{\vec{k}}(\vec{r}) = \left[-\frac{\hbar^2}{2m_\mathrm{e}^*}\nabla^2 + V_\mathrm{c}(\vec{r})\right]\Psi_{\vec{k}}(\vec{r}) = E\Psi_{\vec{k}}(\vec{r}). \tag{2.1}$$

In Eq. 2.1 the effective-mass approximation is used, where the electron is described as Bloch wave in the presence of a periodic lattice potential V_lat. In order to take account for the interaction of the electron with V_lat, the electron is considered to have an effective mass m_e^* that is changed compared to its rest mass m_0. Typically, the effective mass is a tensor and depends on the direction of the electron's movement in the crystal. In the case of parabolic conduction bands the effective mass of electrons becomes a scalar. The material systems GaAs and Bi_2Se_3 both have a parabolic conduction band. Therefore, electrons in the conduction band of these material systems have isotropic effective masses.

The corresponding wave function is $\Psi_{\vec{k}}(\vec{r}) = \exp(i\vec{k}\vec{r})$ and the quasi-continuous energy levels depend quadratically on the electron wave vector $\vec{k} = (k_x,k_y,k_z)$ with

$$E = \frac{\hbar^2 \vec{k}^2}{2m_\mathrm{e}^*}. \tag{2.2}$$

A characteristic quantity that describes the transport properties of an electron is the density of states (DOS) $D(E) = g_\mathrm{s} g_\mathrm{v} V^{-1} \mathrm{d}N(E)/\mathrm{d}E$ with the number of energy states $N(E)$ in an energy range $\mathrm{d}E$ and volume V of the crystal. The spin-degeneracy g_s for fermions is 2 and the Valley degeneracy g_v equals 1 for direct semiconductors. In three dimensions it is

$$D_\mathrm{3D}(E) = \frac{(2m_\mathrm{e}^*)^{3/2}}{2\pi^2\hbar^3}\sqrt{E} \tag{2.3}$$

and changes as the electrons become confined to lower dimensions. In a macroscopic conductor the energy levels are quasi-continuously distributed. The smaller the size of the conductor, i.e. the smaller the confining potential V_c, the more the energy levels are separated from each other. The energetic separation of the energy levels is high enough to enable the observation of quantum effects if the size of V_c along a certain dimension is comparable to the de Broglie-length $\lambda = h/p$ of the conduction electrons [32]. Since the transport properties are dominated by the electrons that are close to the Fermi energy E_F, this wavelength becomes the Fermi wavelength λ_F. In this case, V_c leads to the reduction of the dimensionality of the electron.

The following sections are about the transport properties of electrons in two-dimensional (2D) and one-dimensional (1D) electron gases and about experimental techniques to reduce the dimensionality of electron gases.

Two-dimensional electron gases

In the following it is assumed that V_c confines the electron in the z-direction, i.e. the energy levels in the z-direction are quantized. This prevents the electron from moving in the z-direction and restricts the propagation of the electron wave to the x- and y-direction. The corresponding wave function can be separated into the x,y-part and the z-part with

$$\Psi_{\vec{k}}(\vec{r}) = \Psi_{k_x,k_y}(x,y) \cdot \Psi_j(z) = e^{i(xk_x+yk_y)} \cdot \Psi_j(z) \tag{2.4}$$

with $j \in \mathbb{N}$, the index of the quantized energy level. The energy eigenstates are

$$E_j(k_x,k_y) = \frac{\hbar^2(k_x^2+k_y^2)}{2m_\mathrm{e}^*} + E_j(0,0), \tag{2.5}$$

where $E_j(0,0)$ appears in quantized values. In three dimensions the occupied states in momentum space, i.e. $k \leq k_\mathrm{F}$, form a Fermi sphere at $T = 0$ K, which becomes a circle, as depicted in Fig. 2.1 a) and b). The DOS becomes

$$D_\mathrm{2D}(E) = \frac{m_\mathrm{e}^*}{\pi\hbar^2}\sum_j \Theta[E - E_j(0,0)]. \tag{2.6}$$

The sum over the Heavyside functions $\sum_j \Theta[E-E_j(0,0)]$ takes into account that each occupied energy level contributes $m_\mathrm{e}^*/\pi\hbar^2$ to the density of states D_2D. However, the contribution of each subband does not depend on the energy E. In Fig. 2.1 b) it becomes clear that $D_\mathrm{2D}(E)$ is a staircase function that is enveloped by the DOS in three dimensions $D_\mathrm{3D}(E)$.

One-dimensional electron gases

Modifying the confinement potential V_c so that the energy levels are quantized in a further direction causes the electron to be restricted to forward and backward movement in the remaining dimension. It is now considered, that the x-direction is the only one with energy levels that are quasi-continuous. This causes the wave function to become

$$\Psi_{\vec{k}}(\vec{r}) = \Psi_{k_x}(x) \cdot \Psi_m(y)\Psi_j(z) = e^{i(xk_x)} \cdot \Psi_m(y)\Psi_j(z) \tag{2.7}$$

with $j, m \in \mathbb{N}$ as the index of the quantized energy levels that are created in the y- and z-direction. The energy state of the electron can be expressed with

$$E_{jm}(k_x) = \frac{\hbar^2 k_x^2}{2m_\mathrm{e}^*} + E_{jm}(0). \tag{2.8}$$

Here, $E_{jm}(0)$ describes the combination of the energies, stemming from the energy quantization in y- and z- direction. The density of states for the one-dimensional electron gas (1DEG) is

$$D_\mathrm{1D}(E) = \frac{1}{\pi\hbar}\sqrt{2m_\mathrm{e}^*}\sum_{j,m}\frac{1}{\sqrt{(E - E_{jm})}}\Theta(E - E_{jm}). \tag{2.9}$$

In momentum space the values of k that satisfy $k \leq k_\mathrm{F}$ form a Fermi segment and $D_\mathrm{1D}(E)$ becomes higher around the energies E_{jm}, as depicted in Fig. 2.1 c).

Zero-dimensional electron gases

In the case, that V_c causes the electrons to be confined in all spatial directions, the corresponding energy levels do not have continuous contributions anymore and take the form $E_{jml} = E_j(0,0) + E_m(0,0) + E_l(0,0)$. The discrete nature of the energy levels results in a density of states that only becomes non-zero for these energy states

$$D_\mathrm{0D}(E) = 2\sum_{j,m,l}\delta(E - E_{j,m,l}), \tag{2.10}$$

as depicted in Fig. 2.1 d). In semiconductor physics this system is referred to as 'Quantum Dot' (QD) or 'artificial atoms', due to the similarity to the atom's energy states in the Rutherford-Bohr model.

In this thesis the focus will be on 2D and 1D systems, whose experimental realization will be described in the following sections.

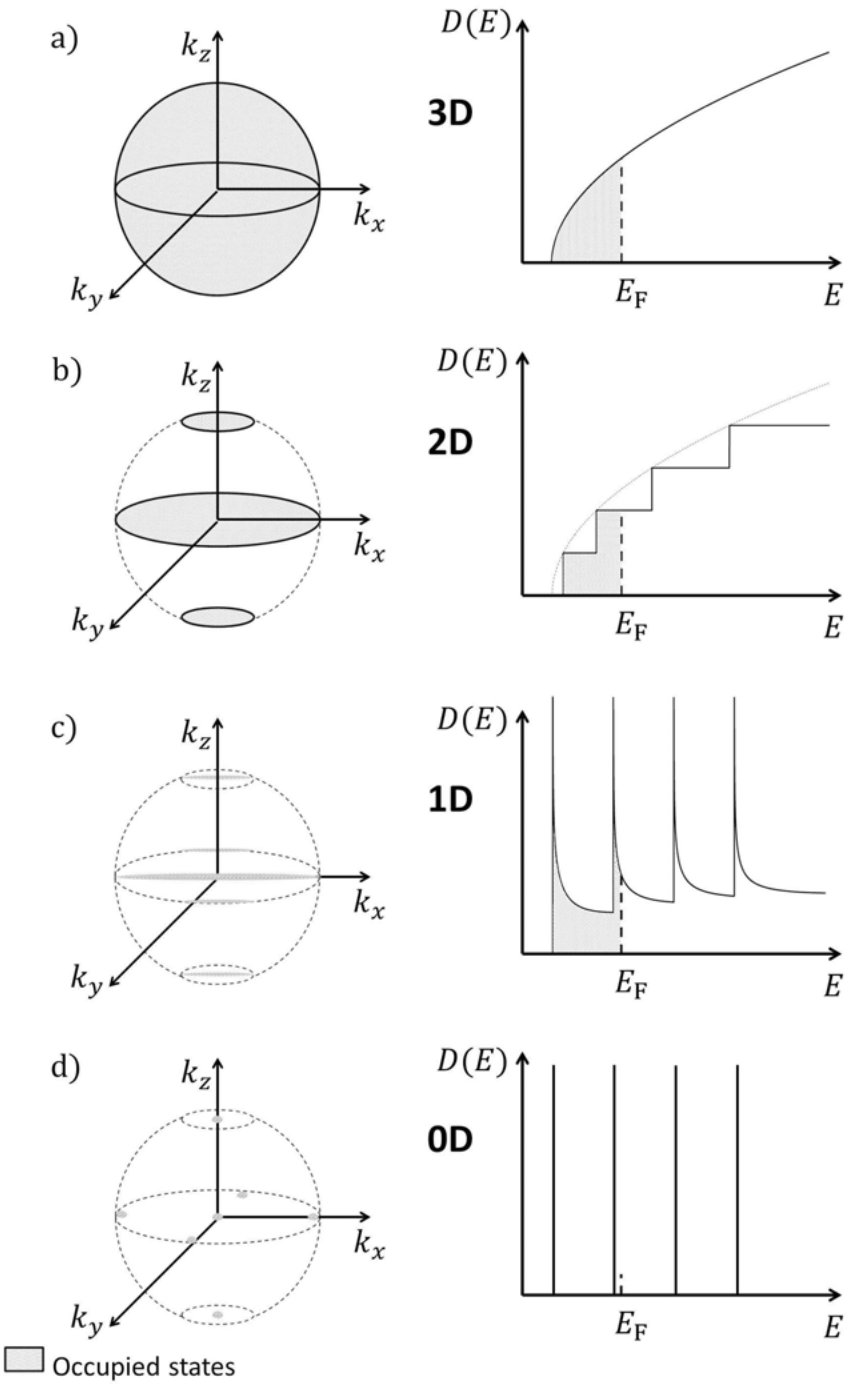

Figure 2.1: Schematic of the energy states of the Fermi energy in momentum space (left) and the corresponding energy-dependent density of states in 3, 2, 1 and 0 dimensions (right). a) In three dimensions the energy states form a Fermi sphere in momentum space. The density of states has a square-root dependence on the energy. b) In the two-dimensional case the energy states with the Fermi level form a Fermi surface in momentum space and the density of energy states follows the three dimensional density of states in quantized steps. c) In the one-dimensional system the density of states forms a Fermi segment and becomes concentrated around the quantized energy levels of the systems and condenses into δ-functions in the zero-dimensional case in d).

2.2 Ballistic 1D transport

In the previous section it was shown that the energetic separation of energy levels of an electron gas increases as the dimensionality of the electron gas is reduced. If the potential wells have a width that is comparable to the Fermi wavelength λ_F of the electron gas, it is possible to observe quantum effects in electrical transport measurements. In the following sections further characteristic length scales will be presented that have an impact on the transport properties of electrons that propagate in the low-dimensional regime.

Characteristic length scales and transport regimes

The **diffusive transport** regime is typical for macroscopic conductors and is characterized by electrons that scatter inelastically and elastically with other particles or quasi-particles. An inelastic scattering event is always accompanied by an exchange of energy and momentum between the scatterers. In order to enable an exchange of energy a dynamical, i.e. time-dependent scattering potential, such as that of phonons, is required. In contrast, elastic scattering events may lead to a change in momentum but conserve the energy of the scatterers, which means that the associated scattering potentials are static, i.e. time-independent. Between two in-/elastic scattering events the electron travels in average the in-/elastic mean free path $l_\mathrm{in}/l_\mathrm{e}$ during the scattering time $\tau_\mathrm{in}/\tau_\mathrm{e}$. Since electrons with the Fermi energy E_F dominate the electrical transport, the relations $l_\mathrm{e} = v_\mathrm{F}\tau_\mathrm{e}$ and $l_\mathrm{in} = v_\mathrm{F}\tau_\mathrm{in}$ hold. According to the Matthiessen rule

$$\tau^{-1} = \tau_\mathrm{in}^{-1} + \tau_\mathrm{e}^{-1} \tag{2.11}$$

an overall scattering time τ can be calculated from scattering events that are independent from each other. In the diffusive transport regime the in-/elastic mean free path is small compared to the size of the conductor $L_{x,y,z}$, i.e. the relation $l_\mathrm{in} \ll L_{x,y,z}$ or $l_\mathrm{e} \ll L_{x,y,z}$ is fulfilled. This allows the application of the semi-classical Boltzman equation to describe the electrical transport.

In contrast, when the conductor's dimensions become smaller than l_in and l_e the transport properties are dominated by the sample boundaries. In this case the electrons are in the **ballistic transport** regime [33, 31], which typically occurs for mesoscopic and microscopic systems such as 1D conductors at low temperatures, where the remaining dimension with quasi-continuous energy levels satisfies $l_\mathrm{in}, l_\mathrm{e} \gg L_\mathrm{x}$. In this regime the wave characteristics of the electrons become important. The electrical transport is then described by the Landauer-Büttiker formalism [34, 35], see Sec. 2.2. If the dimensions of a system are in an intermediate state, such as $l_\mathrm{in}, l_\mathrm{e} < L_\mathrm{x}$ but e.g. $l_\mathrm{in}, l_\mathrm{e} > L_\mathrm{y}$, it is in the **quasi-ballistic transport** regime, where impurity and boundary scattering are equally important. In this regime, quantum effects can still be observed.

However, phase-related effects of electron waves may only be observed in the **phase coherent transport** regime. The phase coherence length l_φ is the average length over which an electron keeps its initial phase until it is lost e.g. due to inelastic scattering events. Other descriptions for l_φ are phase-relaxation length and phase-breaking length. Whereas elastic scattering events conserve the electron's phase, inelastic scattering events lead to a statistical distribution of the electron-phase and are therefore considered to act as 'dephasing'. In contrast, scattering

with magnetic impurities can be elastic or inelastic and leads to dephasing in both cases [36]. It must be mentioned that even after being elastically scattered, the energy of an electron may change according to $\Delta E \approx \hbar/\tau$ with τ being the average lifetime of the electron's energy state [7]. This simply means that dephasing also occurs after sufficient elastic scattering events. Assuming $l_{\mathrm{in}} > l_{\mathrm{e}}$, which is justified in pure materials and metallic-like systems, such as $Al_xGa_{1-x}As/GaAs$ heterostructures at low temperatures, the phase coherence length typically satisfies $l_{\mathrm{in}} \geq l_\varphi > l_{\mathrm{e}}$. Since multiple elastic scattering events happen before the phase is lost, l_φ and its associated phase coherence time τ_φ are related to each other by the diffusion constant D in the form

$$l_\varphi = \sqrt{D\tau_\varphi}, \tag{2.12}$$

rather than by the Fermi velocity v_{F}. The diffusion constant $D = v_{\mathrm{F}} l_{\mathrm{e}}/d$ depends on the dimensionality d of the system. Eq. 2.12 determines the actual phase coherence length at low temperatures. In the ballistic transport regime Eq. 2.12 becomes $l_\varphi = v_{\mathrm{F}}\tau_\varphi$.

At non-zero temperatures electrons have access to an energy range of about $\Delta E = k_{\mathrm{B}}T$ that differs from their energy-state at $T = 0$. Since electrons close to the Fermi energy participate in transport, the energy range is therefore $E_{\mathrm{F}} \pm k_{\mathrm{B}}T$. One electron with E_{F} will approximately propagate coherently with an electron of energy $E_{\mathrm{F}} + k_{\mathrm{B}}T$, despite their different wavelengths, before they both lose their phase relation to each other after having traveled the thermal length [37]

$$l_{\mathrm{T}} = \sqrt{\frac{D\hbar}{k_{\mathrm{B}}T}}. \tag{2.13}$$

In the ballistic approach Eq. 2.13 becomes $l_{\mathrm{T}} = \hbar v_{\mathrm{F}}/k_{\mathrm{B}}T$, which can easily be derived by considering the corresponding characteristic scattering time $\tau_{\mathrm{T}} = l_{\mathrm{T}}/v_{\mathrm{F}}$ and the Heisenberg uncertainty $\tau_{\mathrm{T}}\Delta E \geq \hbar$ with $\Delta E = k_{\mathrm{B}}T$. Both the phase coherence length l_φ and the thermal length l_{T} are an upper limit for the sample's geometric parameters that must not be exceeded in order to enable phase coherent transport. The phase coherent transport regime is the basis of interference effects, which will be discussed in Sec. 2.4.

Quantization of conductance

In the previous section the ballistic transport regime was introduced, where the sample geometry is smaller than the average scattering lengths l_{e} and l_{in} of electrons in this sample. It was already mentioned that in a system, where no scattering occurs, the electrical resistance should be zero. In ballistic 1D conductors, however, it was found that the resistance adopts values of $R = h/2e^2N$ with N being an integer number that is given by the number of occupied energy levels of the 1D constriction. The reason for that is explained in the following by considering an 1D conductor that is connected to electron reservoirs 'source' and 'drain', as depicted in Fig. 2.2 a).

In the Drude model the current density $\vec{j}$ comprises the electron density n and the electron velocity $\vec{v}$ in the form $\vec{j} = -en\vec{v}$. For a 1D conductor with a single occupied

energy level with index j this can be expressed as

$$\begin{aligned} I_{1\mathrm{D},\,j} = en(E)\cdot v(E) = e\int_0^\infty D_{1\mathrm{D}}(E)f(E,\mu_\mathrm{s})\cdot v(E)\mathrm{d}E \\ - e\int_0^\infty D_{1\mathrm{D}}(E)f(E,\mu_\mathrm{d})\cdot v(E)\mathrm{d}E \end{aligned} \tag{2.14}$$

with the chemical potentials μ_d and μ_s that lead to the voltage $V_\mathrm{sd} = (\mu_\mathrm{s} - \mu_\mathrm{d})/e$ between the source and drain contact. Note that in 1D systems the current density and the current are identical. Here, the voltage V_sd is assumed to be small compared to the Fermi energy E_F. This allows to set $f(E,\mu_\mathrm{s}) \approx f(E,E_\mathrm{F}) \approx f(E,\mu_\mathrm{d})$. Note that the Fermi energy is defined only at $T = 0$ K. For higher temperatures the concept of the electrochemical potential is typically applied. However, in this thesis the term 'Fermi energy' will be used to describe systems at $T = 0$ K and at $T > 0$ K. The 1D density state $D_{1\mathrm{D}}$ can be taken from Eq. 2.9. The Fermi-Dirac distribution

$$f(E,E_\mathrm{F}) = \frac{1}{1+\exp(\frac{E-E_\mathrm{F}}{k_\mathrm{B}T})} \tag{2.15}$$

can be approximated as $\Theta(E_\mathrm{F} - E)$ at low temperatures $T \to 0$ and within the limit $\mu_\mathrm{d} \leq E \leq \mu_\mathrm{s}$. With the velocity $\vec{v}(E) = \hbar^{-1}\cdot \mathrm{d}E/\mathrm{d}k$ the Eq. 2.14 then becomes

$$I_{1\mathrm{D},\,j} = e\int_{\mu_\mathrm{d}}^{\mu_\mathrm{s}} \frac{1}{\pi}(\frac{\mathrm{d}E}{\mathrm{d}k})^{-1}\frac{1}{\hbar}\frac{\mathrm{d}E}{\mathrm{d}k}\mathrm{d}E = \frac{e}{\pi\hbar}\int_{\mu_\mathrm{d}}^{\mu_\mathrm{s}} 1\mathrm{d}E = \frac{2e}{h}V_\mathrm{sd}. \tag{2.16}$$

The electrical conductance $G = I_{1\mathrm{D},\,j}/V_\mathrm{sd}$ then becomes $G = 2e^2/h$ for one occupied energy level of a 1D conductor. The inverse conductance $R = G^{-1} = h/2e^2$ is the resistance that stems from a single mode of an 1D conductor. So far, we assumed that electrons are able to perfectly transmit through the 1D conductor. However, this is not necessarily the case in 1D constrictions, and electrons have a certain probability T to transmit through the 1D constriction or to be reflected back into the reservoir with the probability $R = 1 - T$. This is the principle of the Landauer formalism [38, 39], which is extended to multi-terminal devices by Büttiker [40, 35].

Landauer-Büttiker formalism

In the Landauer-Büttiker formalism electrons are considered as waves that each need to occupy a certain energy mode (also called 'subband') in order to participate in the electrical transport. Again, consider two electron reservoirs with quasi-continuous energy modes that are connected to each other by a 1D region, as shown in Fig. 2.2 a). The limited number of energy modes in the 1D region allows few electrons with according energies to pass from one electron reservoir to another, see Fig. 2.2 b). In the absence of tunneling all other electrons are not able to participate in the electrical transport through the 1D region. The resistance that stems from this mechanism can be considered as a contact resistance R_c between 2D and 1D regions. A second contribution to the resistance stems from a barrier that is considered to be located in the 1D region. Whereas the 1D region is defined as ideal, i.e. no scattering occurs, the barrier represents a scattering region for incident electron waves. This mechanism is described with the electron's transmission probability $T_{\alpha,\beta} = |t_{\alpha,\beta}|^2$ to propagate from the mode α in the source reservoir to the mode β in the drain reservoir. Here, $t_{\alpha,\beta}$ describes the corresponding transmission amplitudes. In the absence of channel mixing the transmission probability can be formulated for

one subband with index j as $T_j = |t_j|^2$. Therefore, the second contribution to the resistance R_T stems from a probability of incident electron waves to be scattered back into the electron reservoir at the scattering barrier. The current through the 1D conductor I_1D is the sum of the currents $I_{\mathrm{1D},\,j}$ that are carried by N subbands. Taking the transmission probability into consideration, Eq. 2.16 becomes

$$I_\mathrm{1D} = \sum_j^N I_{\mathrm{1D},\,j} = 2\frac{e}{\pi\hbar}\sum_j^N \int_{\mu_\mathrm{d}}^{\mu_\mathrm{s}} |t_j(E)|^2 \mathrm{d}E = 2\frac{e^2}{h} V_\mathrm{sd} \sum_j^N |t_j|^2, \tag{2.17}$$

where the factor 2 accounts for the spin degeneracy of the energy modes. In the last step the transmission probability is assumed to be energy independent, which is reasonable in the limit $eV_\mathrm{sd} \ll \Delta E_{j,j+1}$, whereas $\Delta E_{j,j+1}$ describes the energy separation of the 1D energy modes j and $j+1$. The electrical conductance $G = I_\mathrm{1D}/V_\mathrm{sd}$ of the system then becomes

$$G = 2\frac{e^2}{h}\sum_j^N T_j, \tag{2.18}$$

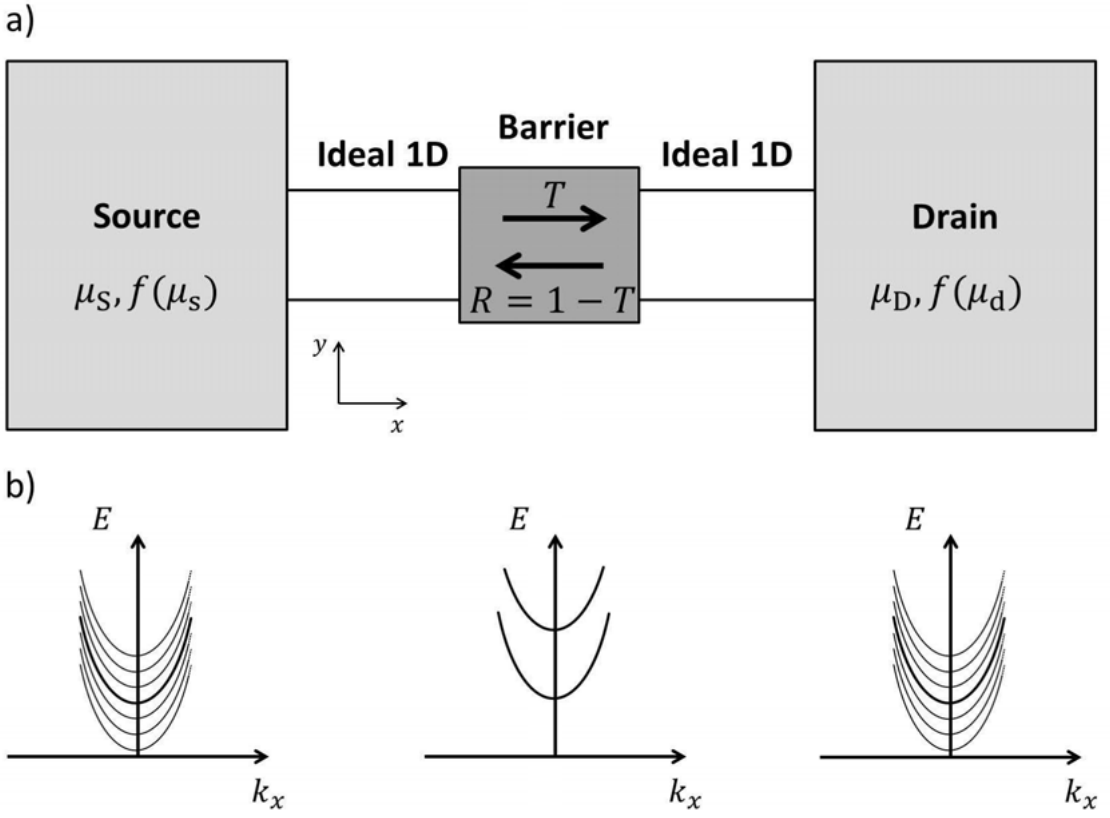

Figure 2.2: Schematic of two electron reservoirs that are connected to each other by an 1D region. a) The 1D region consists of 1D leads, that are ideal, i.e. scattering does not occur. A barrier in the middle of the 1D region acts as scatterer for incident electrons that can transmit the barrier with the probability T or be reflected with the probability $R = 1 - T$ otherwise. b) The energy levels in the electron reservoirs 'source' and 'drain' are quasi-continuous. In contrast, the energy levels in the 1D region are quantized, which allows only few electrons with according energies to transmit from 'source' to 'drain' through the 1D region.

which is known as the Landauer formula. In the absence of scattering, i.e. in the ballistic transport regime, the transmission probability becomes $T \rightarrow 1$ and Eq. 2.18 becomes

$$G = \frac{2e^2}{h} N. \tag{2.19}$$

The electrical resistance that comprises the contributions R_c and R_T is given as

$$R = R_\mathrm{c} + R_\mathrm{T} = \frac{h}{2e^2} + \frac{h}{2e^2}\frac{1-T}{T} = \frac{h}{2e^2 T} \tag{2.20}$$

for a single 1D mode with transmission probability T. In the ballistic transport regime with $T \rightarrow 1$ the resistance is $R = h/2e^2$ and reproduces Eq. 2.19 if divided by N for multiple modes. In contrast, the resistance of the 1D region R_T vanishes, as expected and experimentally demonstrated [41] for a system where no scattering occurs.

Four-point resistance in the Landauer-Büttiker picture

In the last section the transport of electrons was described in terms of transmission probabilities through a 1D constriction in a two-terminal case. Büttiker [35] expanded this formalism to the multi-terminal case, which will be introduced now in a short version. One of Büttiker's aims was to find an expression for the four-point resistance of a sample using the same formalism. In the following a device is considered that consists of a sample, e.g. a quantum ring as in the original work of Büttiker [35], that is connected by a number n of ideal 1D leads to an electron reservoir by each lead. The reservoirs have the chemical potentials μ_1, μ_2, μ_3... μ_n. Again, the transmission of the electrons through the quantum ring is expressed in terms of a transmission probability T_ij to propagate from lead i to lead j. In the picture of Büttiker the transmission probabilities are $T_{ij}(B) = T_{ji}(-B)$ in the presence of a magnetic field due to current conservation and time-reversal invariance. The current I_i in the lead i comprises the current that comes from lead i and is scattered back into lead i with the probability T_{ii} and the current that comes from all other leads and goes to lead i. Thus, the current i is determined to

$$I_i = \frac{2e}{h}(T_{ii}\Delta\mu_i - \sum_{j\neq i} T_{ij}\Delta\mu_j) \tag{2.21}$$

with the energy range $\Delta\mu_i = \mu_i - \mu_0$ and $\Delta\mu_j = \mu_j - \mu_0$ that is given relatively to a reference energy μ_0. The transmission probabilities in Eq. 2.21 are the matrix elements of a transmission matrix $\underline{\underline{T}}$ which establishes a link between the current in one lead an the applied voltage with $I_j = 2e^2/h \cdot T_{ij}V_j$. Hence, this transmission matrix can be interpreted in terms of the electrical conductance. Accordingly, the inverse of this matrix $\underline{\underline{T}}^{-1}$ can be understood as the resistance. The four-point resistance is defined as $R_{ij,kl}$ when the current flow from lead i to lead j and the voltage is measured between the contacts k and l. In this case the currents are $I_i = -I_j$ and $I_k = I_l = 0$. Following the calculations from Büttiker [35], the four-point resistance is then given as

$$R_{ij,kl} = \frac{h}{2e^2}\frac{T_{ki}T_{lj} - T_{kj}T_{li}}{D}. \tag{2.22}$$

Here, D refers to a 3×3 subdeterminant of the matrix $\underline{\underline{T}}$.

Experimental realization of 1D constrictions

The 1D constriction that is described in the previous section is created by a confining potential. This potential can be achieved experimentally in various ways. Some of the most common techniques are the split-gate technique [42], where two gate electrodes on top of the device create a confining electric potential; and the in-plane technique [43], where gate electrodes in the plane of the 2DEG create the confining potential. Another technique is to apply the etching procedure to a 2DEG, as described in chapter 3. A top-gate or back-gate enables to control the Fermi energy in the etched constriction and to populate or depopulate the subbands. In order to allow ballistic transport, the length of the constriction must not exceed the mean free path of the charge carriers, but should be long enough to avoid tunneling through the constriction. Tunneling of electrons may lead to a deviation of the expected conductance plateaus of the 1D region [44]. The resulting 1D constriction is referred to as quantum wire if the length l of the constriction is larger than its width w and is called quantum point contact (QPC) if $l \leq w$.

In the following the focus will be on the QPCs, since the occurrence of quantum effects, e.g. the conductance quantization, is typically more distinct in shorter constrictions since scattering is less likely to occur. The transition from electron reservoir to QPC must not be abrupt (wide-narrow-wide geometry) in order to avoid additional scattering and resonances in the 1D constriction. The transition length should be comparable to the Fermi wavelength λ_{F}, i.e. it should be 'adiabatic'. In adiabatic constrictions each subband contributes to the transport independently from other subbands due to the absence of inter-mode scattering [45] . The saddle-point potential is a well-suited model to approximately describe the potential landscape of a QPC (see Fig. 2.3)

$$V(x,y) = V_0 - \frac{1}{2}m_{\mathrm{e}}^{*}\omega_x^2 x^2 + \frac{1}{2}m_{\mathrm{e}}^{*}\omega_y^2 y^2 \tag{2.23}$$

with the frequencies ω_x and ω_y that characterize the curvature of the saddle-point potential [46]. Whereas ω_y describes the confining potential, ω_x is the barrier of the QPC. The ratio ω_x/ω_y can be considered as an indicator for the visibility of the QPC's conductance plateaus and should be at least 1. Around the saddle-point $(x,y) = (0,0)$ the eigenstates of the parabolic potential are

$$E_j = E_0 + \hbar\omega_y(j - \frac{1}{2}), \tag{2.24}$$

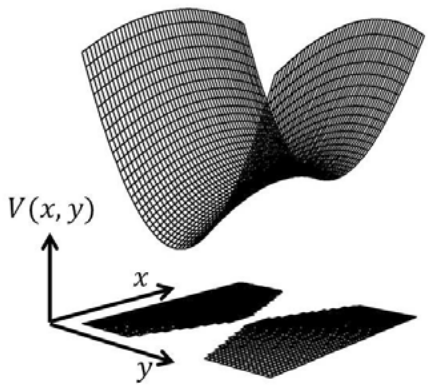

Figure 2.3: Schematic of the saddle point potential of a quantum point contact.

according to the eigenstates of a harmonic oscillator. It is possible to deduce the separation $\Delta E_{j,j+1} = \hbar\omega_y$ of the equidistant energy levels of the QPC by using a technique that is explained in the next subsection. Since ω_x acts as measure for the barrier of the QPC, ω_x is connected to the transmission probability through the QPC

$$T_n = \frac{1}{1 + \exp(-\pi \cdot \epsilon_n)} \tag{2.25}$$

with $\epsilon_n = 2[E - \hbar\omega_y(n+1) - V_0]/\hbar\omega_x$. An increasing value of ω_x leads to a more shallow increase of $G(E_\mathrm{F})$. In experiments E_F is changed by an applied gate voltage V_g. The parameter ω_x can be derived from Eq. 2.25

$$\frac{\mathrm{d}G}{\mathrm{d}V_g} = \frac{2e^2}{h}\frac{\mathrm{d}T_j}{\gamma \mathrm{d}E} = \frac{2e^2}{h}\frac{1}{\gamma}\frac{\pi}{2\hbar\omega_x}, \tag{2.26}$$

as in [46]. Here, $\gamma = \hbar\omega_y/e\Delta V_g$ describes the gate efficiency, which is the ratio of the subband spacing $\hbar\omega_y$ to the gate voltage ΔV_g that is required to populate a new subband. The higher ω_x the more the quantized conductance becomes smeared. A comparable effect is produced by an increase of the temperature T. In Eq. 2.18 the Landauer formula was derived with the assumption that the Fermi function $f(E,E_\mathrm{F})$ is equal to 1 for energies $E \leq E_\mathrm{F}$, which is a reasonable approximation at low temperatures. However, this does not hold for higher temperatures, where Eq. 2.18 becomes

$$G = \frac{2e^2}{h}\sum_{j=1}^{N} f(T,E,E_\mathrm{F}) \tag{2.27}$$

in the ballistic limit ($T_j \to 1$) [47, 48], i.e. if $\omega_x \to 0$. For non-zero values of ω_x the conductance is calculated by [44, 49, 50]

$$G = \frac{2e^2}{h}\sum_{j=1}^{N}\int_0^\infty T_j \cdot \frac{\partial f}{\partial E}\mathrm{d}E. \tag{2.28}$$

In Fig. 2.4 b),c) and d) simulations are performed for a QPC with $\hbar\omega_y = 10$ meV for temperatures in the range 0 K to 60 K and for values of $\hbar\omega_x$ in the range of 0 meV to 40 meV by using Eq. 2.28. Temperatures that are higher than 0 K lead to a smearing effect of the quantized conductance, which is also observed in experiment, as depicted in Fig. 2.4 a). The higher the temperature, the more the quantized conductance becomes smeared out until a characteristic value $T_\mathrm{c} \approx \hbar\omega_y/4k_\mathrm{B}$ is reached where the quantization completely vanishes [48], as represented by the gray areas in Fig. 2.4 c). Higher values of $\hbar\omega_y$ are desirable because they enable the operation of QPCs at higher temperatures. Energetic subband spacings that are achievable in experiment are of the order of about 10 meV [51, 52] for QPCs that are defined by split-gates and are typically higher for etched QPCs up to subband spacing of 20 meV [53]. In Fig. 2.4 b) it can be seen that ω_x has a similar impact on the quantization of the electrical conductance as T. Analogous to T_c a characteristic value ω_c can be defined, as depicted in Fig. 2.4 d).

So far, the assumption was made that the applied voltage between the source and drain contact is relatively small compared to the energetic separation of the subbands $\hbar\omega_y$ of the 1D constriction. This linear response regime ensures that the chemical potential of source and drain contact lead to the same number of occupied

subbands for low temperatures $k_B T \ll \hbar\omega_y$ and lies in the main focus of experimental and theoretical studies [33]. However, in the non-linear regime deviations from Eq. 2.19 occur and enable the estimation of the gate efficiency γ from Eq. 2.26 as well as the determination of the energetic subband separation $\hbar\omega_y$.

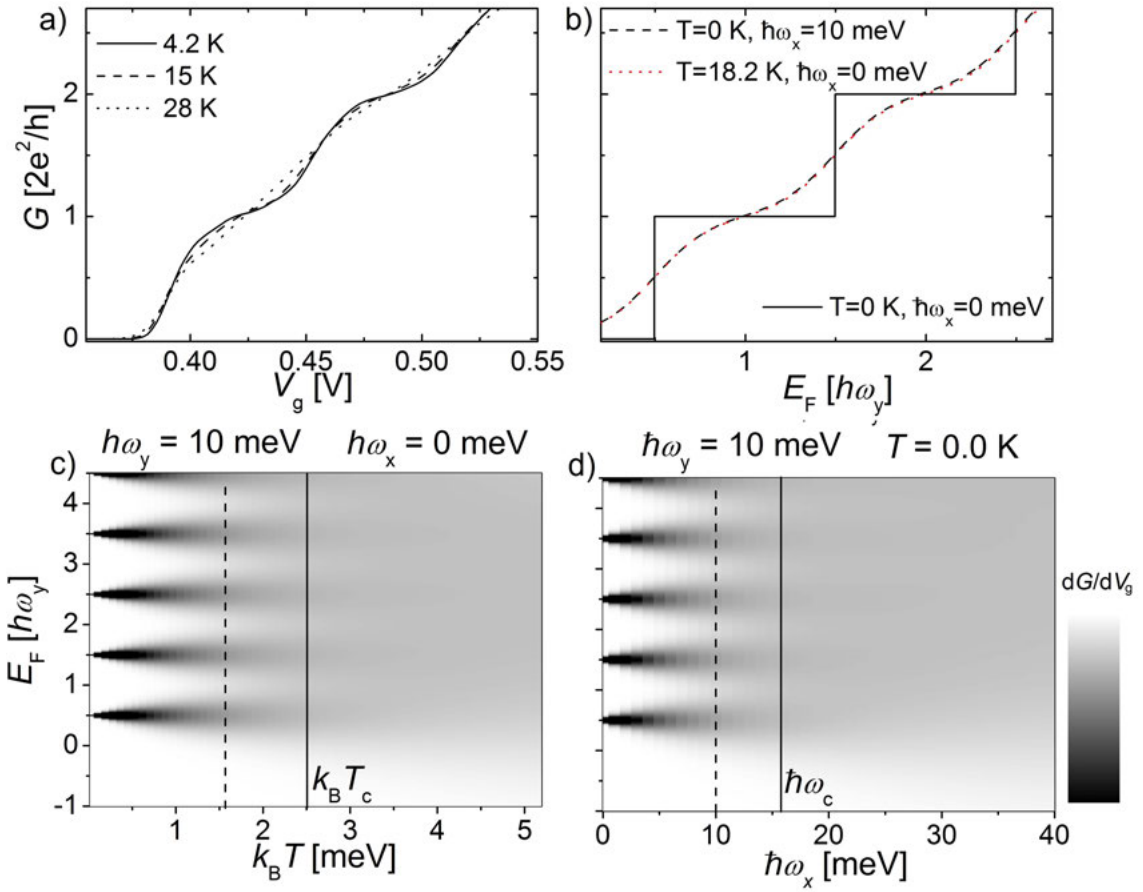

Figure 2.4: a) Quantized conductance of a QPC measured at different temperatures. b) Calculation of the quantized conductance of a QPC using Eq. 2.28. The simulated QPC has $\hbar\omega_y = 10$ meV. Different situations of the smearing due to the temperature T and ω_x are depicted. With $T = 0$ K and $\hbar\omega_x = 0$ meV no smearing occurs and the conductance is a step function. The same smearing situation is achieved by either setting $T = 0$ K and $\hbar\omega_x = 10$ meV or by setting $T = 18.2$ K and $\hbar\omega_x = 0$ meV. Grayscale plots depict the smearing of the quantized depending solely on temperature changes in c) and solely on changes of ω_x in d). Characteristic values ω_c and T_c represent values where the quantized conductance is just smeared out (solid lines). The dashed lines mark the $G(V_g)$-curves that are shown in b). The gray areas correspond to an electrical conductance that is completely smeared out by either T or ω_x.

Non-linear transport regime

A finite source-drain voltage V_{SD} has a crucial impact on the transport properties of an 1D constriction. Whereas in the case $eV_{\mathrm{SD}} > E_{\mathrm{F}}$ the observation of negative differential resistances is predicted [54], the occurrence of 'half plateaus' in the quantized conductance is predicted by Glazman and Khaetskii [55] in the case $eV_{\mathrm{SD}} \approx \hbar\omega_y$. The calculation of the conductivity leads to self-consistent equations, but can be simplified with the assumption of an adiabatic 1D constriction, ballistic transport and a voltage drop βV_{SD}, that occurs between source contact and 1D constriction and a voltage drop $(1-\beta)V_{\mathrm{SD}}$, that occurs between drain contact and 1D constriction. In this picture [56] the energy eigenstates from Eq. 2.24 remain unchanged in the presence of V_{SD} and the chemical potentials can be understood as $\mu_{\mathrm{S}} = E_{\mathrm{F}} + \beta eV_{\mathrm{SD}}$ for the source contact and $\mu_{\mathrm{D}} = E_{\mathrm{F}} - (1-\beta)eV_{\mathrm{SD}}$ for the drain contact. Here, E_{F} refers to the Fermi energy in the case $V_{\mathrm{SD}} \to 0$. The number of populated subbands in the 1D constrictions now have to be distinguished between N_+ for μ_{S} and N_- for μ_{D}. The electrical conductance through the 1D constriction is then calculated as

$$G = \frac{2e^2}{h}(\beta N_+ + (1-\beta)N_-). \tag{2.29}$$

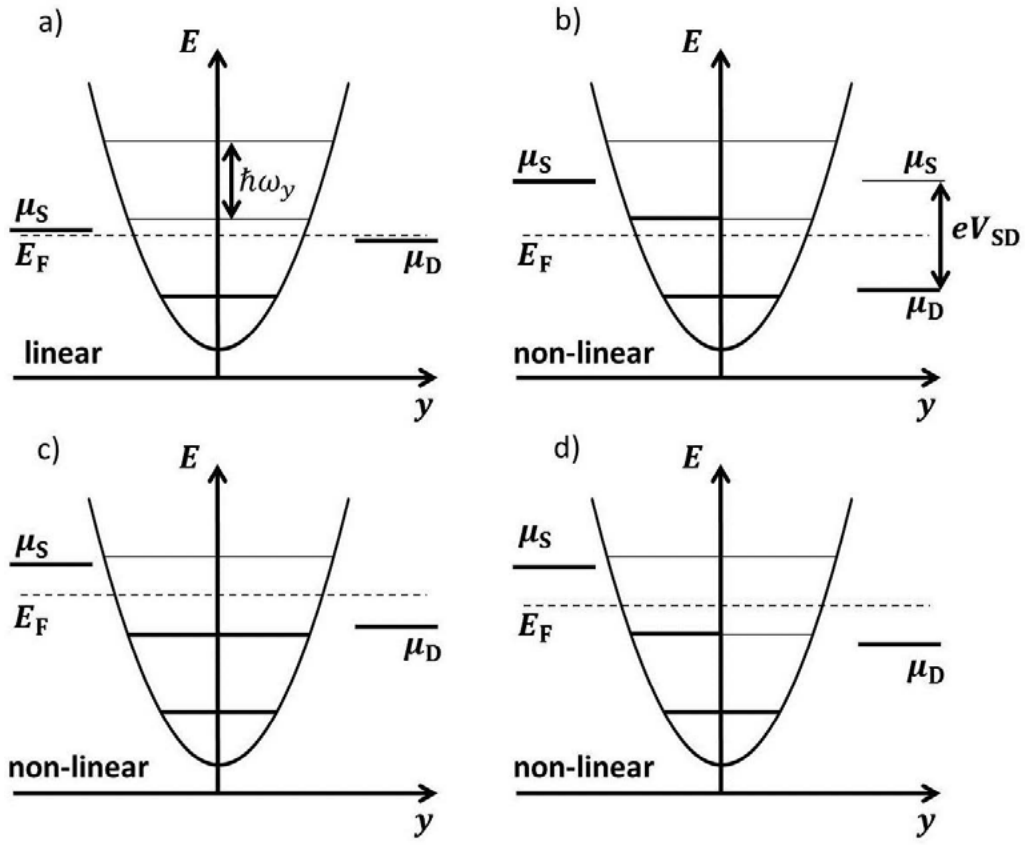

Figure 2.5: Schematic of the occupation of the subbands of an adiabatic 1D constriction in the a) linear and b)-d) non-linear regime with energetic subband separation of $\hbar\omega_y$. a) In the linear regime the applied source-drain voltage is $eV_{\mathrm{SD}} \ll \hbar\omega_y$ and b) $eV_{\mathrm{SD}} \approx \hbar\omega_y$ in the non-linear regime. c) A special case in the non-linear regime is when E_{F} is aligned between two subbands. d) The second special case is when $eV_{\mathrm{SD}} = \mu_{\mathrm{S}} - \mu_{\mathrm{D}} = \hbar\omega_y$. In both special cases c) and d) the parity of $N = N_- + N_+$ (see text) cannot change when c) $E_{\mathrm{F}} = \text{const.}$ and d) $V_{\mathrm{SD}} = \text{const.}$

For adiabatic systems it was calculated that $\beta = 0.5$ is a justified approximation and Eq. 2.29 simplifies to

$$G = \frac{e^2}{h}(N_+ + N_-). \tag{2.30}$$

In the linear regime $V_{\mathrm{SD}} \to 0$ the occupation numbers N_- and N_+ no longer differ from each other and Eq. 2.29 becomes Eq. 2.19 again with $\mu_{\mathrm{S}} \approx E_{\mathrm{F}} \approx \mu_{\mathrm{D}}$ and therefore $N = N_- = N_+$. The occupation of the subbands of an adiabatic 1D constriction in the linear regime can be seen in Fig. 2.5 a). In the non-linear regime the difference of the occupation numbers $\Delta N = N_+ - N_-$ increases for every subband energy that is lower than μ_{S}, but higher than μ_{D}. In this way ΔN may adopt values 0,1,2,3... with increasing V_{SD}. In contrast, ΔN can only be 0 or 1 if $eV_{\mathrm{SD}} < \hbar\omega_y$ and E_{F} is changed because a change of E_{F} simultaneously increases μ_{S} and μ_{D} by the exact same energy. The 'half plateaus' of the quantized conductance appear if ΔN is an odd number, see Fig. 2.5 b), and become normal plateaus of $2e^2/h$ again if ΔN is an even number. This behavior was experimentally verified by Patel *et. al.* [57].

The amount of energy ΔeV_{SD} that is required to change ΔN from odd to even periodically depends on E_{F} and vice versa. However, there are two special cases in which a transition of ΔN from odd to even cannot be achieved. In the first case, E_{F} is perfectly aligned in the center of the energies of two subsequent subbands j and $j+1$ of the constriction, i.e. if $E_{\mathrm{F}} = (E_j + E_{j+1})/2$, as depicted in Fig. 2.5 c). A variation of V_{SD} that causes μ_{S} to surpass the energy of the subband $j+1$ would also cause μ_{D} to drop below the energy of the subband j, thus leaving the parity of ΔN unchanged. This occurs if $e\Delta V_{\mathrm{SD}} = \mu_{\mathrm{S}} - \mu_{\mathrm{D}} = l\hbar\omega_y$ with $l = 0,1,2....$ In the second case, depicted in Fig. 2.5 d), eV_{SD} also adopts an energy, that is equal to $eV_{\mathrm{SD}} = l\hbar\omega_y$ with $l = 0,1,2....$ If E_{F} is sweeped, μ_{S} and μ_{D} surpass the next energy level simultaneously at $E_{\mathrm{F}} = E_j = \hbar\omega_y(j + 1/2)$ and the parity ΔN remains unchanged. In experiment E_{F} is varied by the change of the voltage of a gate electrode $\Delta V_{\mathrm{g}} = \Delta E_{\mathrm{F}}/\gamma e$, which leads to

$$\hbar\omega_y = e\Delta V_{\mathrm{SD}} = \gamma e \Delta V_{\mathrm{g}} \tag{2.31}$$

with the gate efficiency γ. Eq. 2.31 presents the basic concept of the subband spectroscopy in which the non-linear regime is used to measure the subband spacing $\hbar\omega_y$. The systematic transitions between the full conductance plateaus and the 'half plateaus' result in the occurrence of a rhombic structure in a grayscale plot of the transconductance $\mathrm{d}G(V_{\mathrm{g}},V_{\mathrm{SD}})/\mathrm{d}V_{\mathrm{g}}$. In this rhombus each diagonal represents one of the two mentioned special cases, i.e. $\Delta V_{\mathrm{SD}} = \hbar\omega_y/e$ along the V_{SD}-axis and $\Delta V_{\mathrm{g}} = \hbar\omega_y/\gamma e$ along the V_{g}-axis. A schematic of the rhombus pattern is depicted in Fig. 2.6. The usage of the rhombus pattern to determine the subband spacing of an 1D constriction is a widely used technique [57, 52, 58, 59, 60].

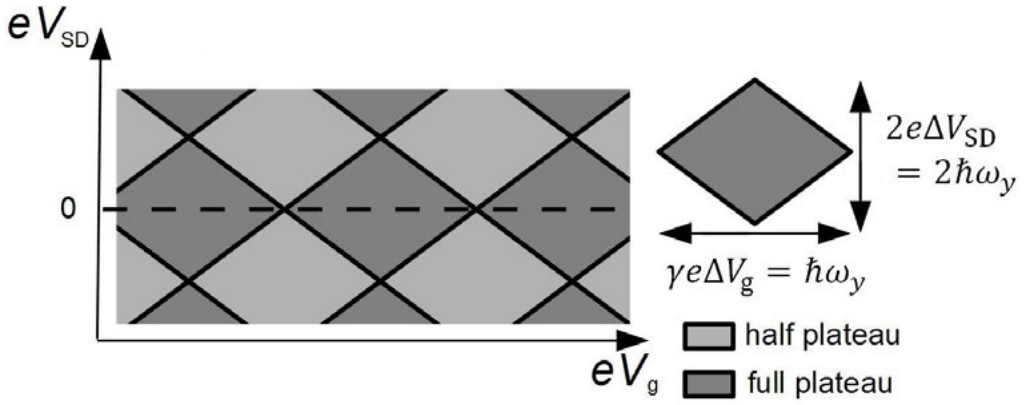

Figure 2.6: Schematic of a grayscale plot of the transconductance with applied DC voltage V_{SD}. The gray regions represent half plateaus (bright) and full plateaus (dark) of the differential conductance and form a rhombus pattern. The dark lines between the different regions represent transitions from one plateau to the next plateau. The form of the rhombus is determined by the subband spacing of the 1D constriction and the gate efficiency γ, as indicated by the single rhombus on the left-hand side.

2.3 Quantum Hall and Shubnikov-de Haas effect

In Sec. 2.1 the concept of low-dimensional electron gases was introduced. It was shown that the energy eigenvalues of the energy of a two-dimensional electron gas (2DEG) can be expressed as

$$E_j(k_x,k_y) = \frac{\hbar^2(k_x^2 + k_y^2)}{2m_e^*} + E_j(0,0), \tag{2.32}$$

when the movement of the electron is restricted to the xy-plane and $E_j(0,0)$ represents the quantized energy eigenvalues in z-direction. Applying a magnetic field B_z perpendicularly to the 2DEG causes the electrons to move on a circular path with the cyclotron frequency $\omega_\mathrm{c} = eB_z/m_\mathrm{e}^*$ if scattering is not considered. Here, it is assumed that the effective mass m_e^* is isotropic in x and y-direction. The circular movement can be described as a superposition of one harmonic oscillator in x-direction and one in y-direction, both with the eigenfrequency ω_c. The energy eigenvalues of the 2DEG with an applied magnetic field are

$$E_{j,n,s} = (n + \frac{1}{2})\hbar\omega_\mathrm{c} + sg\mu_\mathrm{B}B + E_j(0,0), \tag{2.33}$$

where s can adopt values of $s = \pm 1$ and accounts for the spin degeneracy, μ_B is the Bohr magneton and g the Landé factor. Eq. 2.33 shows that the application of the magnetic field leads to a further reduction of the dimensionality of the electron gas. The energy eigenvalues are separated by $\hbar\omega_\mathrm{c}$, are referred to as Landau levels and lead to a splitting of the continuous parabolic subbands from Eq. 2.32 into quantized values. The density of states splits from the 2D step function (see Sec. 2.1) into δ-like functions where the peaks are separated by $\hbar\omega_\mathrm{c}$. Due to defects in the device these peaks are broadened, as can be seen in Fig. 2.7 a).

In Fig. 2.7 b) a typical 2D Hall bar is depicted with applied source-drain voltage $V_\mathrm{SD} = (\mu_\mathrm{S} - \mu_\mathrm{D})/e$ and a perpendicularly applied external magnetic field B. Besides the source and drain contacts, four additional contacts 1-4 with chemical potentials μ_1, μ_2, μ_3 and μ_4 serve to probe the Hall resistance $R_\mathrm{xy} = V_\mathrm{y}/I_\mathrm{x} = (\mu_1 - \mu_4)/eI_\mathrm{x} = (\mu_2 - \mu_3)/eI_\mathrm{x}$ and the longitudinal resistance $R_\mathrm{xx} = V_\mathrm{x}/I_\mathrm{x} = (\mu_1 - \mu_2)/eI_\mathrm{x} = (\mu_3 - \mu_4)/eI_\mathrm{x}$ of the device. At high magnetic fields electrons in the bulk of the device move in closed circular paths (red circle). At the edge of the 2D device this circular path cannot be completed and electrons bounce off the edge elastically and instead move along the edge (blue lines).

Due to the strong bending of the electron trajectories, when elastically reflected by the potential barrier, the energy dispersion in Eq. 2.33 is modified to higher energies in the vicinity of the edge, as illustrated in Fig. 2.7 c). This causes the Landau levels to cross the Fermi energy E_F, even if the Landau levels have far less energy than E_F in the bulk. The strong magnetic field forces the electron to propagate in the same direction, even in the case of scattering with defects, without reducing the electric current I_x, i.e. without dissipation. Note that since the two adjacent edges carry the same current in opposite directions, the net current is zero. If E_F is located in between Landau levels, it is impossible for an electron to scatter from one edge to the adjacent edge since no energy levels can be occupied in the bulk. In this case the chemical potentials are $\mu_\mathrm{S} = \mu_1 = \mu_2$ and $\mu_\mathrm{D} = \mu_3 = \mu_4$ and the resulting resistance R_xx is zero. However, if E_F coincides with a Landau level in the bulk, scattering to the opposite edge is possible and R_xx increases to a

maximum. The position of the Landau levels relative to E_F is shifted according to Eq. 2.33 and therefore allows to populate more edge channels at lower B and less at higher B. Note that broadening of the Landau levels due to sample impurities allows E_F to adopt values between $E_{j,n,s}$ and $E_{j,n+1,s}$ and that the bath temperature has to be very small for a sharp Fermi distribution. This model is referred to as edge-state model.

The dissipationless transport along the edge channels reminds on the ballistic transport in 1D conductors, introduced in Sec. 2.2, and the edge-state model can be interpreted in terms of the Landauer-Büttiker formalism that is presented in Sec. 2.2. If spin-degenerate, each participating channel contributes $2e^2/h$ to the resulting electrical conductance of one edge whose resistance is therefore

$$R_\mathrm{H} = \frac{1}{\nu}\frac{h}{e^2}, \tag{2.34}$$

where ν is the filling factor that represents the number of participating channels and accounts for spin degeneracy. The degeneracy of each Landau level is $N_\mathrm{L} = eB/h$, i.e. depends on the magnetic field. Together with the position of the minima/maxima of R_xx with index i and the corresponding magnetic fields B_i the 2D carrier density (sheet density) can be obtained by using

$$n_\mathrm{s} = \nu N_\mathrm{L} = 2iN_\mathrm{L} = 2i\frac{eB}{h}, \tag{2.35}$$

where in the second step spin degeneracy is considered with $\nu = 2i$. For two adjacent minima or maxima with B_i and B_{i+1} Eq. 2.35 becomes

$$(\frac{1}{B_{i+1}} - \frac{1}{B_i}) = \Delta\frac{1}{B_i} = 2\frac{e}{n_s h}. \tag{2.36}$$

Fig. 2.7 d) shows the measurement of R_xx and R_xy in the Hall bar configuration in an InAs-based device at $T_\mathrm{bath} = 0.3$ K. It can be seen that at higher fields ($B > 2$ T) the Hall plateaus are visible and $R_\mathrm{xy} \equiv R_\mathrm{H}$ is found according to Eq. 2.35. The filling factor indicates a lift of the spin degeneracy of the Landau levels for $B > 2.4$ T. This effect is referred to as quantum Hall effect (QHE) - or integer quantum Hall effect (IQHE) - and was first discovered by Klaus von Klitzing in 1980 [18] for which he was awarded the Nobel prize in 1985. The longitudinal resistance R_xy is zero for $B > 2$ T and forms peaks at magnetic fields that coincide with transition regions between Hall plateaus. These peaks are referred to as Shubnikov-de Haas oscillations. For further insight literature by Ibach and Lüth [61] is recommended at this point.

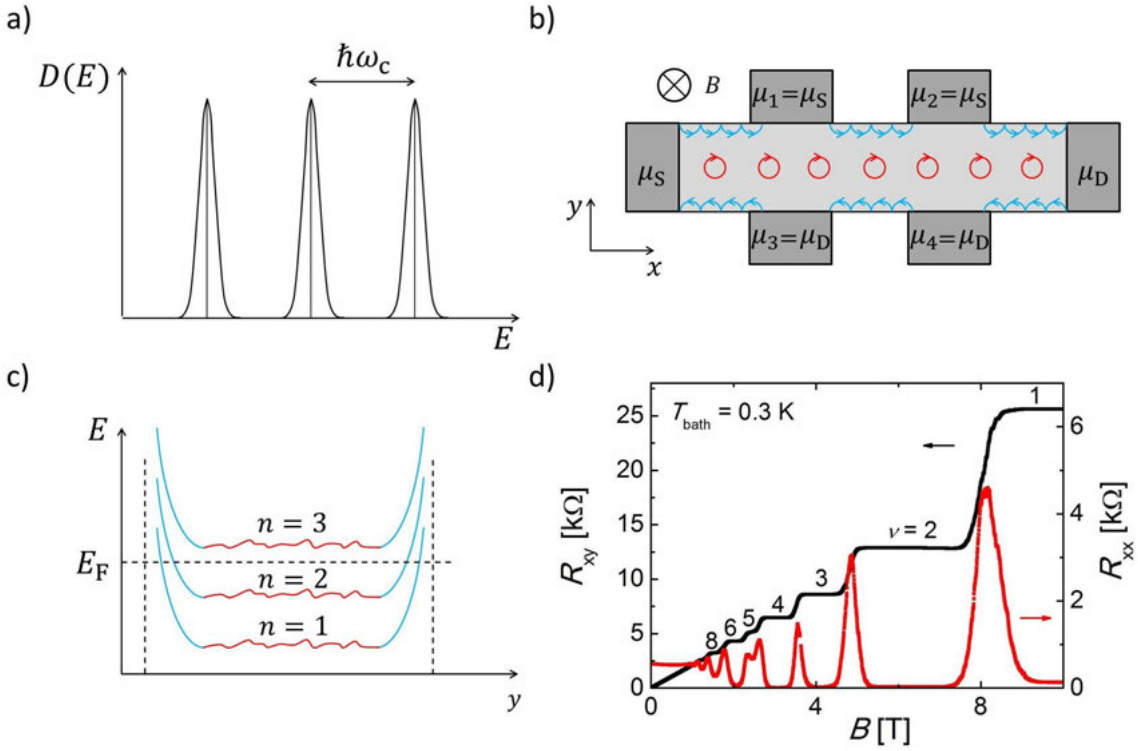

Figure 2.7: a) Density of states $D(E)$ of the 2DEG in the presence of an external magnetic field. The peaks are separated by $\hbar\omega_c$, are referred to as Landau levels and are broadened due to defects in the sample. b) Schematic of the edge-state model in a Hall bar. High magnetic fields cause electrons to move in closed circles, leading to localized states (red). The boundary of the sample prevents this movement and electrons bounce off the edges, leading to edge channels (blue). The strong magnetic field forces electrons to move in one direction when scattering with defects or vacancies, preventing the reduction of the current I_x when the source-drain voltage $V_{SD} = (\mu_S - \mu_D)/e$ is applied. This causes $\mu_S = \mu_1 = \mu_2$ and $\mu_D = \mu_3 = \mu_4$ and therefore $R_{xx} = V_{SD}/I_x = 0$. According to the Landauer-Büttiker formalism each edge channel contributes, if spin-degenerate, $2e^2/h$ to the overall conductance while the localized states in the bulk do not contribute. This effect holds if E_F is aligned in between two Landau levels, as shown in c). c) The peaks in $D(E)$ in a) lead to subbands n = 1,2,3... in the bulk which are modified to higher energies at the boundary due to strongly bent (by elastic reflection) electron trajectories. This allows E_F to cross with the Landau levels at the edges. The fluctuations of the Landau levels originate from scattering of electrons in a non-ideal Hall bar. d) Measured quantum Hall resistance R_{xy} and longitudinal resistance R_{xx} in an InAs-based Hall bar. Plateaus of R_{xy} correspond to an alignment of E_F between Landau levels. Transition regions between plateaus coincide with peaks in R_{xx} and correspond to an alignment of E_F with the Landau levels, allowing scattering between adjacent edge channels. The filling factor ν accounts for the contributing edge channels, taking spin degeneracy into account. Here, lifting of the spin degeneracy is achieved at $B \approx 2.4$ T.

2.4 Quantum interference phenomena

In the last section the wave-like nature of the electron became important when the electric potential led to a spatial confinement in one or more dimensions. The probability density ρ, that is the square of the electron's wave function $\rho = |\Psi|^2$, allows the electron to be at different locations at the same time and also to take different paths at once when traveling from one location to another. The wave function of the electron Ψ can be considered as superposition of the respective wave function for the electron traveling along the different paths

$$\Psi = \sum_{\gamma}^{N} \Psi_{0,\gamma} e^{i\varphi_\gamma}, \tag{2.37}$$

with the number of the paths N, the phase φ_γ and the amplitude $\Psi_{0,\gamma}$ of the electron wave in the path γ.

Magnetic Aharanov-Bohm Effect

In the following, a quantum ring system is considered, with the two arms referred to as γ_1 and γ_2. An electron that is about to propagate the quantum ring will have its wave function split at the first intersection of the ring into the two wave functions Ψ_1 and Ψ_2, as depicted in Fig. 2.8 a). At the second intersection Ψ_1 and Ψ_2 interfere constructively or destructively with each other depending on their phase difference $\Delta\varphi = \varphi_2 - \varphi_1$. The phase difference is accumulated along the covered paths γ_1, γ_2 in the time T_1, T_2 with

$$\Delta\varphi_{1,2} = \int_{\gamma_1,\gamma_2} \vec{k}_{1,2}\ \mathrm{d}\vec{r} = \frac{1}{\hbar}\int_{\gamma_1,\gamma_2} (m\vec{v}_{1,2} + e\vec{A})\ \mathrm{d}\vec{r}, \tag{2.38}$$

where $\vec{A}$ denotes the vector potential that stems from a magnetic field $\vec{B} = \vec{\nabla} \times \vec{A}$. With $\vec{v} = \int \vec{a}\mathrm{d}t = -e/m \int \vec{E}\mathrm{d}t$ and $\vec{E} = -\vec{\nabla}\phi$ Eq. 2.38 becomes

$$\Delta\varphi_{1,2} = \frac{e}{\hbar}(\int_{T_1,T_2} \phi\ \mathrm{d}t + \int_{\gamma_1,\gamma_2} \vec{A}\ \mathrm{d}\vec{r}). \tag{2.39}$$

Here, $\vec{E}$ is an applied electric field and ϕ the electric potential. The phase difference $\Delta\varphi = \varphi_2 - \varphi_1$ that is accumulated due to the vector potential $\vec{A}$ is

$$\Delta\varphi = \frac{e}{\hbar}\oint_{\gamma_1,\gamma_2} \vec{A}d\vec{r} = \frac{e}{\hbar}\int_F \vec{\nabla} \times \vec{A}\mathrm{d}\vec{f}. \tag{2.40}$$

In the last step Stokes' theorem was used with F as the boundary, f as the surface that is enclosed by the two paths γ_1 and γ_2 and $\mathrm{d}\vec{f}$ as the normal vector to f. According to Maxwell's equation $\vec{B} = \vec{\nabla} \times \vec{A}$ Eq. 2.40 can be formed to

$$\Delta\varphi = \frac{e}{\hbar}\int_F \vec{B}d\vec{f} = \frac{e}{\hbar}B_\perp F = \frac{e}{\hbar}\Phi_\mathrm{m} \tag{2.41}$$

with the magnetic flux Φ_m and $B_\perp$ as the part of the magnetic field that is perpendicular to the surface F. The Eq. 2.41 leads to the conclusion that the wave function amplitude changes periodically with $B_\perp$ with a period of $\Phi_\mathrm{m} = 2\Phi_0 = h/e$. This corresponds to the periodicity $\Delta B_\perp = h/(eF)$ of the magnetic field.

Looking at the starting point of the ring, a constructive interference hinders the electron transport, resulting in the rise of the measured resistance, whereas destructive interference leads to a lower resistance. This is observed in several magnetoresistance effects, such as the Aharonov-Bohm effect [6], the weak localization (WL) and the weak anti-localization (WAL) [62, 63]. A similar effect is also observed if an electric scalar potential is applied to the electron trajectories, as observed in the type-II Aharonov-Bohm effect [64].

Electrostatic Aharanov-Bohm Effect

In addition to the presence of a vector potential $\vec{A}$ the phase φ of an electron's wave function can be changed by an electric scalar potential Φ_{el}. If an electron is exposed to a time-dependent scalar potential $\Phi_{\mathrm{el}}(t)$ for the duration T, the accumulated phase can be expressed as

$$\Delta\varphi = \frac{e}{\hbar}\int_{\mathrm{T}} \Phi_{\mathrm{el}}\ \mathrm{d}t. \tag{2.42}$$

Assuming that electrons move with the Fermi velocity $\vec{v}_{\mathrm{F}}$, it is possible to substitute $\mathrm{d}t = \mathrm{d}\vec{r}/|\vec{v}_{\mathrm{F}}|$. In terms of the Fermi wave vector $\vec{k}_{\mathrm{F}} = m_{\mathrm{e}}^{*}\vec{v}_{\mathrm{F}}/\hbar$ with the effective

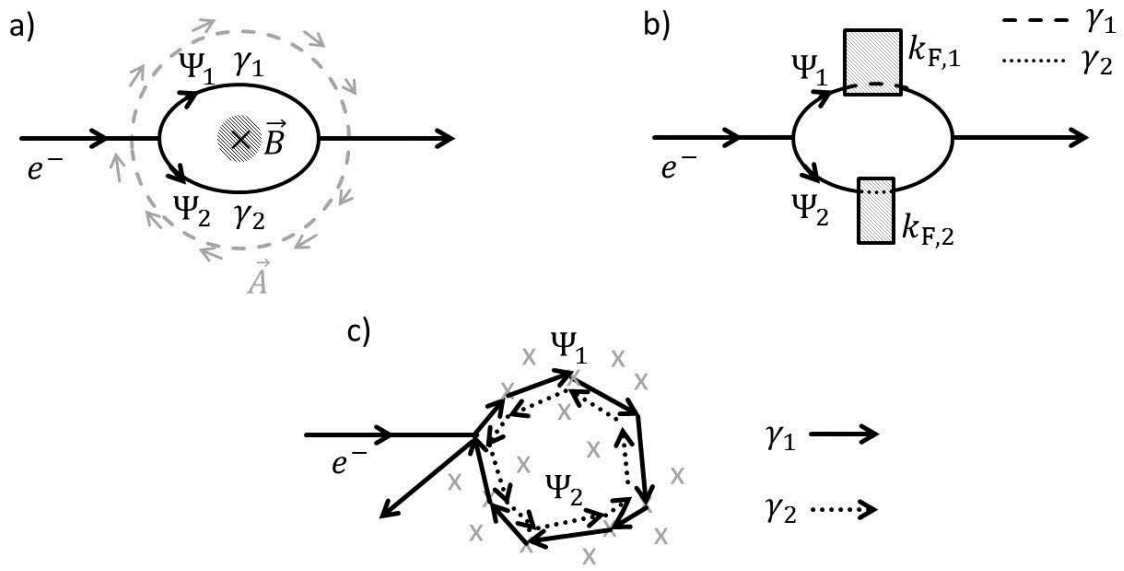

Figure 2.8: Schematic of the interference paths in a) the type-I and b) type-II Aharonov-Bohm effect and in c) the weak localization effect. a) In the type-I Aharonov-Bohm effect an electron wave propagates through the two arms of a quantum ring simultaneously with wave function Ψ_1 through the upper arm and Ψ_2 through the lower arm. The electron waves Ψ_1 and Ψ_2 interfere at the right intersection of the arms. An additional phase may be induced by a vector potential $\vec{A}$ of an applied external magnetic field $\vec{B}$, leading to constructive or destructive interference. b) In the type-II AB effect this additional phase shift is induced by an applied electrostatic potential over the path γ_1 and/or γ_2 that changes the electron's Fermi wavelength λ_{F}. c) An electron that propagates through a disordered system may take several paths at once according to the principle of superposition. Elastic scattering enables the electron to take closed paths. Electron waves Ψ_1 and Ψ_2 that form closed trajectories in opposite directions interfere with each other, leading to a localization.

mass m_e^* this substitution becomes $dt = m_e^* d\vec{r}/|\vec{k}_F|\hbar$ and Eq. 2.42 becomes

$$\Delta\varphi = \frac{e m_e^*}{\hbar^2} \int_\gamma \frac{\Phi_{el}}{|\vec{k}_F|}\, d\vec{r} = \int_\gamma \vec{k}_F\, d\vec{r} \tag{2.43}$$

with the path γ that is traveled in the time T. In the last step the Virial theorem was applied, relating the mean average over time of kinetic energy and the mean average over time of the potential energy, i.e. $e\Phi_{el}/2 = \hbar^2|\vec{k}_F|^2/2m_e^*$. In an interferometer this phase evolution can have similar effects as the magnetic, or type-I, Aharonov-Bohm effect and is referred to as type-II Aharonov-Bohm effect [64].

Consider a quantum ring whose arms are each covered by a finger gate, as schematically depicted in Fig. 2.8. An electron wave propagates through the ring by splitting into the wave functions Ψ_1 and Ψ_2. The two finger gates cover the length γ_1 of the upper arm and the length γ_2 of the lower arm. The corresponding gate voltages V_{g1} and V_{g2} are applied, leading to the Fermi vectors k_{F1} and k_{F2}. According to Eq. 2.43 the accumulated phases are $\Delta\varphi_1 = k_{F1}\gamma_1$ for the upper arm and $\Delta\varphi_1 = k_{F2}\gamma_2$ for the lower arm. The resulting phase shift of the two electron waves relative to each other is then $\Delta\varphi = \varphi_1 - \varphi_2 = k_{F1}\gamma_1 - k_{F2}\gamma_2$. Note that if a global top-gate covers the device, the geometry of the quantum ring device needs to be asymmetric in order to show the type-II Aharonov-Bohm effect. In a symmetric device electron waves would acquire the same phase in both arms, leading to a relative phase shift of 0.

Weak localization and weak anti-localization

Weak localization appears in disordered systems and is considered to be a precursor of the Anderson localization [65], which occurs in systems of high disorder. An electron in the quantum regime that travels from point A to point B may take several paths at once according to the principle of superposition, see Eq. 2.37. The probability W_{AB} of the electron to be found in point B is

$$\begin{aligned} W_{AB} = |\Psi_{AB}|^2 &= \sum_{\gamma,\gamma'}^{N} \Psi_{0,\gamma}\Psi_{0,\gamma'}^* e^{i(\varphi_\gamma - \varphi_{\gamma'})} \\ &= \sum_{\gamma=\gamma'}^{N} \Psi_{0,\gamma}\Psi_{0,\gamma'}^* e^{i(\varphi_\gamma - \varphi_{\gamma'})} + \sum_{\gamma\neq\gamma'}^{N} \Psi_{0,\gamma}\Psi_{0,\gamma'}^* e^{i(\varphi_\gamma - \varphi'_\gamma)} \\ &= W_{cl} + W_{qm}. \end{aligned} \tag{2.44}$$

The first term W_{cl} describes non-interfering paths and represents the classical result. The second term W_{qm} describes wave functions that travel different paths and interfere with each other in point B. Hence, the latter term represents the quantum mechanical contribution to the probability W_{AB}. In order to enable interference, the phase information of the electron has to be conserved, which is achieved at low temperatures, where $\tau_{in} \gg \tau$. Since interfering wave functions mostly travel paths γ with different lengths, in average the accumulated phase difference $\Delta\varphi$ of the wave functions is zero.

$$W_{AB} = W_{cl} = \sum_{\gamma}^{N} \Psi_{0,\gamma}\Psi_{0,\gamma}^*. \tag{2.45}$$

However, if the starting point A and the end point B coincide, W_{AB} becomes the probability R_{AA} for the electron to be reflected to its starting point. If time-reversal

symmetry (TRS) for electrons in this system is given, i.e. the equivalence of states with $-\vec{k}$ and $+\vec{k}$ is valid, taking a path forward (γ) and backward ($\tilde{\gamma}$) results in the same final phase for the electron wave. In this case, the interference of two wave functions that travel the same path backward and forward is constructive due to the same path lengths and Eq. 2.44 becomes

$$R_{\mathrm{AA}} = |\Psi_{\mathrm{AA}}|^2 = \sum_{\gamma}^{N} \Psi_{0,\gamma}\Psi_{0,\gamma}^{*} + \sum_{\gamma,\tilde{\gamma}}^{N} \Psi_{0,\gamma}\Psi_{0,\tilde{\gamma}}^{*} = R_{\mathrm{cl}} + R_{\mathrm{qm}}. \tag{2.46}$$

In the presence of TRS $\Psi_{0,\gamma} = \Psi_{0,\tilde{\gamma}}$ holds and the reflection probability of the electron becomes

$$R_{\mathrm{AA}} = 2 \cdot \sum_{\gamma}^{N} \Psi_{0,\gamma}\Psi_{0,\gamma}^{*} = 2 \cdot R_{\mathrm{cl}}. \tag{2.47}$$

The quantum mechanical term R_{qm} enhances the total reflection probability, i.e. the localization of the electron, compared to the classical reflection probability R_{cl} and is referred to as weak localization $R_{\mathrm{qm}} \equiv R_{\mathrm{WL}} = R_{\mathrm{cl}}$. So far, spin-orbit coupling (SOC) is not considered and also would have no influence on the term R_{cl}. However, strong SOC causes the spin of the electron to rotate by π as it travels along path γ and $-\pi$ along $\tilde{\gamma}$. The total rotation of 2π causes the two wave functions to have opposite signs in their spin states. The periodicity of a fermion's spin is 4π, which means that the quantum correction term changes its sign to $R_{\mathrm{qm}}^{\mathrm{SOC}} \equiv R_{\mathrm{WAL}} = -R_{\mathrm{cl}}$ and Eq. 2.46 becomes

$$R_{\mathrm{AA}}^{\mathrm{SOC}} = R_{\mathrm{cl}} + R_{\mathrm{qm}}^{\mathrm{SOC}} = R_{\mathrm{cl}} - R_{\mathrm{cl}} = 0. \tag{2.48}$$

This is known as weak anti-localization. In the last section it became clear that an electron acquires an additional phase as it travels through a vector potential $\vec{A}$. The acquired phase depends on the length of the covered path. This means that statistically the quantum mechanical terms in Eqs. 2.46 and 2.48 vanish, due to the different lengths of the various paths γ, γ' and $\tilde{\gamma}$, as $|\vec{B}|$ increases. It can be concluded that the localization and hence the electrical conductance G depends on the magnetic field. The magnetic field dependence of the conductance $G(\vec{B})$ of 2D systems can be described by the Hikami-Larkin-Nagaoka equation [66], that is

$$\sigma(B) - \sigma(0) = \alpha \frac{e^2}{2\pi^2\hbar} \left[\ln(\frac{B_\phi}{B}) - \Psi(\frac{1}{2} + \frac{B_\phi}{B}) \right] \tag{2.49}$$

in the limit of strong spin-orbit interaction. Here, $B_\phi = \hbar/4el_\phi^2$ describes the phase coherence characteristic field. The dominant effect is the weak localization if $\alpha = -1$ and weak anti-localization if $\alpha = +1/2$.

2.5 Thermal noise

In signal processing noise is typically considered as a phenomenon that is unwanted and hampers signal detection due to its random nature, especially when measuring the quantum effects presented in the previous sections. However, the randomness of noise mostly obeys a statistic that is specific to its origin. Noise spectroscopy allows to deduce information about the physical properties and processes that generate the corresponding noise and enhance the understanding of the system itself. Noise can have various origins depending on the system that is observed and the circumstances that are created for the system. Thermal noise, 1/f-noise, generation-recombination noise, telegraphic noise and shot noise are the most common noise types and can combine with each other in the power spectral density (PSD) $S_{\mathrm{V}}(f)$, as illustrated in Fig. 2.9 c) for thermal noise and 1/f noise. Thermal noise is the type of noise that is in the focus of this thesis and will be explained in the following.

One basic concept of thermodynamics is that temperature is a measure of the average kinetic energy of a molecule gas or electron gas with the latter being more relevant for this thesis. This thermal agitation causes an electron to have a random component in its movement through an electrical conductor, which leads to random fluctuations of the potential landscape in the conductor. The resulting fluctuations of the voltage $V(t)$ are zero when averaged over time. However, in 1928 J. B. Johnson experimentally found the variance of the voltage to be

$$\overline{V(t)^2} = 4k_{\mathrm{B}}T_{\mathrm{e}}R\Delta f \tag{2.50}$$

with the bandwidth Δf, the electron temperature T_{e}, the conductor's resistance R and the Boltzmann constant k_{B} [67]. The random voltage fluctuations $\overline{V(t)^2}$ are directly connected to the dissipative element with the resistance R and are therefore an application of the fluctuation-dissipation theorem [68]. The effect, described by Eq. 2.50, was theoretically derived by H. T. Nyquist [69] and is therefore known as the Johnson-Nyquist noise or thermal noise. It has to be noted that the fluctuations

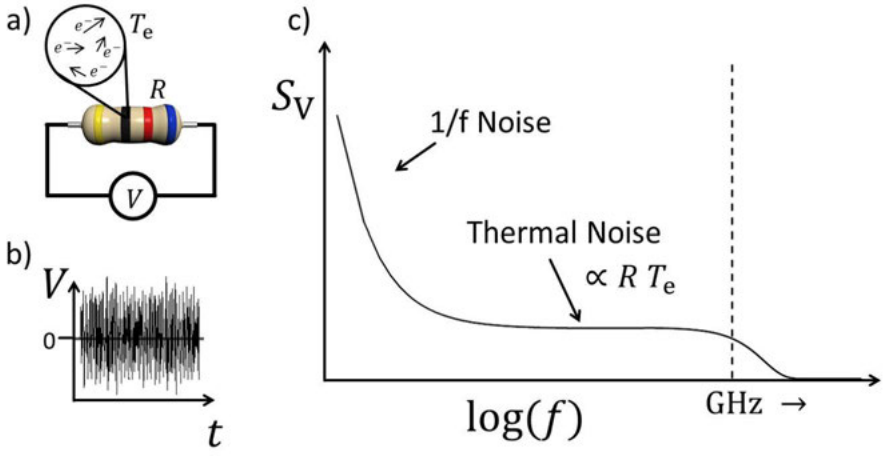

Figure 2.9: a) Illustration of the thermal agitation of electrons in a resistor. b) The voltage probe indicates, that these fluctuations lead to a voltage fluctuation over time. c) A schematic of the power spectral density for thermal noise that is superposed by low-frequency 1/f noise. The dashed line indicates the GHz frequency regime up to which the thermal noise is frequency-independent.

described by Eq. 2.50 also exist in equilibrium in the absence of an external applied voltage. Nyquist's derivation is not based on a resistor with specific properties, which means that thermal noise is expected to occur in any resistive material and is even observed in low-dimensional electron gases of $Al_xGa_{1-x}As/GaAs$ devices [70, 71]. According to the Wiener-Chintschin theorem [72, 73]

$$r_{xx}(\Delta t) = \int_{-\infty}^{\infty} S_{xx}(f) e^{2\pi i f \Delta t} \mathrm{d}f \tag{2.51}$$

the power spectral density $S_{xx}(f)$ can be expressed as the Fourier transformation of the auto-correlation function $r_{xx}(\Delta t) = V(t) \cdot V(t+\Delta t)$ that describes the correlation of a signal $V(t)$ at a time t with the same signal at a time $t + \Delta t$. Since thermal noise is based on a random process, the auto-correlation function is non-zero only if $\Delta t = 0$ s. Therefore, Eq. 2.51 becomes

$$r_{xx}(0) = \int_{-\infty}^{\infty} S_{\mathrm{xx}}(f) \mathrm{d}f = \overline{V(t)^2} = 4 k_{\mathrm{B}} T_{\mathrm{e}} R \Delta f. \tag{2.52}$$

Deriving Eq. 2.52 with respect to f, leads to

$$S_{\mathrm{xx}}(f) = 4 k_{\mathrm{B}} T_{\mathrm{e}} R \equiv S_{\mathrm{V,w}}. \tag{2.53}$$

The PSD of the thermal noise is white, i.e. frequency-independent, and will be named $S_{\mathrm{V,w}}$ in this thesis. Considering that thermal noise is supposed to have the same PSD for all frequencies, Eq. 2.50 would lead to an infinite energy, known as the ultraviolet catastrophe. However, in Nyquist's derivation of the thermal noise it can be seen that Eq. 2.50 is an approximation of

$$\overline{V(t)^2} = \frac{4Rhf}{\exp(hf/k_{\mathrm{B}}T_{\mathrm{e}}) - 1} \Delta f \tag{2.54}$$

if $f \ll k_{\mathrm{B}} T_{\mathrm{e}}/h$ is satisfied. Eq. 2.54 is motivated from Planck's law and therefore prevents the ultraviolet catastrophe. In experiment, this only becomes important in the GHz regime of the noise frequency. However, in this thesis noise signals with $f \ll k_{\mathrm{B}} T_{\mathrm{e}}/h$ will be investigated. This allows the usage of Eq. 2.53, which finds application mainly in diffusive systems, but can also be used in mesoscopic systems in the ballistic transport regime. In the Landauer-Büttiker formalism the current noise $S_{\mathrm{I}} = S_{\mathrm{V}}/R^2$ can be expressed in terms of an electron's transmission probabilities to propagate through an 1D constriction [74] with

$$S_{\mathrm{I}} = 4 k_{\mathrm{B}} T_{\mathrm{e}} \frac{e^2}{h} \sum_j \int \frac{\partial f}{\partial E} T_j(E) \mathrm{d}E. \tag{2.55}$$

Analogous to Eq. 2.28, this simply becomes $S_{\mathrm{I}} = 4 k_{\mathrm{B}} T \cdot 2e^2/h$ in the limit $T_j \to 1$ at low temperatures when a two-fold spin degeneracy is considered.

Eq. 2.53 allows to apply the thermal noise as a thermometer for the electron temperature T_{e} when the resistance R of the sample is known and vice versa. This allows to use thermal noise as a thermometer of the electron temperature, as explained in the next section.

Electron thermometry

In the last section Eq. 2.53 showed the relation between the electron temperature T_e and the resulting fluctuations of the voltage signal which is represented by the frequency-independent part of its PSD $S_\mathrm{V,w}$. This relation can be used to examine the electron temperature of a system by performing noise spectroscopy. Measuring the noise temperature T_e independently from the lattice temperature T_lat becomes necessary for electron gases at low bath temperatures. The reason for this is the reduced exchange of energy between electrons and phonons due to the decreased number of phonons. Since phonons are considered as bosons, this can be easily understood with the Bose-Einstein statistic

$$\overline{f}_0 = \frac{g_i}{e^{(E_i-\mu)/k_\mathrm{B}T} - 1} \tag{2.56}$$

with the chemical potential μ and the degeneracy g_i of the i-th energy state E_i. The decoupling of T_e from T_lat at low temperatures becomes more distinct if electrons are heated by a heating current I_h, which leads to $T_\mathrm{e} > T_\mathrm{lat}$.

Other thermometry methods that measure the electron temperature are the deduction of T_e from the amplitude of Shubnikov-de Haas oscillations [75], as well as the measurement of the thermovoltage of a QPC with a known Seebeck coefficient [76, 50] and the Coulomb blockade thermometry (CBT) [77]. In the latter method the temperature-dependent tunneling probability of electrons through a potential barrier is exploited. However, these methods require - and thus are limited to - specific sample geometries. This is not the case for noise thermometry [78, 71]. However, the sensitivity of the temperature measurement is enhanced if the electrical resistance R of the investigated device dominates the electrical resistance of the leads R_leads. Another beneficial property of noise thermometry is that Eq. 2.53 connects the measured parameter $S_\mathrm{V,w}$ with T_e by well known quantities. It is therefore not necessary to calibrate the measurement system at different temperature before measuring the noise spectra. This is the property of a primary thermometry method and prevents uncertainties from calibrations from occuring. However, the measurement setup for a primary method is typically more complicated than those of secondary thermometry methods, such as resistance thermometry.

The measurement setup that is used to measure the noise spectra $S_\mathrm{V}(f)$ and the method that allows to deduce the thermal noise $S_\mathrm{V,w}$ from $S_\mathrm{V}(f)$ is shown in Sec. 4.4. In the following the most common models to characterize the origin of noise are presented in short. More detailed information about electrical noise can be found in literature [79, 74, 80, 81].

Shot noise

Shot noise describes random fluctuations of an electric DC current in a circuit which can be modeled by a Poisson process and which originates from the discrete nature of the elementary charge e. The corresponding PSD is $S_\mathrm{P} = 2e|I|$ [82] and is referred to as 'Poisson value'. However, the Poisson limit only holds if all energy modes n of the conductor have a small transmission probability $T_n \ll 1$. Energy modes with perfect transmission $T_n = 1$ or non-transmitting channels $T_n = 0$ do not contribute to shot noise [74]. This is the reason why the measured shot noise S_Shot is always smaller than the Poisson value S_P. This is taken into consideration by the Fano factor $S_\mathrm{Shot}/S_\mathrm{P}$. Similar to thermal noise, shot noise is frequency-independent but

only occurs in the presence of a DC current, i.e. in the non-equilibrium. In this thesis noise measurements are performed in the absence of an intentional electric current, which means $S_{\mathrm{Shot}} \to 0$.

Generation-recombination noise

Generation-recombination (GR) noise is created whenever the number of electrons in a channel fluctuates, e.g. due to localized states that can be occupied by electrons. The frequency-dependent PSD is

$$S_{\mathrm{GR}} = \frac{\overline{\Delta N^2}}{N^2} \frac{4\tau}{1 + (2\pi f \tau)^2} \tag{2.57}$$

with the variance $\overline{\Delta N^2}$ of the number of carriers N and the lifetime τ. In doped $Al_xGa_{1-x}As$/GaAs-based devices these traps can be represented by deep donor traps [83, 84], also called DX-centers [85, 86, 87]. The model of the GR noise allows to obtain information about the lifetimes of the process to trap and detrap an electron for each trap. A special case of the GR noise is the random telegraphic noise [88] that fluctuates between two states due to a single trap.

Flicker noise

1/f noise or 'flicker noise' is characterized by a PSD that is proportional to $f^{-\gamma}$, whereas the exponent is assumed to be $\gamma = 1.0 \pm 0.1$ [79], which is observed in epitaxial GaAs devices [89, 90, 91, 92, 83, 84]. However, exponents that are in the range of $0.9 \leq \gamma \leq 1.4$ are found as well [93]. In contrast to the latter three noise phenomena the origin of 1/f noise is an open question to date [79, 93] and is assumed to change from one material system to another. A significant contribution to the field of 1/f noise stems from Hooge, who introduced the empirical [94] relation

$$S_{\mathrm{V,Hooge}} = \frac{\alpha_{\mathrm{H}} V^2}{fN} \tag{2.58}$$

for pure f^{-1} noise, by studying gold films in the presence of a steady current. Here V describes the voltage across the sample, N is the total number of charge carriers and α_{H} is the dimensionless Hooge parameter, that typically has the value $\alpha_{\mathrm{H}} \approx 2 \cdot 10^{-3}$. For a homogeneously Si-doped $Al_xGa_{1-x}As$/GaAs a Hooge parameter of $\alpha_{\mathrm{H}} = 7.1 \cdot 10^{-4}$ was found [91]. It is believed that - at least in metal films - 1/f noise is a bulk effect rather than a surface effect and stems from mobility fluctuations in most material systems.

Besides this bulk model, proposed by Hooge in 1969 [94], an earlier model, developed by McWorther in 1957 [95], attributed the origin of 1/f noise to a material's surface. The basic concept behind this model is to superpose many different spectra of generation-recombination noise with different trapping times which yields the PSD

$$S_{\mathrm{N,Worther}} \propto \overline{\Delta N^2} \int_{\tau_1}^{\tau_2} \frac{1}{\tau} \frac{4\tau}{1 + (2\pi f \tau)^2} = \overline{\Delta N^2} \frac{1}{f} \tag{2.59}$$

for $\tau_2^{-1} \ll 2\pi f \ll \tau_1^{-1}$. The McWorther model is primarily used for MOSFET devices. However, for bipolar transistors the Hooge model is found to be more accurate.

Addition of noise voltages

The addition of two sinusoidal voltage signals $V_1(t) = A_1 \cdot \sin(2\pi ft)$ and $V_2(t) = A_2 \cdot \sin(2\pi ft + \varphi)$ in series with amplitudes A_1 and A_2, the same frequency f and a relative phase shift of φ produces a mean square value of

$$\begin{aligned} V_{\mathrm{rms}}^2 &= \overline{[V_1(t) + V_2(t)]^2} = \frac{1}{T}\int_0^T [A_1 \cdot \sin(\omega t) + A_2 \cdot \sin(\omega t + \varphi)]^2 \mathrm{d}t \\ &= \frac{A_1^2 + A_2^2 + 2A_1A_2\cos(\varphi)}{2} = V_{\mathrm{rms},1}^2 + V_{\mathrm{rms},2}^2 + 2V_{\mathrm{rms},1}V_{\mathrm{rms},2}\cos(\varphi). \end{aligned} \tag{2.60}$$

The mean square value of the resulting wave is the sum of the mean square values V_1^2 and V_2^2 and a factor that depends on the phase relation between V_1 and V_2. A noise signal consists of a very large number of frequencies with a random distribution of amplitudes and phases. Taking thermal noise, as an example, the effective voltage for a given bandwidth Δf, temperature T_e and resistance R is $V_{\mathrm{rms,n}} = \sqrt{4k_\mathrm{B}T_\mathrm{e}R\Delta f}$, according to Eq. 2.50. Adding the voltage signal of two noise sources, connected in series, $V_{\mathrm{rms,n1}}$ and $V_{\mathrm{rms,n2}}$ results in

$$V_{\mathrm{rms,n}}^2 = V_{\mathrm{rms,n1}}^2 + V_{\mathrm{rms,n2}}^2 + 2K \cdot V_{\mathrm{rms,n1}}V_{\mathrm{rms,n2}}, \tag{2.61}$$

with the correlation factor K [81, 96]. It has to be noted that K has a similar function in Eq. 2.61 as $\cos(\varphi)$ in Eq. 2.60. Noise voltages, produced independently from each other, are uncorrelated, i.e. $K = 0$. Two signals that are identical to each other are 100 % correlated, i.e. $K = 1$, even if their amplitudes differ. An example for this are two sine waves that share the same frequency and phase. If these sine waves are phase-shifted by π from each other, the signals are 100 % anti-correlated, i.e, $K = -1$. Correlated noise sources arise when the noise signals share a common source. An example for $K = 1$ is a sinusoidal source feeding two noiseless resistances [81].

If the two noise sources are connected in parallel, the mean square value of the resulting current noise is

$$I_{\mathrm{rms,n}}^2 = I_{\mathrm{rms,n1}}^2 + I_{\mathrm{rms,n2}}^2 + 2K \cdot I_{\mathrm{rms,n1}}I_{\mathrm{rms,n2}}. \tag{2.62}$$

Considering again thermal noise as the underlying phenomenon with the mean square value of the current noise $I_{\mathrm{rms}}^2 = 4k_\mathrm{B}T_\mathrm{e}\Delta fG = S_\mathrm{I}\Delta f$, the resulting PSD can be expressed as

$$S_{\mathrm{I,n}} = S_{\mathrm{I,n1}} + S_{\mathrm{I,n2}} + 2K\sqrt{S_{\mathrm{I,n1}}S_{\mathrm{I,n2}}}. \tag{2.63}$$

Here, the conductance G is the sum of the conductance of the noise producing resistors $G = G_1 + G_2$, i.e. $S_{\mathrm{I,n1}} = 4k_\mathrm{B}T_\mathrm{e}\Delta fG_1$ and $S_{\mathrm{I,n2}} = 4k_\mathrm{B}T_\mathrm{e}\Delta fG_2$.

Chapter 3

Material systems and sample preparation

In the last chapter the transport properties of low-dimensional electron systems were presented. This chapter introduces the functionality of III-V heterostructures and topological insulators that both reduce the dimensionality of an electron gas. The focus will lie on the material systems $Al_xGa_{1-x}As/GaAs$ and Bi_2Se_3 that form the basis of the devices that are used in this thesis. For both materials systems a short overview of the manufacturing of the devices will be given.

3.1 $Al_xGa_{1-x}As/GaAs$ heterostructures

There are different techniques that enable the creation of a confining potential which leads to the transition from 3D to 2D of an electron gas. The reduction from three-dimensional to two-dimensional electron gases (2DEGs) is typically achieved in epitaxially grown heterostructures. Epitaxy is most commonly performed by metal organic chemical vapor epitaxy (MOVPE) or by molecular beam epitaxy (MBE). In MOVPE the crystals are grown by chemical reaction of a pure material with the substrate. It has a relatively high growth rate and is therefore attractive for industrial applications, such as the production of transistors. In the MBE epitaxy the material is heated and deposited in gas form onto the wafer where it condenses. The slow deposition rate, the ultra-high vacuum and the absence of carrier gases lead to grown films with a high purity and a precision of atomic scale. The principles of MBE are well explained in [32].

In this thesis $Al_xGa_{1-x}As/GaAs$ heterostructures with $x = 0.34$ and $x = 0.35$ are investigated, which were MBE-grown by the group of Prof. Dr. Andreas Wieck at the Ruhr-Universität Bochum. These structures belong to the III-V semiconductor compounds, where one element of the third group of the periodic table of elements is combined in equal parts with one element of the fifth group to form a binary compound, like GaAs. Similarly a ternary layer is created from a binary layer, if either the contribution from the third or the fifth group consists of two different elements instead of one. $Al_xGa_{1-x}As$ is an example for a ternary compound, since it consists of the compound of AlAs and GaAs. The composition factor x determines the percentage of AlAs and allows the engineering of the band gap of $Al_xGa_{1-x}As$ between the band gap of AlAs of about 2.228 eV and the band gap of GaAs of about 1.512 eV at a temperature of few Kelvin [97]. The band gap of GaAs is direct, whereas AlAs has an indirect one. The band gap of $Al_xGa_{1-x}As$ becomes indirect

if x exceeds a value of about 0.4, which is typically avoided in the processing of heterostructures by choosing $x < 0.4$.

$Al_xGa_{1-x}As$/GaAs heterostructures consist of several layers each of which contribute to the realization of a 2DEG at the heterojunction of GaAs and $Al_xGa_{1-x}As$. Since GaAs has a smaller energy gap than AlAs, it is possible to have the band gap of GaAs fully contained in the band gap of $Al_xGa_{1-x}As$, i.e. the valence band energies have the relation $E_{V,GaAs} > E_{V,AlGaAs}$ and the conduction band energies have the relation $E_{C,GaAs} < E_{C,AlGaAs}$ at the heterojunction. This prevents electrons and holes that diffuse from the $Al_xGa_{1-x}As$ layer to the GaAs layer from diffusing back without having to overcome a potential barrier at the heterojunction. This situation is referred to as 'type I heterojunction' [14].

A schematic of the grown layers of a $Al_xGa_{1-x}As$/GaAs heterostructure is shown in Fig. 3.1 a). Here, the supply layer consists of Si-doped $Al_xGa_{1-x}As$ and provides the donor electrons for conduction as a result of thermal ionization. In thermal equilibrium these electrons accumulate in the GaAs layer that is spatially separated from the supply layer by an undoped $Al_xGa_{1-x}As$ spacer layer. This spacing aims to minimize the Coulomb interaction between the donor electrons in the 2DEG and the ionized donors and is referred to as modulation doping [98]. In this way scattering with the ionized dopants of the doped $Al_xGa_{1-x}As$ becomes less significant.

The resulting separation of the charge density ρ between the ionized donor atoms and the donor electrons creates an electric field $E(z)$. According to the Poisson equation

$$-\nabla \cdot \vec{E}(z) = \Delta\Phi_{el}(z) = \frac{1}{\epsilon}\rho(z), \tag{3.1}$$

this electric field creates a bend of the electrostatic potential Φ_{el} and therefore a bend of the conduction band edge. This bend can be engineered by the choice

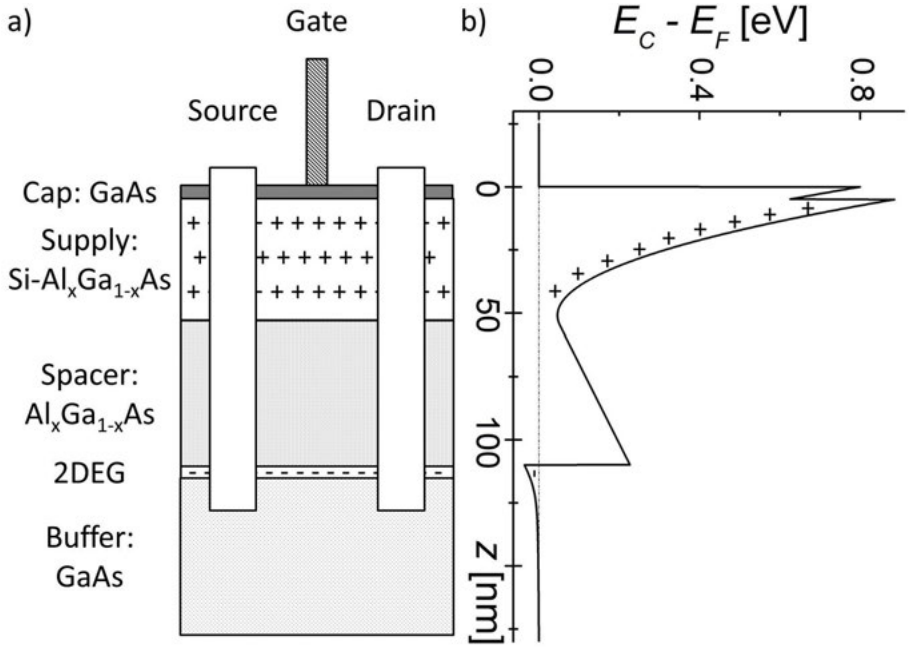

Figure 3.1: a) Schematic of a layered $Al_xGa_{1-x}As$/GaAs heterostructure. b) Simulation of the conduction band edge along the growth direction of a $Al_{0.34}Ga_{0.66}As$/GaAs wafer material with homogeneously distributed donor concentration of $5.3 \cdot 10^{17}$ cm^{-3} in the supply layer.

of the composition factor x, the doping concentration of the supply layer and the thicknesses of the different layers. The band bending leads to the creation of an approximately triangular potential well at the heterojunction of $Al_xGa_{1-x}As$ and GaAs. This can be seen in a simulation of the conduction band in Fig. 3.1 b) for $x = 0.34$ and doping concentration of $5.3 \cdot 10^{17}$ cm^{-3}. Typically the triangular potential well has a width of few 100 nm and thus produces quantized energy levels. In this case the electrons's movement is confined in the growth direction of the heterostructure and the dimensionality of the electron gas is reduced to quasi 2D.

The high mobility of the charge carriers in the 2DEGs of these high electron mobility transistors (HEMTs) is achieved by the following: the number of impurities and vacancies in the channel is strongly reduced due to the unique features of the MBE growth method. Furthermore, both AlAs and GaAs crystallize in the zincblende structure (see Appendix A) and have lattice constants $a_{\mathrm{AlAs}} = 5.661$ Å [99] and $a_{\mathrm{GaAs}} = 5.653$ Å [100] that deviate by only $a_{\mathrm{AlAs}}/a_{\mathrm{GaAs}} \approx 1.4 \cdot 10^{-3}$ from each other and therefore strongly reduce lattice strains and corresponding scattering. Finally, Coulomb scattering between ionized donor atoms in the supply layer and electrons in the 2DEG is reduced because of the spatial separation, mediated by an undoped $Al_xGa_{1-x}As$/GaAs layer, the spacer layer, as mentioned above. The charge carrier density n of the 2DEG can be varied by a metallic top-gate that forms a Schottky contact with the heterostructure. Other methods to change n involve the irradiation with light or the change of the hydrostatic pressure of the structure. Ohmic contacts 'source' and 'drain' enable the electrical characterization of the 2DEG. A summary as well as additional information about III-V heterojunctions can be taken from literature [101, 32].

The reduction from 2DEG to a quasi one-dimensional electron gas (1DEG) is achieved by either applying electron lithography to the 2DEG with subsequent etching or by the utilization of split-gates [42] in the 2DEG. Another method is to apply a strong magnetic field to a 2D channel that has the Hall bar geometry, in which case electrons create a conducting channel at the boundary of the Hall bar. The latter method can be exploited to understand the nature of 'topological insulators' that will be introduced in Sec. 3.3.

3.2 Realization of $Al_xGa_{1-x}As$/GaAs-based quantum devices

The devices that are investigated in this thesis are based on $Al_xGa_{1-x}As$/GaAs heterostructures and were grown by the group of Prof. Dr. Andreas Wieck at the Ruhr-Universität Bochum. In this thesis two different wafer types are used. The stacking order of the layers is in accord with the schematic in Fig. 3.1 and can be examined in detail in Appendix B for both wafers. The 2D electron density $n_{\mathrm{Wieck}} = 2.07 \cdot 10^{11}\mathrm{cm}^{-2}$ (sheet density) and the electron mobility $\mu_{\mathrm{e,Wieck}} = 2.43 \cdot 10^6$ cm^2/Vs is deduced from SdH measurements from the group of Prof. Dr. Andreas Wieck at $T_{\mathrm{bath}} = 4.2$ K in the dark. From these values and the 2D Fermi energy $E_{\mathrm{F,2D}} = \hbar\pi n/m_{\mathrm{e}}^*$ the Fermi wavelength

$$\lambda_{\mathrm{F},11159} = \frac{h}{\sqrt{2m_{\mathrm{e}}^* E_{\mathrm{F,2D}}}} = \frac{h}{\sqrt{2\hbar\pi n_{\mathrm{Wieck}}}} \approx 55 \text{ nm} \tag{3.2}$$

can be estimated, which allows to deduce the dimensionality from the geometry of a device that stems from the wafer 11159. Furthermore, the elastic mean free path

$$l_{\mathrm{e},11159} = v_{\mathrm{F}} \cdot \tau_{\mathrm{e}} = \sqrt{\frac{2E_{\mathrm{F,2D}}}{m_{\mathrm{e}}^*}} \cdot \frac{m_{\mathrm{e}}^* \mu_{\mathrm{e,Wieck}}}{e} = \sqrt{2\hbar^2 \pi n_{\mathrm{Wieck}}} \cdot \frac{\mu_{\mathrm{e,Wieck}}}{e} \approx 18\ \mu\mathrm{m} \quad (3.3)$$

can be derived from $\mu_{\mathrm{e,Wieck}}$ and n_{Wieck}. Here, τ_{e} describes the elastic mean scattering time τ_e and v_{F} the Fermi velocity. Accordingly, for the wafer 12088 the Fermi wavelength is $\lambda_{12088} \approx 45$ nm and the elastic mean free path is $l_{\mathrm{e},12088} \approx 10$ µm.

The 2DEG channel of the heterostructures that is created solely by the layer properties and layer sequence is further treated by applying 'mix and match lithography'. This term generally describes the creation of a lithographic mask by applying different types of lithography. In this case, electron beam lithography (EBL) and photolithography with ultraviolet light (UVL) are combined. Whereas UVL serves as method to create the microscopic 'mesa' structures, EBL is used to define nanostructures. In contrast to photolithography, EBL is practically not limited in its resolution by the particle wavelength, which is about 20 pm for 2 to 5 keV, but rather by the beam diameter and scattering. The lithographic steps were performed by Dr. Sven Buchholz in the laboratories of Prof. Dr. Ulrich Kunze at the Ruhr-Universität Bochum and are explained in the following: after cleaning the wafer in boiling acetone and isopropanol for 5 minutes each, electron beam negative resist MC6AOAc [102] is applied on the wafer surface. Spinning the wafer with 3000 rpm for 30 seconds causes the resist to homogeneously distribute over the wafer before it is prebaked at 170 °C for 30 min. EBL is then performed with energies of 2 to 5 keV to irradiate the resist with the desired pattern. Developing the resist with Xylol for 30 s removes the non-irradiated resist. Postbaking the wafer at 110 °C for 30 min completes the EBL. A similar procedure is performed in the UVL, by applying and spinning the positive photoresist SP2510 on the wafer with 6000 rpm for 5 s and 4500 rpm for 25 s. The prebaking at 95 °C for 5 min is followed by the exposition to UV light, while protecting the desired areas of the surface from irradiation with a lithographic mask for 6 to 7 s. The resist is developed by the diluted photodeposit 160 from Shipley.

The residual resists from EBL and UVL allow to etch the desired pattern into the wafer with citric acid solution $C_6H_8O_7$: H_2O_2 : H_2O. The etching aims at removing parts of the supply layer in order to deplete the corresponding regions in the 2DEG and therefore reaches depths of about 40 nm. This technique is known as shallow mesa etching [103] and is to be preferred over the deep mesa etching for narrow channels, such as QPCs or quantum wires. For deep mesa etching the etching depth reaches down to the conducting 2DEG and may lead to defects at the sidewalls of the defined channels. It should be therefore considered rather for Hall bar geometries. Cleaning the sample again in acetone, isopropanol and subsequent plasma cleaning removes residues of the resist. Mesa structure and nanostructure are accompanied by additional UVL that defines a pattern for contact pads in the same manner as described above. Layers of gold, germanium and nickel are evaporated onto the wafer surface and sonication removes the photoresist together with the waste evaporated metals. The residual metals are heated up to 400 °C for about 20 s in N_2 atmosphere to be alloyed into the wafer down to the 2DEG. These contact pads now form ohmic contacts with the 2DEG. A final lithographic step is needed if the resulting device is supposed to be covered by a gate electrode that allows to change the electron density in the 2DEG. Depending on whether a local 'finger' gate

or a global gate is planned, a final step of either UVL for global or EBL for local gate structures is required. In case of a further EBL for a finger gate, the MC6AOAc negative resist is replaced by PMMA positive resist. In both cases titanium and subsequently gold are evaporated onto the defined pattern. A last lift-off process completes the fabrication of the device. Each substrate has a surface of 4×5 mm^2 and provides enough space to host multiple devices. The substrate with the devices is glued into a chip carrier of the Dual-Inline-Package type. The contact pads of each device and the contact pads of the chip carrier are electrically connected to each other with aluminum bonding wires by ultrasonic bonding.

3.3 Topological insulators

Topology is a subject of mathematics that is concerned with the preservation of a body's properties under continuous, or 'smooth', deformations of that body that do not involve 'tearing' or 'gluing'. The discovery of the integer quantum Hall effect (IQHE), introduced in Sec. 2.3, by von Klitzing, for which he was awarded the Nobel Prize in Physics in 1985, was later interpreted in terms of the topology of quantized energy levels, i.e. Landau levels [22]. In the bulk of a 2D Hall bar the Landau levels are separated by $\hbar\omega_c$ in the presence of a strong magnetic field. If the Fermi energy E_F is located between two Landau levels, the bulk does not participate in the transport. However, at the boundary edge channels are created that distinguish the device from a typical insulator, as depicted schematically in Fig. 3.2 a). Each gapped band structure can be attributed to a topological class, the Chern invariant, that is robust against smooth changes of the Hamiltonian, as long as the energy gap is not closed or further gaps are opened [22]. Generally, at the transition region of two materials with different Chern numbers there has to be a conducting state that leads to the band gap crossing in the Hamiltonian. The Chern number of an insulator is zero, whereas the Chern number of a quantum Hall state is non-zero and corresponds to the number of edge states. The nature of the IQHE requires to break the time-reversal symmetry (TRS) of the system, which is done by the application of the high magnetic field in Hall bars. This means that the Hall conductivity is odd under time reversal. Haldane was the first one who presented the idea of the 'quantum Hall state' and a non-zero Hall conductance σ_{xy} in the absence of a magnetic field [21]. The idea of Haldane concerned the Hamiltonian of a simple nearest neighbor hopping in graphene. By adding a few terms to this Hamiltonian, breaking the TRS and the inversion symmetry of the graphene's band structure lifted the degeneracy at the Dirac points and opened a band gap. The added terms included a local periodic magnetic field that was zero on the average. When applying this model to a semi-infinite graphene ribbon, it was shown that the band structure produced edge states and a non-zero Hall conductance, as can be seen schematically in Fig. 3.2 d).

So far spin-orbit interaction (SOI) has not been considered. The quantum Hall state is a result of the broken TRS in the absence of a strong SOI. However, if SOI is added, a different topological class of insulating band structures with unbroken TRS may occur [104]. In addition to the Chern number that is zero for an insulator there is an additional Z_2 topological invariant ν [105] in the presence of SOI that can adopt the values $\nu = 0$ for trivial insulators and $\nu = 1$ for non-trivial insulators, i.e. topological insulators. Whether an insulator has the topological invariant $\nu = 0$ or $\nu = 1$ depends on the Hamiltonian's properties that may or may not yield edge

states that connect the valence and the conduction band of the material with each other. The underlying theorem is called Kramer's theorem in which electron pairs with spin 'up' and spin 'down' become Kramer pairs in the presence of SOI and the eigenstates of a time invariant Hamiltonian are at least two-fold degenerate. If the Fermi energy intersects the edge states an even number of times in the 1st Brillouin zone, ν becomes $\nu = 0$, and $\nu = 1$ if it intersects the edge states an odd number of times, as illustrated in Fig. 3.3 a) and b). This idea was incorporated by Kane and Mele into the Haldane model by decoupling the Hamiltonian into two independent Hamiltonians for spin 'up' and spin 'down' [104, 105]. This leads to counter-propagating edge-channels with opposite spins. The coupling of the movement direction to the spin of the electron was later denoted as 'helical' transport [106]. The described state is referred to as quantum spin Hall insulator (QSHI) and can schematically be seen in Fig. 3.2 b) with the corresponding schematic band structure in Fig. 3.2 e). Due to their helical nature, QSHIs may act as spin filter.

The appearance of the Dirac cone at the **K** and **K'** points in the Brillouin zone of graphene also has important parallels to the surface of a 3D topological insulator.

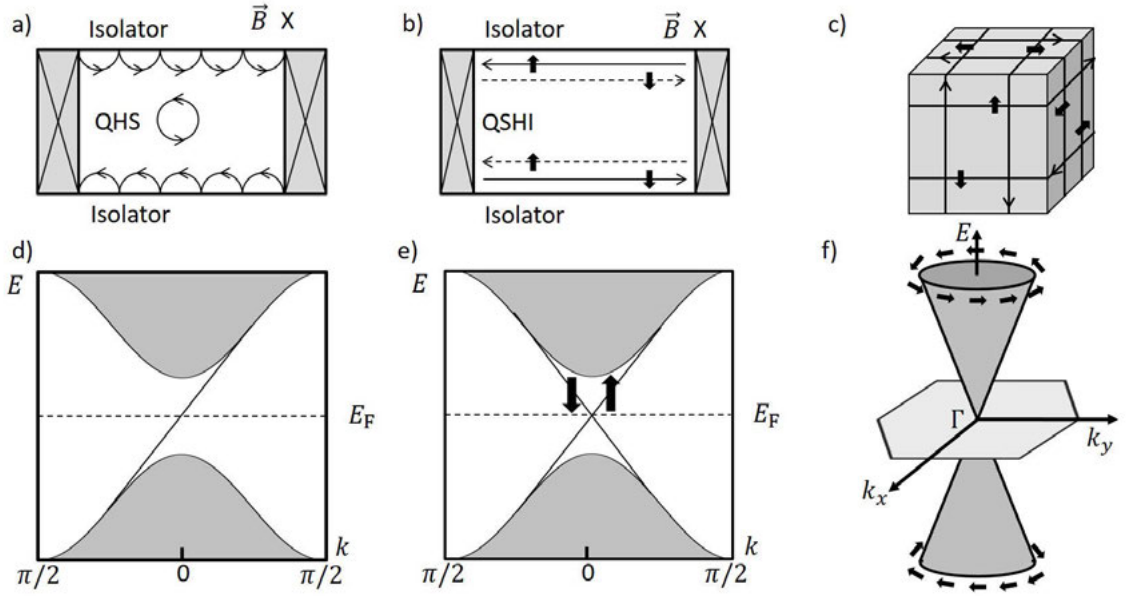

Figure 3.2: Schematic of topological edge states in a) the quantum Hall state (QHS), b) the spin quantum Hall insulator (QSHI) and c) a 3D topological insulator. a) The circular movement of electrons in a conducting 2D channel results in localized states in the bulk of the channel in the QHS. The circular movement cannot be fulfilled at the boundaries of the channel and leads to the creation of edge channels. In the Haldane model the QHS is achieved without an external magnetic field. b) If the spin of the electrons is considered, each channel of the QHS splits into two channels with opposite spin and opposite direction of propagation. c) The picture of the 2D QSHI can also be applied to the 3D topological insulator, where each surface carries the two surface states with opposite spins and opposite direction of propagation. The corresponding band diagram represents the valence and conduction band that are separated by an energy gap from each other. The edge states form d) a single branch in the QHS and e) one branch for each spin state in the QSHI. f) Energy dispersion of the spin non-degenerate surface state of a 3D TI forming a 2D Dirac cone.

However, since carbon is a relatively light element, in graphene only weak spin-orbit coupling is present, which results in a relatively small band gap in the Haldane model. The material HgTe was predicted to be a more promising candidate for the observation of the quantum spin Hall insulator state [106]. In HgTe with a thickness of at least 6.3 nm the p-like valence band edge rises above the s-like conduction band edge, when sandwiched between CdTe-layers. This is known as band inversion [107] which mediates the creation of the helical edge state of a QSHI. The QSHI state theoretically predicted in $Hg_{1-x}Cd_xTe$ [106] was experimentally verified in 2007 [107]. Later, the existence of these 'topological states' was predicted for 3D materials [63, 108, 109]. In particular $Bi_{1-x}Se_x$ was found to act as a topological insulator with many desirable properties in theory [110] and experiment [111]. However, the first 3D topological insulator that was identified by ARPES measurements was $Bi_{1-x}Sb_x$ [112]. A schematic of the helical surface states of an 3D topological insulator is depicted in Fig. 3.2 c) and the according energy dispersion is depicted in Fig. 3.2 f).

3D topological insulators are characterized by four Z_2 invariants ν_0, ν_1, ν_2, ν_3 and strong spin-orbit coupling that leads to the development of a Dirac cone in the 2D surface band structure, induced by band inversion. There are four invariant Dirac points $\Gamma_{1,2,3,4}$ in the surface Brillouin zone. If the Fermi surface intersects a line connecting two Dirac points an odd number of times, the surface states are topologically protected by TRS, in which case the system is referred to as strong topological insulator with $\nu = 1$. However, a weak topological insulator with $\nu = 0$ is given when this line is crossed an even number of times. In this case the surface

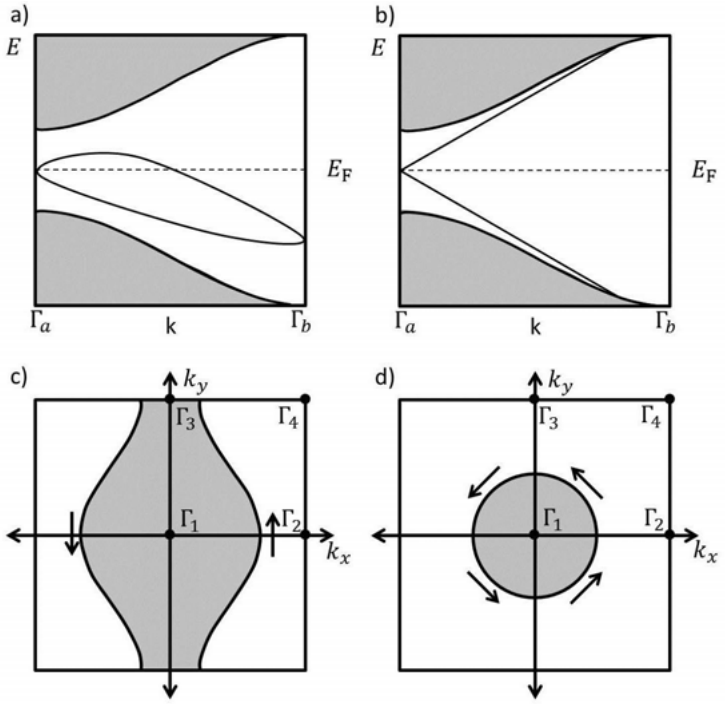

Figure 3.3: Schematic of the band diagram of two insulators with edge states. Only half of the 1st Brillouin-zone is depicted due to time-reversal symmetry that mirrors the band diagram along the E-axis. The number of intersections of Kramer pairs (see text) distinguishes between a) trivial and b) a non-trivial, i.e. 'topological' insulator. The surface Brillouin zone determines whether a topological insulator is c) weak or d) strong.

states are not protected by TRS. The schematic in Fig. 3.3 c) and d) gives an example of a weak and a strong TI. The residual Z_2 invariants ν_1, ν_2, ν_3 can be seen as Miller indices, that give information about the orientation of the layers.

Among the 3D TIs Bi_2Se_3 excels by a relatively large band gap of 0.3 eV, which enables applications at room temperature as well as relatively simple surface states which are described by a single gapless Dirac cone at the Γ point in the surface Brillouin zone. Therefore Bi_2Se_3 is the material of choice in this thesis. The rhombohedral crystal structure with the space group D^5_{3d} ($R\bar{3}m$) with five atoms in one unit cell is shared among Bi_2Se_3, Bi_2Te_3, Sb_2Te_3 and Sb_2Se_3 and is depicted for Bi_2Se_3 in Fig. 3.4 with the lattice parameters $a = b = 4.143$ Å and $c = 28.636$ Å [113]. Along the c-axis the structure has a three-fold rotation symmetry (trigonal axis) and a two-fold rotation symmetry along the a-axis (binary axis). The crystal structure consists of layered structures with a triangle lattice within one layer. Dashed squares in Fig. 3.4 highlight the five-atom layers along the c-axis that are referred to as 'quintuple layers'. One quintuple layer comprises two equivalent Se atoms, two equivalent Bi atoms and one further Se atom. Vacancies of Se are typical in Bi_2Se_3 and act as electron donors which cause the Fermi energy to shift towards the bulk conduction band.

Adjacent atomic layers that belong to the same quintuple layer are strongly coupled to each other. In contrast, two different quintuple layers are just weakly coupled to each other predominantly by van der Waals forces, which allows to fabricate mi-

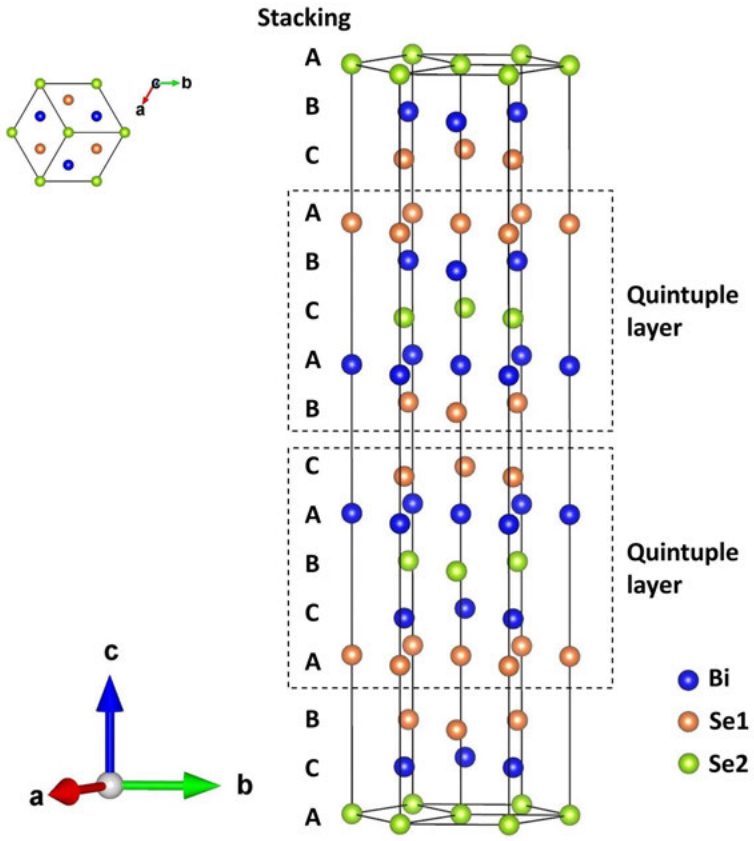

Figure 3.4: Crystal structure of Bi_2Se_3 with three primitive lattice vectors. The crystal structure is of the rhombohedral type with a space group of D^5_{3d} ($R\bar{3}m$). In this layered crystal structure five consecutive atom layers form a quintuple layer that is highlighted by dashed squares.

croflakes by applying the exfoliation technique.

3.4 Preparation of Bi_2Se_3 microflakes

The Bi_2Se_3 samples that are used in this thesis are single crystals, grown from melt with the Bridgman technique [114] at the Moscow State University in the group of Prof. Dr. Lada Yashina. In this technique a crucible is placed in an oven with two separate areas and is filled with a polycrystalline material. The first area of the oven is set to a temperature that is higher - and the second area is set to a temperature that is lower than the melting temperature of this material. The crucible also contains a seed crystal that serves to determine the crystallographic orientation of the crystal that is grown. The growth of the crystal is initiated by slowly moving the crucible out of the hotter part of the oven into the cooler part which causes the melt to crystallize. The fabricated Bi_2Se_3 crystals had a growth time of approximately 2 weeks for a 50 g crystal and yield a carrier density of about $1.9 \cdot 10^{19}$ cm^{-3}. The nominally undoped crystal was cleaved along the [00.1] growth direction. Due to the weak van der Waals forces that mediate the bonding between the Bi_2Se_3 planes, the exfoliation technique is applied with adhesive tape to produce the Bi_2Se_3 microflakes.

Exfoliation

In this thesis the crystals, that were grown in the Moscow State University, are prepared in order to perform electrical characterization in the presence of magnetic fields. The preparation starts with the exfoliation technique that is similar to the extraction of graphene flakes from graphite [115]. Although the source bulk single crystal is stored in N_2, one exfoliation step is performed to remove the top layers of the crystal. In this way, the influence of oxidation on the source bulk single crystal is further minimized. A subsequent exfoliation step includes folding and

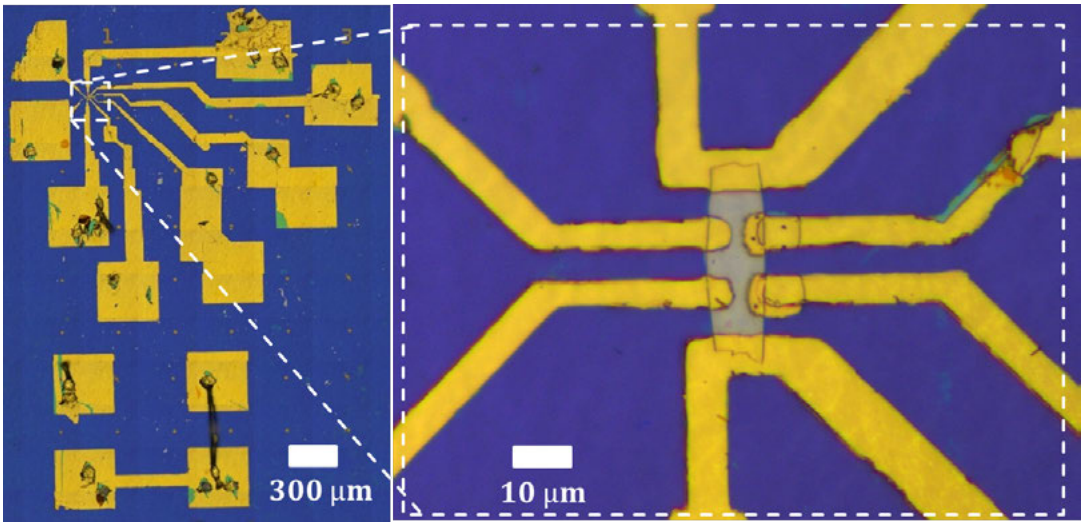

Figure 3.5: Optical microscope image of a contact pattern (left) and the exfoliated Bi_2Se_3 microflake (right). Bondpads enable the contacting of the microflake to the chip carrier. In the lower part of the pattern separate bond pads are located, which allows to verify that the substrate is electrically insulating.

unfolding the adhesive tape about 3 times, depending on the amount of exfoliated material, before the flakes are positioned onto a 300 nm thick SiO_2 layer, grown on a boron-doped Si substrate. Prior to and after the exfoliation the SiO_2 is cleaned with acetone, isopropanol and sonication. One purpose of the second sonication is to remove flakes that just weakly stick to the substrate. A higher number of flakes on the substrate would raise the probability that a residual flake causes an electrical shortcut in the contact pattern. After the exfoliation process, the flakes are investigated with the optical microscope Sensofar Plμ Neox in confocal mode in order to identify microflakes with the desired geometry.

Photolithography

In order to contact the Bi_2Se_3 microflakes, optical lithography is applied. Therefore, a $2-3$ μm thick, homogeneous layer of positive photoresist AZ ECI 3027 is coated onto the 5×5 mm^2 substrate and an individual contact pattern is written for each flake with the program CleWin 4. The pattern is transferred to the photoresist by the MicroWriter ML^{TM} from Durham Magneto Optics Ltd, whose lasers reach a resolution down to 1 μm. Developing the pattern in the developer AZ 326 MIF removes the exposed parts of the photoresist. Subsequently, plasma cleaning with the Zepto AQ12-1889 MF plasma cleaner with oxygen for 60 s and hydrogen for 300 s is applied to remove organic residues from the substrate. The sputter coater Q 300T D enables the deposition of 5 nm of titanium and 50 nm of gold onto the sample. The titanium acts as adhesive material, whereas the gold prevents the oxidation of the contacts. A further reason to separate the Bi_2Se_3 from the coated gold is the fact that gold particles were found to diffuse through Bi_2Te_3 [116]. A lift-off process removes the residual photoresist and the waste Ti and Au in order to finish the pattern. The pattern consists of leads that contact the microflake to bond pads. Separate bond pads allow to verify that the SiO_2 substrate is electrically insulating. Finally, the substrate is glued with the GE7031 varnish into a chip carrier and is contacted with Al-bonds. In Fig. 3.5 an exfoliated and contacted microflake of Bi_2Se_3 is shown. In Fig. 3.6 a schematic is depicted that summarizes each step of the optical lithography. Further details of the preparation of the Bi_2Se_3 microflakes can be taken from Appendix C.

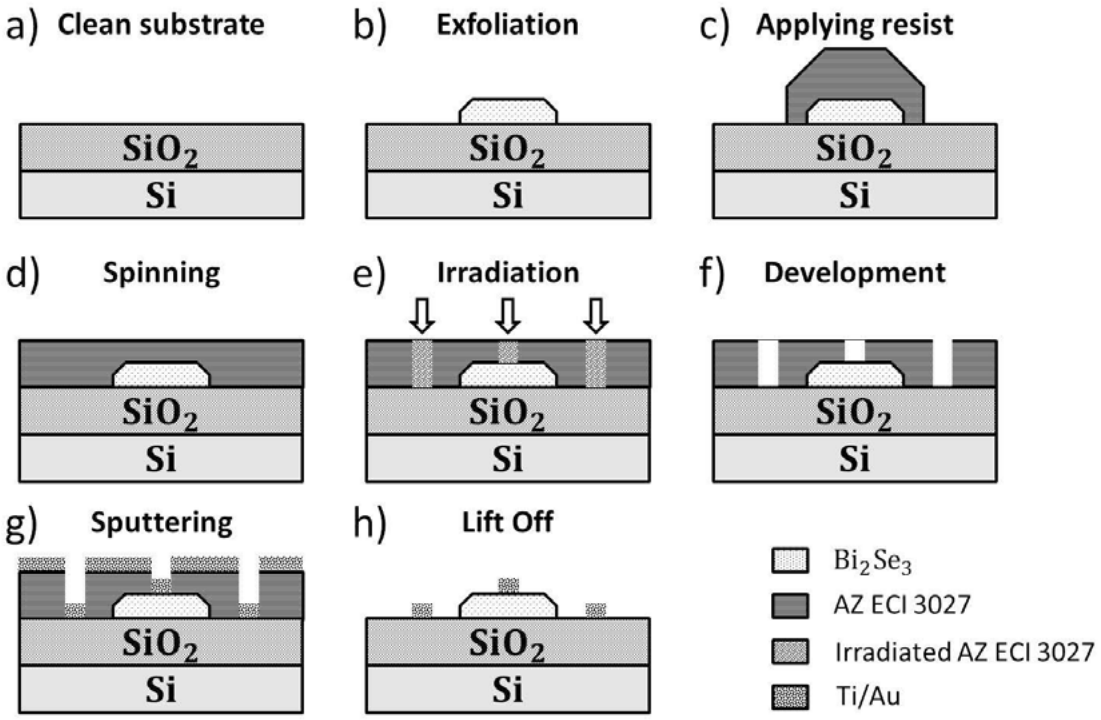

Figure 3.6: Schematic of the photolithographic steps. a) The presented steps start with a cleaned Si substrate topped by a 300 nm thick SiO_2 layer. The following steps involve: b) Mechanic exfoliation of the Bi_2Se_3 single crystal along the [001] direction, c) Application, d) spinning, e) irradiation and f) development of the positive resist, g) sputtering of a 5 nm Ti layer and a 50 nm thick Au layer, h) removing residual metal in the lift-off.

Chapter 4

Experimental methods

In the course of this thesis, a variety of different measurement techniques was applied and further improved. The following sections are supposed to give an insight into the electrical characterization of the investigated samples. The samples are characterized with respect to their electrical differential conductance g and its dependence on an external magnetic field $\vec{B}$, the gate voltage V_g and an DC offset voltage V_{SD}. A further section deals with the measurement of the noise characteristics of the samples. At the end of this chapter an overview of the utilized measurement devices is given. The first subsection deals with the realization of a low bath temperature required to observe quantum effects in the investigated systems.

4.1 Cryogenic methods

In order to establish a bath temperature down to 250 mK, a ^{3}He cryostat was used. ^{3}He is a stable isotope of Helium and has an occurrence of 1.38 ppm in Helium gas. Compared to ^{4}He, it has a reduced boiling point of approximately 3.2 K at atmospheric pressure which becomes 250 mK at pressures of the order of magnitude of 10^{-6} bar [117]. In this thesis the Heliox VL inset from Oxford instruments is used. A schematic of this cryostat is depicted in Fig. 4.1. Moving the evacuated Heliox VL inset into a ^{4}He dewar, reduces the inset temperature down to 4.2 K due to an exchange gas. The exchange gas is automatically absorbed by a sorption pump during the cooling process. Pumping ^{4}He through a needle valve, causes the temperature to drop to about 1.5 K in the 1 K plate. A further sorption pump absorbs gaseous ^{3}He if the sorb's temperature is at about 3.2 K or lower. Heating the sorb to 30 K causes the sorb to release the absorbed ^{3}He gas, which is pressed through the 1 K plate. The ^{3}He condenses at the 1 K plate and fills the ^{3}He pot. Cooling the temperature of the sorption pump again, strongly reduces the pressure above the ^{3}He pot, which lowers the boiling temperature of the liqud ^{3}He to 250 mK. The sample is thermally coupled to the ^{3}He bath by a copper block. Bath temperatures between 0.04 K and 45 K can be measured by the ruthenium oxide thermometer 'LakeShore RX-202A-AA-0.05B'-thermometer, that is positioned next to the sample. The sample is surrounded by a 2 T-superconducting magnet that is mounted to the ^{3}He inset and creates a field that is perpendicular to the surface of the sample. The temperature controller 'Mercury iTC' and the controller for the magnetic field 'Mercury iPS' are automatically accessed by a custom LabView program.

For some measurements with bath temperatures $T_{\text{bath}} \geq 4.2$ K a ^{4}He dewar

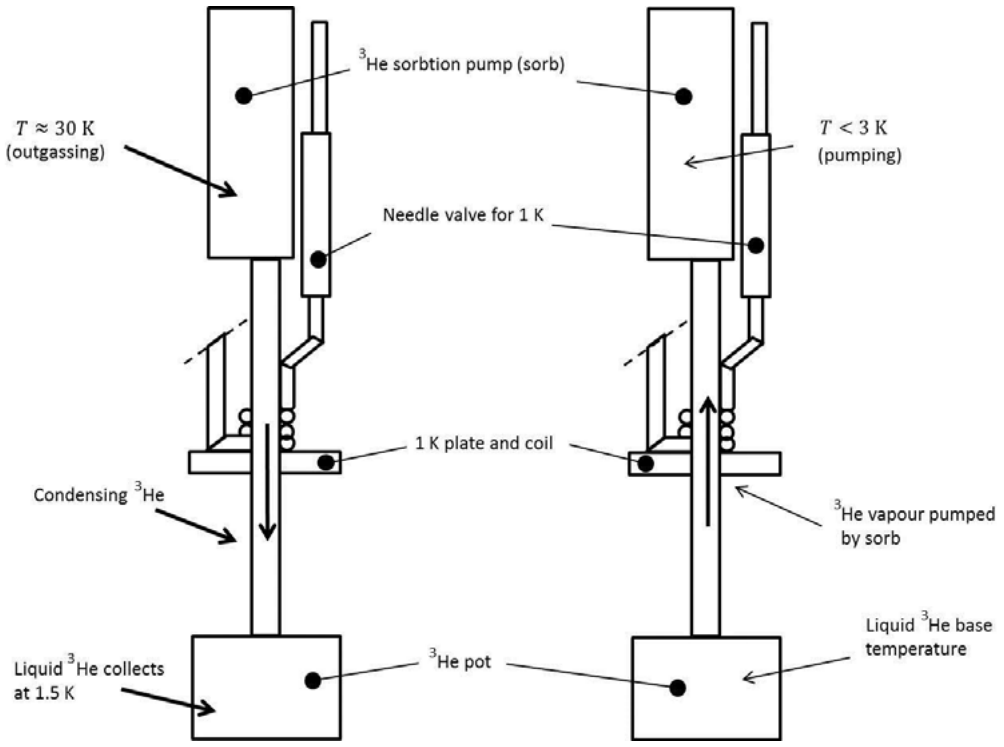

Figure 4.1: Schematic of the Heliox VL inset from Oxford instruments. The image is adapted from [118].

was used due to the strongly decreased required measurement effort. The sample's temperature was changed by positioning the sample above the level of liquid ^{4}He and measuring this temperature with a DT-670 Si Diode.

4.2 Electrical characterization

Most of the information about the physical properties of the investigated samples is directly or indirectly taken from their electrical resistance R and their electrical conductance $G = 1/R$. The measurement of quantum effects requires a measurement setup that is of particular low noise. This is in large part warranted by the usage of a lock-in amplifier. A lock-in amplifier allows to perform AC measurements while acting as a narrow bandpass filter. This enables the detection of the measurement signal even if it is superposed by a dominating noise background. In the two-point configuration the lock-in applies an oscillating voltage V_{Osc} with a certain frequency and detects the part of the incoming current I_{Osc} that has the same frequency. This allows the calculation of the differential conductance $g = \mathrm{d}I_{\mathrm{Osc}}/\mathrm{d}V_{\mathrm{Osc}}$.

The measurement setup for two-point lock-in measurements is depicted in Fig. 4.2 a). In order to measure in the linear response regime when investigating 1D constrictions (see Sec. 2.2), the AC excitation voltage has to be smaller than the subband spacing of the constriction $eV_{\mathrm{Osc}} \ll \Delta E_{n,n+1}$. The minimum excitation voltage of the SR830 lock-in amplifier is 4 mV, but is further reduced by making use of a 100:1 transformator at the 'source'-side. The 'drain'-sided 1:10 transformator is supposed to reduce the effective input resistance of the lock-in from 1 kΩ to 12 Ω. A further benefit of the transformators is the galvanic isolation to avoid ground loops. In all experiments the frequency of the excitation signal was 433 Hz. This value is

chosen to avoid a harmonic of the power supply frequency of 50 Hz and to be higher than the inverse of the time constant that is set between $\tau = 100$ ms and $\tau = 1$ s. The chosen time constant cuts off signals that stem from conductance fluctuations with a fluctuation time of few ms, such as telegraphic noise [88, 119, 120].

Measurements in the non-linear transport regime are established by the usage of the measurement setup that is depicted in Fig. 4.2 b). The AC Signal of the lock-in SR830 is offset by a DC voltage that stems from one of the four auxiliary DC voltage outputs. The 1:100 transformator is used to combine the AC and DC voltage signal. An active voltage divider reduces the DC output voltage of the lock-in. An alternative measurement setup incorporates a passive voltage divider and receives the DC voltage from the SIM928 isolated voltage source. Measurements with this setup may result to signals with less noise and are always performed when measurements with the setup in Fig. 4.2 b) are too noisy. This alternative measurement setup is depicted in Appendix D.

The obtained electrical conductance always comprises the contact resistances in the two-point measurement setup. This has to be taken into consideration when evaluating the electrical conductance. A four-point measurement directly detects the potential difference that is caused by the sample's resistance and therefore neglects contributions from the leads and contacts. The four-point measurement setup is depicted in Fig. 4.2 c). In order to send an electric current I through the sample that is independent of the sample's resistance R, a 10 MΩ resistor is connected with the sample in series.

4.3 Interferometric measurements

Due to their noise-sensitive nature, interferometric measurements require further effort to lower the noise that is produced by the measurement setup. The setup that is used for measurements of the Aharonov-Bohm effect in $Al_xGa_{1-x}As/GaAs$ heterostructures is presented in Fig. 4.3 a). The excitation signal is produced by the function generator DS360. The reference signal is transmitted to the lock-in SR830 via an optocoupler. The optocoupler serves as galvanic isolator and avoids the creation of ground loops. According to the four-point measurement setup in Fig. 4.2 c), a 10 MΩ resistor is connected in series with the sample in order to control the excitation current I. The voltage drop across the sample is detected by the SRS SR560 voltage preamplifier and amplified by a factor of 100. The amplified voltage signal is sent to the lock-in SR830. The usage of isolation tranformators and the battery operation of the SRS SR560 voltage preamplifier further reduces the occurrence of ground loops. A SIM928 isolated DC voltage source serves to operate as a gate electrode. This setup is known as star grounding, which connects all measurement devices to one common ground in order to avoid influences from ground loops. Here, the ground is provided by the magnet that is connected to the ^{3}He cryostat.

The measurement of localization effects and the Hall resistance of Bi_2Se_3 flakes are performed by using the setup that is presented in Fig. 4.3 b). The current I_x is sent through the sample by an external function generator with a 10 MΩ resistance is series. The voltage signals V_x and V_y are detected and amplified by a factor 100 by one of the two voltage preamplifiers SR560. Both of the amplified voltage signals are transferred to one of the two lock-in amplifiers, which both take the reference signal from the function generator.

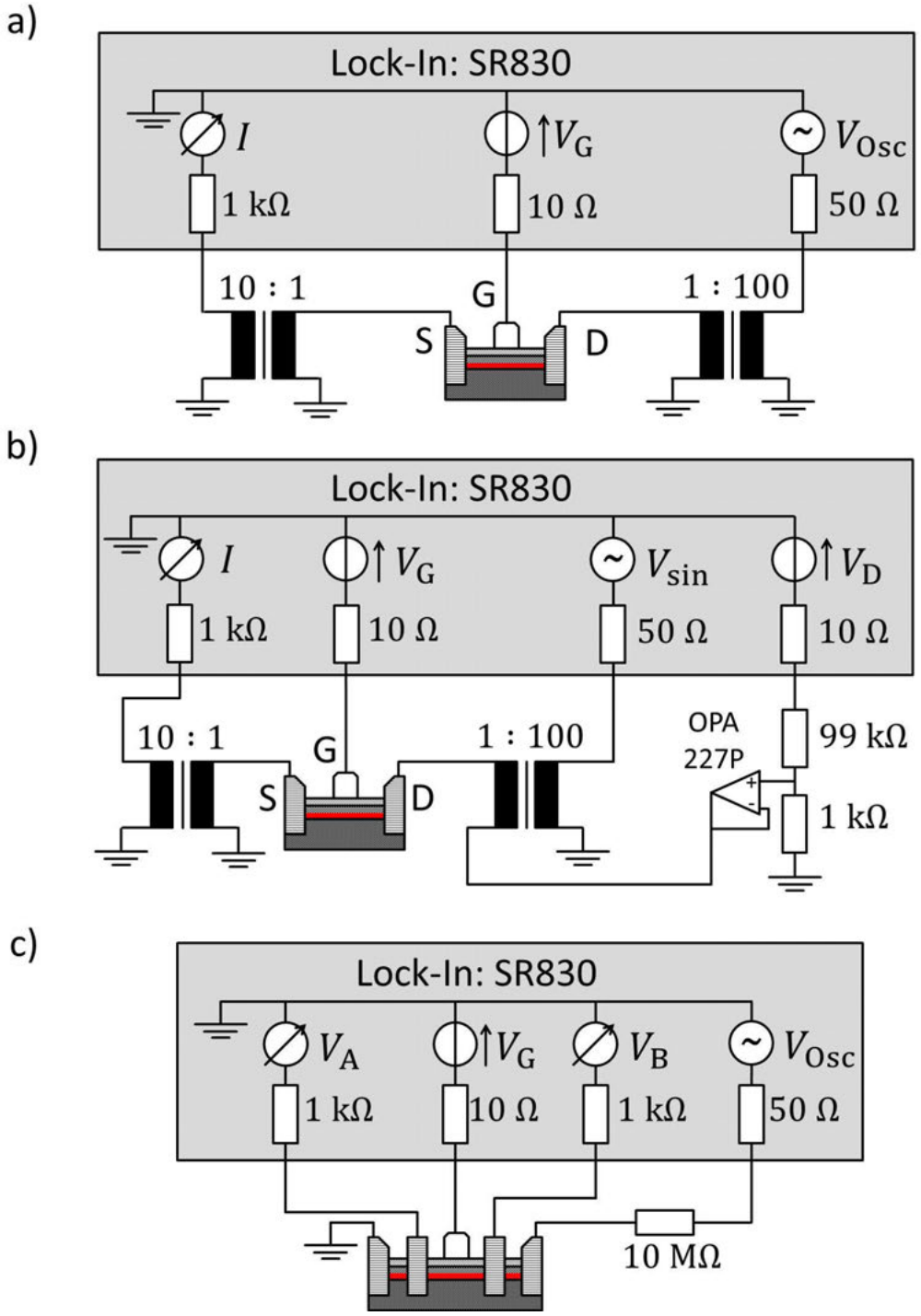

Figure 4.2: Measurement setup for a), b) two-point and c) four-point measurement configuration with the lock-in SR830. a) Two-point setup for measurements in the linear transport regime with two additional transformers to reduce the amplitude of the excitation signal as well as the effective input resistance of the lock-in. b) Two-point setup for measurements in the non-linear transport regime with transformers as in a) and additional active voltage divider. An alternative setup is presented with a passive voltage divider in Appendix D. c) Four-point setup for measurements of the input resistance.

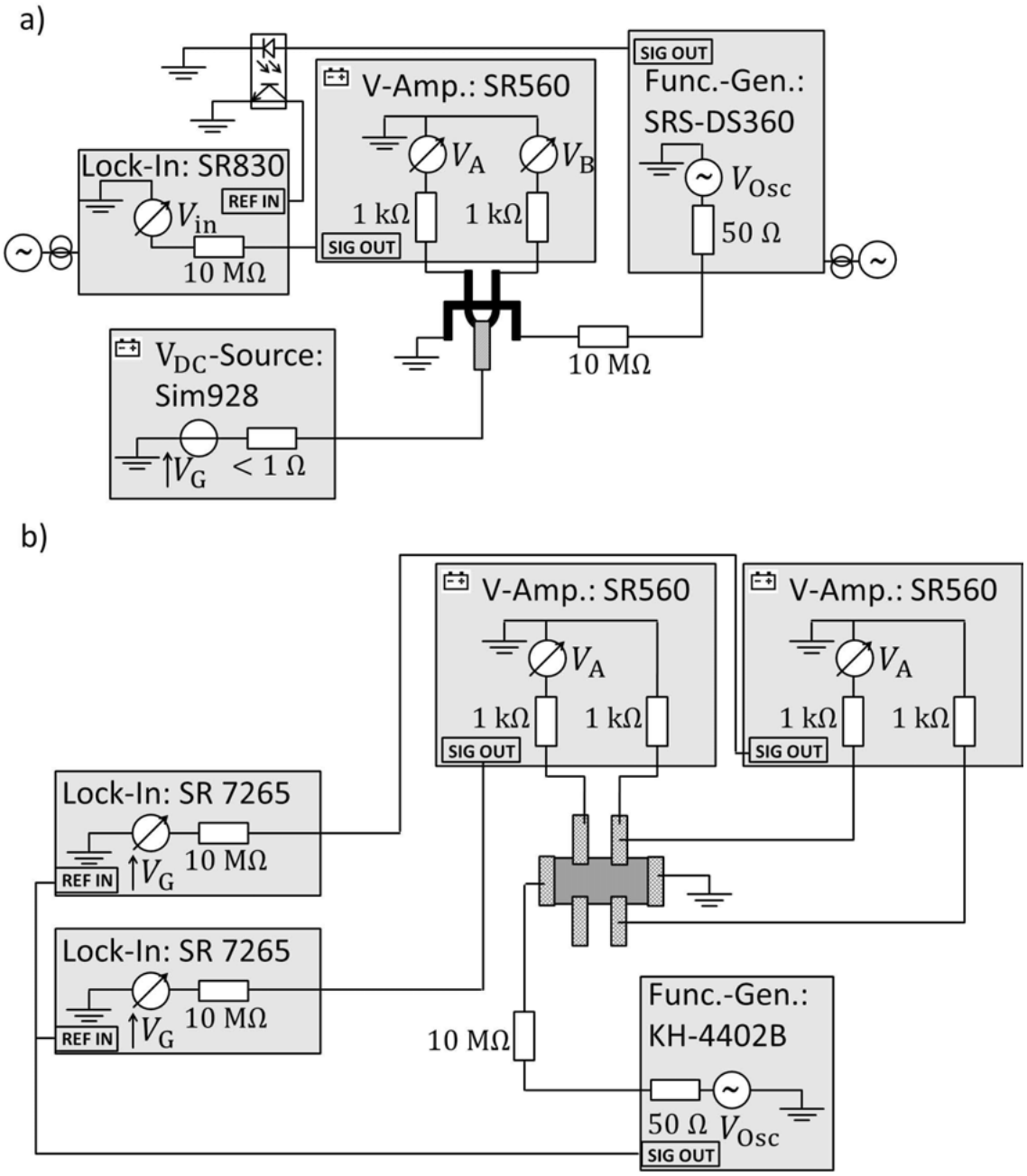

Figure 4.3: Measurement configuration for four-point measurements in the presence of a magnetic field. a) The setup for Aharonov-Bohm measurements in Al_xGaAs_{1-x}/GaAs devices consists of an external function generator SRS-DS360, a voltage amplifier SR650 and the lock-in SR830. The reference signal is transmitted from the function generator to the lock-in by an opto-isolator for galvanic isolation. A Sim928 isolated DC voltage source provides the voltage for a gate structure. b) The setup for measurements of the weak anti-localization effect consists of a function generator KH-4402B and one voltage amplifier SR560. Using a further lock-in SR 7265 allows to perform Hall measurements and Shubnikov-de Haas measurements.

4.4 Measurement setup of noise thermometry

In Sec. 2.5 the concept of thermal noise and noise thermometry was presented. In this section it will be shown how to measure the power spectral density (PSD) $S_{\mathrm{V}}(f)$ of a sample and how to extract the thermal noise $S_{\mathrm{V,w}}$ and the electron temperature T_{e} from $S_{\mathrm{V}}(f)$.

In order to measure the PSD of a device, the spectrum analyzer SR785 from Stanford Research Systems is employed. The input noise of the SR785 spectrum analyzer is about $S_{\mathrm{V,SR785}} \approx 10^{-16}$ V^2/Hz. The signal of a device with few kΩs at $T \approx 4.2$ K is typically of the order of magnitude of 10^{-18} V^2/Hz. Therefore, the two ultra low-noise voltage preamplifiers Model 5184 from Signal Recovery are used, see Fig. 4.4. Since the input noise of these amplifiers is also of the order of magnitude of 10^{-18} V^2/Hz, the cross-correlation technique is applied [121]. According to Eq. 2.53 the cross-correlation spectrum is

$$S_{xy}(f) = \int_{-\infty}^{\infty} R_{xy}(\tau) e^{-2\pi i f \tau} \mathrm{d}\tau \tag{4.1}$$

with the cross-correlation function

$$R_{xy} = \int_{-\infty}^{\infty} [V_{\mathrm{sig},1}(t) + V_{\mathrm{amp},1}(t)] \cdot [V_{\mathrm{sig},2}(t+\tau) + V_{\mathrm{amp},2}(t+\tau)] \mathrm{d}t. \tag{4.2}$$

Here, $V_{\mathrm{sig},1}(t)$ and $V_{\mathrm{sig},2}(t)$ describe the voltage fluctuation of the sample that is amplified by the preamplifiers 1 and 2. The terms $V_{\mathrm{amp},1}(t)$ and $V_{\mathrm{amp},2}(t)$ refer to the input noise of the preamplifiers. Due to its random nature, thermal noise from a source is not correlated with thermal noise stemming from another source. Thus, Eq. 4.2 becomes independent of the terms that stem from the amplifiers

$$\begin{aligned} R_{xy} = \int_{-\infty}^{\infty} V_{\mathrm{sig},1}(t) V_{\mathrm{sig},2}(t+\tau) \mathrm{d}t + \underbrace{\int_{-\infty}^{\infty} V_{\mathrm{sig},1}(t) V_{\mathrm{amp},2}(t+\tau) \mathrm{d}t}_{\to 0} \\ + \underbrace{\int_{-\infty}^{\infty} V_{\mathrm{amp},1}(t) V_{\mathrm{sig},2}(t+\tau) \mathrm{d}t}_{\to 0} + \underbrace{\int_{-\infty}^{\infty} V_{\mathrm{amp},1}(t) V_{\mathrm{amp},2}(t+\tau) \mathrm{d}t}_{\to 0}. \end{aligned} \tag{4.3}$$

Although the voltage noise of the amplifiers is largely avoided by the cross-correlation, the amplifiers still influence the measured signal. The contribution of the offset noise that stems from the amplifiers can be calculated, as done in literature [122, 71], and modifies Eq. 2.53 to

$$S_{\mathrm{V,Th}} = 4 k_{\mathrm{B}} T_{\mathrm{e}} R + 2 \cdot 4 k_{\mathrm{B}} T_{\mathrm{amp}} R_{\mathrm{amp}}^{-1} R^2 \tag{4.4}$$

with the amplifier's temperature $T_{\mathrm{amp},1/2} \approx 300$ K and resistance $R_{\mathrm{amp},1/2} = 5$ MΩ. In this thesis Eq. 4.4 is used to calculate the theoretical values that are expected for a system with given two-point resistance R and electron temperature T_{e}.

In the Appendix E it can be seen that the operation range of the preamplifiers is optimized to reduce the amplifier's input noise. In Fig. 4.4 the measurement setup for noise measurements is presented. It can be seen that ground loops are avoided by setting only one voltage preamplifier to 'ground' and by keeping the SR785 spectrum analyzer's inputs floating. The presented measurement setup inevitably comprises parasitic capacities C_{par}, e.g. in the Bayonet Neill Concelman (BNC)

cables. These capacities form a low-pass filter with the setup's electrical resistance which is observed in the resulting PSD. In order to extract the white part of the noise from the PSD, the fit

$$S_{\mathrm{V}}(f) = \frac{S_{\mathrm{V,w}}}{1 + (2\pi f R C_{\mathrm{par}})} \tag{4.5}$$

is applied to each measurement that is an average over time of 500 recorded PSD. The presented setup yields experimental values of $S_{\mathrm{V,w}}$ that are in accord with $S_{\mathrm{V,Th}}$ for resistances in the range 1 kΩ $\leq R \leq$ 60 kΩ and for temperatures in the range 4.2 K $\leq T_{\mathrm{e}} \leq$ 70 K for a 2DEG in a $Al_xGa_{1-x}As$/GaAs heterostructure [70, 123]. In this regime the deviation between $S_{\mathrm{V,w}}$ and $S_{\mathrm{V,Th}}$ is less than 1 %. In addition to the SR785 spectrum analyzer, the SRS SIM928 is used to apply a clean gate voltage and heating currents [124] to the investigated device, as depicted in Fig. 4.4.

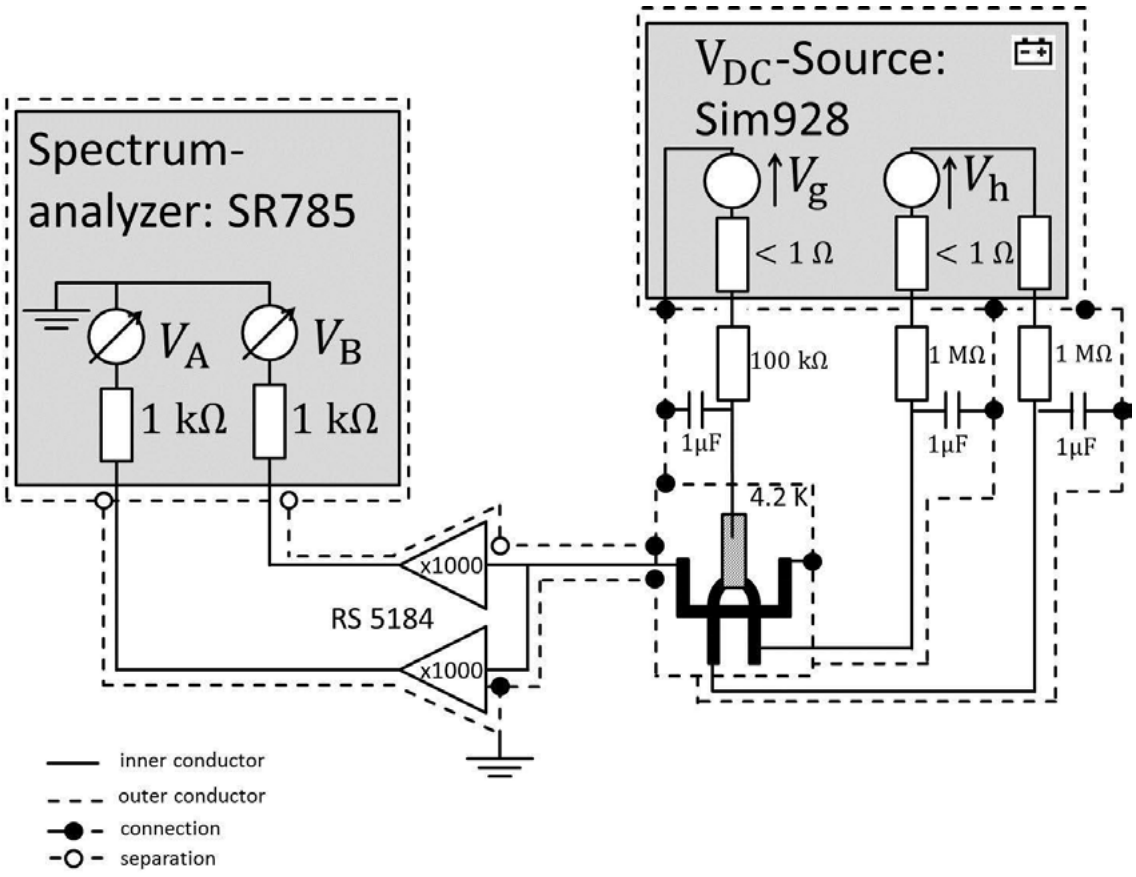

Figure 4.4: Measurement configuration of thermal noise measurements. The setup consists of two voltage amplifiers that are set parallel to amplify the voltage noise of the sample. The amplified noise signal is sent to the spectrum analyzer SR785 to identify the cross-correlation spectrum. The gate electrode is connected to an isolated DC voltage source which also provides the voltage to apply a heating current to the sample. Low-pass filters reduce disturbances from unwanted external fields that are picked up by the circuit.

4.5 Description of the measurement devices

Lock-in amplifier SR830 and SR7265

A lock-in amplifier creates an AC signal and phase-sensitively detects the incoming modulated version of the signal, while acting as a narrow bandpass filter. This technique offers the possibility to detect signals that are accompanied by a dominating background noise. The lock-in amplifier SR830 [125] produces an AC voltage signal with a frequency range of 1 mHz $\leq f \leq$ 102.4 kHz and a voltage range of 4 mV $\leq V_{\mathrm{Osc}} \leq$ 5 V that is sent through the sample and is also kept as reference signal in the lock-in. The modulated signal that comes from the sample is $V_{\mathrm{Sig}} \sin(\omega_{\mathrm{Sig}} t + \varphi_{\mathrm{Sig}})$ and the reference sample is $V_{\mathrm{Ref}} \sin(\omega_{\mathrm{Ref}} t + \varphi_{\mathrm{Ref}})$. The detected signal is amplified and multiplied with the reference signal

$$\begin{aligned} V_{\mathrm{Detected}} &= V_{\mathrm{Sig}} \sin(\omega_{\mathrm{Sig}} t + \varphi_{\mathrm{Sig}}) \cdot V_{\mathrm{Ref}} \sin(\omega_{\mathrm{Ref}} t + \varphi_{\mathrm{Ref}}) \\ &= \frac{1}{2} V_{\mathrm{Sig}} V_{\mathrm{Ref}} \cos(\omega_{\mathrm{Sig}} t - \omega_{\mathrm{Ref}} t + \varphi_{\mathrm{Sig}} - \varphi_{\mathrm{Ref}}) \\ &- \frac{1}{2} V_{\mathrm{Sig}} V_{\mathrm{Ref}} \cos(\omega_{\mathrm{Sig}} t + \omega_{\mathrm{Ref}} t + \varphi_{\mathrm{Sig}} + \varphi_{\mathrm{Ref}}). \end{aligned} \tag{4.6}$$

In the lock-in SR830 a low-pass filter is applied to the detected signal V_{Detected}, which causes the lower term with $\omega_{\mathrm{Sig}} t + \omega_{\mathrm{Ref}} t$ to vanish and also the upper term with $\omega_{\mathrm{Sig}} t - \omega_{\mathrm{Ref}} t$ to vanish, except for the case $\omega_{\mathrm{Sig}} t \approx \omega_{\mathrm{Ref}} t$. The detected signal is then

$$V_{\mathrm{Detected}} = \frac{1}{2} V_{\mathrm{Sig}} V_{\mathrm{Ref}} \cos(\varphi_{\mathrm{Sig}} - \varphi_{\mathrm{Ref}}). \tag{4.7}$$

Thus, the lock-in amplifier only detects signals whose frequencies are close to ω_{Ref}. The bandwidth of the bandpass filter $\Delta\omega_{\mathrm{B}}$ is coupled to the time constant τ over which the detected signal is integrated according to $\tau = \Delta\omega_{\mathrm{B}}^{-1}$. The DC voltage source of the rear panel has a range of -10 V to +10 V with a resolution of 1 mV and is therefore well-suited for both supplying the gate electrode and providing a DC offset voltage for the non-linear transport regime. The lock-in amplifier SR7265 works in a similar way and can also function as a spectrum analyzer and as a noise measurement unit which simplifies the detection of noise sources in the setup.

Spectrum analyzer SRS SR785 and SR model 5184 ultra low-noise voltage preamplifier

The dual-channel spectrum analyzer SR785 is of interest for this thesis due to its capability to apply the cross-correlation to the signals of the input channel 1 and input channel 2. The frequency range from few Hz up to 102 kHz is well-suited to record the low frequency contributions of the noise signals. In this regime the internal noise of the ultra low-noise amplifiers model 5184 is minimal for resistances in the range of 1 kΩ to about 100 kΩ, see Appendix E. The amplifiers are required due to the input noise of the channels of the SR785 which is about 10 nVrms/$\sqrt{\mathrm{Hz}}$ above 200 Hz. This input noise is of the order of magnitude of a sample's thermal noise at low temperatures with a resistance of few kΩ. The averaging ability of the SR785 reduces the influence of disturbances that are picked up from the setup and improves the signal-to-noise ratio.

Keithley 6221/2182A

The combination of the AC and DC current source Keithley 6221 [126] and the low-noise nanovoltmeter Keithley 2182A [127] provides the possibility to measure the I-V characteristics of a sample in the four-point configuration precisely. Both measurement devices are coupled with each other by a serial interface. The nanovoltmeter Keithley 2182A has an input resistance of more than 10 GΩ and has a measurement range of 1 nV to 100 V. The AC current source Keithley 6221 has a measurement range of 100 fA to 105 mA.

SRS SIM928

The isolated voltage source provides DC voltage signals in the range from -20 V to +20 V with a resolution of 1 mV. A unit comprises two separate batteries, each of which having a lifetime of up to 12 hours. Whereas one battery stands ready to provide the voltage for the experiment, the second battery is recharged by an earth-referenced charging circuit. The active SR Sim928 battery is always optically isolated from this circuit, which helps to avoid the creation of ground loops.

Chapter 5

Characterization of the electrical transport properties

In this chapter transport properties of the $Al_xGa_{1-x}As/GaAs$ quantum ring devices and an 1D constriction are investigated. An overview of the studied $Al_xGa_{1-x}As/GaAs$ devices can be consulted in Appendix F. The investigated properties are the differential conductance $g = dI_{Osc}/dV_{Osc}$, the transconductance dg/dV_g and the energy subband spacing $\Delta E_{i,i+1} = \hbar\omega_y$ between subbands with index i and $i+1$. The subband spacing $\hbar\omega_y$ is determined by measuring the transconductance of the device in the non-linear transport regime. An alternative approach for measuring in the non-linear transport regime is presented in the last section of this chapter. Moreover, the effective mass m_e^* of the narrow 2D heating channel of a quantum device is derived from Shubnikov-de Haas (SdH) measurements at a bath temperature of $T_{bath} = 0.3$ K and $T_{bath} = 4.2$ K in the dark, i.e. in the absence of illumination. This effective mass will be used for calculations in the subsequent sections for the quantum ring devices.

5.1 Determination of the effective mass

The knowledge of the effective mass m_e^* of a device is needed to derive important physical parameters, such as the Fermi energy E_F and the ballistic thermal length $l_\mathrm{T,b}$. A possibility to measure m_e^* is a Hall bar configuration, as depicted in Fig. 5.1 a) for the device QRC. As explained in Sec. 2.3, this configuration yields oscillations of the four-point resistance, known as Shubnikov-de Haas (SdH) oscillations [129], when the magnetic field is sweeped. The measured SdH oscillations for the device QRC are shown in Fig. 5.1 b) for the bath temperatures $T_\mathrm{bath} = 0.3$ K and $T_\mathrm{bath} = 4.2$ K. The maxima and minima for both temperatures are shifted along the B-axis relative to each other. However, calculating the sheet density n from the SdH oscillations yields $n(4.2\ \mathrm{K}) = (1.90 \pm 0.08) \cdot 10^{11}\ \mathrm{cm}^{-2}$ and $n(0.3\ \mathrm{K}) = (1.83 \pm 0.06) \cdot 10^{11}\ \mathrm{cm}^{-2}$. The sheet density is calculated from the magnetic fields B_i and B_{i+1} that correspond to two adjacent maxima or minima with index i and $i+1$, using the equation

$$\frac{1}{B_{i+1}} + \frac{1}{B_i} = \frac{2e}{nh}. \tag{5.1}$$

The found sheet densities deviate from the sheet density $n_\mathrm{Wieck} = 2.07 \cdot 10^{11}\ \mathrm{cm}^{-2}$ that is measured for this wafer by the group of Prof. Dr. Andreas Wieck at $T_\mathrm{bath} =$

4.2 K. This deviation is attributed to the lateral confinement of the heater line with a width of 2 µm. Similarly, a deviation from the electron mobility $\mu_{\text{Wieck}} = 2.43 \cdot 10^6 \text{cm}^2/\text{Vs}$, measured at $T_{\text{bath}} = 4.2$ K by the group of Prof. Dr. Andreas Wieck, is observed for the electron mobility of the heater

$$\mu_{\text{e}}(4.2\text{ K}) = \frac{l}{w}\frac{1}{n(4.2\text{ K})eR(B=0)} = (3.65 \pm 0.08) \cdot 10^5\ \text{cm}^2/\text{Vs} \tag{5.2}$$

with $R(B = 0) = 18$ kΩ, the length $l = 410$ µm and the width $w = 2$ µm of the heater for $T_{\text{bath}} = 4.2$ K. Accordingly, $\mu_{\text{e}}(0.3\text{ K}) = (3.79 \pm 0.09) \cdot 10^5$ cm^2/Vs is found. Due to the broadening of the Landau levels at higher T_{bath} the amplitude $A(B,4.2\text{ K})$ of the SdH oscillations at $T_{\text{bath}} = 4.2$ K is significantly lower than the amplitude $A(B,0.3\text{ K})$ at $T_{\text{bath}} = 0.3$ K. Note however, that the amplitude is not enveloped in a beating pattern, which suggests a negligible spin-orbit interaction in the device. The ratio of the amplitudes allows to deduce the effective mass according

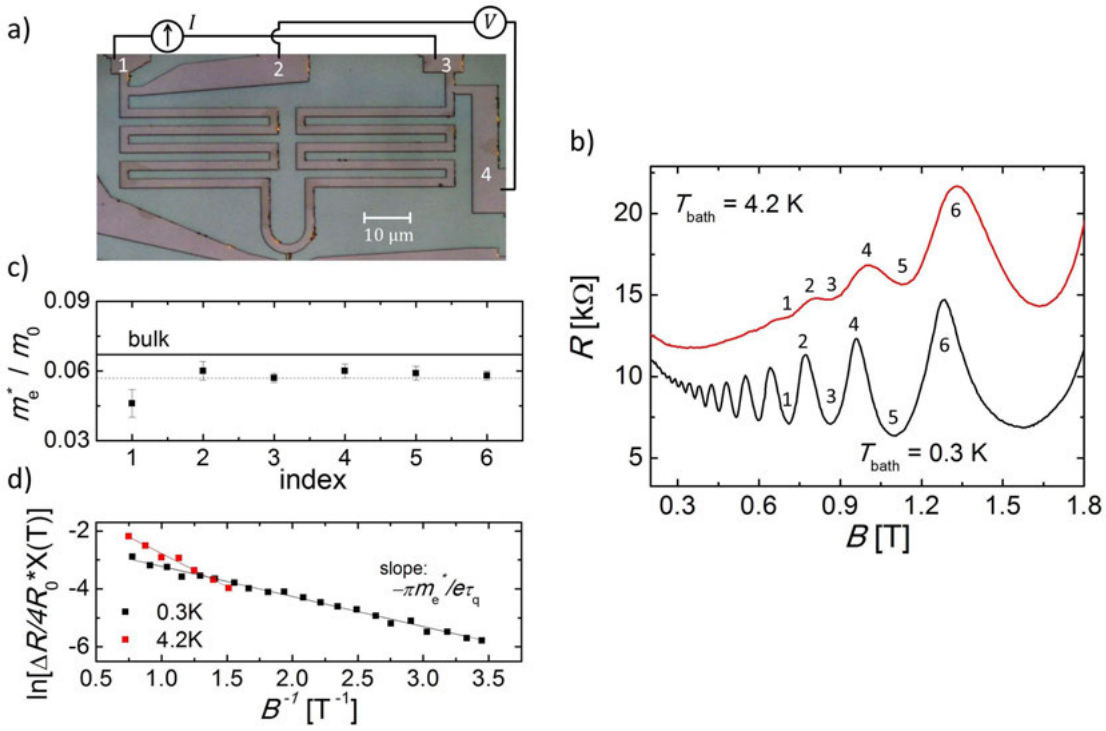

Figure 5.1: Shubnikov-de Haas measurements (SdH) at different bath temperatures $T_{\text{bath}} = 0.3$ K and $T_{\text{bath}} = 4.2$ K of a 2 µm-wide heater line attached to the quantum ring device QRC. a) An optical micrograph of the device [128] with contacts labeled 1 to 4 and a schematic of the four-point measurement setup. b) The measured magnetoresistance $R_{13,24} = V_{24}/I_{13}$ shows SdH oscillations for both bath temperatures. The maxima and minima of $R_{13,24}$ are shifted along the B-axis relative to each other. Corresponding maxima and minima are indexed by integer numbers 1-6. Since the according sheet density n for both temperatures is the same within the measurement uncertainty, the effective mass can be calculated and c) is depicted for every index 1-6. An average of $m_{\text{e}}^* = (0.057 \pm 0.005)m_0$ is found. d) Dingle plot of the SdH oscillation amplitude ΔR for both T_{bath}. The slope of the Dingle plot $-m_{\text{e}}^*\pi/e\tau_{\text{q}}$ yields information about the quantum lifetime τ_{q}.

to the equation [130]

$$\frac{A(B,\,T_1)}{A(B,\,T_2)} = \frac{T_1 \sinh[\frac{2\pi k_\mathrm{B} T_2 m_\mathrm{e}^*}{\hbar e B}]}{T_2 \sinh[\frac{2\pi^2 k_\mathrm{B} T_1 m_\mathrm{e}^*}{\hbar e B}]}. \tag{5.3}$$

This expression can analytically be solved for $T_1 = 2 \cdot T_2$ or $T_2 = 2 \cdot T_1$. Here, Eq. 5.3 is solved numerically for m_e^*. For the SdH oscillations at $T_\mathrm{bath} = 4.2$ K three maxima and three minima are observed. The ratios $A(B_i,\, 4.2\ \mathrm{K})/A(B_i,\, 0.3\ \mathrm{K})$ for the corresponding magnetic fields B_i yield the effective masses m_e, which are depicted in Fig. 5.1 c). The solid line corresponds to the bulk value $m^*_{\mathrm{e,\ GaAs}} = 0.067\ m_0$ [131] and is higher than the measured values whose average yields $m_\mathrm{e}^* = (0.057 \pm 0.005)\ m_0$. A similar deviation is also observed in other $\mathrm{Al_xGa_{1\text{-}x}As/GaAs}$ devices [132, 133, 134]. Coleridge *et al.* investigated m_e^* of $\mathrm{Al_xGa_{1\text{-}x}As/GaAs}$ samples by means of SdH measurements and found m_e^* to systematically decrease as the sheet density decreases in the range $10^{11}\ \mathrm{cm^{-2}} < n < 10^{12}\ \mathrm{cm^{-2}}$ [133]. Tan *et al.* performed similar measurements and found the effective mass m_e^* to increase with decreasing sheet density for $n < 10^{11}\ \mathrm{cm^{-2}}$ [134]. Both investigations indicate that $m_\mathrm{e}^* \approx 0.06\ m_0$ is to be expected for $n \approx 1.9 \cdot 10^{11}\ \mathrm{cm^{-2}}$. This fits $m_\mathrm{e}^* = (0.057 \pm 0.005)\ m_0$ with $n(4.2\ \mathrm{K}) = (1.90 \pm 0.08) \cdot 10^{11}\ \mathrm{cm^{-2}}$, measured in this thesis for the narrow 2D channel. Here, the obtained effective mass m_e^* allows to calculate a Fermi energy of $E_\mathrm{F} = \hbar^2 \pi n / m_\mathrm{e}^* = (7.7 \pm 0.9)$ meV when the electron density $n(0.3\ \mathrm{K}) = (1.83 \pm 0.06) \cdot 10^{11}\ \mathrm{cm^{-2}}$ is used. This value is in accordance with the Fermi energy of $E_\mathrm{F,sim} = 7.2$ meV that is found from energy band simulation, shown in Sec. 3.2.

From the increase of the oscillation amplitude with increasing magnetic field B the quantum lifetime τ_q can be calculated. The quantum lifetime is the mean time an electron remains in a particular energy state. According to Ando [135], the envelope function of the SdH amplitudes can be expressed as

$$\frac{\Delta R}{R_0} = 4X(T)^{-1} \cdot e^{-\pi/\omega_\mathrm{c}\tau_\mathrm{q}} \tag{5.4}$$

with $X(T) = \sinh(A_\mathrm{T})/A_\mathrm{T}$ with $A_\mathrm{T} = 2\pi^2 k_\mathrm{B} T_\mathrm{bath}/\hbar\omega_\mathrm{c}$, the cyclotron frequency $\omega_\mathrm{c} = eB/m_\mathrm{e}^*$, the amplitude ΔR and the resistance $R_0 = R(B = 0)$. The effective mass is considered to be $m_\mathrm{e}^* = 0.057\ \mathrm{m_0}$. Typically the SdH amplitudes are shown in a Dingle plot, i.e. $\ln[\Delta R/4R_0 \cdot X(T)]$ versus 1/B. Following Eq. 5.4 the slope of the Dingle plot is $-\pi m_\mathrm{e}^*/e\tau_\mathrm{q}$. In Fig. 5.3 d) the Dingle plot for the measured SdH oscillations for both bath temperatures is depicted. The quantum lifetime is $\tau_\mathrm{q} = 9.8 \cdot 10^{-13}$ s for $T_\mathrm{bath} = 0.3$ K and $\tau_\mathrm{q} = 4.4 \cdot 10^{-13}$ s for $T_\mathrm{bath} = 4.2$ K. The elastic scattering time is $\tau_\mathrm{e} = m_\mathrm{e}^* \mu_\mathrm{e}(4.2\ \mathrm{K})/e = (12 \pm 1) \cdot 10^{-12}$ s at $T_\mathrm{bath} = 4.2$ K, using $m_\mathrm{e}^* = 0.057\ m_0$. The same elastic scattering time can be calculated from $\mu_\mathrm{e}(0.3\ \mathrm{K})$ for $T_\mathrm{bath} = 0.3$ K. The relation $\tau_\mathrm{e}/\tau_\mathrm{q}$ provides information about the scattering mechanism. Here, $\tau_\mathrm{e}/\tau_\mathrm{q} \approx 27$ is found for $T_\mathrm{bath} = 4.2$ K and $\tau_\mathrm{e}/\tau_\mathrm{q} \approx 12$ for $T_\mathrm{bath} = 0.3$ K. Both are comparable to the ratio $\tau_\mathrm{e}/\tau_\mathrm{q}$, found for the high mobility 2DEG formed in $\mathrm{Al_xGa_{1\text{-}x}As/GaAs}$ heterostructures [136]. Such a high ratio suggests the dominant scattering mechanism to be long-range scattering from remote ionized impurities, as expected for modulation-doped $\mathrm{Al_xGa_{1\text{-}x}As/GaAs}$ heterostructures [137]. Here, these ionized impurities are considered to be located in the Si-doped $\mathrm{Al_xGa_{1\text{-}x}As/GaAs}$ supply layer.

5.2 Determination of the subband spacing

The devices QRA, QRB and ConstrA include QPCs. The energy separations of the subbands of these QPCs will be determined in this section by measuring the transconductance $\mathrm{d}g/\mathrm{d}V_\mathrm{g}$ of the QPC, while applying a DC voltage V_SD. This approach follows the widely used technique that is explained in Sec. 2.2. First, the results of the device ConstrA are presented. The differential two-point conductance g and the transconductance for $V_\mathrm{SD} = 0$ mV of the device ConstrA at $T_\mathrm{bath} = 4.2$ K are depicted in Fig. 5.2 a). The conductance plateaus of the measured differential two-point conductance $g_\mathrm{meas.}(V_\mathrm{g})$ are not perfectly aligned with integer values of $2e^2/h$ due to a series resistance

$$R_\mathrm{s} = \frac{1}{g_\mathrm{meas.}} - \frac{h}{2e^2} \tag{5.5}$$

of the device that is determined to be $R_\mathrm{s} = 142\ \Omega$. In Fig. 5.2 a) the raw measurement of the differential two-point conductance is represented as dashed line, whereas the solid line shows the same curve that is corrected by R_s. The gate voltage is set to values up to $V_\mathrm{g,max} = 0.6\ V$, which is used as maximum voltage for all devices in this thesis. High gate voltages lead to leakage currents l_leak between the 2DEG and the gate electrode due to the increased potential difference. The choice of $V_\mathrm{g,max} = 0.6\ V$ is based on the characterization of the leakage current of the quantum devices used in this thesis. This characterization can be consulted in Appendix G and shows the general relation $V_\mathrm{g} \propto I^2_\mathrm{leak}$, which is typical for III-V heterostructures.

In Fig. 5.2 b) the differential two-point conductance is shown for DC voltages ranging from $V_\mathrm{SD} = 0$ mV up to $V_\mathrm{SD} = 14$ mV with a resolution of $\Delta V_\mathrm{SD} = 0.2$ mV in a waterfall plot. The measurement is corrected by R_s and each curve is shifted along the x-axis by $+20 \cdot V_\mathrm{SD}$ for a better visibility. It can be seen that the plateaus

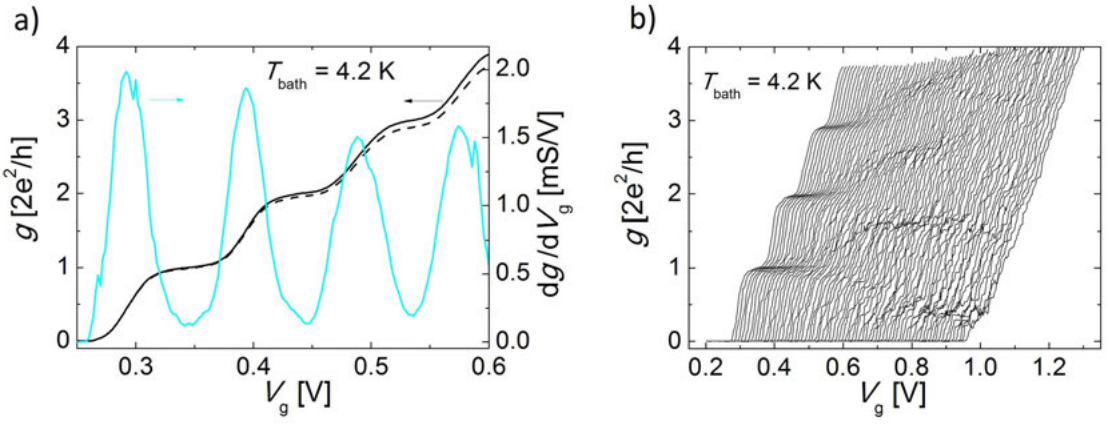

Figure 5.2: Differential conductance of the device ConstrA with applied DC voltage V_SD at $T_\mathrm{bath} = 4.2$ K. a) The differential conductance g (black line) and the corresponding transconductance $\mathrm{d}g/\mathrm{d}V_\mathrm{g}$ (blue line) are shown for $V_\mathrm{SD} = 0$ mV. The dashed line represents the raw measurement. The solid black line is the raw measurement that is corrected by a series resistance of $R_\mathrm{s} = 142\ \Omega$. b) The differential conductance is shown for applied DC voltages, ranging from $V_\mathrm{SD} = 0$ mV to $V_\mathrm{SD} = 14$ mV in steps of 0.2 mV in waterfall plot. The curves are shifted along the x-axis by $20 \cdot V_\mathrm{SD}$. All measurement curves are corrected by a series resistance of $R_\mathrm{s} = 142\ \Omega$.

of the differential conductance have integer values of $2e^2/h$ for $V_{\mathrm{SD}} \to 0$. For $V_{\mathrm{SD}} > 0$ these plateaus split into half plateaus, whereas the half plateau at $1.5 \cdot 2e^2/h$ has the best visibility. The half plateaus around $0.5 \cdot 2e^2/h$ are formed at higher V_{SD} than the $1.5 \cdot 2e^2/h$ plateaus. The half plateau at $2.5 \cdot 2e^2/h$ is just weakly present and the half plateau at $3.5 \cdot 2e^2/h$ can hardly be identified. For each measurement the transconductance $\mathrm{d}g/\mathrm{d}V_{\mathrm{g}}$ is calculated and oscillates between minima and maxima that represent the conductance plateaus and transitions between these plateaus.

The transconductances are typically presented in a grayscale plot, as shown in Fig. 5.3. In this plot the transconductances form a rhombic pattern that is evaluated according to the explanation in Sec. 2.2. The subband spacing $\Delta E_{j,j+1} = E_{j+1} - E_j = \hbar\omega_y$ between the subbands j and $j+1$ is evaluated by dividing the length of the diagonal of the rhombus along the eV_{SD}-axis by 2. The gate efficiency $\gamma = \Delta E_{j,j+1}/\Delta V_{\mathrm{g}}$ is calculated by comparing the subband spacing and the gate voltage ΔV_{g} that is required to populate a new subband with electrons. Subsequently, the characteristic value $\hbar\omega_x$ that characterizes the saddle-point potential can be determined by using Eq. 2.26. The relation ω_y/ω_x gives an estimation about the confinement of the 1D constriction. Higher ratios of ω_y/ω_x result in a better

Subbands	ΔV_{g} [mV]	γ [%]	$\hbar\omega_y$ [meV]	$\hbar\omega_x$ [meV]	ω_y/ω_x
$1 \to 2$	100 ± 2	11 ± 3	11 ± 2	5 ± 1	2.2 ± 0.6
$2 \to 3$	96 ± 2	9 ± 2	9 ± 2	5 ± 1	1.8 ± 0.6
$3 \to 4$	87 ± 2	8 ± 2	7 ± 1	5 ± 1	1.4 ± 0.5

Table 5.1: Results of the subband spectroscopy of the device ConstrA.

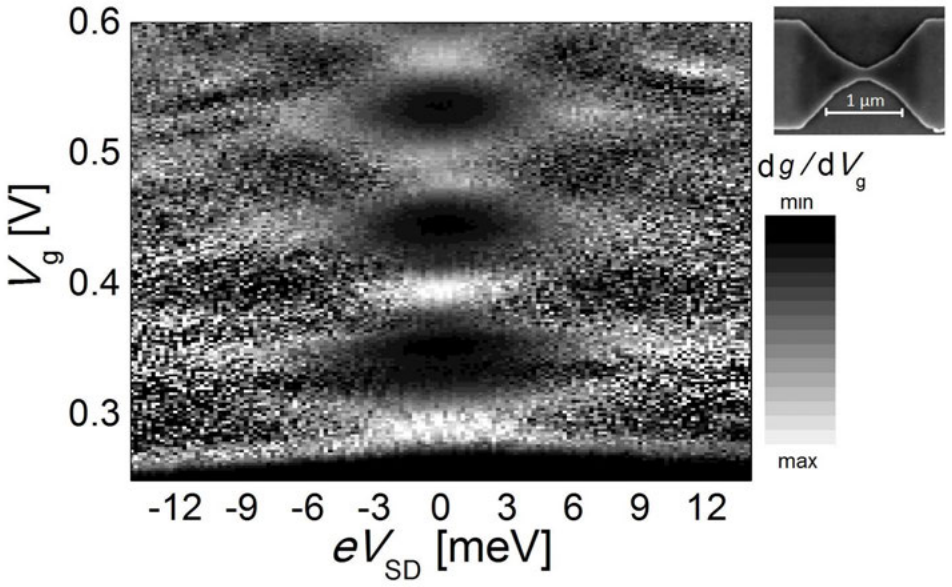

Figure 5.3: Grayscale plot of the transconductance $\mathrm{d}G/\mathrm{d}V_{\mathrm{g}}$ of the device ConstrA with applied source-drain voltage V_{SD}. Dark areas refer to plateaus of the electrical conductance $G(V_{\mathrm{g}},V_{\mathrm{SD}})$ and bright areas refer to transitions between conductance plateaus. The resolution of the measurement is $\Delta V_{\mathrm{g}} = 2$ mV and $\Delta V_{\mathrm{SD}} = 0.2$ mV. The rhombic pattern of the transconductance allow to determine the subband spacings $\Delta E_{N,N+1}$ and the gate efficiency γ. The scanning electron micrograph in the upper right shows a QPC with comparable geometry [138].

visibility of the conductance plateaus. The mentioned characteristic properties are summarized in Tab. 5.1 for the first three subband spacings of the device ConstrA. In contrast to the schematic in Fig. 2.6, the experimentally derived rhombus pattern does not result in identical rhombus geometries for all V_{SD} and V_{g}. This is explained by a constriction potential that is not perfectly parabolic. Furthermore, higher values of V_{g} lead to a change of the effective constriction potential.

The characterization of the QPCs that are embedded in the quantum rings in the devices QRA and QRB are performed in the same way as for the device ConstrA. However, the measured differential two-point conductance comprises the contribution of both arms of a ring. In Fig. 5.4 a) a SEM image of the quantum ring device QRB is depicted. The four terminals are labeled 1 to 4. A finger gate covers the QPC that is incorporated in the straight arm. Sweeping the finger gate in the

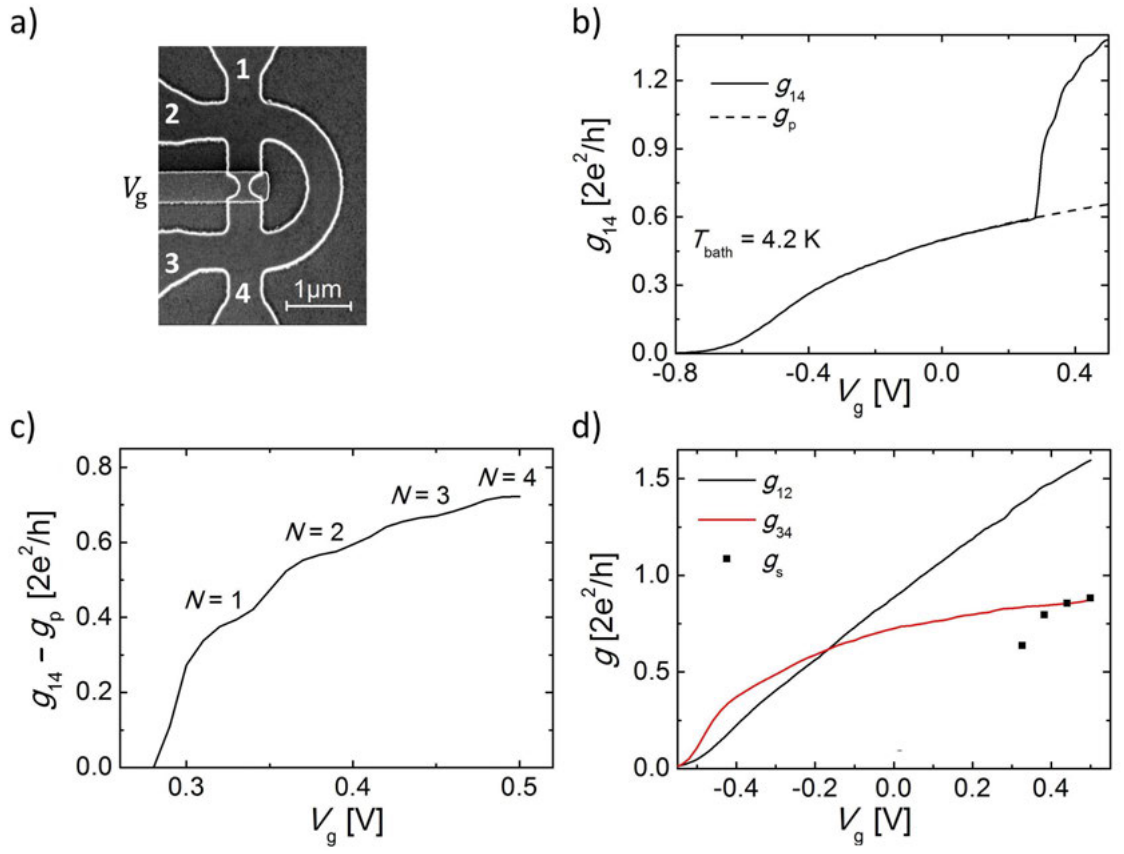

Figure 5.4: Electrical differential two-point conductance of the device QRB with applied DC voltage. a) A SEM image [138] of the quantum ring device QRB with contacts labeled 1 to 4. A QPC is embedded in the straight arm of the quantum ring and is covered by a finger gate. b) The differential two-point conductance g_{14} (solid line) comprises the contribution of the bent arm with a threshold voltage of about $V_{\mathrm{th}} \approx -0.7$ V and the straight arm with a threshold voltage of about $V_{\mathrm{th}} \approx 0.27$ V. The contribution to g_{14} from the bent arm is approximated with a polynom of 4th order and extrapolated to $V_{\mathrm{g}} = 0.5$ V (dashed line). c) The conductance $g_{14} - g_{\mathrm{p}}$ is shown which represents the contribution of the straight arm to g_{14}. The plateaus of $g_{14} - g_{\mathrm{p}}$ stem from the confinement of the QPC and are labeled $N = 1$, 2, 3 and $N = 4$. d) The differential two-point conductances g_{12}, g_{34} and g_{s} (see text) are shown.

range $-0.8\ \mathrm{V} \leq V_\mathrm{g} \leq 0.5\ \mathrm{V}$ results in the differential two-point conductance g_{14} that is shown in Fig. 5.4 b) (solid line). The contribution from the bent arm with a threshold voltage of about $V_\mathrm{th} \approx -0.7$ V and from the straight arm with a threshold voltage of about $V_\mathrm{th} \approx 0.27$ V can clearly be distinguished. The conductance plateaus for $V_\mathrm{g} > 0.27$ V are visible, albeit weakly pronounced. In order to separate the contributions of the arms to g_{14} from each other, a fourth degree polynomial function is fitted to g_{14} in the range $-0.2\ \mathrm{V} \leq V_\mathrm{g} \leq 0.27\ \mathrm{V}$ and extrapolated up to $V_\mathrm{g} = 0.5$ V (dashed line). The extrapolated conductance g_p is then subtracted from g_{14} to obtain the contribution of the straight arm to g_{14}, which is shown in Fig. 5.4 c). The conductance plateaus are labeled $N = 1$, 2, 3 and $N = 4$ and are each used to calculate the series resistance R_s of the QPC in the straight arm. Translating R_s into the corresponding conductance $g_\mathrm{s} = 1/R_\mathrm{s}$ allows to compare the series resistance with the measured conductances g_{12} and g_{34} that are depicted in Fig. 5.4 d). The series resistance of the leads is found to be about 700 Ω by further two-point measurements in the leads. This is by one order of magnitude lower than $1/g_{34}$, $1/g_{12}$ and $1/g_\mathrm{s}$. Therefore, the series resistance of the QPC is dominated by the 1D waveguides of the quantum ring, which is important for the thermal noise measurements in the subsequent section. The reason for this is that the measurement setup to measure the spectrum of the thermal noise is a two-point setup and is more sensitive to higher resistances.

The transconductance measurements are performed for the QPCs of both devices QRA and QRB and are depicted in Fig. 5.5 for the QPC of the device QRB. The characteristic values ΔV_g, γ $\hbar\omega_y$ and ω_x are drawn from these measurements for both devices and summarized in Tab. 5.2 and 5.3.

Whereas the gate efficiency γ is approximately 10% for all three QPCs, the subband spacing $\hbar\omega_y$ is almost reduced by half in the QPCs of both quantum ring devices compared to the single QPC device. This expected deviation stems from the different widths of the 1D constriction. While the QPC of the device ConstrA has a width of about 100 nm, the QPCs of the devices QRA and QRB have a width of about 170 nm. Since $\hbar\omega_x \approx 5$ meV is almost identical in all devices, the ratio ω_y/ω_x is reduced by approximately a half in the QPCs that are embedded in the quantum rings QRA and QRB compared to ConstrA. The rhombus pattern in the grayscale plot of the transconductance of QRA and QRB is therefore not as distinct as in ConstrA.

The knowledge of the parameters of the 1D constriction that were acquired in this section serve as basis for the investigations in the following sections. In order to further enhance the reliability of the acquired subband spacings, an alternative approach to deduce the gate efficiency γ is presented in the following section.

Subbands	ΔV_g [mV]	γ [%]	$\hbar\omega_y$ [meV]	$\hbar\omega_x$ [meV]	ω_y/ω_x
$1 \rightarrow 2$	57 ± 2	11 ± 2	6.3 ± 1.0	5 ± 1	1.3 ± 0.3
$2 \rightarrow 3$	55 ± 2	10 ± 2	5.5 ± 0.9	5 ± 1	1.1 ± 0.3
$3 \rightarrow 4$	54 ± 1	9 ± 1	4.8 ± 0.7	6 ± 1	0.8 ± 0.2

Table 5.2: Results of the subband spectroscopy of the device QRB.

5.3 Thermal subband spectroscopy

In the previous section the subband spacing $\hbar\omega_y$, the gate efficiency γ and the parameter ω_x were determined by means of subband spectroscopy in the non-linear transport regime. Due to the relatively high uncertainties of the experimentally derived parameters $\hbar\omega_y$, $\hbar\omega_x$ and γ in this section, an additional approach is chosen to derive γ and ω_y. The idea of this approach is comparable to the one of Kristensen *et al.* [53] in which the measured electrical conductance $G(V_g)$ through a QPC is fitted with

$$G = \frac{2e^2}{h} \sum_{j=1}^{N} \int_0^\infty T_j(E) \cdot \frac{\partial f}{\partial E} \mathrm{d}E \tag{5.6}$$

with the Fermi-Dirac distribution f, the transmission probability $T_j(E) = (1 + \exp(-\pi\epsilon_j))^{-1}$ of the electron to propagate through the QPC at the energy mode $\epsilon_j = 2(E - \hbar\omega_y(n+1) - V_0)/\hbar\omega_x$ and the number of occupied subbands N of the

Subbands	ΔV_g [mV]	γ [%]	$\hbar\omega_y$ [meV]	$\hbar\omega_x$ [meV]	ω_y/ω_x
$1 \rightarrow 2$	56 ± 2	10 ± 2	5.5 ± 0.4	4 ± 1	1.4 ± 0.3
$2 \rightarrow 3$	54 ± 1	9 ± 1	4.8 ± 0.3	5 ± 1	1.0 ± 0.3
$3 \rightarrow 4$	52 ± 1	8 ± 1	4.0 ± 0.3	5 ± 2	0.8 ± 0.2

Table 5.3: Results of the subband spectroscopy of the device QRA.

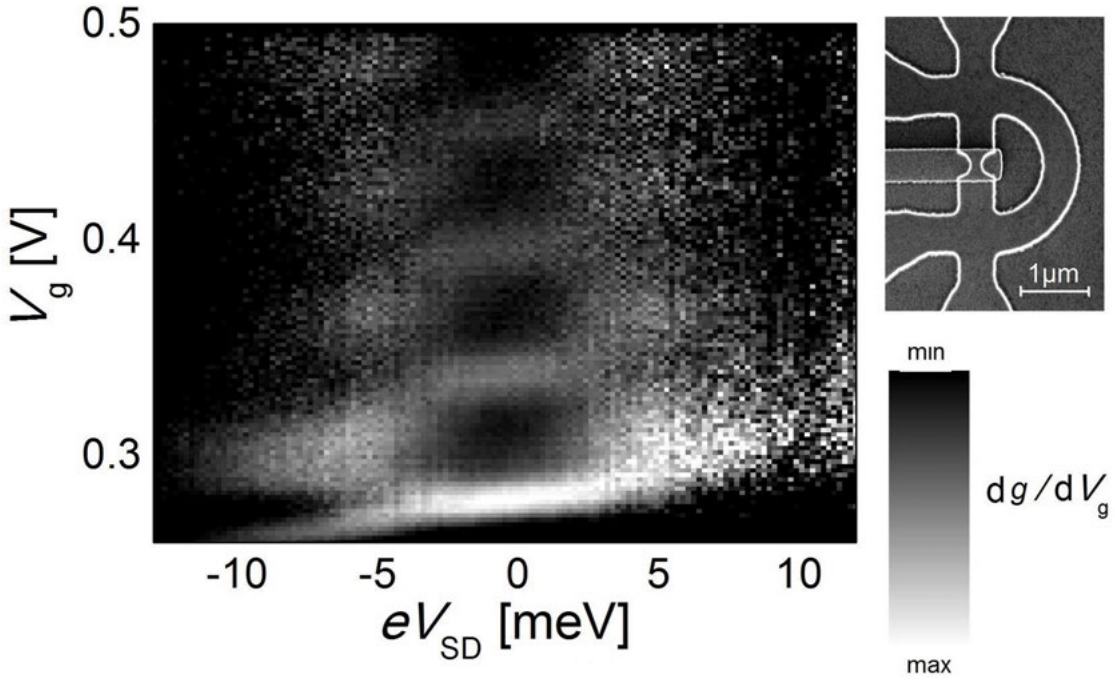

Figure 5.5: Grayscale plot of the transconductance $\mathrm{d}g/\mathrm{d}V_g$ of the device QRB with applied source-drain voltage V_{SD}. Dark areas refer to plateaus of the differential electrical conductance $g(V_g,V_{SD})$ and bright areas refer to transitions between conductance plateaus. The contrast in $\mathrm{d}g/\mathrm{d}V_g$ is linearly increased along positive V_g for better visibility. The resolution of the measurement is $\Delta V_g = 2$ mV and $\Delta V_{SD} = 0.2$ mV. The scanning electron micrograph in the upper right shows the device QRB [138].

QPC (as introduced in Sec. 2.2). The 1D subband energy spacing $\hbar\omega_y$ is estimated by fitting the measured temperature dependence of the QPC conductance to Eq. 5.6.

In this thesis a similar approach is chosen. The main difference is that the electrical conductance is measured near the threshold voltage V_{th} multiple times by sweeping the gate voltage V_{g} back and forth. This procedure is performed at temperatures between $T_{\mathrm{bath}} = 4.2$ K and $T_{\mathrm{bath}} = 60$ K. In Fig. 5.6 a) the measured electrical conductance of the device ConstrA is depicted. Due to the 'smearing' of the Fermi-Dirac distribution $f = [1 + \exp((E - E_{\mathrm{F}})/k_{\mathrm{B}}T_{\mathrm{bath}})]^{-1}$ the threshold voltage V_{th} decreases with increasing bath temperature T_{bath}. In the following, V_{th} is defined as the gate voltage where the corresponding electrical conductance is $G(V_{\mathrm{g}} = V_{\mathrm{th}}) \equiv G_{\mathrm{th}} = \xi \cdot 2e^2/h$. The coefficient ξ is chosen to represent an electrical conductance with a high slope $\mathrm{d}G/\mathrm{d}V_{\mathrm{g}}$ while at the same time allowing a relatively high change of the threshold voltage with the bath temperature $\mathrm{d}V_{\mathrm{th}}/\mathrm{d}T_{\mathrm{bath}}$.

In order to find the gate efficiency γ of the QPC's global top-gate, $G(E_{\mathrm{F}})$ is simulated by using Eq. 5.6, as depicted in Fig. 5.6 b) for $\hbar\omega = 5$ meV and $\hbar\omega_y = 10$ meV. Similarly to V_{th}, a Fermi energy $E_{\mathrm{F,Th}}$ can be found where $G(E_{\mathrm{F}} = E_{\mathrm{F,Th}}) \equiv G_{\mathrm{th}}$. Comparing $\Delta V_{\mathrm{th}} = V_{\mathrm{th}}(T_{\mathrm{bath}}) - V_{\mathrm{th}}(4.2\ \mathrm{K})$ and $\Delta E_{\mathrm{F,Th}} = E_{\mathrm{F,Th}}(T_{\mathrm{bath}}) - E_{\mathrm{F,Th}}(4.2\ \mathrm{K})$ with each other allows to find the gate efficiency $\gamma = \Delta E_{\mathrm{F,Th}}/\Delta V_{\mathrm{th}}$.

In Fig. 5.6 c) the measured $\Delta V_{\mathrm{th}}(T_{\mathrm{bath}})$ of the device ConstrA is depicted and compared with the simulated $\Delta E_{\mathrm{F,Th}}/\gamma$ for $\xi = 0.2$, $\hbar\omega_x = 5$ meV, $\hbar\omega_y = 10$ meV and $\gamma = 0.16 \pm 0.03$. It can be seen that measured values (black squares) follow the calculated values for $\gamma = 0.16$ (solid line) and are enveloped by the calculated values for $\gamma = 0.19$ and $\gamma = 0.13$ (dashed lines each). The same is found if $\xi = 0.3$ is chosen, as depicted in 5.6 d).

In the previous section the subband spacing of the device ConstrA is found to be $\hbar\omega_y = (11 \pm 2)$ meV with the gate efficiency $\gamma = 0.11 \pm 0.03$. The uncertainty of the gate efficiency γ remains unchanged by the method that is presented in this section. However, the best fit for the calculated to the measured values $\Delta V_{\mathrm{th}}(T_{\mathrm{bath}})$ is found for $\hbar\omega_y = 10$ meV, which narrows the uncertainty of the experimentally determined $\hbar\omega_y$ and makes the value $\hbar\omega_y = (11 \pm 2)$ meV more reliable.

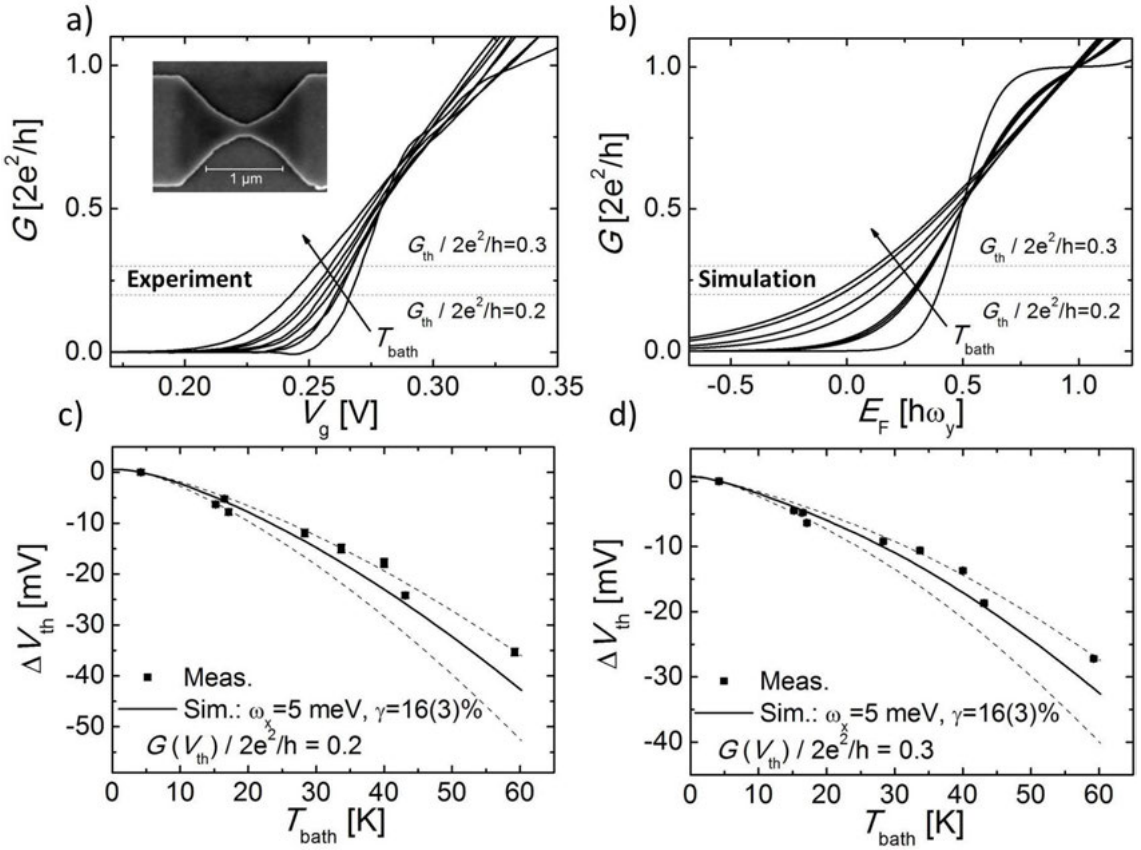

Figure 5.6: Thermal subband spectroscopy (see text) of a quantum point contact. a) Measured electrical conductance of a QPC with $\hbar\omega_y = (11 \pm 2)$ meV at the temperatures 4.2 K, 15.2K, 16.5 K, 17.1 K, 28.3 K, 33.7 K, 40 K, 43.1 K and 59.2 K. b) Simulated electrical conductance according to Eq. 2.28 of a QPC with $\hbar\omega_x = 5$ meV and $\hbar\omega_y = 10$ meV at the temperatures 4.2 K, 15.2 K, 16.2 K, 17.2 K, 28.2 K, 33.2 K, 40.2 K and 43.2 K. c) Comparison of the shift of the threshold voltage ΔV_{th} of the theoretical (dashed lines) and experimental values (squares) of the electrical conductance due to increased temperature. Here, the electrical conductance that defines V_{th} is set to $G(V_{\mathrm{th}}) = 0.2\ e^2/h$ and to d) $G(V_{\mathrm{th}}) = 0.3\ e^2/h$.

Chapter 6

Analysis of the noise spectrum in the $Al_xGa_{1-x}As$/GaAs quantum devices

In this chapter measurements as well as an analysis of the noise spectrum of the 1D constrictions and the quasi-1D quantum rings are presented. For an overview of the devices Appendix F can be consulted. In the first section measurements of the thermal noise $S_{V,w}$ are performed in two-terminal bent and straight 1D constrictions as well as in the multi-terminal quantum rings. Whereas in 1D constrictions the measured thermal noise $S_{V,w}$ agrees with the theoretically expected value $S_{V,Th}$ within the measurement uncertainty, in quantum rings $S_{V,w}$ exceeds $S_{V,Th}$ by up to 60%. This section aims to analyze the excess noise $S_{V,excess}$, i.e. the part of the measured white part of the noise spectrum that exceeds the theoretically expected value $S_{V,excess} = S_{V,w} - S_{V,Th}$. The systematic measurement of the noise spectra in a large variety of samples helps to exclude possible origins of the excess noise, such as the wafer material, the curvature of the device as well as the length of the waveguide. The temperature dependence of the excess noise in a quantum ring is measured in order to test the hypothesis whether correlated noise sources, caused by the phase coherent behavior of the electron waves in the quantum ring, can be the origin of the excess noise. Note that this explanation is not linked to 'phase noise' that describes the frequency uncertainty of periodic signals.

6.1 Current state of research

In signal processing, noise is considered as an unwanted phenomenon, which imposes a limit on the achievable accuracy of measurement devices. However, the noise spectrum follows a statistic that is specific to the origin of the noise and provides information about the investigated system. In Sec. 2.5 the most common noise models thermal noise, shot noise, generation-recombination noise and 1/f noise along with their respective statistics were introduced.

The first description of noise as measurable fluctuation of current can be found in the pioneering work of W. Schottky, who studied fluctuations of current in vacuum tubes [82], which is known as shot noise nowadays [82, 74]. Shot noise is created whenever an electric current has to overcome a potential barrier which may or may not be achieved by an electron with a certain probability. Trying to verify the results of Schottky in low frequency circuits, J.B. Johnson discovered the $1/f$ noise, or 'flicker noise', in 1925 [139]. W. Schottky subsequently described Johnson's experiment mathematically. Many years later, in 1957, McWhorter created a model in which the 'flicker noise' is explained in terms of trapping and detrapping of electrons in surface states [95]. According to McWhorter's model, the noise therefore originates from a fluctuation of the number of charge carriers. According to its name, flicker noise is characterized by a PSD that is proportional to $f^{-\gamma}$, whereas the exponent is assumed to be $\gamma = 1.0 \pm 0.1$ [79], which is observed in epitaxial GaAs devices [89, 90, 91, 92, 83, 84]. However, exponents that are in the range of $0.9 \leq f \leq 1.4$ are found as well [93]. A significant contribution to the field of 1/f noise was done by Hooge, who introduced the empirical [94] relation $S_\mathrm{V} = \alpha_\mathrm{H} V^2/fN$ for pure f^{-1} noise by studying gold films in the presence of a steady current. Here V describes the voltage across the sample, N the total number of charge carriers and α_H is the dimensionless Hooge parameter. For homogeneously Si-doped $\mathrm{Al_xGa_{1\text{-}x}As/GaAs}$ a Hooge parameter of $\alpha_\mathrm{H} = 7.1 \cdot 10^{-4}$ was found [91]. It is believed that, at least in metal films, 1/f noise is a bulk effect rather than a surface effect and stems from fluctuations of the charge carrier mobility in the bulk. This is in clear contrast to McWhorter's model. The Hooge model is found to provide a good approximation for the 1/f spectrum in many materials. However, the origin of 1/f noise is an open question [79, 140] and is assumed to change from one material system to another.

In 1928 J.B. Johnson and H. Nyquist discovered the thermal noise [69]. Thermal noise is intrinsic to all resistors and yields information about the electron temperature of a device with known resistance and vice versa. Thermal noise is a well understood phenomenon and can be derived in multiple ways and for various devices [80, 74, 68].

Noise signals S_1 and S_2 that stem from different and independent sources typically sum up to a total noise $S_\mathrm{tot} = S_1 + S_2$. This is the case if the noise sources are not correlated with each other [141]. However, when correlation between noise sources exists, the resulting total noise differs from $S_1 + S_2$ [96, 142, 143, 80], due to the additional correlation term in S_tot that depends on the coupling between the noise sources. This correlation is observed for 1/f noise in $\mathrm{Al_xGa_{1\text{-}x}As/GaAs}$ heterojunction bipolar transistors [142] between base and collector noise sources. However, the correlation of the PSD of different noise sources is rarely taken into consideration as noise sources are mostly uncorrelated. In addition, the origin of the correlation itself is also rarely discussed. Therefore the consideration of noise sources from different electron waveguides whose correlation is used as indicator of

phase coherence in the system is a new idea that is not investigated so far.

(!) Note: in the following the term 'excess noise' will be used to describe the part of the measured thermal noise $S_{\mathrm{V,w}}$ that exceeds the theoretically expected thermal noise $S_{\mathrm{V,Th}}$, derived from Eq. 4.4. It must not be confused with the 'excess noise ratio' which refers to an increase of the thermal noise due to a heated system or to noise contributions, such as 1/f noise or shot noise that exceed the PSD of the thermal noise.

6.2 Excess noise in 1D constrictions

In this thesis several $Al_xGa_{x\text{-}1}As/GaAs$-based quantum devices were characterized with respect to their noise spectrum. As presented in Sec. 2.5 the power spectral density (PSD) of the noise is a superposition of all noise contributions, such as thermal noise and 1/f noise. In most $Al_xGa_{1\text{-}x}As/GaAs$-based devices that are investigated in this thesis the PSD is dominated by frequency-independent, i.e. white noise, $S_{\mathrm{V,w}}$. This noise is identified as thermal noise since $S_{\mathrm{V,w}}$ agrees with the theoretically predicted value $S_{\mathrm{V,Th}}$ within the measurement uncertainty. In contrast, the contribution of 1/f noise is restricted to frequencies $f < 1$ kHz, which is small compared to the measurement range of up to 100 kHz. Therefore, the contribution of 1/f noise will not be further discussed in this section. As derived in Sec. 4, the theoretical value of the thermal noise is calculated with the equation

$$S_{\mathrm{V,Th}} = 4k_{\mathrm{B}}T_{\mathrm{e}}R + 2 \cdot 4k_{\mathrm{B}}T_{\mathrm{amp}}\frac{R^2}{R_{\mathrm{amp}}} \tag{6.1}$$

with the electron temperature of the sample T_{e}, the two-point resistance of the sample R, the input resistance $R_{\mathrm{amp}} = 5$ MΩ and the temperature $T_{\mathrm{amp}} = 300$ K of the two voltage amplifiers. The contribution of the 1D devices to the resistance, and therefore to the thermal noise, is dominant compared to the contribution of the leads. As mentioned in Sec. 4, the noise measurement setup is well-suited for temperatures in the range 4.2 K $\leq T_{\mathrm{bath}} \leq$ 70 K and for resistances in the range 1 kΩ $\leq R \leq$ 60 kΩ. The corresponding range of electrical conductance is $12.9 \cdot 2e^2/h \geq G \geq 0.2 \cdot 2e^2/h$. This is found for 2D and ballistic 1D devices based on $Al_xGa_{1\text{-}x}As/GaAs$ heterostructures that do not form multichannel quantum rings. However, in quantum rings the measured noise is found to exceed $S_{\mathrm{V,Th}}$, as will be shown later in this section.

The noise spectra of the device ConstrA, a QPC with a width of about 100 nm, are taken according to the setup shown in Fig. 6.1 a) for different gate voltages V_{g} of a global top-gate. In Fig. 6.1 b) the measured two-point differential conductance g is presented. From the conductance plateaus a series resistance of $R_{\mathrm{s}} = g^{-1} - (2Ne^2/h)^{-1} \approx 142\ \Omega$ is deduced, which stems from the leads to the QPC and is negligible compared to the resistance of the QPC. The measured noise spectra are therefore dominated by the contribution of the QPC. From g and the bath temperature $T_{\mathrm{bath}} = 4.2$ K the expectation value $S_{\mathrm{V,Th}}$ is calculated for gate voltages in the range from $V_{\mathrm{g}} = 0.3$ V to $V_{\mathrm{g}} = 0.6$ V with a step size of $\Delta V_{\mathrm{g}} = 2$ mV. Here, T_{bath} is assumed to be identical to the electron temperature of the device, i.e. $T_{\mathrm{bath}} = T_{\mathrm{e}}$. In this range noise measurements are performed with a step size of $\Delta V_{\mathrm{g}} = 5$ mV. The noise spectra for $V_{\mathrm{g}} = 348$ mV and $V_{\mathrm{g}} = 528$ mV are given as example in Fig. 6.1 c). For $V_{\mathrm{g}} = 528$ mV, i.e. a relatively low resistance, the noise

spectrum shows a frequency-independent PSD. For $V_g = 348$ mV, i.e. a relatively high resistance, the spectrum shows the behavior of a low-pass filter. As mentioned in Sec. 4, the spectrum $S_V(f)$ is fitted with the function

$$S_V(f) = \frac{S_{V,w}}{1 + (2\pi f R C_{Par})^2} \tag{6.2}$$

with the parasitic capacitance of the order of $C_{Par} \approx 4 \cdot 10^{-10}$ F, and the white part of the noise $S_{V,w}$ as free parameters. In the observed range of V_g the values of the thermal noise $S_{V,w}$, derived from the fit, agree with the expected value $S_{V,Th}$ within the uncertainty of the measurement, as depicted in Fig. 6.1 d).

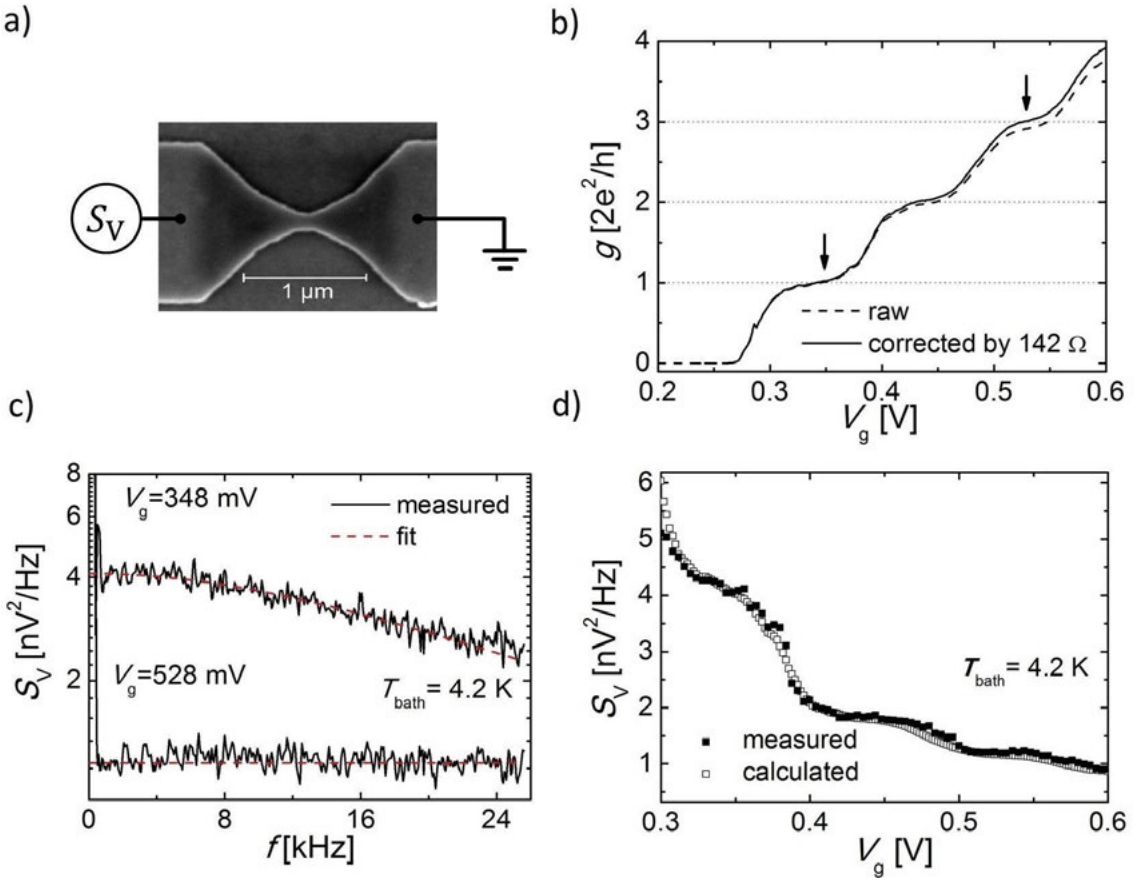

Figure 6.1: Measurement of the noise spectra S_V of the device ConstrA at $T_{bath} = 4.2$ K. a) A SEM image of the device, a QPC with a width of about 100 nm [138]. b) The measured two-point differential conductance of the QPC (dashed line) which allows to estimate the series resistance to $R_s \approx 142\ \Omega$ and to conclude that the noise spectrum is dominated by the QPC. The solid line is calculated from the dashed line when subtracting R_s. c) Two noise spectra (solid black lines) for $V_g = 348$ mV and $V_g = 528$ mV are shown. These gate voltages are indicated with arrows in b). Noise spectra with lower resistance have a PSD that is dominated by frequency-independent noise, whereas noise spectra of higher resistances show a low-pass behavior that is fitted to the noise spectra (red dashed line). d) A comparison between the measured thermal noise $S_{V,w}$ (solid squares) and the expectation value $S_{V,Th}$ (open squares) shows that $S_{V,w}$ and $S_{V,Th}$ agree with each other in the gate voltage range from $V_g = 0.3$ V to $V_g = 0.6$ V. The expectation value $S_{V,Th}$ is calculated from $g(V_g)$ and T_{bath}.

In an ideal ballistic device a resistance R and an electron temperature T_e can not be defined locally due to the lack of scattering of the electrons. It may therefore appear counter-intuitive to measure the noise spectrum of a ballistic device. The solution for this can be found in the Landauer-Büttiker formalism, where the properties of the ballistic electrons inherit the properties of the electron reservoirs, such as the electron temperature. In the ideal system the resistance, and therefore any fluctuation, results from the scattering of the electron wave functions at the transition from 2D leads to 1D constriction. Hence, the quantized resistance of a QPC $R_\mathrm{QPC} = (2Ne^2/h)^{-1}$ that depends on the number of populated subbands N produces the thermal noise $S_\mathrm{V,w} = 4k_\mathrm{B}T_\mathrm{e}R_\mathrm{QPC}$ [74] (see Sec. 2.2 and Sec. 4).

Further 1D constrictions were investigated with respect to their noise spectrum at $T_\mathrm{bath} = 4.2$ K to show that the agreement of $S_\mathrm{V,w}$ and $S_\mathrm{V,Th}$ is still given if an 1D constriction is bent or has an increased length. Therefore, the two-terminal device ConstrB, a bent waveguide with a width of $w = 285$ nm and a length of $l = 3.8$ µm, and the device ConstrC, a straight waveguide with a width of $w = 285$ nm and a length of $l = 2.8$ µm, are chosen. Note that these lengths do not exceed the elastic mean free path of $l_\mathrm{e} \approx 18$ µm. The SEM images of these devices can be seen in Figs. 6.2 c) and d). It has to be noted that the devices ConstrA, ConstrB and ConstrC were fabricated from the same wafer material. Sweeping the gate voltage V_g of the global top-gate results in the two-point differential conductance that is depicted in Fig. 6.2 a) for ConstrB and in Fig. 6.2 b) for ConstrC. In both devices the conductance quantization is weakly pronounced, but allows an estimate of the series resistance that is found to be $R_\mathrm{s} = 580\ \Omega$ for the device ConstrB and $R_\mathrm{s} = 710\ \Omega$ for the device ConstrC. From the two-point conductance the expectation values $S_\mathrm{V,Th}$ are derived and found to fit the measured values $S_\mathrm{V,w}$ of the thermal noise in the measured range of V_g, as shown in Fig. 6.2 c) for ConstrB and in Fig. 6.2 d) for ConstrC.

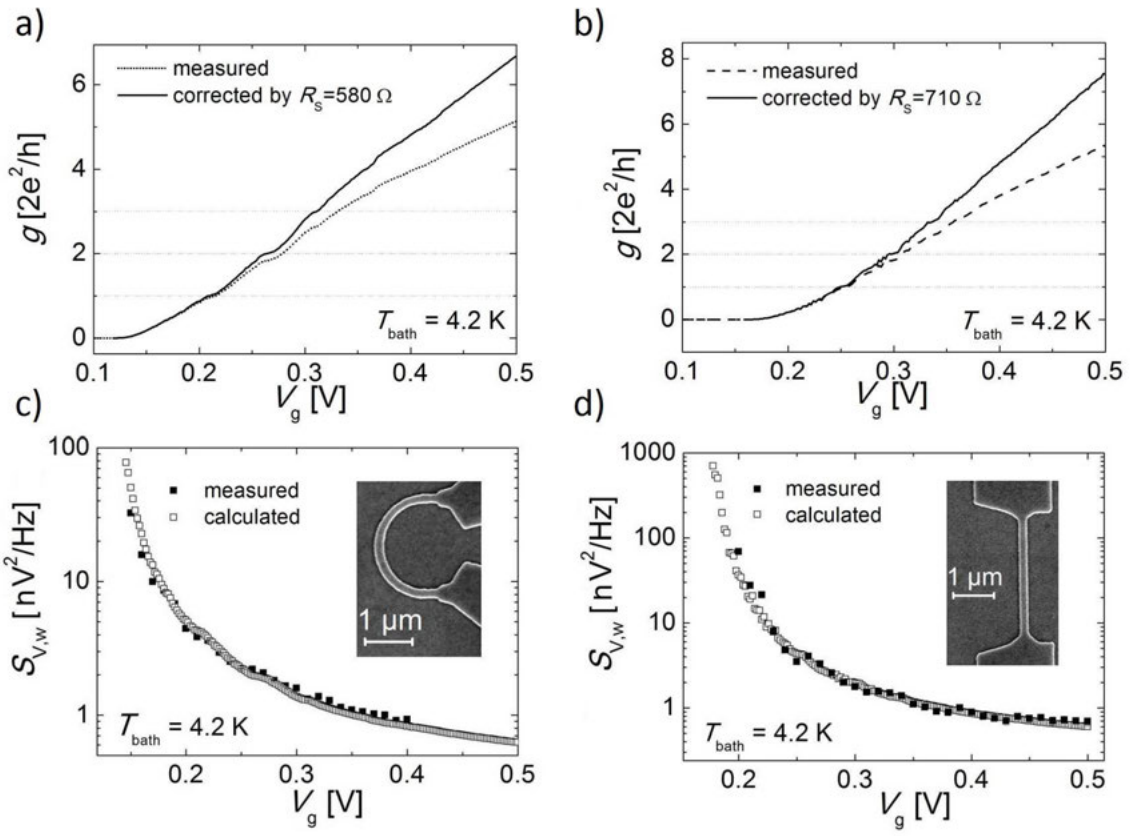

Figure 6.2: Measurements of the electrical conductance (dashed line) of a) the device ConstrB, a bent waveguide with a width of $w = 285$ nm and a length of $l = 3.8$ µm and b) the device ConstrC, a straight waveguide with a width of $w = 285$ nm and a length of $l = 2.8$ µm at $T_{\mathrm{bath}} = 4.2$ K each. From the weakly pronounced conductance plateaus that are highlighted by horizontal dotted lines the series resistance can be determined to be $R_{\mathrm{s}} = 580\ \Omega$ for the device ConstrB and to be $R_{\mathrm{s}} = 710\ \Omega$ for the device ConstrC. It is therefore concluded that the measured noise spectra are dominated by the 1D constrictions. The solid lines represent the raw data that is corrected by R_{s}. The results of the noise measurements are depicted in c) for the device ConstrB and d) for the device ConstrC (black squares). White squares refer to the thermal noise calculated from the measured conductance values according to Eq. 6.1. The insets show SEM images of the samples [138].

6.3 Excess noise in quantum ring devices

The quantum ring devices QRA, QRC and QRD are investigated in the same way as the 1D constrictions. The device QRD comprises waveguides with a width of $w \approx 170$ nm, whereas the waveguides of the devices QRA and QRC have a width of $w \approx 510$ nm. All quantum rings have an asymmetric geometry, with one arm that is bent and one arm that is straight. For all quantum ring devices the length of the straight arm is about 2 µm and about 2.8 µm for the bent arm. Note that the length of the ring arms is comparable to the length of the 1D devices ConstrB and ConstrC and that the curvature of the bent arm is comparable to the device ConstrB.

In Fig. 6.3 a) the configuration for measuring the noise spectra of the device QRA is depicted with contacts labeled from 1 to 4. The structure has two finger gates, each covering one arm of the asymmetric quantum ring device. In the straight

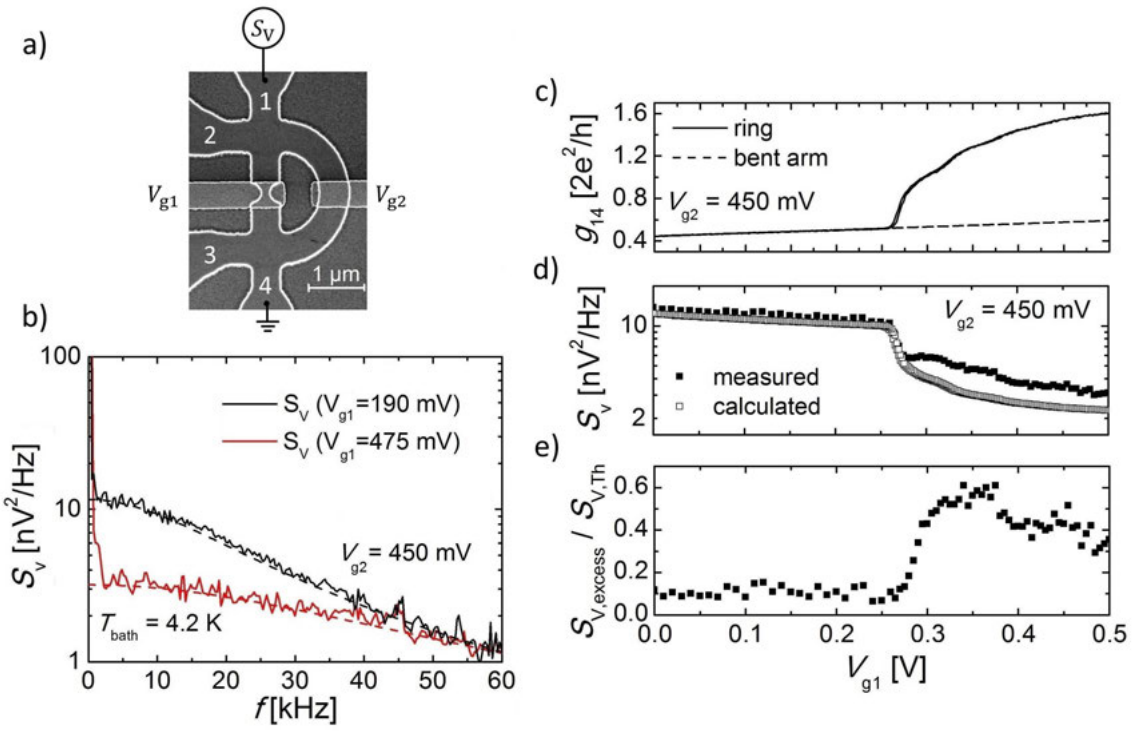

Figure 6.3: Measurement of the thermal noise in the device QRA at $T_{\mathrm{bath}} = 4.2$ K. a) SEM image [138] of the quantum ring device with contacts labeled 1 to 4 and the measurement configuration of the noise measurements. The straight arm hosts a QPC and both arms are covered by a finger gate each. Here, V_{g1} refers to the gate that covers the QPC. The voltage of the other finger gate is kept constant at $V_{\mathrm{g2}} = 450$ mV. b) The noise spectra at $V_{\mathrm{g1}} = 190$ mV and at $V_{\mathrm{g1}} = 475$ mV are depicted for $V_{\mathrm{g2}} = 450$ mV. c) The measured two-point differential conductance g_{14} is shown (solid line). The dashed line represents the extrapolated polynomial function that is fitted to g_{14} for V_{g1} to visualize the contribution of each arm to g_{14}. This allows to estimate the series resistance of the QPC. d) The measured thermal noise $S_{\mathrm{V,w}}$ (solid squares) and the expected values $S_{\mathrm{V,Th}}$ (open squares) that are calculated from g_{14} and T_{bath} are depicted. The relative excess noise $S_{\mathrm{V,excess}}/S_{\mathrm{V,Th}} = (S_{\mathrm{V,w}} - S_{\mathrm{V,Th}})/S_{\mathrm{V,Th}}$ is shown in e).

arm a QPC is embedded. In the experiment the gate voltage V_{g1} of the gate that covers the QPC is swept, whereas the gate voltage of the bent arm is kept constant at $V_{g2} = 450$ mV in order to keep it electrically conducting. The measured two-point differential conductance g_{14} is shown in Fig. 6.3 b) (solid lines). Similar to the investigation of the device QRB in the previous section, the contribution of each arm to g_{14} can be distinguished. For a better visualization the contribution of the bent arm ($V_{g1} < 0.27$ V) is fitted with a polynomial function and extrapolated up to $V_{g1} = 0.5$ V (dashed line). The quantization of the QPC is just weakly pronounced, but allows to estimate the V_{g1}-dependent series resistance of the QPC. It is found that the series resistance is comparable to the corresponding resistance values of g_{12} and g_{34} (not shown here) as found for the device QRB in the previous section.

From g_{14} and the bath temperature $T_{bath} = 4.2$ K the expectation value $S_{V,Th}$ is calculated and compared with the measured values of the thermal noise $S_{V,w}$. In Fig. 6.3 c) the absolute values of $S_{V,w}$ and $S_{V,Th}$ are compared with each other and the relative excess noise $S_{V,excess}/S_{V,Th} = (S_{V,w} - S_{V,Th})/S_{V,Th}$ is depicted in Fig. 6.3 d). The relative excess noise is $S_{V,excess}/S_{V,Th} = 0.1 \pm 0.1$ for gate voltages $V_{g1} < 0.27$ V. In a transition regime in the range $0.27\text{ V} \leq V_{g1} \leq 0.33$ V the relative excess noise increases from $S_{V,excess}/S_{V,Th} = 0.1 \pm 0.1$ to about $S_{V,excess}/S_{V,Th} \approx 0.6$ with increasing V_{g1}. For gate voltages $0.33 \leq V_{g1} \leq 0.5$ the relative excess noise decreases from $S_{V,excess}/S_{V,Th} \approx 0.6$ to $S_{V,excess}/S_{V,Th} \approx 0.4$ with increasing V_{g1}. This means that the excess noise is present if both arms of QRA are electrically conducting and is strongly reduced if only the bent arm of the ring is electrically conducting.

In addition, the same measurement configuration is used for $V_{g2} = -0.29$ V, i.e. when the bent arm of the ring is non-conducting. The electrical conductance g_{14} is depicted in Fig. 6.4 b). From g_{14} and $T_{bath} = 4.2$ K the expected thermal noise $S_{V,Th}$ is calculated. $S_{V,Th}$ is depicted in Fig. 6.4 c) and compared with the measurement values $S_{V,w}$. It can be seen that no excess noise is present if only the straight arm of the quantum ring device QRB is electrically conducting.

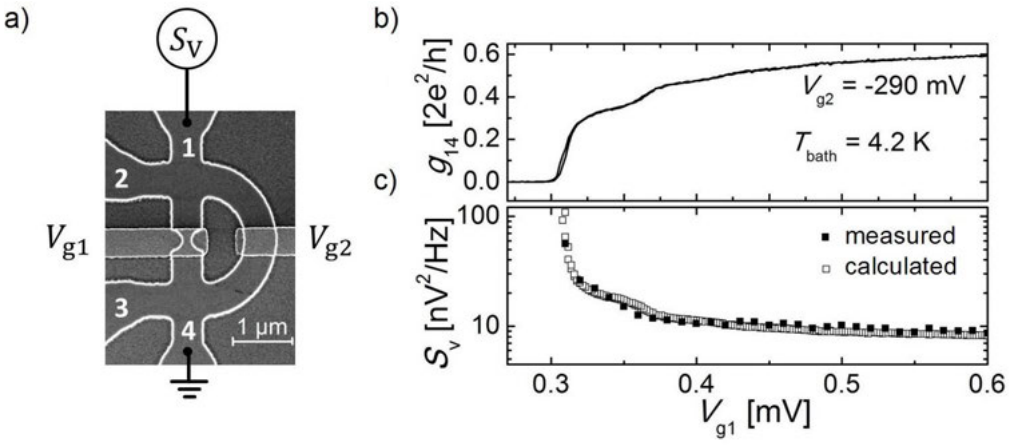

Figure 6.4: Measurement of the thermal noise in the device QRA at $T_{bath} = 4.2$ K. a) The measurement setup is depicted with contacts labeled 1 to 4. From the electrical differential conductance g_{14}, depicted in b), and T_{bath} the c) expected thermal noise $S_{V,Th}$ (open squares) is calculated and compared with the measurement values (solid squares) at $T_{bath} = 4.2$ K with $V_{g2} = -0.29$ V, i.e. when the bent arm is electrically non-conducting.

The excess noise $S_{\mathrm{V,excess}} = S_{\mathrm{V,w}} - S_{\mathrm{V,Th}} > 0$ is also observed in the device QRD, an asymmetric quantum ring that is completely covered by a global top-gate, when applying the measurement configuration that is depicted in Fig. 6.5 a) at $T_{\mathrm{bath}} = 4.2$ K. A noise measurement at $V_{\mathrm{g}} = 380$ mV is depicted in 6.5 b) to serve as an example. The measured electrical two-point differential conductance g_{12} is shown in 6.5 c) from which the expectation value $S_{\mathrm{V,Th}}$ is calculated. Again, $S_{\mathrm{V,Th}}$ is compared with the thermal noise $S_{\mathrm{V,w}}$, which is measured in the range $0.3\ \mathrm{V} \leq V_{\mathrm{g}} \leq 0.5\ \mathrm{V}$ with a step size of $\Delta V_{\mathrm{g}} = 2$ mV, in Fig. 6.5 d). The relative excess noise $S_{\mathrm{V,excess}}/S_{\mathrm{V,Th}}$, found for the studied range of V_{g}, varies between $S_{\mathrm{V,excess}}/S_{\mathrm{V,Th}} \approx 0.3$ and $S_{\mathrm{V,excess}}/S_{\mathrm{V,Th}} \approx 0.6$, as shown in Fig. 6.5 e). Local minima of $S_{\mathrm{V,excess}}/S_{\mathrm{V,Th}}$ occur at gate voltages where a conductance plateau is visible. For gate voltages that correspond to the transition between two conductance plateaus local maxima of $S_{\mathrm{V,excess}}/S_{\mathrm{V,Th}}$ are found. A similar observation is made for shot noise measurements in QPCs [144, 145]. However, since no DC currents are applied to the device and leakage currents are negligible for $V_{\mathrm{g}} \leq 0.6$ V shot noise is not further taken into consideration as possible source for this excess noise.

Furthermore, the measurement of the thermal noise of the device QRC, an asymmetric quantum ring that has no gate structure, is performed at $T_{\mathrm{bath}} = T_{\mathrm{e}} = 4.2$ K. The magnification of an optical micrograph is shown in Fig. 6.6 a) with contacts

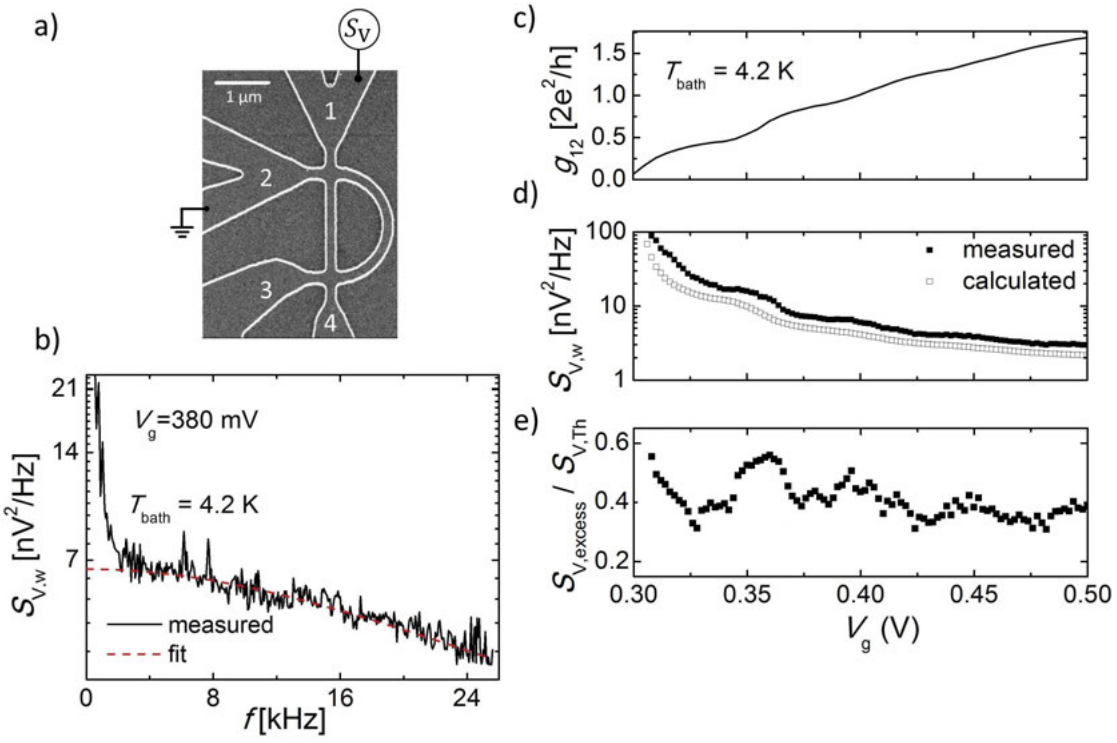

Figure 6.5: Measurement of the thermal noise in the device QRD at $T_{\mathrm{bath}} = 4.2$ K. a) SEM image [138] of the quantum ring device with contacts labeled 1 to 4 and the measurement configuration of the noise measurements. The quantum ring device is covered by a global top-gate. b) The noise spectrum at $V_{\mathrm{g1}} = 380$ mV is depicted. c) The measured two-point differential conductance g_{12} is shown (solid line). d) The measured thermal noise $S_{\mathrm{V,w}}$ (solid squares) and the expected values $S_{\mathrm{V,Th}}$ (open squares) that are calculated from g_{12} and T_{bath} are depicted. The relative excess noise $S_{\mathrm{V,excess}}/S_{\mathrm{V,Th}} = (S_{\mathrm{V,w}} - S_{\mathrm{V,Th}})/S_{\mathrm{V,Th}}$ is shown in e).

labeled 1-6. The noise measurement is performed for all combinations of the contacts 1 to 4, i.e. those that directly include a part of the quantum ring. Further noise measurements are performed for the contact combinations 4-6 and 1-5 which do not include the quantum ring but an 1D waveguide with the same width as the quantum ring. The absolute values of $S_{\mathrm{V,w}}$ and $S_{\mathrm{V,Th}}$ for the investigated contact pairs as well as the corresponding relative excess noise $S_{\mathrm{V,excess}}/S_{\mathrm{V,Th}}$ are given in Tab. 6.1. It can be seen that all contact pairs that include the quantum ring show excess noise with a ratio of $S_{\mathrm{V,excess}}/S_{\mathrm{V,Th}} = 0.29$ to $S_{\mathrm{V,excess}}/S_{\mathrm{V,Th}} = 0.54$. For the contact pairs that do not include the quantum ring the measured value $S_{\mathrm{V,w}}$ agrees with the expectation value $S_{\mathrm{V,Th}}$. It has to be mentioned that for the measurement combinations 4-6 and 5-1 the resistance is up to three times higher than for the remaining contact combination, which is due to an additional heating structure that is attached to contact 5 and 6 each. Therefore the relative contribution of excess noise that stems from the quantum ring would be strongly reduced in the contact pairs 4-6 and 5-1. However, the absolute deviation of $S_{\mathrm{V,w}}$ from $S_{\mathrm{V,Th}}$ is $S_{\mathrm{V,w}} - S_{\mathrm{V,Th}} \approx 10^{-20}$ V^2/Hz for the contact pairs 4-6 and 5-1 which is small compared to the deviation $S_{\mathrm{V,w}} - S_{\mathrm{V,Th}}$ of the remaining contact pairs. It can be concluded that excess noise is not measured within the measurement uncertainty for the contact pairs 4-6 and 5-1, i.e. if the quantum ring is not included. It can also be concluded that the width of the quantum ring's 1D waveguides does not lead to excess noise.

The results so far lead to the hypothesis that the excess noise is a property of the multi-terminal quantum ring devices and might therefore originate from interference of electron waves. In this case the relative excess noise $S_{\mathrm{V,excess}}/S_{\mathrm{V,Th}}$ in a quantum ring should reduce and approach the value $S_{\mathrm{V,excess}}/S_{\mathrm{V,Th}} \to 0$ if the phase coherence length is reduced, e.g. as it is for increased bath temperatures T_{bath}. In Fig. 6.6 the results of additional noise measurements in the quantum ring device QRC are presented for the contact pairs 4 to 3 and 4 to 1 for temperatures $T_{\mathrm{bath}} \geq 4.2$ K. For each

includes ring

Contact	4-3	2-4	3-2	2-1	1-3	1-4
$S_{\mathrm{V,w}}$ [nV^2/Hz]	2.55(2)	2.57(2)	2.20(3)	2.85(2)	2.94(4)	3.22(2)
$S_{\mathrm{V,Th}}$ [nV^2/Hz]	1.66(2)	2.00(2)	1.71(1)	1.92(3)	2.01(2)	2.43(2)
$S_{\mathrm{V,excess}}/S_{\mathrm{V,Th}}$	0.54(2)	0.29(2)	0.29(2)	0.48(3)	0.46(2)	0.33(1)

does not include ring

Contact	4-6	5-1
$S_{\mathrm{V,w}}$ [nV^2/Hz]	5.47(4)	8.51(3)
$S_{\mathrm{V,Th}}$ [nV^2/Hz]	5.46(6)	8.53(4)
$S_{\mathrm{V,excess}}/S_{\mathrm{V,Th}}$	0.00(1)	0.00(1)

Table 6.1: Comparison of the measured thermal noise $S_{\mathrm{V,w}}$ with the expectation value $S_{\mathrm{V,Th}}$ of the quantum ring QRC. All two-point combinations of the contacts 1-4 that do include the quantum ring (upper table) as well as the contact combinations 4-6 and 5-1 that do not include the quantum ring (lower table) are depicted. Contact pairs that include the quantum ring show $S_{\mathrm{V,excess}}/S_{\mathrm{V,Th}} > 1$, whereas contact pairs that do not include the quantum ring show $S_{\mathrm{V,excess}}/S_{\mathrm{V,Th}} \approx 1$.

bath temperature and each contact pair the noise measurement was performed six times in order to estimate the uncertainty of the relative excess noise $S_{\mathrm{V,excess}}/S_{\mathrm{V,Th}}$. In Fig. 6.6 b) the ratio $S_{\mathrm{V,excess}}/S_{\mathrm{V,Th}}$ for both contact pairs and bath temperatures from $T_{\mathrm{bath}} = 4.2$ K to $T_{\mathrm{bath}} = 12$ K with a step size of 2 K is shown. It can be seen that the relative excess noise $S_{\mathrm{V,excess}}/S_{\mathrm{V,Th}}$ decreases with increasing bath temperature and reaches the value $S_{\mathrm{V,excess}}/S_{\mathrm{V,Th}} \approx 0$ at $T_{\mathrm{bath}} = 12$ K. Further noise measurements at the bath temperatures $T_{\mathrm{bath}} = 20$ K and $T_{\mathrm{bath}} = 30$ K, not depicted in Fig. 6.6 b), are performed and yield $S_{\mathrm{V,excess}}/S_{\mathrm{V,Th}} \approx 0$ for both contact pairs. In Fig. 6.6 c) and d) examples of the noise spectra for both contact pairs at $T_{\mathrm{bath}} = 4.2$ K, 8 K and $T_{\mathrm{bath}} = 12$ K are shown.

If the excess noise is related to electron interference, the decrease of $S_{\mathrm{V,excess}}/S_{\mathrm{V,Th}}$ with increasing bath temperature should be comparable to the decrease of the phase

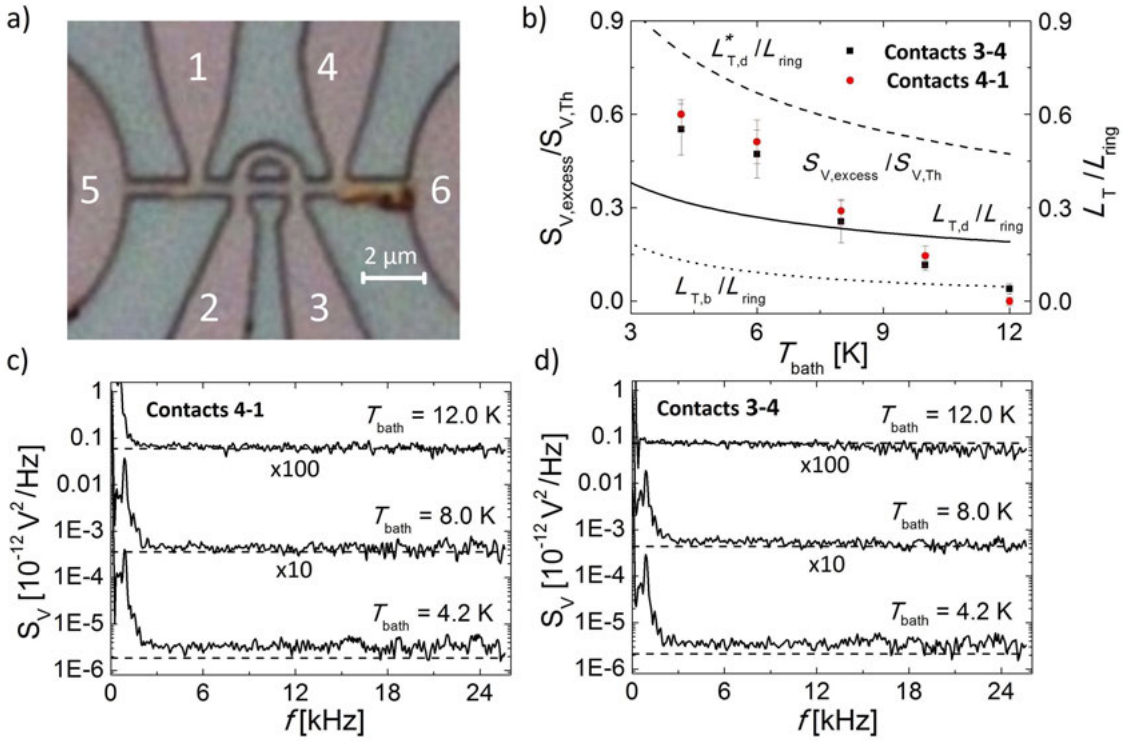

Figure 6.6: Measurement of the excess noise in the quantum ring QRC at temperatures $T_{\mathrm{bath}} \geq 4.2$ K. a) An optical micrograph [138] of the investigated sample with contacts labeled 1-6. b) The relative excess noise $S_{\mathrm{V,excess}}/S_{\mathrm{V,Th}}$ is presented for temperatures in the range $T_{\mathrm{bath}} = 4.2$ K to $T_{\mathrm{bath}} = 12$ K with a step size of 2 K for the contact pair 3-4 (black squares) and the contact pair 4-1 (red circles). The ratio of the thermal length L_{T} to the length of the bent arm of the quantum ring $L_{\mathrm{ring}} = 3.2$ µm is shown. The dashed line represents the diffusive thermal length $L^*_{\mathrm{T,d}}$ that is calculated, using the mobility found by the group of Prof. Dr. Andreas Wieck. The solid line refers to the diffusive thermal length $L_{\mathrm{T,d}}$ that is calculated, using the mobility found by SdH measurements from Sec. 5.1. The dotted line refers to the ballistic thermal length $L_{\mathrm{T,b}}$. Examples of the measured noise spectra (solid lines) are depicted in c) for the contacts 4-1 and in d) for the contacts 3-4 for the bath temperatures $T_{\mathrm{bath}} = 4.2$ K, 8 K and $T_{\mathrm{bath}} = 12$ K. The noise spectra are multiplied by 10 for $T_{\mathrm{bath}} = 8$ K and by 100 for $T_{\mathrm{bath}} = 12$ K for a better visualization. The dashed lines refer to the corresponding expectation value $S_{\mathrm{V,Th}}$.

coherence length l_φ with increasing bath temperature. Thermal averaging is one dephasing mechanism (see Sec. 2.2) that is based on the smearing of the Fermi distribution due to the broadening of the occupiable energy levels around E_F by about $k_\mathrm{B}T$ and is often considered as one possible dephasing mechanism in 1D quantum rings [146, 147, 148]. The thermal length is defined as

$$L_\mathrm{T,d} = \sqrt{\frac{\hbar D}{k_\mathrm{B}T_\mathrm{bath}}} = \sqrt{\frac{\hbar}{k_\mathrm{B}T_\mathrm{bath}} \frac{2E_\mathrm{F}}{m_\mathrm{e}^*} \cdot \frac{m_\mathrm{e}^* \mu_\mathrm{e}}{ed}} = \sqrt{\frac{2\hbar^3 \pi n \mu_\mathrm{e}}{k_\mathrm{B}T_\mathrm{bath} m_\mathrm{e}^* ed}} \tag{6.3}$$

for a diffusive system, where the diffusivity $D = v_\mathrm{F} l_\mathrm{e}/d$ is calculated from the Fermi velocity $v_\mathrm{F} = \sqrt{2E_\mathrm{F}/m_\mathrm{e}^*}$, the electron mobility μ_e and the dimension $d = 1$ of the electron system. Here, the Fermi energy, obtained from the SdH measurements in Sec. 5.1, $E_\mathrm{F} = \hbar^2 \pi n / m_\mathrm{e}^* \approx 7.7$ meV is used to calculate v_F.

In the ballistic transport regime the ballistic thermal length that is applied for estimating dephasing in QPCs [149, 150] and quantum rings [151] is defined as

$$L_\mathrm{T,b} = \frac{\hbar v_\mathrm{F}}{k_\mathrm{B}T_\mathrm{bath}} = \frac{\hbar^2}{k_\mathrm{B}T_\mathrm{bath}} \frac{\sqrt{2\pi n}}{m_\mathrm{e}^*}. \tag{6.4}$$

Both $l_\mathrm{T,d}$ and $L_\mathrm{T,b}$ are calculated with the effective mass $m_\mathrm{e}^* = 0.057\ m_0$ and the sheet density $n(0.3\ \mathrm{K}) = 1.83 \cdot 10^{11}\ \mathrm{cm}^2$, both of which are also obtained in Sec. 5.1. The diffusive thermal length $L_\mathrm{T,d}$ is calculated, using the electron mobility $\mu_\mathrm{e}(0.3\ \mathrm{K}) = 3.79 \cdot 10^5\ \mathrm{cm}^2/\mathrm{Vs}$, obtained from the SdH in Sec. 5.1. In addition the diffusive thermal length $L_\mathrm{T,d}^*$ is calculated when $\mu_\mathrm{e,Wieck} = 2.43 \cdot 10^6\ \mathrm{cm}^2/\mathrm{Vs}$, given by the group of Prof. Dr. Andreas Wieck, is used due to the significant deviation between $\mu_\mathrm{e}(0.3\ \mathrm{K})$ and $\mu_\mathrm{e,Wieck}$.

In Fig. 6.6 b) the ratio of the thermal lengths $L_\mathrm{T,d}$, $L_\mathrm{T,d}^*$ and $L_\mathrm{T,b}$ to the length of the bent waveguide $L_\mathrm{ring} = 3.2\ \mu\mathrm{m}$ is shown and is compared to the relative excess noise $S_\mathrm{V,excess}/S_\mathrm{V,Th}$. Here, L_ring is chosen as reference value for $L_\mathrm{T,d}$ and $L_\mathrm{T,b}$ because it is the length over which electrons have to keep their initial phase information in order to cause visible interference effects. Hence, the visibility of interference effects is increased as $L_\mathrm{T,d}/L_\mathrm{ring}$ and $L_\mathrm{T,b}/L_\mathrm{ring}$ increase.

It can be seen that $L_\mathrm{T,d}/L_\mathrm{ring}$, $L_\mathrm{T,d}^*/L_\mathrm{ring}$ and $L_\mathrm{T,b}/L_\mathrm{ring}$ are qualitatively comparable to the temperature-dependent relative excess noise $S_\mathrm{V,excess}/S_\mathrm{V,Th}$, i.e. they are decreasing as T_bath increases. Quantitatively, the relative excess noise is lower than $L_\mathrm{T,d}^*/L_\mathrm{ring}$ for all investigated bath temperatures, but exceeds $L_\mathrm{T,b}/L_\mathrm{ring}$ for $4.2\ \mathrm{K} \leq T_\mathrm{bath} < 12\ \mathrm{K}$. The relative excess noise is quantitatively higher than $L_\mathrm{T,d}/L_\mathrm{ring}$ at $T_\mathrm{bath} < 10$ K, but lower for $T_\mathrm{bath} \geq 10$ K. Taking dephasing due to electron-electron interaction into account would reduce the phase coherence length even more. In 2D systems at low temperatures dephasing is attributed to electron-electron interaction [152, 153] and can be estimated by calculating the scattering times of electron-electron interaction. In ballistic 1D systems the relation between the phase coherence length l_φ and the bath temperature T_bath was investigated in literature [146, 147, 148] for ballistic 1D systems and found to be $l_\varphi \propto T_\mathrm{bath}^{-1}$. However, the exact dephasing mechanism in ballistic 1D systems is not fully understood in the current state of research. Therefore, the thermal length can be seen as upper limit for the actual phase coherence length.

In this section measurements of the thermal noise were performed in quantum ring devices and two-terminal 1D constrictions. The results indicate that excess

noise is present in quantum ring structures, but is not observed in the 1D constrictions. Measurements of the thermal noise in a quantum ring structure at higher bath temperatures show that the excess noise is reduced with increased bath temperature. Hence, the hypothesis is made that the excess noise is linked to interference of the electron waves. The calculated diffusive thermal lengths $l_{\mathrm{T,d}}$ and $l^{*}_{\mathrm{T,d}}$ are qualitatively in fair agreement with the relative excess noise. However, calculating the ballistic thermal length $l_{\mathrm{T,b}}$ reveals that dephasing of ballistic electrons should occur at about $T_{\mathrm{bath}} = 4.2$ K already. A model that explains the observed excess noise in a device with multiple noise sources is the correlation of noise signals that stem from different sources. This will be discussed in Sec. 6.4.

6.4 Model of correlated noise sources

The measurements from Sec. 6.2 and Sec. 6.3 can be summarized as follows: all investigated multi-terminal quantum rings, i.e. the devices QRA, QRC and QRD, showed a measured thermal noise $S_{\mathrm{V,w}}$ that exceeds the expected thermal noise $S_{\mathrm{V,Th}}$. The expected value $S_{\mathrm{V,Th}}$ is calculated from Eq. 6.1. In this thesis $S_{\mathrm{V,excess}} = S_{\mathrm{V,w}} - S_{\mathrm{V,Th}}$ is referred to as excess noise. This excess noise is not a feature of the bending of the arm of the quantum ring since the two-terminal bent waveguide of the device ConstrB did not show excess noise. It is also not a consequence of the chosen wafer material since the devices ConstrA, ConstrB and ConstrC, that stem from the wafer 12088, as well as the narrow 2DEG of the device QRC, that stems from the wafer 11159, do not show excess noise. The noise measurements of the devices ConstrA, ConstrB, ConstrC and the connecting 1D waveguides of the device QRC prove that the observed excess noise is also not a feature of 1D constrictions, which is consistent with literature [154, 74]. In the investigated devices a possible origin of the excess noise can be traced back to the geometry of the multi-terminal closed quantum rings.

A model that explains some aspects of the observed excess noise in the multi-terminal closed quantum rings consists in treating the two arms of a quantum ring as correlated noise sources, see Fig. 6.7. In this system the potential fluctuations,

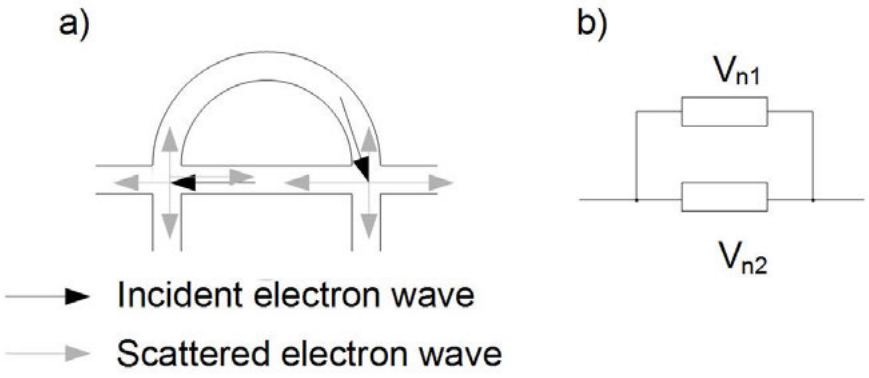

Figure 6.7: Equivalent circuit of a quantum ring as parallel resistances. a) An electron wave propagates through the quantum ring and has a possibility to be scattered in any direction at a crossing point. b) The arms of the quantum ring can be considered as parallel circuit of two resistances that act as noise sources V_{n1} and V_{n2}.

measured as thermal noise, are assumed to be random according to the fluctuation-dissipation [68] theorem. However, the potential fluctuations, produced by one arm, is not independent of the propagation of the potential fluctuations in the other arm. The reason for this is the probability of electron waves to elastically scatter into the other arm, when reaching the intersection of the two arms if the phase coherence length of the electron waves is of the order of the quantum ring's size.

In a given system with multiple noise sources two noise sources $n1$ and $n2$ are typically not coupled to each other. The corresponding voltage signals $V_{\mathrm{n1}}(t)$ and $V_{\mathrm{n2}}(t)$ of statistically independent noise sources add like orthogonal vectors. The mean square value is then $V^2_{\mathrm{rms,n}} = V^2_{\mathrm{rms,n1}} + V^2_{\mathrm{rms,n2}}$ if they are connected in series. If the two noise sources are connected in parallel, the corresponding current noise adds according to $I^2_{\mathrm{rms,n}} = I^2_{\mathrm{rms,n1}} + I^2_{\mathrm{rms,n2}}$. The noise spectra of a parallel circuit of two macroscopic resistors is found to verify the latter statement, as can be consulted in Appendix H.

However, noise signals that share a common source may lead to an excess noise [142]. If the noise sources are fully correlated, i.e. the signals $V_{\mathrm{rms,n1}}$ and $V_{\mathrm{rms,n1}}$ are identical, these relations become $V_{\mathrm{rms,n}} = V_{\mathrm{rms,n1}} + V_{\mathrm{rms,n2}}$ if the noise sources are connected in series and $I_{\mathrm{rms,n}} = I_{\mathrm{rms,n1}} + I_{\mathrm{rms,n2}}$ if they are connected in parallel [96]. The resulting PSD of the latter, already introduced in Sec. 2.5, is

$$S_{\mathrm{I,n,corr}} = S_{\mathrm{I,n1}} + S_{\mathrm{I,n2}} + 2K\sqrt{S_{\mathrm{I,n1}} S_{\mathrm{I,n2}}}. \tag{6.5}$$

The term $2K\sqrt{S_{\mathrm{I,n1}} S_{\mathrm{I,n2}}}$ accounts for the correlation of the two noise sources with the dimensionless correlation coefficient $-1 \leq K \leq 1$ that distinguishes between a system that is fully correlated $K = 1$, fully anti-correlated $K = -1$, uncorrelated $K = 0$ and any system in between these cases. The ratio of $S_{\mathrm{I,n,corr}}$ to the current noise of uncorrelated noise sources, i.e. $S_{\mathrm{I,n,uncorr}} = S_{\mathrm{I,n1}} + S_{\mathrm{I,n2}}$, yields

$$\frac{S_{\mathrm{I,n,corr}}}{S_{\mathrm{I,n,uncorr}}} = 1 + 2K\frac{\sqrt{S_{\mathrm{I,n1}} S_{\mathrm{I,n2}}}}{S_{\mathrm{I,n1}} + S_{\mathrm{I,n2}}} = 1 + 2K\frac{\sqrt{G_1 G_2}}{G_1 + G_2} = 1 + 2K\frac{\sqrt{R_1 R_2}}{R_1 + R_2} = \frac{S_{\mathrm{V,n,corr}}}{S_{\mathrm{V,n,uncorr}}}. \tag{6.6}$$

In the last step the relations $S_{\mathrm{I,n,corr}} \cdot R^2 = S_{\mathrm{V,n,corr}}$ and $S_{\mathrm{I,n,uncorr}} \cdot R^2 = S_{\mathrm{V,n,uncorr}}$ are used, whereas the electrical resistance $R^{-1} = R_1^{-1} + R_2^{-1}$ is the same in the correlated and the uncorrelated system.

The theoretical value $S_{\mathrm{V,Th}}$ is calculated without taking correlated noise sources into account and therefore corresponds to $S_{\mathrm{V,n,uncorr}}$. If the measured $S_{\mathrm{V,w}}$ includes the contribution of the correlation of noise sources, the excess noise can be understood as

$$S_{\mathrm{V,excess}} = S_{\mathrm{V,w}} - S_{\mathrm{V,Th}} \equiv S_{\mathrm{V,n,corr}} - S_{\mathrm{V,n,uncorr}} \tag{6.7}$$

and the relative excess noise could be expressed as

$$\frac{S_{\mathrm{V,excess}}}{S_{\mathrm{V,Th}}} = \frac{S_{\mathrm{V,n,corr}} - S_{\mathrm{V,n,uncorr}}}{S_{\mathrm{V,n,uncorr}}} = 2K\frac{\sqrt{R_1 R_2}}{R_1 + R_2}. \tag{6.8}$$

From Eq. 6.8 it becomes clear that the relative excess noise reaches its maximum for $K = 1$ and $R_1 = R_2$ if it is a feature of correlated noise sources. In contrast, it becomes zero as either of the resistances R_1 and R_2 dominates the other one, i.e. if $R_1/R_2 \to 0$ or if $R_2/R_1 \to 0$. The relative excess noise also becomes zero as $K \to 0$. This is illustrated by the grayscale plot in Fig. 6.8.

If the correlation of the noise sources is considered to stem from phase coherence of the quantum ring, i.e. $K = K(l_\varphi)$, the decrease of $(S_{\mathrm{V,n,corr}} - S_{\mathrm{V,n,uncorr}})/S_{\mathrm{V,n,uncorr}}$ with decreasing K corresponds to the decrease of $S_{\mathrm{V,excess}}/S_{\mathrm{V,Th}}$ with increasing T_{bath}. The reason for this is the decrease of l_φ with increasing T_{bath} due to electron-electron interaction and thermal averaging. Note that the ballistic thermal length $L_{\mathrm{T,b}}$ is smaller than the length of the quantum ring's arms at $T_{\mathrm{bath}} \geq 4.2$ K, as shown in Sec. 6.2. This means that only a small fraction of electrons propagate phase-coherently through the quantum ring.

The relative excess noise that is observed in the quantum ring devices QRA, QRC and QRD adopts values of $0 < S_{\mathrm{V,excess}}/S_{\mathrm{V,Th}} < 1$, which is in the range of values that can be explained by correlated noise sources. In Fig. 6.3 the measured excess noise of the device QRA was presented for different electrical conductances of the straight arm. In Fig. 6.9 c) the dependence of the relative excess noise on the ratio of the resistance of the straight arm R_1 to the resistance of the bent arm R_2 is shown. The relative excess noise is maximal in the range $1.0 < R_1/R_2 < 1.5$ and decreases for $R_1/R_2 < 1.0$ and for $1.5 < R_1/R_2$. This means that the excess noise decreases as one of the resistances R_1 or R_2 dominates the other one, as expected from Eq. 6.8. In Fig. 6.9 d) the measured relative excess noise of the device QRC is taken from Fig. 6.6. The relative excess noise decreases as the bath temperature increases. This can be understood as the decrease of the excess noise as the correlation coefficient K decreases.

To summarize, applying the model of correlated parallel noise sources is a possibility to explain the measured excess noise in the quantum rings qualitatively.

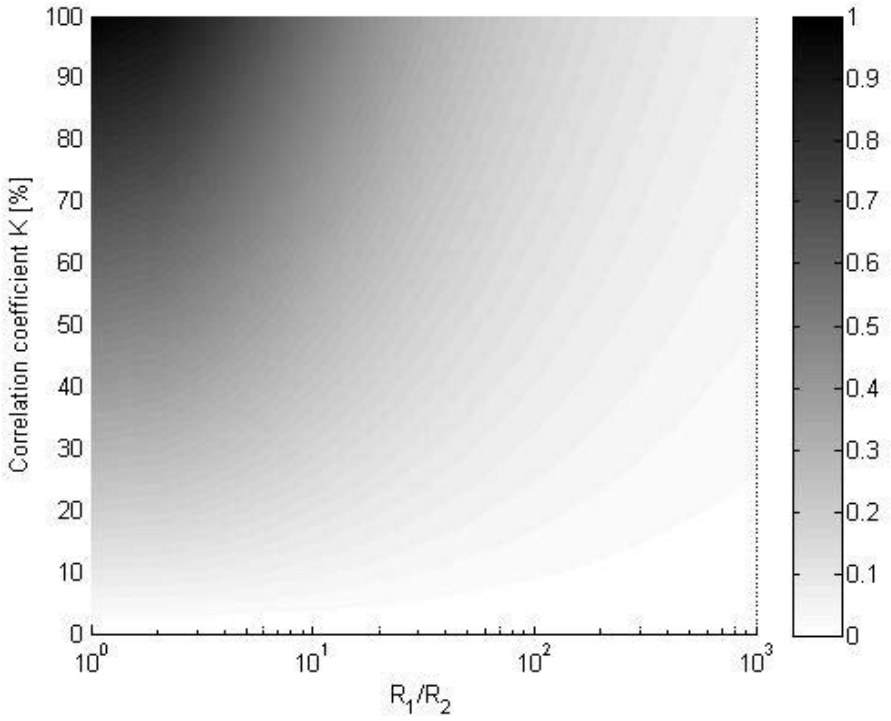

Figure 6.8: Calculation of the relative excess noise due to correlation of noise sources for two parallel resistors with resistances R_1 and R_2. Darker areas represent regions with high excess noise and bright areas correspond to regions with low excess noise.

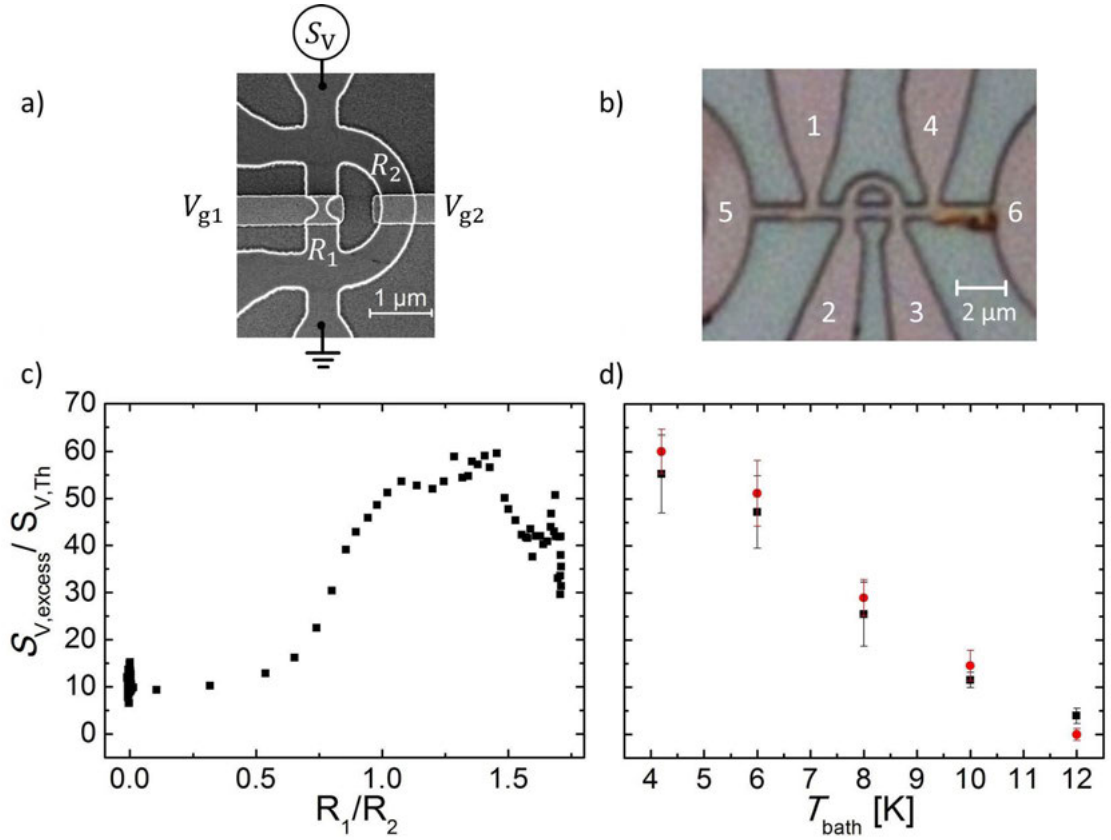

Figure 6.9: a) SEM image of the device QRA with a schematic of the measurement setup. The electrical resistance of the straight arm is denoted with R_1, the resistance of the bent arm is denoted with R_2. b) Optical image of the device QRC with contacts labeled 1-6. c) The measured relative excess noise of the device QRA $S_{\mathrm{V,excess}}/S_{\mathrm{V,Th}}$ and its dependence on the resistance ratio R_1/R_2. The measurement is taken from Fig. 6.3. d) The measured relative excess noise of the device QRC $S_{\mathrm{V,excess}}/S_{\mathrm{V,Th}}$ and its dependence on the bath temperature T_{bath}. The measurement is taken from Fig. 6.6.

Chapter 7

Mode-selected heat flow through a quantum wire network

A heating current in a narrow 2D area next to a quantum ring establishes a thermal gradient across the device. In this non-equilibrium state noise thermometry is applied to gain information about the temperature increase in the device and hence to gain information about the heat flow in the quantum ring. These investigations are of importance due to the fact that the phase coherence length in such interferometers depends on the temperature of the device. The device temperature therefore strongly affects the observability of interference effects, such as the Aharonov-Bohm effect. In a first step the results of the noise thermometry for different heating currents are presented. The electrical conductance of the investigated part of the structure shows the quantization that is observed in 1D constrictions and offers the possibility to perform the noise measurements for multiple population numbers of the waveguide. In a second step a model is presented that describes the heat flow through the device. The experimental data and the heat branching model point towards a switching behavior of the heat flow through the sample. This means that for lower Fermi energies of the device the heat only flows through one part of the device, whereas it flows through the whole device at higher Fermi energies. Additional wave packet analysis in Sec. 7.4, performed by Dr. Tobias Kramer and Dr. Christoph Kreisbeck, supports the discussion of this behavior.

7.1 Current state of research

The investigation of quantum devices requires the knowledge of the characteristic length scales that are responsible for the creation of quantum effects, such as the mean free path or the Fermi wavelength. In quantum interferometers the phase coherence length has an important role since it should be at least as high as the device's geometry in order to observe interference effects, such as the Aharonov-Bohm effect [6]. The phase breaking time τ_φ is experimentally accessible by localization effects [155, 156] and the Aharonov-Bohm effect [71, 148, 146, 157]. In a diffusive transport regime at low temperatures the dominant scattering mechanism that leads to dephasing is electron-electron interaction [158]. This was also found for 2D ballistic electrons [153, 152] in a high-mobility 2DEG of a $Al_xGa_{1-x}As/GaAs$ heterostructure that serves as modified version of Young's double-slit experiment. The phase breaking time τ_φ and the electron-electron scattering time τ_{e-e} are therefore closely related in these regimes. In ballistic mesoscopic systems with dimension lower than

2 the phase breaking mechanism is not well understood to date.

In interference experiments that are based on the Aharonov-Bohm effect in quasi 1D quantum rings the development of the phase coherence length l_φ is shown to decrease with increased temperature of the device or in the presence of a temperature gradient [71, 148, 146, 157, 159]. This observation is attributed to enhanced electron-electron interaction, i.e. inelastic scattering, at higher bath temperatures. It is also attributed to the thermal averaging of the electron waves, i.e. the dephasing of electron waves due to energies that are uncertain by roughly $k_\mathrm{B}T$. The effect of thermal averaging makes it important to know the distribution of electric currents that may lead to a local increase of the device temperature by electron-electron or electron-phonon interaction. In $Al_xGa_{1-x}As$/GaAs-based mesoscopic low-dimensional devices the Wiedemann-Franz relation was found to hold [160, 161, 50], i.e. the electrical conductivity and the thermal conductivity are proportional to each other. For 1D structures this means that the heat conductance is also expected to form plateaus. The Landauer-Büttiker formalism [34, 35] treats electrical transport as a transmission problem between reservoirs and can be generalized to thermal transport [162, 49]. The plateaus of the thermal conductivity were found in an experiment later [160, 161]. In the above mentioned experiments electrons were driven through an 1D constriction by the presence of a temperature gradient. The electric current between the 'hot' and the 'cold' reservoir led to an increase of the measured electron temperature that is proportional to the number of the populated energy modes of the 1D constriction.

These experiments were performed so far in single 1D constrictions rather than in quantum ring structures where the study would be important due to thermal averaging of electrons that can cause dephasing.

7.2 Out-of-equilibrium noise measurements in a quantum wire network

In this section the asymmetric quantum ring QRD with a width of $w \approx 170$ nm and a radius of $r \approx 1$ µm is investigated. The ring is based on the wafer material 11159 and therefore has an elastic mean free path of $l_e \approx 18$ µm and a Fermi wavelength of $\lambda_F \approx 55$ nm. The device is depicted in Fig. 7.1 and comprises 1D electron waveguides of 1 to 3 µm length, that are connected to 2D leads, labeled A to F. A global top-gate allows to change the carrier concentration of the whole device by varying the gate voltage V_g.

Comparing the length of the 1D electron waveguides and the elastic mean free path $l_e \approx 18$ µm the electron transport through the quantum ring can be classified as ballistic and becomes diffusive in the 2D leads. The leads A and B as well as E and F form a pair and lead to the shared electron reservoirs AB and EF. The leads C and D form separate electron reservoirs. The electron waveguide arm of the quantum ring that connects the reservoirs AB and EF with each other can be understood as a series of a 2D, 1D, 1D and a 2D electron system [163]. The corresponding differential electrical conductance $g_{\text{AB-EF}}$ appears in quantized steps and is depicted in Fig. 7.2 a). The quantization of the conductance of this waveguide can be understood by considering a series of two QPCs that each produce the same energy levels. When the momentum of an electron is filtered after having passed the first QPC, the second QPC will not have any further impact on the electron's

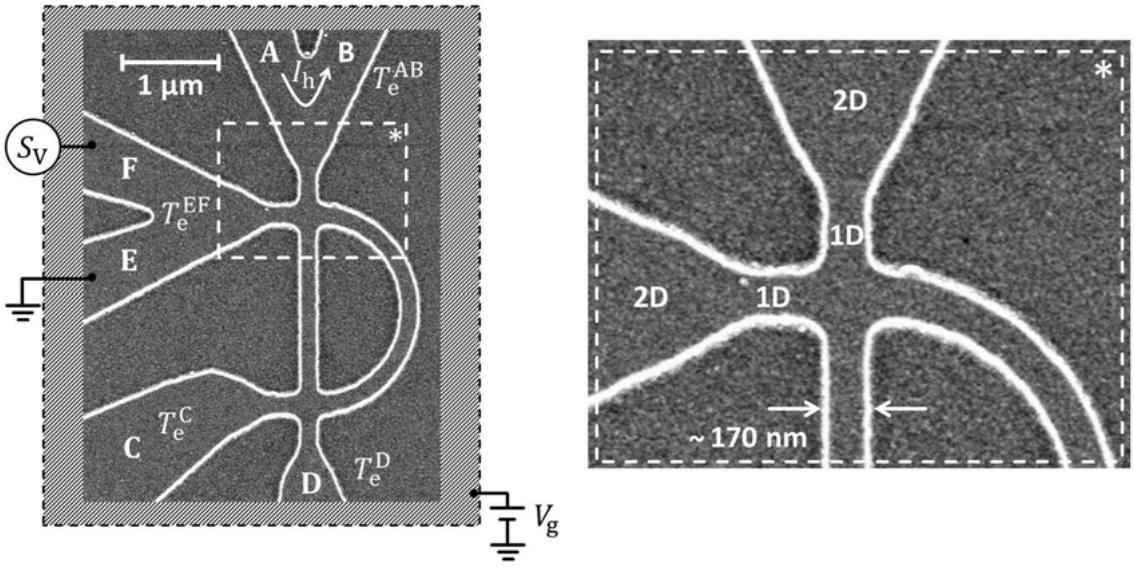

Figure 7.1: A scanning electron micrograph (SEM) of a sample [138] that is identical to the quantum ring QRD. The left image shows the 1D quantum ring and the 2D leads that are labeled A to F. The 2D leads A and B form the electron reservoir AB and the 2D leads E and F form the reservoir EF. The leads C and D form separate electron reservoirs. A heating circuit is attached to the reservoir AB, as indicated by I_h, and the noise measurement setup is attached to the reservoir EF, represented by S_V. A global top-gate covers the whole device. The details of the attached circuits are shown in Fig. 4.4. The right image shows a magnification of the upper crossing area of the quantum ring in the left image. It highlights the transition from 2D to 1D regions between electron reservoirs and the quantum wires.

momentum, leading to the same electrical conductance that is observed for one QPC [164].

In order to investigate the propagation of electrons through the quantum ring in the presence of a temperature gradient, noise thermometry is performed in reservoir EF and heating currents in the push-pull configuration, ranging from $I_\mathrm{h} = 0$ µA to $I_\mathrm{h} = 8$ µA, are applied to the electron reservoir AB of the sample (see Sec. 4). The applied gate voltages V_g are chosen to occupy the $N = 0$, 1, 2 and $N = 3$ energy modes of the electron waveguide that connects the reservoirs AB and EF. The noise thermometry is used to measure an increase of the electron temperature $\Delta T_\mathrm{e}^\mathrm{EF}$ in the reservoir EF by solving Eq. 4.4 for the temperature increase

$$\Delta T_\mathrm{e}^\mathrm{EF} = [\frac{S_\mathrm{V,w}(I_\mathrm{h})}{4k_\mathrm{B}R(I_\mathrm{h})} - \frac{2T_\mathrm{Amp}R(I_\mathrm{h})}{R_\mathrm{Amp}}] - [\frac{S_\mathrm{V,w}(0)}{4k_\mathrm{B}R(0)} - \frac{2T_\mathrm{Amp}R(0)}{R_\mathrm{Amp}}] \qquad (7.1)$$

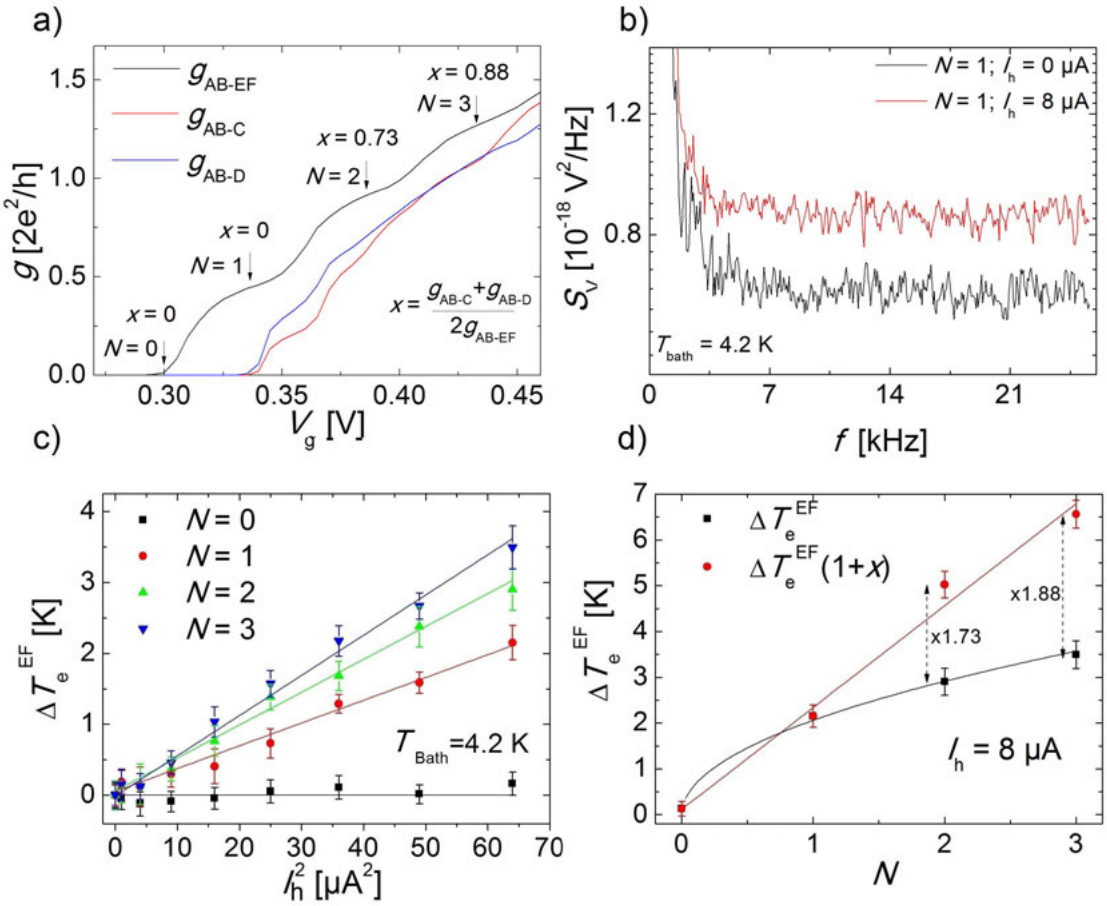

Figure 7.2: Measured electrical differential conductance and noise measurements of the quantum ring QRD. a) The electrical conductance $g_\mathrm{AB\text{-}EF}$, $g_\mathrm{AB\text{-}C}$ and $g_\mathrm{AB\text{-}D}$ of the device QRD is depicted. The factor x describes the ratio between the electrical conductance $g_\mathrm{AB\text{-}C}$ and $g_\mathrm{AB\text{-}D}$ to $g_\mathrm{AB\text{-}EF}$ (see text) and is evaluated for the plateaus $N = 0$, 1, 2 and for $N = 3$ of $g_\mathrm{AB\text{-}EF}$. b) Two examples of the noise spectra at $N = 1$ for $I_\mathrm{h} = 0$ µA and $I_\mathrm{h} = 8$ µA are depicted. c) Increase of the electron temperature $\Delta T_\mathrm{e}^\mathrm{EF}$ in reservoir EF due to the heating current I_h that is applied to the electron reservoir AB. d) Values of $\Delta T_\mathrm{e}^\mathrm{EF}(I_\mathrm{h} = 8$ µA) for $N = 0$,1,2,3 (black squares) do not fit the linearity $\Delta T_\mathrm{e}^\mathrm{EF} \propto N$. The same values multiplied by the factor $(1 + x)$ (red circles) fit the linearity $\Delta T_\mathrm{e}^\mathrm{EF} \propto N$ (see text).

with $\Delta T_e^{EF} = T_e^{EF}(I_h) - T_e^{EF}(0)$. As already mentioned in Sec. 4, $T_{Amp} = 300$ K and $R_{Amp} = 5$ MΩ refer to the temperature and the input resistance of the voltage amplifiers. Here $R(I_h)$ and $R(0)$ refer to the two-point resistances of the sample when heated with $I_h > 0$ and non-heated with $I_h = 0$. However, none of the measured resistances shows a significant deviation between $R(I_h)$ and $R(0)$. It is therefore reasonable to set $R = R(I_h) = R(0)$. Consequently, Eq. 7.1 reduces to

$$\Delta T_e^{EF} = \frac{S_{V,w}(I_h) - S_{V,w}(0)}{4k_B R}. \tag{7.2}$$

The noise measurements allow to investigate the mode-dependent behavior of the electron propagation through the quantum ring in the presence of different temperature gradients along the device. When the electron reservoir AB is heated by I_h, the electron temperature T_e^{EF} in reservoir EF is expected to rise due to the propagation of 'hot' electrons from reservoir AB to the colder reservoirs C, D and EF. The experiment was carried out at $T_{bath} = 4.2$ K. The results of the thermal noise measurements for $N = 0$, 1, 2 and $N = 3$ and $I_h = 0$ μA to $I_h = 8$ μA are depicted in Fig. 7.2 c). For each combination of I_h and N the thermal noise $S_{V,w}$ was measured six times. The standard deviation of these six measurements defines the error bars of $S_{V,w}$ in Fig. 7.2 c). Two examples of the noise spectra for $N = 1$ with $I_h = 0$ μA and $I_h = 8$ μA are shown in Fig. 7.2 b).

From the measured $\Delta T_e(N,I_h)$ three conclusions can be drawn. First, the increase of the electron temperature fulfills $\Delta T_e^{EF} \propto I_h^2$ for $N \geq 1$, which is in accord with Joule's law. Second, for $N = 0$, i.e. when the 1D electron waveguide is electrically not conducting, an increase of the electron temperature is not observed within the experimental uncertainty. This can be interpreted in terms of an electron-phonon interaction that is not strong enough to mediate a significant heat exchange between the reservoirs AB and EF. Third, for a given heating current I_h the relation between ΔT_e^{EF} and N is not proportional, but is rather $\Delta T_e^{EF} \propto \sqrt{N}$. For $I_h = 8$ μA the dependence $\Delta T_e^{EF}(N)$ is depicted in Fig. 7.2 d). Note that this relation is the same for all applied heating currents I_h due to the relation $\Delta T_e^{EF} \propto I_h^2$. As mentioned in the previous section, this relation was found to be $T_{e,\,lit}(V_g)|_{I_h=const} \propto N$ for single 1D constrictions that were connected to 2D electron reservoirs in the presence of a temperature gradient across the 1D constriction [50, 161, 160].

The most obvious reason for this deviation is the branching of the 1D waveguides that defines the quantum ring and that is not present in a single 1D constriction. In the branched device QRD a portion of the 'hot' electrons that stem from reservoir AB not only flow to reservoir EF, but also to the electron reservoirs C and D. However, in a quantum ring, where the electron waveguides have the same widths, the occupation of the electron modes in the waveguides should establish the same relative change of the electrical conductance for all waveguides if the Fermi energy is globally changed by the top-gate. A device with electron waveguides of unequal thicknesses leads to different threshold voltages and prevents the same relative change of the electrical conductance. The Wiedemann-Franz relation

$$\kappa = L \cdot GT \tag{7.3}$$

connects the electrical conductance G with the thermal conductance κ of a system at temperature T, whereas L is the temperature-dependent proportionality factor, the Lorenz number. Eq. 7.3 is shown to be applicable in low-dimensional $Al_xGa_{1-x}As$/GaAs-based devices [50, 161, 160]. In a device, where the electron

waveguides have the same widths, the thermal conductance of the electron waveguides is expected to have the same relative change when the global Fermi energy is changed since it is directly coupled to the electrical conductance by Eq. 7.3.

The flow of 'hot' electrons along a temperature gradient ΔT can be expressed by the rate of heat flow

$$\frac{\mathrm{d}Q}{\mathrm{d}t} = \dot{Q} = -\lambda \Delta T A \tag{7.4}$$

in a device with the cross section A and the thermal conductivity λ. Note that in 1D devices the thermal conductivity λ is the same as the thermal conductance κ and that in Eq. 7.4 the cross section A becomes the width of the 1D constriction. Assuming that the flow of the 'hot' electrons from reservoir AB to reservoir EF establishes the measured increase $\Delta T_{\mathrm{e}}^{\mathrm{EF}}$ and considering Eqs. 7.3 and 7.4, it is reasonable to expect $\Delta T_{\mathrm{e}}^{\mathrm{EF}} \propto N$ in non-branched and branched devices when the waveguides have the same width.

In Fig. 7.3 the SEM image of a device that is identical to the quantum ring QRD does not show any asymmetry along the x-axis so that the waveguides all have the same width. However, considering the shift of the threshold voltages in Fig. 7.2 a) it seems that such an asymmetry is present in the actual device QRD. The threshold voltages for the electrical conductance of the long waveguides and the waveguide in the lower crossing of the device QRD are almost identical. This suggests that a potential asymmetry is located in a spot of the device that affects all waveguides except the waveguide between the reservoirs EF and AB, i.e. the waveguide in the upper crossing. The most probable location for the potential asymmetry is therefore the environment of the lower crossing of the quantum ring, as indicated by the dashed circle in Fig. 7.3.

In order to give further information about the heat flow in this device, further noise measurements are performed in the electron reservoirs C and D at $T_{\mathrm{bath}} = 4.2$ K. For these measurements a temperature gradient is established by sending a

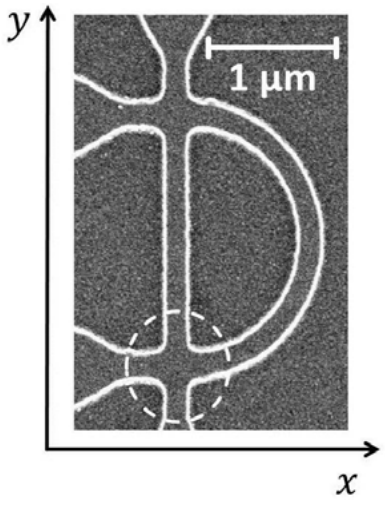

Figure 7.3: SEM image of a sample that is identical to the device QRD. Axes are added to the figure in order to simplify argumentation concerning potential symmetries in the device. In the lower crossing of the quantum ring a circle highlights the spot that is expected to host a potential disturbance in the actual device. Such a potential disturbance would break the symmetry of the device along the x-axis.

heating current ranging from $I_\mathrm{h} = 0$ µA up to $I_\mathrm{h} = 5$ µA with a resolution of 0.5 µA through the electron reservoir AB while having the occupation numbers $N = 0$, 1, 2 and $N = 3$ for the electron waveguide in the upper crossing again. For $N < 2$ the noise spectra did not show a significant change for any I_h. In contrast an increase of S_V is observed for $N \geq 2$ as I_h increases. Two examples of the noise spectra are given in Fig. 7.4 a) for $N = 1$ and $N = 2$ at $I_\mathrm{h} = 0$ µ A and $I_\mathrm{h} = 5$ µ A each. These noise measurements indicate that the rate of heat flow $\dot{Q}$ from the electron reservoir AB to the electron reservoirs C and D is zero for $N < 2$. In contrast, the rate of heat flow from the electron reservoirs AB to the electron reservoir EF is non-zero for $N > 0$.

To summarize this section, the relation $\Delta T_\mathrm{e}^\mathrm{EF} \propto \sqrt{N}$ was observed in the quantum ring device QRD. The contrast to $\Delta T_\mathrm{e} \propto N$ that is observed in literature for single 1D constrictions is assumed to stem from a potential asymmetry in the lower crossing of the device. This idea is supported by a shift of the threshold voltages of the electrical conductance and noise measurements in the reservoirs C and D. So far, it is not clear whether the absence of such a potential asymmetry would lead to $\Delta T_\mathrm{e}^\mathrm{EF} \propto N$. In order to approach this question, the next section will examine the branching of the rate of heat flow in the device QRD in more detail.

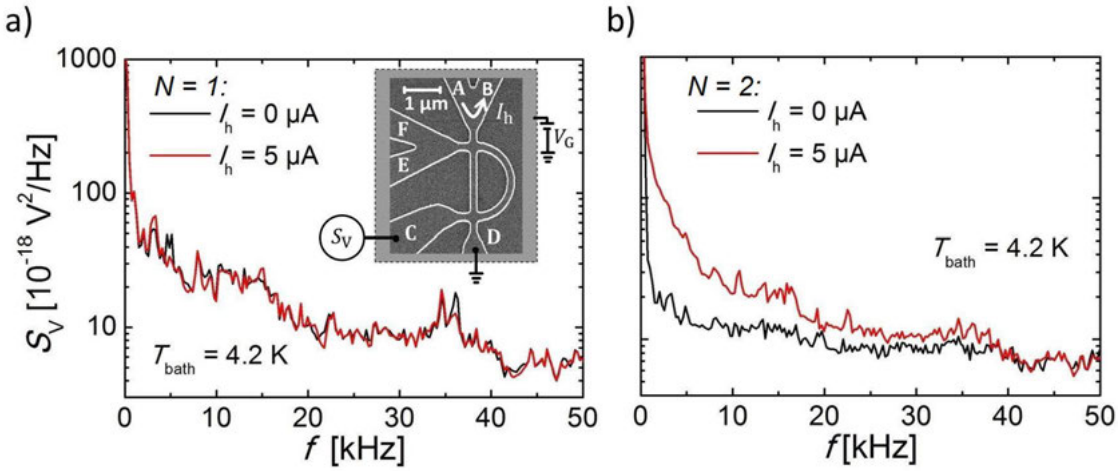

Figure 7.4: Noise measurements in the device QRD at a) $N = 1$ and b) $N = 2$ at $T_\mathrm{bath} = 4.2$ K. The measurement setup is depicted in the inset in a). Black lines represent the noise measurements if no heating current is applied, i.e. $I_\mathrm{h} = 0$ µA. Red curves represent thermal noise measurements at $I_\mathrm{h} = 5$ µA.

7.3 Model of the heat flow branching in a quantum wire network

Following the nomenclature of Fig. 7.1, in the steady state the heat flow from the electron reservoir AB into the waveguide network is split into the heat flows

$$\dot{Q}_{\mathrm{AB}} = \dot{Q}_{\mathrm{EF}} + \dot{Q}_{\mathrm{C}} + \dot{Q}_{\mathrm{D}} + \dot{Q}_{\mathrm{e\text{-}ph}} \tag{7.5}$$

that run from the waveguide network into the reservoirs EF, C and D as well as to the lattice of the device. Eq. 7.5 and the subsequent equations are graphically represented and can be followed in Fig. 7.5. The heat flows that stream from the waveguide network into the reservoirs are denoted as $\dot{Q}_{\mathrm{EF}}$, $\dot{Q}_{\mathrm{C}}$ and $\dot{Q}_{\mathrm{D}}$. As already mentioned in Fig. 7.2 c), it can be seen that the increase in temperature in reservoir EF due to the heating current I_{h} is not significantly different from $\Delta T_{\mathrm{e}}^{\mathrm{EF}} = 0$ K if the connecting electron waveguide is electrically non-conducting, i.e. for $N = 0$. This gives rise to the believe that the electron-phonon interaction in the device is not strong enough to cause an observable heat exchange between the reservoirs AB and EF when the connecting 1D waveguide is electrically non-conducting. Therefore, the heat flow from reservoir AB to the lattice is relatively small compared to the observed heat flows. Hence, Eq. 7.5 becomes

$$\dot{Q}_{\mathrm{AB}} \approx \dot{Q}_{\mathrm{EF}} + \dot{Q}_{\mathrm{C}} + \dot{Q}_{\mathrm{D}}. \tag{7.6}$$

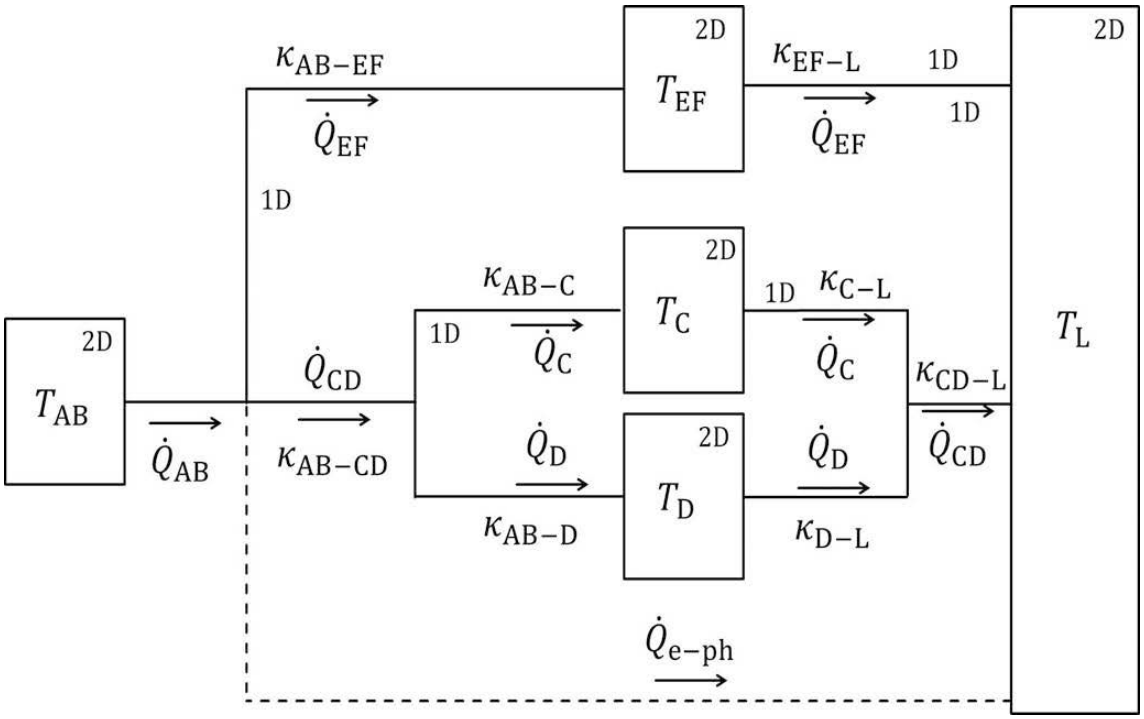

Figure 7.5: Schematic of the heat flow in the heated quantum ring device. Squares represent 2D electron reservoirs, whose labels can be read from the index of the corresponding temperatures T_{XY}. The temperatures refer to the electron temperature of the system with the exception of the lattice temperature that is $T_{\mathrm{L}} = 4.2$ K. The lattice temperature is assumed not to be changed by the incoming heat flow due to its size. The reservoirs C and D are formally separated, but are treated as one electron reservoir (see text). The dashed lines correspond to the heat flow of electrons to the lattice due to electron-phonon interaction.

The heat flow from the waveguide network to reservoir EF is composed of the heat conductivity $\kappa_{\text{AB-EF}}$ of the connecting waveguide between reservoirs AB and EF as well as of the difference of the electron temperature of these reservoirs $T_{\text{e}}^{\text{EF}} = \Delta T_{\text{L}} + T_{\text{e}}^{\text{EF}}$ and $T_{\text{e}}^{\text{AB}} = \Delta T_{\text{L}} + T_{\text{e}}^{\text{AB}}$. Thus the heat flow becomes

$$\begin{aligned} \dot{Q}_{\text{EF}} &= \kappa_{\text{AB-EF}}(T_{\text{e}}^{\text{AB}} - T_{\text{e}}^{\text{EF}}) \\ &= \kappa_{\text{AB-EF}}[(T_{\text{L}} + \Delta T_{\text{e}}^{\text{AB}}) - (T_{\text{L}} + \Delta T_{\text{e}}^{\text{EF}})] \\ &= \kappa_{\text{AB-EF}}[\Delta T_{\text{e}}^{\text{AB}} - \Delta T_{\text{e}}^{\text{EF}}], \end{aligned} \tag{7.7}$$

where $T_{\text{L}} = 4.2$ K denotes the temperature of the lattice. In contrast, the terms $\Delta T_{\text{e}}^{\text{AB}}$ and $\Delta T_{\text{e}}^{\text{EF}}$ refer to the increase of the electron temperature above T_{L} in the corresponding reservoir due to the applied heating current I_{h}. Accordingly, the heat flow from the waveguide network to the reservoirs C and D is

$$\begin{aligned} \dot{Q}_{\text{C}} &= \kappa_{\text{AB-C}}[\Delta T_{\text{e}}^{\text{AB}} - \Delta T_{\text{e}}^{\text{C}}] \\ \dot{Q}_{\text{D}} &= \kappa_{\text{AB-D}}[\Delta T_{\text{e}}^{\text{AB}} - \Delta T_{\text{e}}^{\text{D}}]. \end{aligned} \tag{7.8}$$

The reservoirs C and D are separated from each other by an 1D electron waveguide. However, measurements of the electrical conductance from reservoir AB to the reservoirs C and D are approximately identical to each other $g_{\text{AB-C}} \approx g_{\text{AB-D}}$, see Fig. 7.2 a), and are therefore considered as one merged electron reservoir CD with

$$\dot{Q}_{\text{CD}} = \kappa_{\text{AB-CD}}[\Delta T_{\text{e}}^{\text{AB}} - \Delta T_{\text{e}}^{\text{CD}}]. \tag{7.9}$$

The concept of this approach aims for the explanation of the deviation between $T_{\text{e}}^{\text{EF}}(V_{\text{g}})|_{I_{\text{h}}=\text{const}} \propto \sqrt{N}$ and $T_{\text{e, lit}}(V_{\text{g}})|_{I_{\text{h}}=\text{const}} \propto N$ and is based on the heat flow branching in the quantum ring. This has now reduced to the search for the ratio of $\dot{Q}_{\text{EF}}$ to $\dot{Q}_{\text{CD}}$. By dividing Eq. 7.9 by Eq. 7.7 this ratio can be expressed as

$$\frac{\dot{Q}_{\text{CD}}}{\dot{Q}_{\text{EF}}} = \frac{\kappa_{\text{AB-CD}}(\Delta T_{\text{e}}^{\text{AB}} - \Delta T_{\text{e}}^{\text{CD}})}{\kappa_{\text{AB-EF}}(\Delta T_{\text{e}}^{\text{AB}} - \Delta T_{\text{e}}^{\text{EF}})}. \tag{7.10}$$

In order to deduce more information from Eq. 7.10, the heat conductivities have to be re-expressed by using the Wiedemann-Franz relation

$$\begin{aligned} \kappa_{\text{AB-EF}} &= L \cdot g_{\text{AB-EF}}(T_{\text{e}}^{\text{AB}} + T_{\text{e}}^{\text{EF}})/2 \\ &= L \cdot g_{\text{AB-EF}}[(T_{\text{L}} + \Delta T_{\text{e}}^{\text{AB}}) + (T_{\text{L}} + \Delta T_{\text{e}}^{\text{EF}})]/2 \\ &= L \cdot g_{\text{AB-EF}}[2T_{\text{L}} + \Delta T_{\text{e}}^{\text{AB}} + \Delta T_{\text{e}}^{\text{EF}}]/2 \end{aligned} \tag{7.11}$$

for the heat conductivity of the 1D waveguide that connects the reservoirs AB and EF. Accordingly, the heat conductance of the 1D electron waveguide that connects the reservoirs AB and CD can be expressed as

$$\kappa_{\text{AB-CD}} = L \cdot g_{\text{AB-CD}}[2T_{\text{L}} + \Delta T_{\text{e}}^{\text{AB}} + \Delta T_{\text{e}}^{\text{CD}}]/2. \tag{7.12}$$

Here, L refers to the Lorenz number, that is assumed to be the same for all 1D waveguides of the quantum ring. Eq. 7.11 and 7.12 can now be used to replace the heat conductivities in Eq. 7.10 and to obtain

$$\frac{\dot{Q}_{\text{CD}}}{\dot{Q}_{\text{EF}}} = \frac{g_{\text{AB-CD}}}{g_{\text{AB-EF}}} \times \frac{2T_{\text{L}} + \Delta T_{\text{e}}^{\text{AB}} + \Delta T_{\text{e}}^{\text{CD}}}{2T_{\text{L}} + \Delta T_{\text{e}}^{\text{AB}} + \Delta T_{\text{e}}^{\text{EF}}} \times \frac{\Delta T_{\text{e}}^{\text{AB}} - \Delta T_{\text{e}}^{\text{CD}}}{\Delta T_{\text{e}}^{\text{AB}} - \Delta T_{\text{e}}^{\text{EF}}}. \tag{7.13}$$

The rise of the electron temperature $\Delta T_\mathrm{e}^\mathrm{EF}$ is smaller than the lattice temperature $T_\mathrm{L} = 4.2$ K for heating currents $I_\mathrm{h} \lesssim 3$ µA, as can be seen in Fig. 7.2 c). In this regime, assuming $\Delta T_\mathrm{e}^\mathrm{EF}$, $\Delta T_\mathrm{e}^\mathrm{CD} \ll T_\mathrm{L}$, $\Delta T_\mathrm{e}^\mathrm{AB}$ is justified and Eq. 7.13 becomes

$$\frac{\dot{Q}_\mathrm{CD}}{\dot{Q}_\mathrm{EF}} = \frac{g_\mathrm{AB\text{-}CD}}{g_\mathrm{AB\text{-}EF}} \equiv x. \tag{7.14}$$

The ratio of the heat flows through the quantum ring in this approximation is dominated by the ratio of the electrical conductance, which appears intuitive in terms of the Wiedemann-Franz relation. Here, the factor x is introduced to represent this ratio in order to simplify the subsequent expressions.

The deviation between $T_\mathrm{e}^\mathrm{EF}(V_\mathrm{g})|_{I_\mathrm{h}=\mathrm{const}} \propto \sqrt{N}$ and $T_{\mathrm{e,\,lit}}(V_\mathrm{g})|_{I_\mathrm{h}=\mathrm{const}} \propto N$ is assumed to be based on the branching of the waveguide network that is not present in a QPC. By setting $\dot{Q}_\mathrm{CD} = 0$, the quantum ring becomes comparable to a QPC and the whole heat flows from reservoir AB to reservoir CD. The corresponding heat flow in this system is

$$\dot{Q}_\mathrm{AB} = \dot{Q}_\mathrm{EF}^\mathrm{max} = \kappa_\mathrm{AB\text{-}EF}^\mathrm{max}[\Delta T_\mathrm{e}^\mathrm{AB} - \Delta T_\mathrm{e}^\mathrm{EF,max}]. \tag{7.15}$$

According to Eq. 7.11 the heat conductance of this system is

$$\kappa_\mathrm{AB\text{-}EF}^\mathrm{max} = L g_\mathrm{AB\text{-}EF}^\mathrm{max}[2T_\mathrm{L} + \Delta T_\mathrm{e}^\mathrm{AB} + \Delta T_\mathrm{e}^\mathrm{EF,max}]/2. \tag{7.16}$$

Here, the electrical conductance $g_\mathrm{AB\text{-}EF}^\mathrm{max}$ is identical to $g_\mathrm{AB\text{-}EF}$ since the 1D electron waveguide from reservoir AB to EF was not changed by setting $\dot{Q}_\mathrm{CD} = 0$ and because V_g is constant. Having $g_\mathrm{AB\text{-}EF}^\mathrm{max} = g_\mathrm{AB\text{-}EF}$ allows to rewrite Eq. 7.6 by using Eqs. 7.14 and 7.15 to receive

$$\dot{Q}_\mathrm{EF}^\mathrm{max} \approx \dot{Q}_\mathrm{EF} + \dot{Q}_\mathrm{CD} \approx \dot{Q}_\mathrm{EF}(1 + x). \tag{7.17}$$

By taking the expressions in Eqs. 7.7 and 7.15 the rise of the temperature $\Delta T_\mathrm{e}^\mathrm{AB}$ in reservoir AB, induced by current heating, can be replaced to obtain

$$\kappa_\mathrm{EF}^\mathrm{max} \Delta T_\mathrm{e}^\mathrm{EF,max} \approx \kappa_\mathrm{AB\text{-}EF} \Delta T_\mathrm{e}^\mathrm{EF}(1 + x). \tag{7.18}$$

The expressions for the heat conductance in Eqs. 7.11 and 7.16 can now be included in Eq. 7.18 to obtain

$$\begin{aligned} &(2T_\mathrm{L} + \Delta T_\mathrm{e}^\mathrm{AB} + \Delta T_\mathrm{e}^\mathrm{EF,max}) \cdot (\Delta T_\mathrm{e}^\mathrm{AB} - \Delta T_\mathrm{e}^\mathrm{EF,max}) \\ \approx\ &(2T_\mathrm{L} + \Delta T_\mathrm{e}^\mathrm{AB} + \Delta T_\mathrm{e}^\mathrm{EF}) \cdot (\Delta T_\mathrm{e}^\mathrm{AB} - \Delta T_\mathrm{e}^\mathrm{EF}) \cdot (1 + x). \end{aligned} \tag{7.19}$$

Making use of the approximation $\Delta T_\mathrm{e}^\mathrm{EF}$, $\Delta T_\mathrm{e}^\mathrm{CD} \ll T_\mathrm{L}$, $\Delta T_\mathrm{e}^\mathrm{AB}$ again simplifies Eq. 7.19 and leads to

$$\Delta T_\mathrm{e}^\mathrm{EF,max} \approx \Delta T_\mathrm{e}^\mathrm{EF}(1 + x) = \Delta T_\mathrm{e}^\mathrm{EF} \cdot (1 + \frac{g_\mathrm{AB\text{-}CD}}{g_\mathrm{AB\text{-}EF}}). \tag{7.20}$$

Eq. 7.20 gives an estimation of the relative deviation of the increase in electron temperatures due to current heating in a branched quantum ring system compared to the non-branched QPC. In Fig. 7.2 a) the measured electrical conductances $g_\mathrm{AB\text{-}EF}$, $g_\mathrm{AB\text{-}C}$ and $g_\mathrm{AB\text{-}D}$ are shown and allow an estimation of the factor x. This estimation yields $x = 0$ for $N = 0$, $x \approx 0$ for $N = 1$, $x \approx 0.73$ for $N = 2$ and $x \approx 0.88$ for $N = 3$. According to Eq. 7.20 this means that for $N \lesssim 1$ the heat flow is limited to flow from reservoir AB to the reservoir EF exclusively, similar to the heat

flow in a QPC. In this case $\Delta T_\mathrm{e}^{\mathrm{EF,max}} = \Delta T_\mathrm{e}^{\mathrm{EF}}$ holds. For $N \gtrsim 1$ the heat flow branches in the quantum ring and causes the deviation of ΔT_e from $T_\mathrm{e}^{\mathrm{EF,max}}$ and subsequently provides an explanation for the deviation of $T_\mathrm{e}^{\mathrm{EF}}(V_\mathrm{g})|_{I_\mathrm{h}=\mathrm{const}} \propto \sqrt{N}$ from $T_{\mathrm{e,\,lit}}(V_\mathrm{g})|_{I_\mathrm{h}=\mathrm{const}} \propto N$. The approximation $\Delta T_\mathrm{e}^{\mathrm{EF}}$, $\Delta T_\mathrm{e}^{\mathrm{CD}} \ll T_\mathrm{L}$, $\Delta T_\mathrm{e}^{\mathrm{AB}}$ that was used for this explanation is justified for heating currents $I_\mathrm{h} \lesssim 3$ µA. However, in Fig. 7.2 d) it can be seen that Eq. 7.20 also holds for $T_\mathrm{h} = 0$ µm, i.e. for the non-linear regime [161]. In Appendix I the increase of the electron temperature $\Delta T_\mathrm{e}^{\mathrm{EF}}(N)$ can be consulted for $I_\mathrm{h} = 3$ µA, 6 µA and $I_\mathrm{h} = 8$ µA.

In the analysis above it became clear that the branching of the heat in the investigated quantum ring changes from a QPC-like behavior to an 1D waveguide network-like behavior at about $N \approx 1$. However, this should not be the case in an ideal, symmetric landscape. In the following subsection theoretical simulations, that are performed by Dr. Tobias Kramer and Dr. Christoph Kreisbeck [165, 166], will be used to discuss, to what extend a disturbed potential, that cannot be seen in Fig. 7.1, can explain this switching behavior of the heat flow through the quantum ring.

7.4 Wave packet analysis

In this section time resolved simulations of the wave packet propagation of the electrons through the quantum ring are presented. These simulations are performed by Dr. Tobias Kramer and Dr. Christoph Kreisbeck. The potential landscape of the quantum ring is chosen to be asymmetric and to have four electron reservoirs in order to resemble the device QRD. Two of the reservoirs are labeled A^* and E^* that represent the reservoirs AB and EF. The reservoirs C and D are denoted, using the nomenclature in Fig. 7.1. The simulated potential landscape is depicted in Fig. 7.6. The 1D electron waveguides of the quantum ring are confined with a harmonic effective potential in order to produce energetic equidistant subband spacing, see Eq. 2.24. Two different approaches of the quantum ring device geometries are

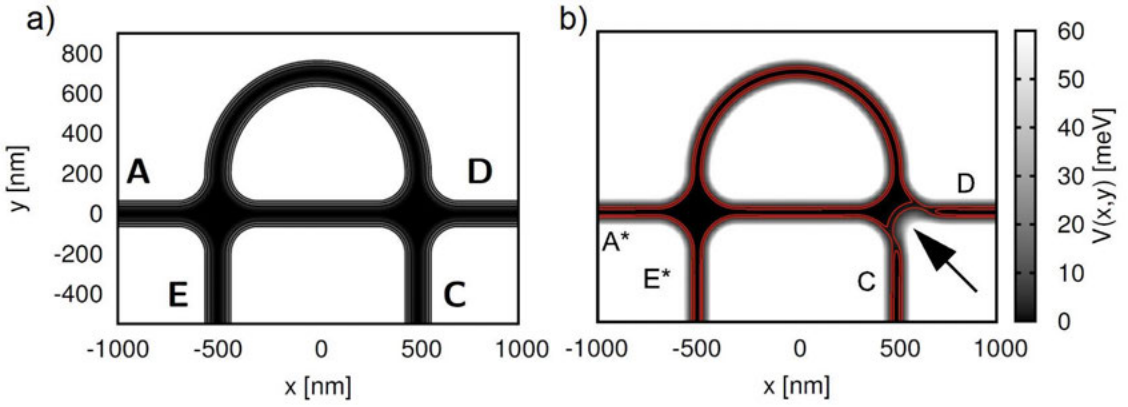

Figure 7.6: Simulated potential landscape of the quantum ring. The potential has been chosen to be a) symmetric and b) asymmetric with a Gaussian obstacle of the form $V_\mathrm{sc}(x,y) = V_0 e^{-[(x-o_x)^2+(y-o_y)^2]/a^2}$ with $V_0 = 50$ meV, $a = 80$ nm, $o_x = 590$ nm and $o_y = -90$ nm. Red lines in b) represent equipotential lines and highlight the Gaussian obstacle, that is indicated by an arrow. The panel b) is adapted from [165]. In both cases the 1D waveguides are confined by a harmonic potential.

chosen: the symmetric device in Fig. 7.6 a) and the asymmetric device in Fig. 7.6 b). Here, the term 'asymmetric' must not be confused with the breaking of the symmetry along the symmetry axis x that occurs due to the definition of the lithographic pattern and is given in both device models. The term rather refers to the breaking of the symmetry along the symmetry axis y by introducing a Gaussian obstacle in the right arm of the device, which is indicated by an arrow in Fig. 7.6 b). The asymmetric device is motivated by the shift of the threshold voltages of the electrical conductance $g_{\text{AB-C}}$, $g_{\text{AB-D}}$ and $g_{\text{C-D}}$ compared to $g_{\text{AB-EF}}$, see Fig. 7.2 a). In the following the wave packet simulations of both, the symmetric and the asymmetric device geometries, are compared with each other.

In the theoretical approach the heat flow is simulated in terms of an energy current Q. For 1D electron conductors the energy current is connected to the thermal conductance by the analytical expression [167, 168, 162]

$$\kappa = -\frac{Q}{\Delta T}|_{I=0} \tag{7.21}$$

in the absence of electric current I. In Eq. 7.21 $\Delta T = (T_2 - T_1)$ refers to the temperature difference of two reservoirs, labeled with 1 and 2. Similarly to the estimations from the previous subsection, the Wiedemann-Franz relation $\kappa = LTG$ with the Lorenz number $L = k_{\text{B}}^2\pi^2/(3e^2)$ [50] and the average temperature $T = (T_1 + T_2)/2$ is used to re-express the thermal conductance of the 1D conductor κ in Eq. 7.21, which yields

$$Q_{\text{max}} = -\frac{\pi^2 k_{\text{B}}^2}{3h}(T_2^2 - T_1^2). \tag{7.22}$$

Here, the electrical conductance G is taken from Eq. 2.19 for $N = 1$, i.e. $G = 2e^2/h$ is used. The energy current is labeled Q_{max} because so far bending of the 1D conductor has not been taken into consideration. Bending of the 1D conductor leads to a backscattering induced reduction of the transmission probability of an electron

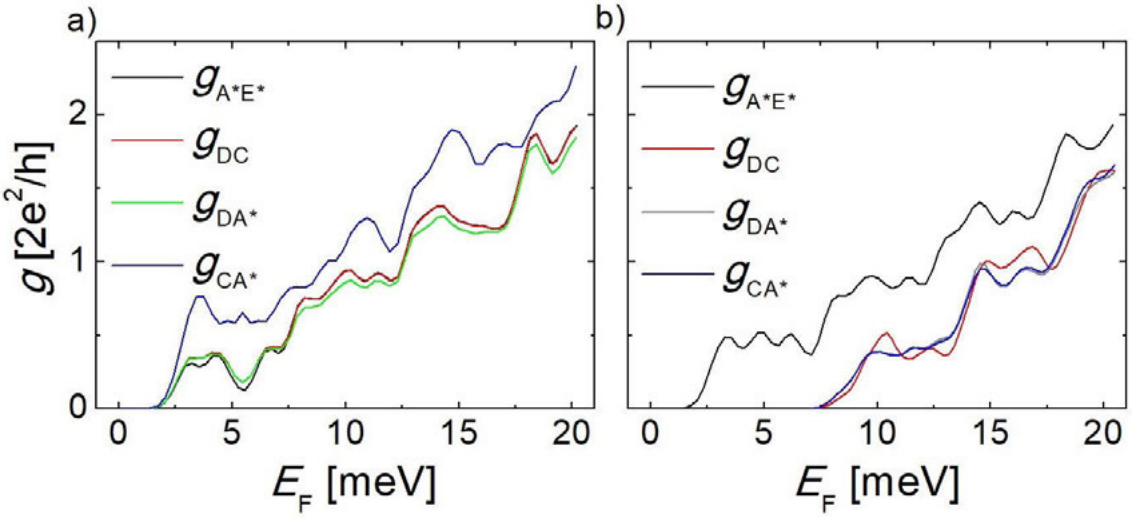

Figure 7.7: Comparison of the simulated electrical conductance for a a) symmetric and b) an asymmetric device model. The threshold voltage is identical for $g_{\text{A}^*\text{E}^*}$, g_{DC}, g_{DA^*} and g_{CA^*} in the symmetric device model. In the asymmetric device model the threshold voltages of g_{DC}, g_{DA^*} and g_{CA^*} are also identical to each other, but shifted relatively to $g_{\text{A}^*\text{E}^*}$.

though the conductor, which limits the energy current $Q < Q_{\max}$. Moreover, the quantum ring has additional leads compared to a single 1D conductor. This fact can be incorporated by the multi-terminal approach of the Landauer-Büttiker formalism

$$Q_i = \frac{2}{h}\int_0^\infty \mathrm{d}E E \sum_{j\neq i,n_i,n_j} [f(E,\mu_i,T_i) - f(E,\mu_j,T_j)]|t_{i,n_i,j,n_j}(E)|^2 \tag{7.23}$$

with the transmission probability t_{i,n_i,j,n_j} of an electron to propagate from lead i with lead modes n_i to the lead j with lead modes n_j. The transmission probability is assumed to be completely determined by the device geometry. Electron-electron interactions are explicitly not taken into consideration. Thus, the energy current through the device is solely determined by the choice of the potential landscape. Similarly, the electric current is calculated by

$$I_i = \frac{2e}{h}\int_0^\infty \mathrm{d}E \sum_{j\neq i,n_i,n_j} [f(E,\mu_i,T_i) - f(E,\mu_j,T_j)]|t_{i,n_i,j,n_j}(E)|^2. \tag{7.24}$$

Eq. 7.24 is used to simulate the electrical conductance of the device for Fermi energies in the range from 0 meV to 20 meV with a resolution of 0.3 meV for the symmetric and the asymmetric device model, as depicted in Fig. 7.7. In the symmetric device model the threshold voltages of $g_{\mathrm{A^*E^*}}$, g_{DC}, $g_{\mathrm{DA^*}}$ and $g_{\mathrm{CA^*}}$ are identical to each other. In the asymmetric device model the threshold voltages of g_{DC}, $g_{\mathrm{DA^*}}$ and $g_{\mathrm{CA^*}}$ are also identical to each other, but differ from that of $g_{\mathrm{A^*E^*}}$, which closely matches the experimental observation in Fig. 7.2 a). This indicates that the presence of a Gaussian obstacle is a reasonable assumption for the given quantum ring.

The energy current Q_i through the device is simulated by evaluating Eq. 7.23. Here, the device heating is simulated by setting the temperature of the reservoir

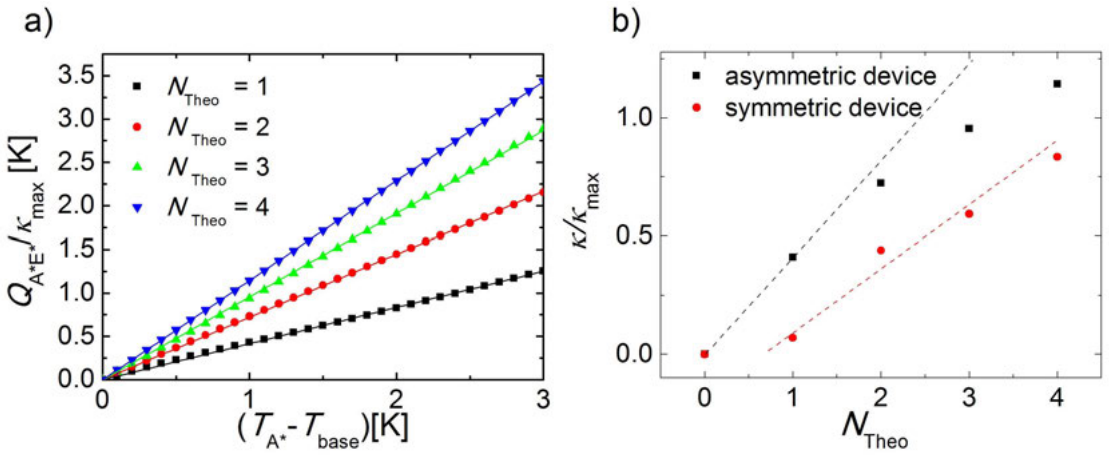

Figure 7.8: Simulation of the energy current Q from reservoir $\mathrm{A^*}$ to reservoir $\mathrm{E^*}$. a) The simulation is performed for the asymmetric device model (shown) and the symmetric device model (not shown) for the number of occupied subbands $N_{\mathrm{Theo}} =$ 1, 2, 3 and $N_{\mathrm{Theo}} = 4$ and temperatures ranging from 0 K to 3 K with a resolution of 0.1 K. b) The slope of $\frac{\mathrm{d}[Q_{\mathrm{A^*E^*}}/\kappa_{\max}]}{\mathrm{d}[T_{\mathrm{A^*}} - T_{\mathrm{base}}]} = \kappa/\kappa_{\max}$ is shown for the asymmetric device model (black squares) and for the symmetric device model (red circles). An onset is observable for the symmetric device model. The dashed lines are a guide to the eye and indicate the linearity of $= \kappa/\kappa_{\max} \propto N$ for the symmetric device model and the non-linearity for the asymmetric device model.

A to a higher value compared to the temperature of the other electron reservoirs, i.e. $T_{\mathrm{A}^*} > T_{\mathrm{E}^*}$, T_{C}, T_{D}. The electrons are assumed to adopt the temperature of the reservoir they come from, which is a reasonable assumption in terms of the Landauer-Büttiker formalism. Furthermore, the zero-current condition is enforced, which compensates the current of 'hot' electrons, stemming from reservoir A^*, to the colder reservoirs by an equal current of electrons from the cold reservoirs to reservoir A^*. The resulting transport of heat is represented by Q_i. The Fermi energy is chosen to lead to an occupation of $N_{\mathrm{theo}} = 0$, 1, 2, 3, and $N_{\mathrm{theo}} = 4$ subbands of the waveguide, that connects reservoir A^* with reservoir E^*, to be comparable to the experimental results. The heating in reservoir A^* is set to temperatures ranging from $T_{\mathrm{A}^*} - T_{\mathrm{base}} = 0$ K to $T_{\mathrm{A}^*} - T_{\mathrm{base}} = 3$ K with a resolution of 0.1 K. The simulated energy current from reservoir A^* to E^*, which is labeled $Q_{\mathrm{A}^*\mathrm{E}^*}$, is shown in Fig. 7.8 a) for the asymmetric model.

In experiment the increase of $T_{\mathrm{e}}^{\mathrm{EF}}$ was measured. In order to compare the energy current with this temperature increase, $Q_{\mathrm{A}^*\mathrm{E}^*}$ is divided by the heat conductance that is carried by one energy mode $\kappa_{\mathrm{max}} = L(T_{\mathrm{A}^*} + T_{\mathrm{base}})e^2/h$, see Eqs. 7.21 and 7.22. The relation between the x-values of Fig. 7.2 c), i.e. I_{h}^2, and those of Fig. 7.8 a), i.e. $T_{\mathrm{A}^*} - T_{\mathrm{base}}$, is given by Joule's law, that is observed in experiment with $\Delta T_{\mathrm{e}}^{\mathrm{EF}} \propto I_{\mathrm{h}}^2$ for the reservoir EF. The simulations show the linearity $Q_{\mathrm{A}^*\mathrm{E}^*} \propto (T_{\mathrm{A}^*} - T_{\mathrm{base}})$, which indicates the validity of the Wiedemann-Franz relation

$$\kappa(N_{\mathrm{Theo}}) = \Delta Q_{\mathrm{A}^*\mathrm{E}^*}(N_{\mathrm{Theo}})/(T_{\mathrm{A}^*} - T_{\mathrm{base}}), \tag{7.25}$$

that was also assumed in the estimations of the heat flow branching in the previous subsection. Fig. 7.8 b) shows the slope

$$\frac{\mathrm{d}[Q_{\mathrm{A}^*\mathrm{E}^*}/\kappa_{\mathrm{max}}]}{\mathrm{d}[T_{\mathrm{A}^*} - T_{\mathrm{base}}]} = \kappa/\kappa_{\mathrm{max}} \tag{7.26}$$

of the asymmetric and the symmetric device. In the symmetric device model an onset is present at $N_{\mathrm{theo}} = 1$ and follows an approximate linear behavior $\kappa/\kappa_{\mathrm{max}} \propto N_{\mathrm{Theo}}$. In contrast, in the asymmetric device model this onset is not present. Furthermore, $\kappa/\kappa_{\mathrm{max}}(N_{\mathrm{Theo}})$ deviates from a linear behavior and rather follows the dependence that is observed in experiment.

In conclusion, the experimental data are qualitatively reproduced by wave packet analysis with respect to the electrical conductance and the heat flow, or energy current, through the quantum ring QRD. The onset of the electrical conductance that intersects the crossing next to reservoir C and D can be explained with a Gaussian scatterer that leads to a further asymmetry in the device model. This asymmetry also leads to energy currents that fit the observed heat flow better than in the symmetric device model. In experiment a quantitative determination of Q would require measurements of the thermal noise in the heated reservoir AB. However, 1/f noise increases [169] and dominates the spectral density and S_{V}. Hence, $S_{\mathrm{V,w}}$ cannot be deduced if the reservoir AB is heated.

Chapter 8

Interference measurements in quantum rings

In this chapter $Al_xGa_{1-x}As$/GaAs-based quantum ring devices are investigated with respect to their magnetoresistance. In the presented experiments a perpendicular magnetic field is applied to the plane of the 2DEG. As the electron propagates through one of the quantum ring's arms the vector potential leads to an additional accumulation of an electron phase in the two arms of the ring, as explained in Sec. 2.4. The accumulated phase has different signs for the two arms and leads to constructive or destructive interference of the electron waves depending on the accumulated phase difference. This means that sweeping the magnetic field causes the electrical resistance of the quantum ring to oscillate, which was first demonstrated by Aharonov and Bohm in 1959 [6].

8.1 Current state of research

Currently, there is a large variety of interference experiments that are based on the superposition of electron waves in a system that preserves a static phase relation between the interfering electron waves. The electron phase is sensitive to an external applied magnetic field $\vec{B}$. The reason for this is the vector potential $\vec{A}$ whose curl is equal to $\vec{B}$. The vector potential experienced a transition from being a mathematical tool to simplify Maxwell's relations to an important physical property by the work of Aharonov and Bohm in 1959 [6]. The two scientists predicted that electrons accumulate a phase along a path when exposed to an external magnetic field that does not necessarily has to cross this path and proposed an interference experiment to verify their prediction. In this experiment an electron beam is split into two paths which rejoin after having traveled a length smaller than the phase coherence length of the electrons. The prediction concerns the interference pattern that oscillates between constructive and destructive as a perpendicular magnetic field is sweeped. The period of this oscillation corresponds to the enclosed magnetic flux $2\Phi_0 = h/e$. Indeed, this so-called Aharonov-Bohm (AB) effect was later proven to exist in vacuum [170], gold films [171], parallel 2DEGs of a $Al_xGa_{1-x}As$/GaAs heterostructure [172], a $Al_xGa_{1-x}As$/GaAs quantum ring [173], carbon nanotubes [174], graphene [175] and Bi_2Se_3 nanoribbons [176]. Further quantum interference experiments with electrons followed and were partly inspired by optical experiments.

Thomas Young's interference experiments with light [1] were based on the usage of a double-slit whose distance from an observing screen determines the interfer-

ence pattern. The double-slit experiment was later realized for a beam of electrons [177] that is diffracted by a copper film with slits of 0.3 µm width. Subsequently, Feynman's assumption that this interference pattern should also be visible for single electrons [178] was confirmed experimentally [179]. The double-slit experiment was followed by several other interference experiments with light that were accompanied by their electronic counterparts. One example is the Mach-Zehnder interferometer [180, 181], that is an advanced version of the Jamin interferometer [182] to detect phase shifts of light as well as the refraction index of an optical medium. In the original version of the Mach-Zehnder interferometer a beam of light is split into two paths and recombined by a set of mirrors. In the electronic counterpart edge states are created in the quantum Hall regime and are split and recombined by quantum point contacts [183]. The optical version of a Fabry-Pérot interferometer [184] makes use of an optical cavity to filter a single wavelength from light with a wide spectrum. The idea of such a resonator can be applied to carbon nanotubes that define a cavity between two nanotube-electrode interfaces [185].

Quantum interference also becomes very important in disordered metallic systems where the phase evolution - and thus the interference - of the electron waves is determined by the setup of the disorder. An applied electric field E changes the potential landscape and therefore the interference paths. This leads to a fluctuation of the interference and therefore to a fluctuation of the resulting electrical conductance when sweeping E. This effect is referred to as universal conductance fluctuation [186, 37]. Disorder may also cause electron waves to propagate along closed circles rather than propagating along a potential gradient. The interference of a time-reversed pair of electron waves causes localization [65] which increases the electrical resistance in the absence of a magnetic field. Strong spin-orbit interaction of the localized electrons causes the opposite effect and leads to an increase of the conductance in the absence of a magnetic field [9]. The presence of a magnetic field leads to a suppression of both effects.

The sensitivity of the above mentioned quantum interference experiments to scattering and an applied magnetic field enables to probe the phase evolution in a device, as done with quantum dots [187, 188, 189] whose influence on the electron phase is studied by means of the AB effect. A typical feature of two-terminal AB interferometer devices is the restriction of the phase evolution to 0 or π jumps, be it in the presence [187, 190] or in the absence [191, 192] of quantum dots. This effect is referred to as 'phase rigidity' and can be understood in terms of time-reversal symmetry and current conservation in a closed system [35]. This leads to the symmetry of the transmission probabilities $T_{ij}(B) = T_{ji}(-B)$ of the electrons to propagate from channel i to j and vice versa and consequently leads to the Onsager reciprocity $R_{\mathrm{ij}}(B) = R_{\mathrm{ji}}(-B)$ [193]. The origin of phase rigidity can also be expressed in terms of multiple reflections of the electron waves at the crossing points in the interferometer device [194]. In order to break the phase rigidity, the reduction of the device symmetry is required, e.g. by attaching additional leads to the ring [195]. This was demonstrated for four-terminal ring devices [188]. Note that even in four-terminal devices the measurement setup may still lead to a symmetry in the system causing phase rigidity [148, 194].

Depending on the observed system, electrons may change or even lose their phase relation. Elastic scattering, i.e. scattering of electrons with static potentials, such as potential barriers in an 1DEG, changes an electron's phase. However, these changes do not vary with time and the phase shift is fix for all electrons. Therefore, elastic

scattering preserves the phase coherence of a given system. In contrast, inelastic scattering randomizes the electron's phase and breaks the phase coherence, i.e. it acts 'dephasing' with a dephasing rate of τ_φ^{-1}. Such a randomization also occurs due to thermal averaging of the electron phase, which describes the smearing of the Fermi wave vector and the subsequent loss of the initial phase information after traveling the thermal length. This can be expressed with the thermal dephasing rate τ_T. Hence, the total dephasing rate is $\tau_\mathrm{deph}^{-1} = \tau_\varphi^{-1} + \tau_\mathrm{T}^{-1}$. At low temperatures electron-electron interactions are found to dominate the dephasing scattering in 2DEGs [158], i.e. $\tau_\varphi \to \tau_{ee}$, and the according relaxation time is predicted [196, 197] to be $\tau_{ee} \propto (T_\mathrm{bath}^2 \ln T_\mathrm{bath})^{-1}$.

In ballistic 1DEGs the dephasing processes are not fully understood. The amplitude of the characteristic Aharonov-Bohm oscillations is a measure of the phase relaxation time in 1D quantum rings. In recent experiments [146, 147, 148] the amplitude of the oscillations is found to be $R_\mathrm{AB} \propto T_\mathrm{bath}^{-1}$. A similar observation is made for an increased excitation current I_Osc [198]. Another method to analyze the phase coherence ring in a quantum ring is linked to the harmonics of the base oscillation frequency. Beyond the base frequency, each further visible harmonic in the Fourier spectrum corresponds to electrons propagating an additional time around the ring [199, 200, 146], allowing to estimate the phase coherence length in units of the ring circumference. The second harmonic is often associated with the Al'tshuler-Aronov-Spivak (AAS) effect [201]. The AAS oscillations were first observed in cylindrical metal films [202], subsequently in networks of thin metallic wires in the diffusive regime [203], in antidot lattices [204, 205] and in quantum rings [206, 207]. In contrast to the AB oscillations, the AAS oscillations can still occur in disordered systems [208] and occur if both interfering electrons have traveled the complete circumference of the device [209]. Depending on the experimental conditions either one or both effects can be present at the same time.

8.2 Influence of re-cooling the device

The quantum ring device QRC is investigated with respect to the magnetoresistance in the presence of a magnetic field $\vec{B}$ that is applied perpendicularly to the plane of the 2DEG. The detailed four-point measurement setup is depicted in Sec. 4 and is schematically depicted in the inset of Fig. 8.1 a) for the device QRC. The excitation voltage is applied between the contacts 4 and 1 in order to establish the current $I_\mathrm{Osc} = I_{41}$ with an excitation frequency of 133 Hz. In Aharonov-Bohm interferometers the observed interference amplitude is found to decrease with increasing excitation current with $\propto \exp(-I_\mathrm{Osc})$ [198, 71], similarly to an increased bath temperature T_bath [148]. The interference amplitude is a measure of the electron phase coherence length and can thus be used to analyze dephasing processes. A decrease of the amplitude with I_Osc or T_bath can therefore be attributed to an increased dephasing electron-electron interaction and thermal averaging. In this context the visibility v can be defined

$$v = \frac{R_\mathrm{max} - R_\mathrm{min}}{R_\mathrm{max} + R_\mathrm{min}}, \tag{8.1}$$

which is the ratio of the oscillation amplitude $(R_\mathrm{max} - R_\mathrm{min})/2$ to the background resistance $(R_\mathrm{max} + R_\mathrm{min})/2$. In this thesis an excitation current of 1 nA to 10 nA is found to yield the best visibilities of the magnetoresistance oscillations.

For the device QRC the excitation current is chosen to be $I_{41} = 5$ nA. The voltage is measured between the contacts 3 and 2, which allows to calculate the electrical four-point resistance $R_{41,32} = V_{32}/I_{41}$. The magnetic field is sweeped from -30 mT to +30 mT with a sweep rate of 2.4 mT/min and the four-point resistance $R_{41,32}$ was measured each second. From the device geometry the expected period of the Aharonov-Bohm oscillations can be calculated with $\Delta B = h/eF$ (see Sec. 2.4) with the area F that is enclosed by the arms of the ring. By using $F = \pi r^2/2$ the expected oscillation period becomes $\Delta B = (2.2 \pm 0.4)$ mT with a radius $r = (1.1 \pm 0.1)$ µm. The measured magnetoresistance is depicted in Fig. 8.1 a) and shows a reproducible aperiodic background. This background is attributed to transmission probabilities that vary with the magnetic field as well as to universal conductance fluctuations. In the present experiment these effects are considered parasitic and are created due to the fact that the magnetic field does not only penetrate the enclosed area F, but also the electron waveguides. The background is modulated by resistance oscillations that have an amplitude of few Ω and become

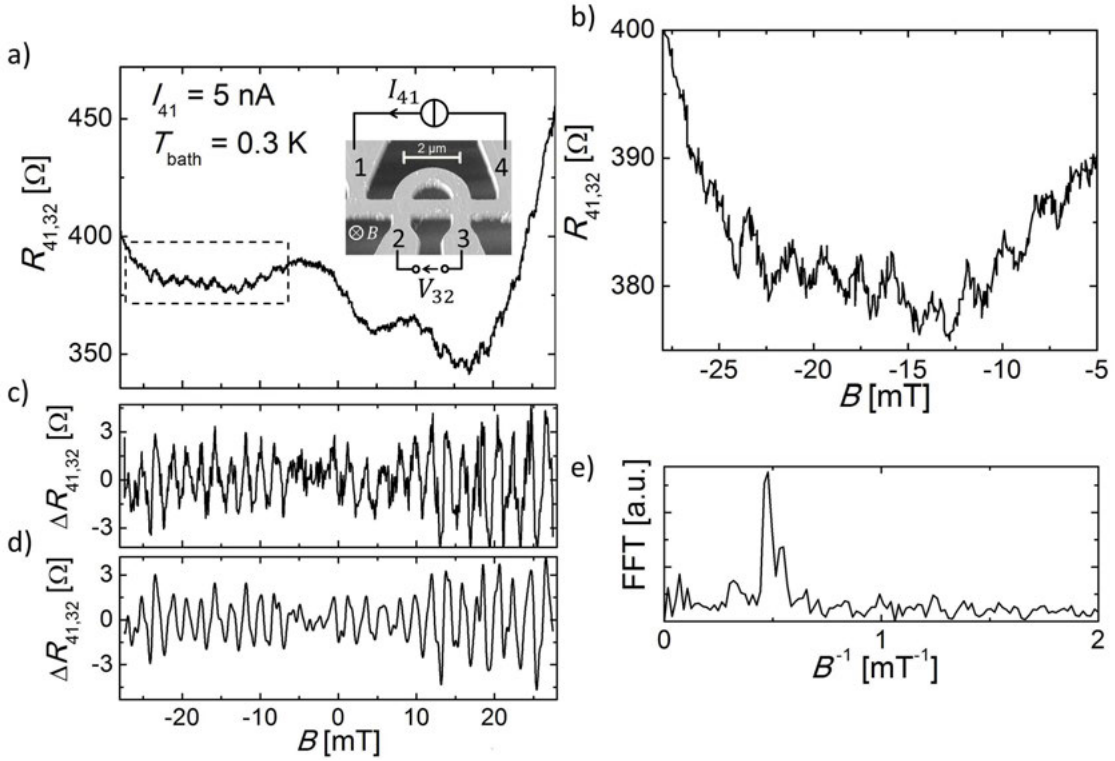

Figure 8.1: Magnetoresistance measurements of the quantum ring device QRC with an applied perpendicular magnetic field at $T_{\text{bath}} = 0.3$ K and an excitation current of 5 nA. The inset in a) shows an optical micrograph [138] of the device with contacts labeled 1 to 4 and a schematic of the four-point measurement setup. The electrical four-point resistance $R_{41,32} = V_{32}/I_{41}$ shows an aperiodic background. The dashed rectangle indicates the measurement range that is magnified in b), showing the magnetoresistance oscillations. The raw measurement from a) is smoothed and subtracted by the smoothed function, leading to the resistance oscillations in c). d) Data from c) after applying a bandpass filter with a lower cutoff frequency of 0.15 mT^{-1} and an upper cutoff frequency of 1.5 mT^{-1}. e) The Fourier transformation of the data from c) shows a clear peak at ~ 0.5 mT^{-1}, which is attributed to the base frequency of the Aharonov-Bohm oscillation.

visible in the enlargement in Fig. 8.1 b). The period of the oscillations is about 2 mT over the entire measured range of B. In order to separate the magnetoresistance oscillations from the aperiodic background, the raw measurement is smoothed with the method 'moving average'. In this method a window includes a predefined number of data points whose average is calculated and attributed to the data point that is placed in the center of the window. This is done for all arguments of the data with the same window size. Here, the window size is chosen to be about 2 mT, i.e. the period of the measured magnetoresistance. The resulting smooth function is subtracted from the raw magnetoresistance.

The pure magnetoresistance oscillation signal is depicted in Fig. 8.1 c). In order to suppress the high frequency part of these oscillations, a fast Fourier transformation and a subsequent bandpass filter is applied with a lower cutoff frequency of 0.15 mT^{-1} and an upper cutoff frequency of 1.5 mT^{-1}. The filtered signal of the magnetoresistance oscillations is shown in Fig. 8.1 d). The Fourier transformation is performed for the data in the whole range from - 28 mT to + 28 mT and shows a clear peak at 0.5 mT^{-1}, which can be seen in Fig. 8.1 e). The corresponding period of 2 mT is in accord with the expected period and is therefore attributed to the base frequency of the Aharonov-Bohm oscillation.

Since no harmonics of the base oscillation are observable in the Fourier transformation, it can be concluded that electrons do not perform multiple loops [199, 200] in the quantum ring but rather directly propagate through it. Furthermore, from the lack of the first harmonic the absence of the AAS effect, observed among others in $\mathrm{Al_xGa_{1\text{-}x}As/GaAs}$ etched quantum rings [206] and in electrostatically defined quantum rings with incorporated quantum dots [207], can be concluded.

According to Sec. 6.3 the ballistic thermal length $l_{\mathrm{T,b}} = \hbar^2\sqrt{2n\pi}/k_{\mathrm{B}}T_{\mathrm{bath}}m_{\mathrm{e}}^* = (5.6 \pm 0.4)$ µm is calculated for $T_{\mathrm{bath}} = 0.3$ K with the effective mass $m_{\mathrm{e}}^* = (0.057 \pm 0.005)\ m_0$ and the electron density $n(0.3\ \mathrm{K}) = (1.83 \pm 0.06) \cdot 10^{11}\ \mathrm{cm}^{-2}$, deduced from the SdH oscillations from Sec. 5.1. Comparing the length of the straight arm $l_{\mathrm{straight}} = (2.2 \pm 0.1)$ µm and the length of the bent arm $l_{\mathrm{bent}} = (3.4 \pm 0.2)$ µm of QRC with $l_{\mathrm{T,b}}$ shows that the phase coherence length l_φ is not long enough to enable electrons to perform multiple loops in the quantum ring while keeping their phase coherence. This is in accord with the missing harmonics in the FFT for the presented magnetoresistance oscillations. Note that in this estimate dephasing due to inelastic electron-electron scattering is not considered, making $l_{\mathrm{T,b}}$ an upper limit for the actual phase coherence length l_φ.

From the filtered magnetoresistance oscillations the visibility $v = 0.9 \pm 0.2\%$ is deduced. This value is relatively small compared to the visibilities of about 3-5 % of etched quantum rings with similar size at $T_{\mathrm{bath}} = 0.3$ K [148] and comparable excitation current I_{Osc} . Etched two-terminal $\mathrm{Al_xGa_{1\text{-}x}As/GaAs}$-based quantum rings show visibilities of typically 10 % [146, 192] up to more than 50 % [210].

The identification of magnetoresistance oscillations for the quantum ring device QRC is not always possible. Whether the magnetoresistance oscillations are observable is linked to the cooling process of the device. Typically the observability of the AB oscillations will remain until the device is warmed up again. In Fig. 8.2 a) the measured magnetoresistance of the quantum ring QRC is depicted for two measurements with a perpendicularly applied magnetic field that is sweeped in the range -30 mT to +30 mT. The measurement setup for these measurements is identical to each other and the same, as depicted in the inset of Fig. 8.1 a). For these measurements an excitation current of $I_{41} = 10$ nA with an excitation frequency of

133 Hz is chosen. Between these two measurements the device was warmed up to $T_{\mathrm{bath}} = 70$ K and re-cooled over a period of three hours each. Comparing the two measurements shows significant differences in the background signal. Furthermore, the magnetoresistance measurement, recorded before the re-cooling process, has a higher noise contribution and also shows no observable magnetoresistance oscillations. In contrast, magnetoresistance oscillations can be deduced from the measurement after the re-cooling process by subtracting the background from the raw data. The filtered oscillations are depicted in Fig. 8.2 b) and are attributed to Aharonov-Bohm oscillations since the observed oscillation period of 2 mT is in accord with the expected period $2h/e\pi r^2$. The visibility is found to be $v \approx 0.5 \pm 0.1$ %. The Fourier transformations for the magnetoresistance measurements before and after the re-cooling process are depicted in Fig. 8.2 c) and d). The measurement, taken before the re-cooling process, shows no peak. In contrast, a clear peak is visible at $B^{-1} = 0.5$ mT^{-1} for the measurement after the re-cooling process besides a slightly reduced noise contribution.

Note that the filtered oscillations in Fig. 8.2 a) show a modulation that resembles a beating pattern with a period of $\Delta B_{\mathrm{beat}} \approx 30$ mT. Beating in a periodic signal occurs when the signal is composed of two frequencies f_1 and f_2 that only deviate slightly from each other, leading to the beating frequency $f_{\mathrm{beat}} = |f_1 - f_2|$. The occurrence of the beating pattern will be discussed in Sec. 8.4.

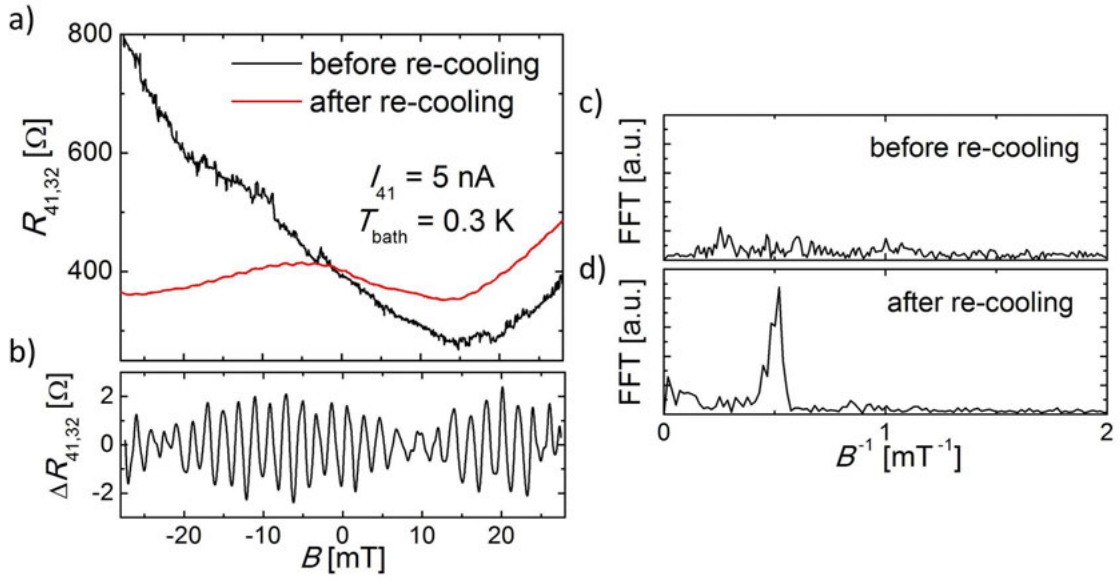

Figure 8.2: a) Comparison of the magnetoresistance of the device QRC at $T_{\mathrm{bath}} = 0.27$ K before (black line) and after (red line) re-cooling of the device. The measurement before re-cooling does not show oscillations. b) The measurement after re-cooling with subtracted background and applied FFT bandpass filter. Two periods of a beating pattern are visible. The Fourier transformation for the magnetoresistance c) before and d) after re-cooling are shown.

8.3 Phase rigidity in asymmetric quantum rings

In this section the quantum ring device QRA is studied with respect to its magnetoresistance at $T_{\mathrm{bath}} = 0.3$ K by applying a perpendicular magnetic field to the device. A SEM of the sample is shown in Fig. 8.3 a) with contacts labeled 1 to 4. The two arms of the asymmetric quantum ring device are each covered by a Ti/Au finger gate. In the straight arm of the device a QPC is incorporated. The subband population of this QPC is controlled by the gate voltage V_{g1} of a finger gate.

Fig. 8.3 b) shows the two-point differential conductance g_{14} at $T_{\mathrm{bath}} = 4.2$ K and at $T_{\mathrm{bath}} = 0.3$ K. For these measurements the gate voltage of the finger gate, covering the bent arm of the quantum ring, is set fix to $V_{\mathrm{g2}} = 400$ mV, which allows electron transport through the bent arm. Note that both measurements are taken during the same cooling process. The two-point conductance g_{14} at $T_{\mathrm{bath}} = 4.2$ K shows two plateaus that are attributed to the QPC. The plateaus in $g_{14}(V_{\mathrm{g1}})$ are hardly visible at $T_{\mathrm{bath}} = 0.3$ K and show fluctuations which are typically explained in terms of universal conductance fluctuations [146] or energy-dependent resonances [192, 138] and are an indicator of phase coherent transport through the device.

The magnetotransport measurements are performed in the range 430 mV $\leq V_{\mathrm{g1}} \leq$ 510 mV with a step size of 10 mV and 15 mV. The chosen range of V_{g1} covers the regime of the 1st and the 2nd resistance plateau of the QPC as well as

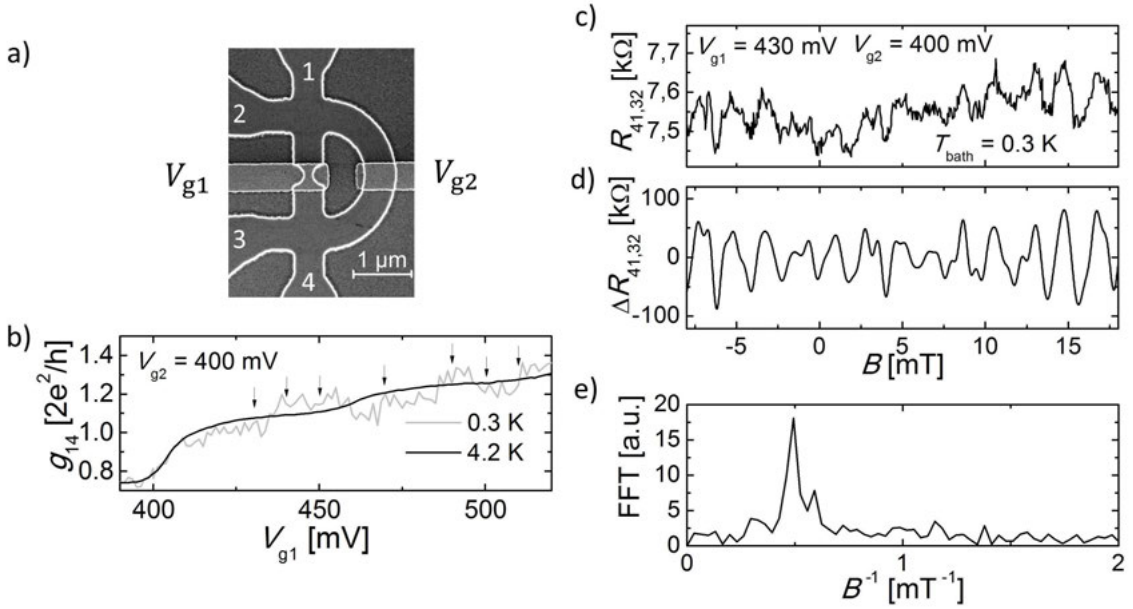

Figure 8.3: Magnetoresistance measurements of the quantum ring device QRA at $T_{\mathrm{bath}} = 0.3$ K. a) A SEM of the device [138] that shows the asymmetric quantum ring with contacts labeled 1 to 4 as well as the QPC that is incorporated in the straight arm of the device. Both arms are covered by a finger gate. b) The two-terminal differential conductance g_{14} at $T_{\mathrm{bath}} = 4.2$ K (black line) shows a quantization, whereas g_{14} at $T_{\mathrm{bath}} = 0.3$ K (gray line) shows fluctuations that make the plateaus hard to identify. c) The measured raw data of the magnetoresistance $R_{14,23}$ at $V_{\mathrm{g1}} = 430$ mV and $V_{\mathrm{g2}} = 400$ mV. The oscillations have a visibility of about 1 %. d) The data from c) with subtracted background and applied FFT filter. e) The fast Fourier transformation is shown for the raw data and shows a peak at $B^{-1} = 0.5$ mT^{-1}.

the transition regime at $V_{g1} = 475$ mV. Similar to the calculation of the expected Aharonov-Bohm oscillation of the quantum ring device QRC from the previous section, the expected magnetoresistance oscillations are calculated to $\Delta B = h/(eF) = (2.2 \pm 0.4)$ mT. Here, the area $F = \pi r^2/2$, enclosed by the quantum ring with the radius $r = (1.1 \pm 0.1)$ µm, is used for the calculation of ΔB. For $V_{g1} = 430$ mV and $V_{g2} = 400$ mV the measured four-point magnetoresistance $R_{41,32}(B)$ is depicted in Fig. 8.3 c). Subtracting the background and applying a FFT bandpass filter with 0.15 mT^{-1} as lower and 1.5 mT^{-1} as upper cutoff frequency results in the filtered oscillations, depicted in Fig. 8.3 d). The FFT, presented in Fig. 8.3 e), shows a peak at 0.5 mT^{-1}, which indicates that the observed magnetoresistance oscillations stem from the Aharonov-Bohm effect. Several oscillation maxima form a double peak, indicating that further harmonics of the base oscillation frequency may contribute to the measured magnetoresistance. However, besides a shoulder peak of the base frequency, in the FFT no contribution of harmonics can be identified.

The FFT filtered oscillations of the measured magnetoresistance for all investigated gate voltages V_{g1} are depicted in Fig. 8.4. All magnetoresistance measurements show a peak at 0.5 mT^{-1} in the FFT (not shown here). For the transition region at $V_{g1} = 470$ mV the oscillations are found to have more irregularities than for the other gate voltages V_{g1}. However, in addition to the h/e oscillations $h/2e$ oscillations can be seen for all V_{g1} indicated by the double peaks in the oscillation pattern. These double peaks may point towards oscillations that belong to the second harmonic or to the AAS effect. The mean visibilities of the oscillations are summarized in Tab. 8.1 and are found to range from 1% to 1.4% for the first plateau and from 0.7% to 1.0% for the second plateau.

As explained in Sec. 2.4, the phase of the electron wave functions is changed

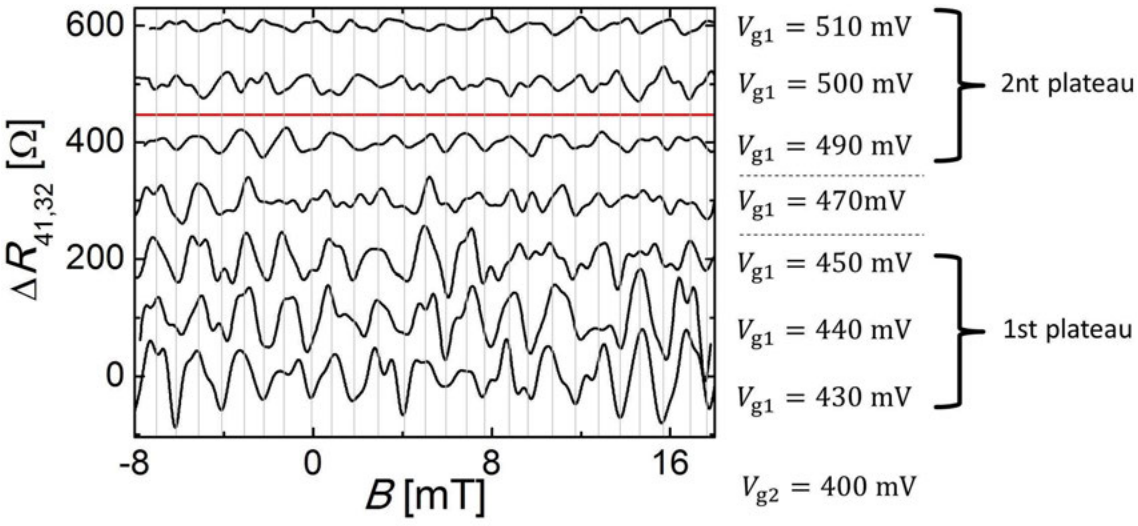

Figure 8.4: Overview of the magnetoresistance measurements in the device QRA at different gate voltages V_{g1} for the fixed gate voltage $V_{g2} = 400$ mV at $T_{bath} = 0.3$ K. The chosen gate voltages correspond to the 1st and 2nd conductance plateau at $T_{bath} = 4.2$ K of the QPC that is incorporated in the straight arm of the ring. Gray vertical lines serve as guide to the eye and indicate minima and maxima of the magnetoresistance oscillation that appear at the same B fields for different gate voltages V_{g1} and therefore indicate phase rigidity. The red line indicates a π jump of the electron's phase between $V_{g1} = 490$ mV and $V_{g1} = 500$ mV.

	1st plateau				2nd plateau		
V_{g1} mV	430	440	450	470	490	500	510
v [%]	1.0(1)	1.3(2)	1.4(2)	0.6(1)	1.0(1)	0.9(1)	0.7(1)

Table 8.1: Measured visibilities of device QRA.

if a gate voltage is applied to the electrons while they propagate through the ring. Gray vertical lines in Fig. 8.4 serve as guide to the eye for the position of maxima and minima of the magnetoresistance oscillations. It can be seen that the majority of the maxima and minima shares the same values of B with another maximum or minimum from a measurement with a different V_{g1}. For the gate voltages $V_{g1} = 430$ mV to $V_{g1} = 490$ mV several maxima fit with a maximum of another V_{g1} which also holds for many minima. The same can be stated for the maxima and minima for the gate voltages $V_{g1} = 500$ mV and $V_{g1} = 510$ mV. In these cases the phase of the electron wave does not evolve by the applied electrostatic potential.

However, comparing the maxima and minima of the oscillations with gate voltages from $V_{g1} = 430$ mV to $V_{g1} = 490$ mV with those of the gate voltages $V_{g1} = 500$ mV and $V_{g1} = 510$ mV, it can be seen that the electron phase abruptly jumps by π. The region where the π jump occurs is indicated by a red horizontal line in Fig. 8.4. The fact that the phase evolution of the electron wave is restricted to 0 and π jumps suggests that phase rigidity is present in the chosen measurement setup. The phase rigidity, observed in two- [187, 190, 191, 192] and four-terminal devices [148, 194], occurs whenever a symmetry of the transmission probability $T_{ij}(B) = T_{ji}(B)$ is given which is induced by device symmetries and is accompanied by $R(B) = R(-B)$ [193]. The symmetry in Fig. 8.3 d) is, apart from details, given around $B = 0$. The geometry of the asymmetric quantum ring device QRA breaks the symmetry in one dimension, leaving one symmetric dimension. The measurement setup is chosen to keep this symmetry. Therefore, the oscillations in Fig. 8.3 show that the remaining symmetry axis is sufficient to favour phase rigidity in a quantum ring. This is in accord with recent findings [148, 194].

In order to reproduce the findings from QRA in a similar device, further magnetoresistance measurements are performed in the quantum ring device QRB. This device has the same geometry and stems from the same batch as QRA. A notable difference in the design between QRA and QRB is the lack of a finger gate that covers the bent ring arm of QRB. A SEM of the device is depicted in Fig. 8.5 a) with contacts labeled 1 to 4. The two-point differential conductance g_{14} at $T_{bath} = 0.3$ K is shown in Fig. 8.5 b). Similar to the conductance measurement of QRA, the conductance of QRB shows fluctuations that make the conductance plateaus hard to identify at $T_{bath} = 0.3$ K. However, the conductance plateaus of the device QRB are also hard to identify at $T_{bath} = 4.2$ K. The magnetoresistance $R_{41,32}$ is measured for various gate voltages V_{g1}, using the same measurement setup as for QRA. The raw measurements for $V_g = 335$ mV and for $V_g = 360$ mV are depicted in Fig. 8.5 c) and d) (gray). Since the oscillation is not clearly visible in the raw data, a high-pass filter with a cutoff frequency of 0.55 mT^{-1} is applied (black). Again, the background signal, i.e. the smoothed raw data, is subtracted from the raw measurement and the FFT is performed, yielding the FFT amplitudes in Fig. 8.5 e) and f). A peak at 0.5 mT^{-1} corresponds to the Aharonov-Bohm base frequency which is the same

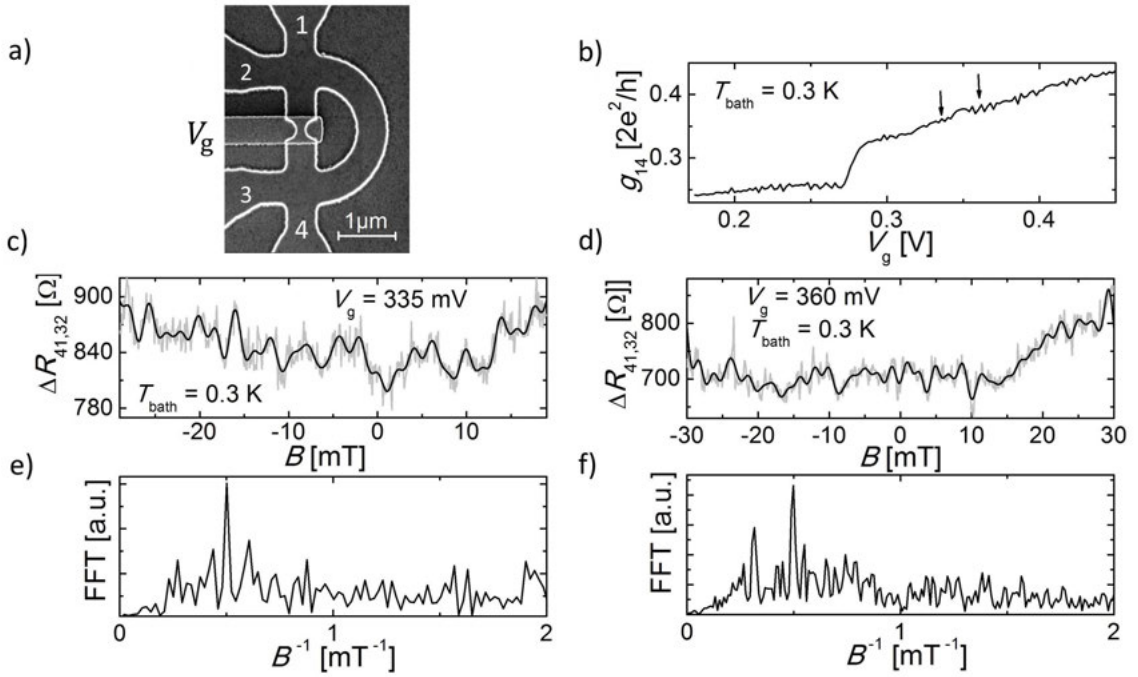

Figure 8.5: Magnetoresistance measurements of the quantum ring device QRA at $T_{\mathrm{bath}} = 0.3$ K. a) SEM of the quantum ring device QRB [138] with contacts labeled 1 to 4. b) Measured two-point differential conductance g_{14} at $T_{\mathrm{bath}} = 0.3$ K. Measured four-point resistance of the magnetoresistance $R_{41,32} = V_{32}/I_{41}$ (gray) and magnetoresistance that is FFT filtered with a high-pass filter with a cutoff frequency of 0.55 mT^{-1} (black) for c) $V_{\mathrm{g}} = 335$ mV and d) $V_{\mathrm{g}} = 360$ mV. FFT of the raw measurement that shows a weak pronounced peak at 0.5 mT^{-1}for e) $V_{\mathrm{g}} = 335$ mV and f) $V_{\mathrm{g}} = 360$ mV.

as for QRA. However the FFT is rather noisy for both depicted V_{g} as well as for all other measurements taken for QRB. In Fig. 8.5 f) an unexpected peak at 0.27 mT^{-1} can be seen. Whereas the symmetry $R(B) = -R(B)$ is as roughly given in Fig. 8.5 c) as for QRA, the background signal in Fig. 8.5 d) shows a clear asymmetry. The strong fluctuations of $R_{41,32}$ in QRB prevent to follow the evolution of the electron wave's phase. However, the break of the symmetry in $R(B)$ may be an indication of the lift of the phase rigidity. Despite the same measurement setup as for QRA a lift of the rigidity could be a result of asymmetries in the device geometry that cannot be detected in the SEM in Fig. 8.5 a).

8.4 Discussion of the quantum oscillations

In Sec. 8.2 the Aharonov-Bohm oscillations were only visible after re-cooling of the device QRC. Furthermore, the background signal changed and the fluctuations of the measured magnetoresistance were significantly higher before re-cooling. A possibility to explain these effects can be found in the presence of DX centers in the $Al_xGa_{1-x}As$ donor layer of the heterostructure [85]. These deep donor levels are suggested to be a complex formed with a substitutional donor atom (D), i.e. Si in this case, and a lattice defect (X), e.g. an As vacancy. Depending on whether these states are occupied or ionized, they may have a considerable impact on the

conductance of the 2DEG of a heterostructure. In this context, it can be shown that biasing the gate of an $Al_xGa_{1-x}As/GaAs$ heterostructure causes the threshold-voltage of a QPC in the 2DEG to shift to higher gate voltages if the bias voltage is positive and to lower gate voltages if the bias is negative [211]. This is also shown for the device ConstrA in Appendix J. The reason for this is the occupation of donors. At room temperature donors are free to change their occupation. If a positive bias is applied, electrons are attracted to the donor layer. If the device is cooled down to $T_{\mathrm{bath}} < 100$ K [85, 211], while the bias is still applied, the occupation of the donors becomes fixed because thermal ionization is not possible anymore. The ionization situation of the donor layer therefore depends on the details of the cooling process. Further investigations [212] revealed that the low-frequency noise in $Al_xGa_{1-x}As/GaAs$ is strongly affected by generation-recombination processes of DX centers. In the device QRC no top-gate structure is available. Due to the finding that the quality of the measured magnetoresistance oscillations is influenced by the cooling process, subsequent magnetoresistance measurements of the devices QRA and QRB were initiated with a small bias cooling of 0-100 mV, applied to the finger gate that covers the QPC.

The amplitude of the AB oscillations at $T_{\mathrm{bath}} = 0.3$ K after re-cooling the device showed a modulation that appears to be two periods of a beating pattern. The occurrence of beating patterns in electron interferometer experiments are typically attributed to an additional phase, induced by spin-orbit interaction, as done for quantum rings based on a *p*-type GaAs [213] and InAs/AiSb [214]. However, the $Al_xGa_{1-x}As/GaAs$ structures, investigated here, have a negligible spin-orbit coupling, as indicated by the lack of beating of the measured SdH oscillations in Sec. 2.3. Beating patterns in the magnetoresistance are also observed in metal rings [171] as well as in an electrostatically defined [215, 216] and in an etched [173] quantum ring made from a $Al_xGa_{1-x}As/GaAs$ heterostructure. These beating oscillations are found to be aperiodic.

An approach to explain the beating pattern in material systems with negligible spin-orbit interaction is the occupation of different energy modes in the quantum ring's arms. This leads to slightly different trajectories for the interfering electrons if multiple energy modes are occupiable, leading to a different enclosed magnetic flux Φ_{m} [217, 218, 219]. If only two modes contribute to the interference, the beating pattern can be found to be periodic [219] and aperiodic if multiple modes participate

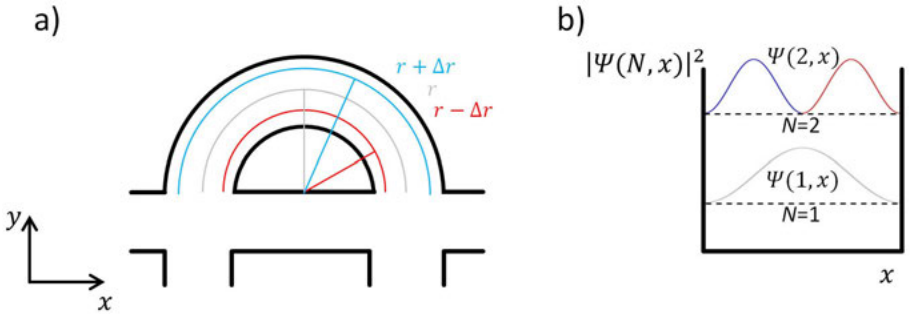

Figure 8.6: Schematic of mode-dependent electron trajectories in a quantum ring. a) A schematic of the potential landscape of an etched quantum ring with the mean ring radius r (gray) and two further ring radii (blue and red) that deviate by Δr from r. b) The mean radius r depends on the probability density function $|\Psi(N,x)|^2$ with the number of populated subbands N.

in the transport [218]. The quantum ring device QRC has a width of $w \approx 510$ nm. Considering a rectangular potential well, the approximate number of populated spin-degenerate subbands can be calculated to be

$$N \leq \sqrt{\frac{2m_e E_F}{\hbar^2}(\frac{w}{\pi})^2} = 17, \tag{8.2}$$

with the Fermi energy $E_F \approx 7.7$ meV, found from SdH oscillations in Sec. 5.1. From the observed beating periods in the magnetoresistance of the device QRC it can be estimated that the beating is aperiodic since the first period is ≈ 30 mT and the second period can be estimated to be ≈ 20 mT. Fig. 8.6 a) illustrates the trajectories in the quantum ring for two populated subbands. The density probability function $|\Psi(N,x)|^2$ for electrons has a maximum in the center of the bent arm for the first transport mode $N = 1$. For a higher number of populated energy modes, i.e. $N > 1$, the number of maxima of $|\Psi(N,x)|$ increases and the spatial separation between maxima decreases, as illustrated in Fig. 8.6 b) for $N = 1$ and $N = 2$. In the case $N = 2$ the according oscillation frequencies are $B_1^{-1} = e\pi(r + \Delta r)^2/2h$ and $B_2^{-1} = e\pi(r - \Delta r)^2/2h$, using the nomenclature from Fig. 8.6. The resulting beating frequency is $\Delta B_{beat}^{-1} = |B_1^{-1} - B_2^{-1}| = 2\pi r \Delta r/h$. For $N > 2$, however, this calculation becomes by far more complicated.

In Sec. 8.3 the magnetoresistance oscillations of the device QRA was measured for seven gate voltages. The oscillations did not show a continuous evolution of the electron phase φ when an electric field is applied but are rather pinned to 0 and π jumps, indicating phase rigidity. Note that $R_{41,32}(V_g)$ is not directly measured while sweeping V_g due to fluctuations that are attributed to universal conductance fluctuations. Phase rigidity is typically induced in two-terminal quantum rings [187, 190, 191, 192] due to current conservation and time-reversal invariance. This leads to the symmetry of the transmission coefficients $T_{ij}(B) = T_{ji}(-B)$ and to $R_{ij}(B) = R_{ji}(-B)$ [193]. In a four-terminal device time-reversal symmetry leads to $R_{kl,mn}(B) = R_{nm,kl}(-B)$ and current conservation with respect to the measurement leads is no longer given. This means that a symmetry of $R_{kl,mn}$ does not necessarily occur. Therefore, attaching additional leads to the device lifts the phase rigidity [195, 188]. The asymmetric geometry of the quantum ring devices QRA, QRB, QRC and QRD additionally serves to break the symmetries in the transmission probability. However, the measured magnetoresistance of the asymmetric quantum ring QRA shows that phase rigidity still occurs, even in a four-terminal device. This is most probably due to the mirror symmetric four-point measurement geometry that preserves the symmetry in the device and therefore favors phase rigidity, as suggested by recent investigations [148, 194]. The measured four-point magnetoresistance of QRB was too noisy to study the evolution of φ. However, a clear asymmetry in the background signal indicates that the phase rigidity is broken, although the same mirror symmetric measurement setup is used as for QRA. A reason for this may be other sources that break the symmetry of the device, such as disorder, impurities or asymmetries due to fabrication processes of the device [194].

Chapter 9

Magnetotransport properties of topological insulator Bi_2Se_3 microflakes

In this chapter four Bi_2Se_3 microflakes with a thickness of $d \ll 1\ \mu m$ are investigated. All microflakes stem from exfoliation of a nominally undoped Bi_2Se_3 bulk single crystal, grown by the Bridgman technique at the Moscow State University by the group of Prof. Dr. Lada Yashina. An overview of the investigated Bi_2Se_3 samples can be consulted in Appendix K. The single-crystallinity is proven by selected area electron diffraction (SAED). Angle-resolved photoemission spectroscopy (ARPES) measurements are performed by the group of Prof. Dr. Oliver Rader at the synchrotron of Bessy II in Berlin. They confirm the 2D nature of the topological surface states (TSS) of the single crystal. These measurements can be consulted in Appendix L. Additional photo emission electron microscopy (PEEM), also performed by the group of Prof. Dr. Oliver Rader, of an exfoliated and contacted microflake confirm that the chemical composition of the Bi_2Se_3 flakes is stable to ambient atmosphere and to the lithographic process. However, additional peaks in the PEEM spectrum indicate a minor oxidation at the flake's surface. The results of the PEEM analysis can be consulted in Appendix M. In a first step the temperature dependence of the microflakes' electrical resistance is studied. Three flakes show metallic $R(T_{bath})$ characteristics that can be fitted with the Bloch-Grüneisen relation. However, one flake shows semiconducting $R(T_{bath})$ characteristics. In a second step, the magnetoresistance of the microflakes in the low-field regime is presented.

9.1 Current state of research

The field of topological insulator (TI) experienced a lot of interest [20, 220, 221, 222] and the TI characteristics were predicted [106] and experimentally identified [107] in $Hg_{1-x}Cd_xTe$-based quantum well structures. In this system the edge states are a result of band inversion that is created due to the strong spin-orbit interaction of the electrons [223]. Later these characteristics were predicted [63] in 3D systems and observed in $Bi_{1-x}Sb_x$ [112]. However, since the band gap of $Bi_{1-x}Sb_x$ [112] is rather small and the surface structure rather complicated, the search for TIs with a larger band gap started and was found in the topological insulators of the second generation [224], such as Bi_2Te_3 and Bi_2Se_3 [111]. Besides the higher band gap of ~ 0.3 eV, which preserves the TI characteristics at room temperature, another advantage of Bi_2Se_3 over $Bi_{1-x}Sb_x$ is the stoichiometry that is a pure compound rather than an alloy and therefore tends to have higher purity and less disorder. Furthermore, only one surface state is present in Bi_2Se_3 and the electronic dispersion is similar to a single idealized Dirac cone [111] rather than including several different surface bands as in $Bi_{1-x}Sb_x$. Recent trends in the field of topological insulators aim for even higher band gaps to achieve a better separation of the edge states and bulk states. Bi_2Te_2Se [225, 226, 227] belongs to this new generation of TIs.

The interest in TIs is based on the time-reversal symmetry (TRS) protected topological surface states (TSS), that were detected by angle-resolved photoemission spectroscopy and scanning tunnel spectroscopy [112, 111, 228, 229, 230]. The TSS are predicted to have peculiar properties that can be exploited for future electronic devices in spintronics and quantum computation [231, 232, 233, 19, 234, 235]. The TSS of Bi_2Se_3 are associated with a Dirac cone in the band structure. In ARPES measurements [236] they can even be identified in the presence of Se vacancies, which dominate the defect chemistry of Bi_2Se_3 [237]. However, the identification of TSS becomes hampered in highly doped Bi_2Se_3 that show indications of layered 2D transport [238, 239, 27, 240]. Se vacancies are known to shift the Fermi energy of Bi_2Se_3 towards the bulk conduction band and may cause metallic $R(T_{\mathrm{bath}})$ characteristics [241, 242]. In contrast, semiconducting $R(T_{\mathrm{bath}})$ characteristics are expected if the Fermi energy is located between the bulk valence and bulk conduction band [243].

Another important feature of a TI's edge states is the spin-momentum locking of the electrons, which is connected to the TRS. This means that the spin eigenvalues of states with opposite momentum are also exactly opposite, so that an electron cannot backscatter into a state with opposite momentum due to spin mismatch. This prohibition of backscattering can also be expressed in terms of the Berry phase of π, a predominant property of massless Dirac fermions [221, 244]. Another consequence of the π Berry phase concerns the interference of time-reversed scattering paths. Weak localization (WL), a precursor of Anderson localization [65], occurs [245] in disordered materials. This effect describes the localization of electrons due to constructive interference of the electron wave functions between two time-reversed paths. However, acquiring a Berry phase of π before interfering causes the interference to become destructive, which leads to an anti-localization (WAL) effect [244]. Another reason for the occurrence of WAL instead of WL is a strong spin-orbit coupling (SOC) of a system, causing a spin rotation whenever an electron is scattered off an impurity [221]. In Bi_2Se_3 thin films WAL is frequently observed [246, 62, 247, 248, 249].

9.2 Temperature dependence of the electrical resistivity

As mentioned in Sec. 9.1, the defect chemistry in Bi_2Se_3 is dominated by Se vacancies that shift the Fermi energy towards the conduction band. This may cause the observation of a metallic-like temperature dependence of the electrical resistance $R(T_{\mathrm{bath}})$, as found in literature for Bi_2Se_3 bulk samples [250, 241], thin films [242, 251] and exfoliated nanoribbons with more than 50 QL [252]. ARPES measurements, performed by the group of Prof. Dr. Oliver Rader, can be consulted in Appendix L and show the Fermi energy of the investigated Bi_2Se_3 crystal to be located in the bulk conduction band probably due to Se vacancies. Before measuring the magnetoresistance $R(B)$ of the microflakes, the temperature dependence of the resistance $R(T_{\mathrm{bath}})$ is measured in this section.

Fig. 9.1 a) shows an optical micrograph of the microflake A. The thickness d of the microflakes is determined by using the confocal mode of the Sensofar Plμ Neox. The profile is taken only over areas that are covered with Au to prevent errors due to varying reflectivities. The corresponding profile is shown in Fig. 9.1 b) that gives information about the sample's thickness, found to be $d = (340 \pm 10)$ nm, and its homogeneity.

Fig. 9.2 shows the results of the measurement of the electrical resistance R for various bath temperatures T_{bath} in the range $T_{\mathrm{bath}} = 8$ K to $T_{\mathrm{bath}} = 300$ K for microflake A. An optical image of the flake is depicted in the inset of Fig. 9.2 which also shows the four-point measurement configuration. The electrical four-point resistance is obtained by measuring the linear V-I characteristics of the device. The lower right inset shows the V-I characteristics at bath temperatures $T_{\mathrm{bath}} =$ 13 K, 140 K and $T_{\mathrm{bath}} = 300$ K and proves the current and voltage contacts to be ohmic. The resistance translates into the resistivity $\rho = R \cdot dw/l$ with the width $w = (26 \pm 1)$ μm, the length $l = (39 \pm 1)$ μm and thickness d of the sample. The width w in this setup is the overlap of the microflake and the Au contacts that measure the voltage. The length l is determined by measuring the distance between

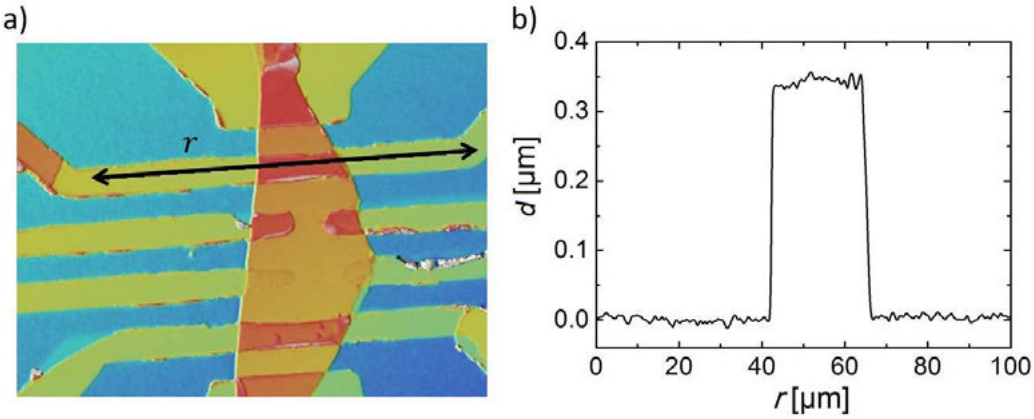

Figure 9.1: Profile along microflake A. a) Optical micrograph of microflake A that is taken in confocal mode of the Sensofar Plμ Neox. The black arrow highlights the line along the sample that is represented by the profile in b). The profile is measured along an Au contact line to minimize errors due to varying reflection coefficients. The profile indicates a homogeneous sample with a thickness of $d = (340 \pm 10)$ nm.

the voltage contacts. The measured four-point resistance decreases as the bath temperature T_{bath} decreases, which is a signature of metals. For metallic $R(T_{\mathrm{bath}})$ characteristics the Bloch-Grüneisen equation

$$\rho = \rho_0 + C_{\mathrm{BG}}(v_{\mathrm{F}})(\frac{T_{\mathrm{bath}}}{\Theta_{\mathrm{D}}})^5 I_5(\frac{\Theta_{\mathrm{D}}}{T_{\mathrm{bath}}}) \tag{9.1}$$

with the Debye temperature Θ_{D} and the residual resistance $\rho(T=0) = \rho_0$ is applied. The prefactor C_{BG} is a constant that depends on the Fermi velocity. In order to solve this equation for ρ, the integral

$$I_5(\frac{\Theta_{\mathrm{D}}}{T_{\mathrm{bath}}}) = \int_0^{\Theta_{\mathrm{D}}/T_{\mathrm{bath}}} \frac{x^5 \mathrm{d}x}{(e^x - 1)(1 - e^{-x})} \tag{9.2}$$

has to be solved. Eq. 9.1 is fitted to the measured $\rho(T_{\mathrm{bath}})$ and is presented by the solid black curve in Fig. 9.2. The free parameters return a residual resistivity of $\rho_0 = (3.2 \pm 0.1)$ μΩm. This yields a residual resistance ratio (RRR) of $\rho_{300\mathrm{K}}/\rho_0 \approx 1.7$, which is in fair agreement with what is found for bulk Bi_2Se_3 crystals [242] and films [241, 242]. The Debye temperature is found to be $\Theta_{\mathrm{D}} = (345 \pm 3)$ K. In order to verify that the measured $\rho(T_{\mathrm{bath}})$ values are not the result of a shortcut of the Ti/Au contacts, the temperature coefficient $\alpha(T_{\mathrm{bath}}) = R^{-1}\mathrm{d}R/\mathrm{d}T \approx 0.0018\ \mathrm{K}^{-1}$ for $T_{\mathrm{bath}} = 300$ K is evaluated. This is comparable to the $R(T_{\mathrm{bath}})$ characteristic of Bi_2Se_3 thin films of 120 nm thickness [242] from which a temperature coefficient

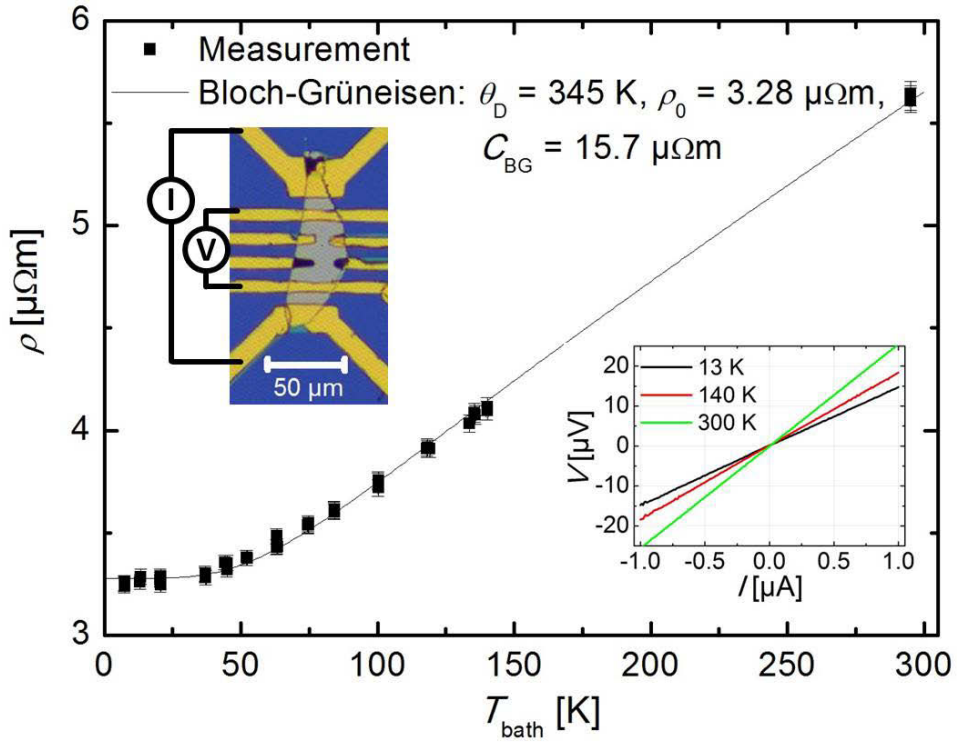

Figure 9.2: Temperature dependence of the resistivity of microflake A. Black squares are the measured four-point resistivity from linear V-I measurements. The solid line represents a Bloch-Grüneisen fit. The four-point measurement configuration, as well as an optical image of the contacted flake, is depicted in the inset in the upper left. Three examples of V-I characteristics for 13 K, 140 K and 300 K are given in the inset in the lower right.

of $\alpha_{300\,\mathrm{K}} \approx 0.002\ \mathrm{K}^{-1}$ can be determined. For a Bi_2Se_3 thin film with a thickness of 256 QL, i.e. of about 256 nm, the $R(T_{\mathrm{bath}})$ characteristic allows to estimate a temperature coefficient of $\alpha_{300\,\mathrm{K}} \approx 0.0018\ \mathrm{K}^{-1}$ [251]. For a Bi_2Se_3 thin film with thickness of about 45 QL the temperature coefficient can be estimated to be $\alpha_{300\,\mathrm{K}} \approx 0.0018\ \mathrm{K}^{-1}$ [253]. The temperature coefficient of gold thin films is found to be $\alpha_{300\mathrm{K,Au}} \approx 0.0034\ \mathrm{K}^{-1}$ at room temperature [254] and is clearly different from the temperature coefficient that is found for microflake A. Therefore it can be excluded that the measured metallic $\rho(T_{\mathrm{bath}})$ characteristic stems from the contact material.

Microflake B serves as another example of the microflake's metallic $R(T_{\mathrm{bath}})$ characteristic that can be fitted with Eq. 9.1. The electrical resistance is measured in a four-point configuration that is depicted in the inset of Fig. 9.3. Similar to microflake A, the measured four-point resistance R yields the electrical resistivity $\rho = R \cdot dw/l$ with the width $w = (20 \pm 1)$ µm, the length $l = (17 \pm 1)$ µm and the thickness $d = (130 \pm 7)$ nm of microflake B. The temperature dependence of the resistivity $\rho(T_{\mathrm{bath}})$ is depicted in Fig. 9.3. The Debye temperature is found to be $\Theta_{\mathrm{D}} = (402 \pm 5)$ K and the residual resistance is $\rho_0 = (3.0 \pm 0.1)$ µΩm, which yields a RRR of $\rho_{300\mathrm{K}}/\rho_0 \approx 1.8$. The temperature coefficient is $\alpha_{300\,\mathrm{K}} \approx 0.0018\ \mathrm{K}^{-1}$, as found for microflake A. The inset depicts the I-V characteristic at the bath temperatures 30 K and 122 K that show a linear behavior for $1.0\ \mu\mathrm{A} \geq |I| > 0.2\ \mu\mathrm{A}$. The non-linearity between I and V for $|I| \leq 0.2$ µA is due to the current contacts that do not form perfect ohmic contacts with the sample. This can be seen in two-point measurements between the current contacts (not shown here).

In addition to microflakes A and B in cooperation with Dr. Olivio Chiatti the

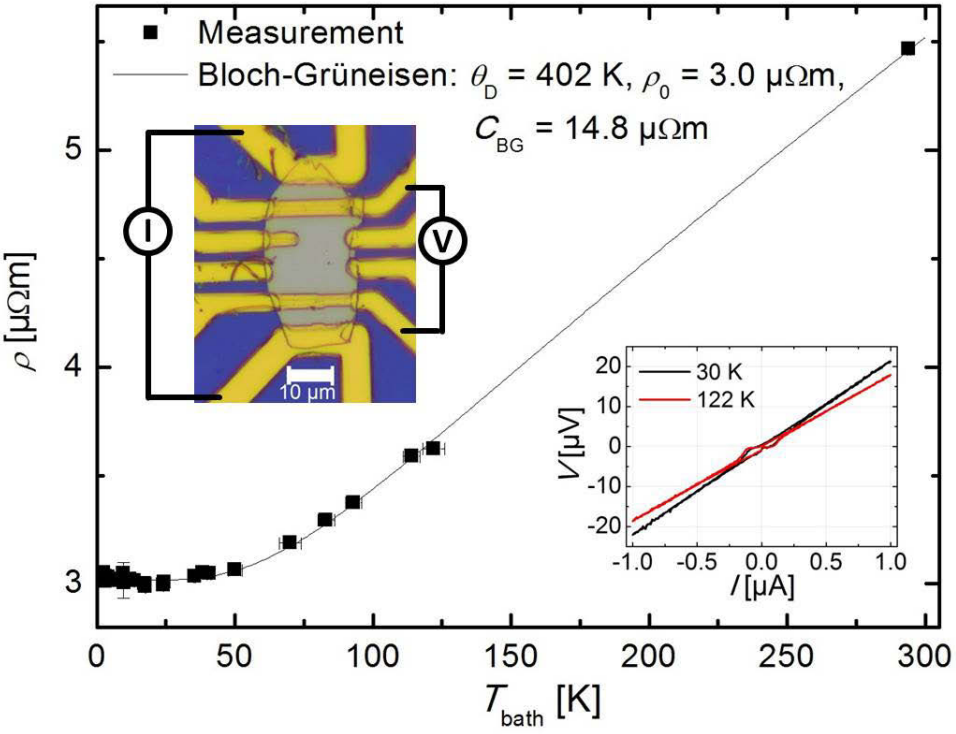

Figure 9.3: Temperature dependence of the resistivity of microflake B. Black squares are the measured resistivity from V-I measurements. The solid line represents a Bloch-Grüneisen fit. The four-point measurement configuration as well as an optical image of the contacted flake is depicted in the inset in the upper left. Three examples of V-I characteristics for 30 K and 122 K are given in the inset in the lower right.

microflakes C and D are investigated with respect to their $R(T_{\mathrm{bath}})$ characteristics and their $R(B)$ characteristics by means of lock-in measurements. Optical micrographs and a schematic of the measurement configuration are depicted in Fig. 9.4 a) for microflake C and in Fig. 9.4 c) for microflake D. The $R(T_{\mathrm{bath}})$ characteristics for microflake C are depicted in Fig. 9.4 b) and show a metallic behavior. Note that the longitudinal resistance R_{xx} is not translated into a resistivity due to Au shortcuts in the contact pattern that prevent four-point measurements. Fitting the measured $R(T_{\mathrm{bath}})$ to Eq. 9.1 yields a Debye temperature of $\Theta_{\mathrm{D}} = (420 \pm 10)$ K, which is comparable to microflake A and B. Furthermore, a residual resistance ratio of $\rho_{300\mathrm{K}}/\rho_0 \approx 1.3$ is identified. The metallic behavior of $R(T_{\mathrm{bath}})$ of the microflakes A, B and C are in agreement with recent findings in highly doped Bi_2Se_3 crystals [241]. Similar results were found in Bi_2Te_3 single crystals [255] and for a Bi_2Se_3 thin films [242, 253]. For microflake D the resistivity $\rho(T_{\mathrm{bath}})$ is calculated from the measured four-point resistance $R(T_{\mathrm{bath}})$ and the thickness $d = (220 \pm 10)$ nm, the length $l = (6 \pm 1)$ µm and the width $w = (5 \pm 1)$ µm. In Fig. 9.4 d) the semiconducting $\rho(T_{\mathrm{bath}})$ characteristic can be seen. Microflake D is exfoliated from the same Bi_2Se_3 crystal as microflakes A, B and C. Possible reasons for the semiconducting $R(T_{\mathrm{bath}})$ characteristic of microflake D are discussed in Sec. 9.4.

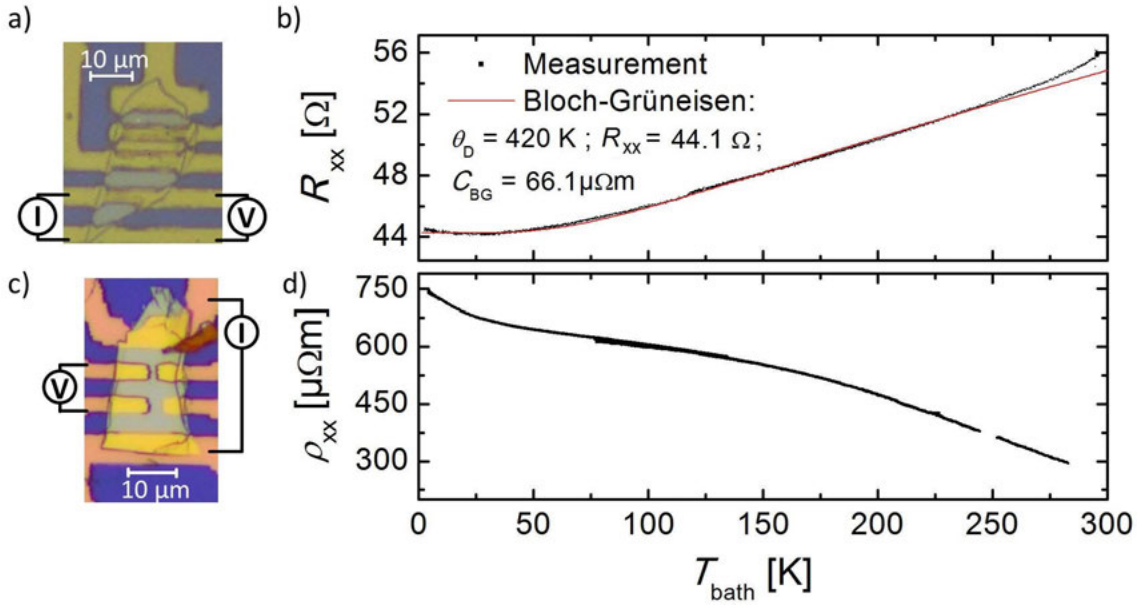

Figure 9.4: Measured temperature dependence of the resistance of b) microflake C and the resistivity of d) microflake D. For microflake C a Bloch-Grüneisen fit is applied (red solid line). A schematic of the corresponding measurement setup is depicted in an optical micrograph of a) microflake C and c) microflake D.

9.3 Magnetoresistance measurements of Bi_2Se_3 microflakes

In this section magnetoresistance measurements of the exfoliated Bi_2Se_3 microflakes are presented. The Au contact geometry of microflake A allows to perform Hall measurements, which can be seen in the optical micrograph in Fig. 9.5 a) together with a schematic of the measurement setup for $R_{xx} = V_x/I_x$ and $R_{xy} = V_y/I_I$. The Hall measurement is performed at $T_{bath} = 0.3$ K and is depicted in Fig. 9.5 b). The Hall resistance measurement $R_{xy}(B)$ can be used to derive the electron density

$$n = -\frac{BI_x}{dV_y e} = -\frac{B}{dR_{xy}e} = (1.8 \pm 0.1) \cdot 10^{19}\ \mathrm{cm}^{-3}. \tag{9.3}$$

The measured electron density is comparable to what is found in literature for Bi_2Se_3 flakes [239] and bulk single crystals [256, 257, 238] and is considered to indicate relatively high n-doping, probably due to Se vacancies. In order to derive the electron mobility, the longitudinal resistance $R_{xx} = V_x/I_x = (14.3 \pm 0.2)\ \Omega$ is measured. This translates into a resistivity of $\rho_{xx} = R_{xx} \cdot wd/l = (3.3 \pm 0.3)\ \mu\Omega$m with the width $w = (26 \pm 1)\ \mu$m, the length $l = (39 \pm 1)\ \mu$m and a thickness of $d = (340 \pm 10)$ nm. From this the electron mobility can be derived with

$$\mu = \frac{1}{\rho_{xx}(B=0)ne} = (1050 \pm 70)\ \mathrm{cm}^2/\mathrm{Vs}. \tag{9.4}$$

The $R_{xx}(B) = V_x(B)/I_x$ characteristics considerably varied over time, i.e. they were not reproducible. It is assumed that this is due to the measurement contacts that degraded over time.

Accordingly, microflake B is studied with respect to its four-point magnetoresistance at $T_{bath} = 0.3$ K. In Fig. 9.6 b) the longitudinal four-point magnetoresistance $R_{xx}(B)$ of microflake B is depicted for bath temperatures ranging from $T_{bath} = 0.3$ K to $T_{bath} = 10$ K. An optical micrograph of the microflake is shown in Fig. 9.6 a)

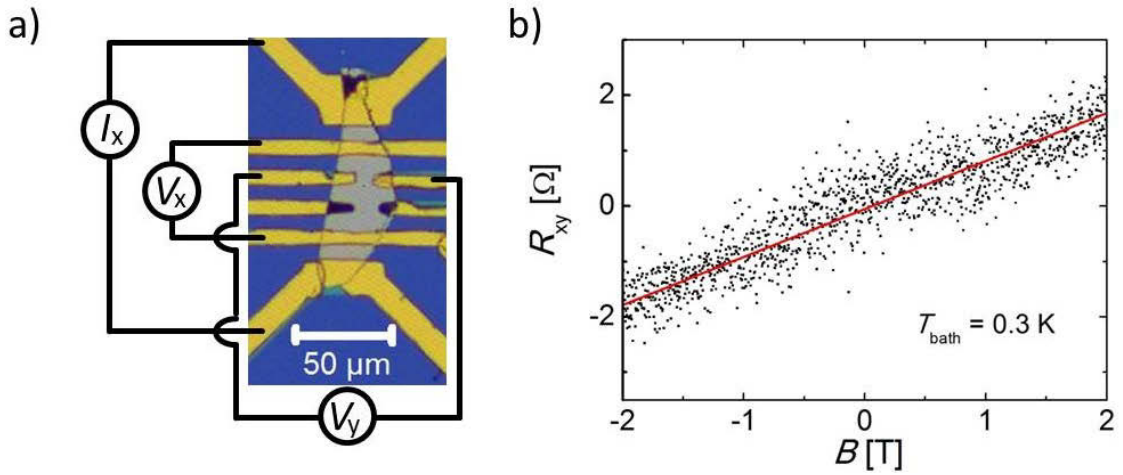

Figure 9.5: Magnetoresistance measurements of the Bi_2Se_3 microflake A. a) Optical micrograph of the microflake with a schematic of the four-point measurement setup. b) A Hall measurement at $T_{bath} = 0.3$ K is presented and allows the calculation of σ_{xx} and the determination of the electron density $n = (1.8 \pm 0.1) \cdot 10^{19}\ \mathrm{cm}^{-3}$ and the electron mobility $\mu = (1050 \pm 70)\ \mathrm{cm}^2/\mathrm{Vs}$.

together with the measurement configuration. The longitudinal magnetoresistance shows a cusp around $B = 0$ as well as a linear background, as can be seen in Fig. 9.6 b). The cusp is well pronounced for the low bath temperatures and becomes less pronounced as the bath temperature increases. The relative change of $R_{xx}(B)$ by the cusp is about 10 % at $T_{bath} = 0.3$ K. The reduction of the cusp's visibility at higher T_{bath} is a hallmark for the reduction of the phase coherence length that is observed in the weak anti-localization effect in Bi_2Se_3 thin films [258, 259]. The measurement at $T_{bath} = 10$ K does not show a cusp anymore, but the linear background only. Subtracting the measurement at $T_{bath} = 10$ K from the other measurements eliminates the linear background and leaves the cusp. The resulting magnetoresistance is then divided by $R_{xx}(B = 0)$, as depicted in Fig. 9.6 c), which makes the relative change of the magnetoresistance visible.

In order to identify whether the cusp for $T_{bath} < 10$ K is the result of weak anti-localization of electrons in the sample, the Hikami-Larkin-Nagaoka (HLN) equation [66] can be applied to the data. Therefore the electrical longitudinal conductance

$$\sigma_{xx,3D} = \frac{\rho_{xx}}{\rho_{xx}^2 + \rho_{xy}^2} \tag{9.5}$$

has to be calculated. This requires the knowledge of the resistance R_{xy} that is measured and depicted in Fig. 9.6 d) for $T_{bath} = 0.3$ K. Note that the slope dR_{xy}/dB is higher than the linear background in Fig. 9.6 a). The linear background may therefore stem from a R_{xy} component in the raw R_{xx} signal. The longitudinal resistivity is $\rho_{xx} = R_{xx} \cdot dw/l$ with the width $w = (20 \pm 1)$ µm, the thickness $d = (130 \pm 7)$ nm and the length $l = (17 \pm 1)$ µm. Accordingly, the Hall resistivity is calculated to $\rho_{xy} = R_{xy} \cdot dw'/l'$ with $l' = (20 \pm 1)$ µm and $w' = (5.0 \pm 0.5)$ µm, which is the thickness of the Au Hall contacts. The contribution of ρ_{xy} to σ_{xx} is about 1% and is therefore largely negligible. However, an electron density of $n = (1.28 \pm 0.03) \cdot 10^{19}$ cm^{-2} and an electron mobility of $\mu = (1660 \pm 80)$ cm^2/Vs can be calculated which are in fair agreement with n and μ of microflake A. Weak anti-localization is considered to be a 2D effect that is connected to the surface of the Bi_2Se_3 microflake. In order to calculate the 2D conductance $\sigma_{xx,2D}$, the 3D conductance is multiplied by the flake thickness, i.e. $\sigma_{xx,2D} \equiv \sigma_{xx} = \sigma_{xx,3D} \cdot d$. The resulting electrical conductivity σ_{xx} is expressed as change of the longitudinal electrical conductivity $\Delta\sigma_{xx} = \sigma_{xx}(B) - \sigma_{xx}(0)$, which is attributed to the WAL. As introduced in Sec. 2.4 for materials with a high spin-orbit coupling, the simplified version of the HLN equation

$$\Delta\sigma_{xx} = \alpha \frac{e^2}{2\pi^2\hbar}[\ln(\frac{B_\varphi}{B}) - \Psi(\frac{1}{2} + \frac{B_\varphi}{B})] \tag{9.6}$$

can be applied with the digamma function Ψ and the phase coherence characteristic magnetic field $B_\varphi = \hbar/4el_\varphi^2$ that depends on the phase coherence length l_φ. The prefactor α is set to be $\alpha = +1/2$ for weak anti-localization and to be $\alpha = -1$ for weak localization. The Eq. 9.6 is fitted to $\Delta\sigma_{xx}(B)$ for the bath temperatures $T_{bath} = 0.3$ K, 0.7 K, 0.9 K, 1.35 K and $T_{bath} = 1.5$ K. The fit to the data yields the free parameters α and l_φ.

The parameter α adopts values that exceed $\alpha_{WAL} = 0.5$, expected for weak anti-localization, by roughly two orders of magnitude. Recent investigations of the quantum Hall effect (QHE) in n-type highly doped, i.e. $n \geq 2 \cdot 10^{19}$ cm^{-3}, Bi_2Se_3 single crystals yield evidence for the sample acting as many parallel 2D electron

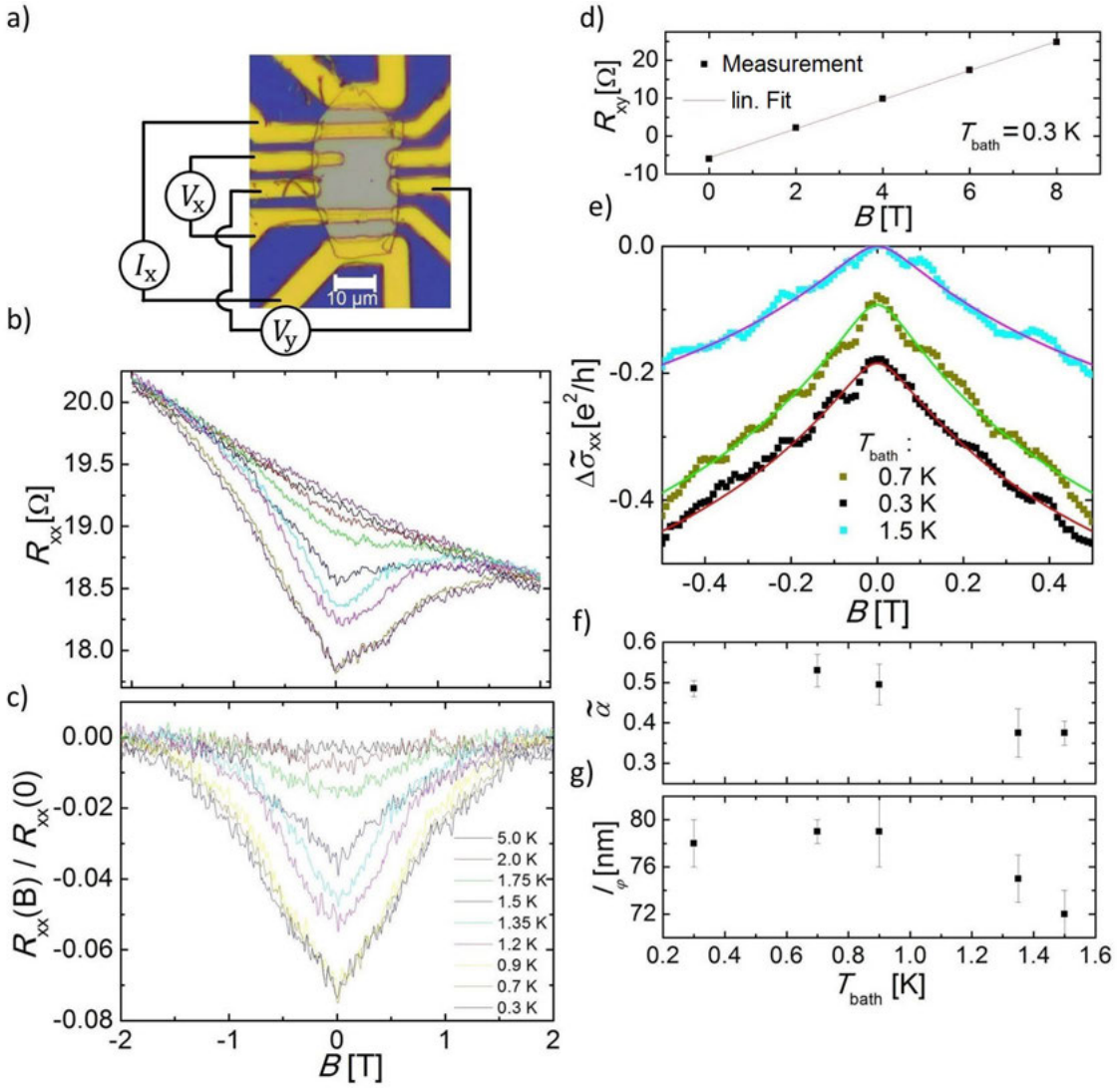

Figure 9.6: Magnetoresistance measurements of the Bi_2Se_3 microflake B. a) An optical micrograph of microflake B and the four-point measurement configuration. b) Four-point resistance measurement at bath temperatures $T_{\mathrm{bath}} = 0.3$ K to $T_{\mathrm{bath}} = 10$ K. A cusp is formed around $B = 0$ T that becomes less pronounced as T_{bath} increases and is not visible anymore at $T_{\mathrm{bath}} = 10$ K. The measurement at $T_{\mathrm{bath}} = 10$ K also shows a linear background. c) The magnetoresistance measurements are subtracted by the measurement $T_{\mathrm{bath}} = 10$ K in order to subtract the linear background. The measurements are then divided by the value at $B = 0$ T. d) An example of the Hall measurements is shown for $T_{\mathrm{bath}} = 0.3$ K and allows to calculate the electrical conductance σ_{xx} and to determine the electron density $n = (1.28 \pm 0.03) \cdot 10^{19}$ cm^{-3} and the electron mobility $\mu = (1660 \pm 80)$ cm^2/Vs. e) The change of the conductance $\Delta\tilde{\sigma}_{\mathrm{xx}} = \tilde{\sigma}_{\mathrm{xx}}(B) - \tilde{\sigma}_{\mathrm{xx}}(0) = [\sigma_{\mathrm{xx}}(B) - \sigma_{\mathrm{xx}}(0)]/65$ (see text) for $T_{\mathrm{bath}} = 0.3$ K, 0.7 K and $T_{\mathrm{bath}} = 1.5$ K is shown (squares) and fitted (solid lines) with the Hikami-Larkin-Nagaoka equation (HLN). The conductance change $\Delta\tilde{\sigma}_{\mathrm{xx}}$ for $T_{\mathrm{bath}} = 0.7$ K is shifted along the y-axis by $-0.1\ e^2/h$ and for $T_{\mathrm{bath}} = 0.3$ K by $-0.2\ e^2/h$ for a better visualization. The prefactor $\tilde{\alpha} = \alpha/65$ and the phase coherence length l_φ result as free parameters from the HLN fit and are depicted in f) and g).

systems. Each 2D electron system is understood to be represented by one QL of the sample [27, 260]. The resulting QHE is therefore interpreted to arise from the bulk of the sample rather than from the sample surface, which is supported by the fact that dividing the QHE conductance by the number of quintuple layers Z results in $\tilde{G} = 2e^2/NhZ$ with $N = 0,1,2...$. The bulk conduction is possible, since the high n doping due to Se vacancies causes the Fermi energy to shift from the band gap into bulk conduction band, as it is the case for the samples presented in this thesis (see Appendix L).

Following this approach the data are interpreted as the result of parallel 2D systems. Here, each second quintuple layer of the 130 nm thick microflake is considered to participate in the layered 2D transport. Hence, the prefactor α has to be divided by the number of participating quintuple layers. The thickness of a quintuple layer is about 1 nm, which yields 65 2D layers that contribute to the creation of the WAL cusp. The effective prefactor is then $\tilde{\alpha} = \alpha/65$ for each participating quintuple layer. Accordingly, the longitudinal conductivity of a single contributing QL is $\Delta\tilde{\sigma}_{xx} = \Delta\sigma_{xx}/65$. The HLN fits for $\Delta\tilde{\sigma}_{xx}$ that are shown in Fig. 9.6 e) are calculated with $\tilde{\alpha}$. The parameter B_φ in Eq. 9.6 determines the curvature of σ_{xx} and is independent of the prefactor α. Therefore l_φ is not affected by introducing the concept of layered 2D transport to $\Delta\sigma_{xx}$. For each temperature that is fitted with the HLN equation the free parameters l_φ and $\tilde{\alpha}$ are depicted in Fig. 9.6 f) and g).

The phase coherence length is $l_\varphi = (78 \pm 2)$ nm at $T_{\mathrm{bath}} = 0.3$ K, remains largely unchanged up to $T_{\mathrm{bath}} = 0.9$ K and subsequently decreases to $l_\varphi = (72 \pm 2)$ nm at $T_{\mathrm{bath}} = 1.5$ K. The decrease of l_φ with increasing T_{bath} is expected [261, 248] due to increasing thermal averaging of the electron phase and increasing inelastic scattering. The phase coherence length of microflake B is relatively small compared to $l_\varphi \approx 1.0$ µm, found in Bi_2Se_3 thin films with a thickness of 40 QL with $n \approx 1.0 \cdot 10^{19}$ cm^{-3} at $T_{\mathrm{bath}} = 1.8$ K [261], 45 QL with $n = 2.27 \cdot 10^{19}$ cm^{-3} at $T_{\mathrm{bath}} = 0.5$ K [259] and 100 QL with $n \approx 1.0 \cdot 10^{19}$ cm^{-3} at $T_{\mathrm{bath}} = 1.5$ K [249]. Furthermore, 10 QL thin films yield $B_\varphi = 4$ mT to $B_\varphi = 12$ mT l_φ at $T_{\mathrm{bath}} = 1.8$ K, i.e. $l_\varphi = \sqrt{\hbar/4eB_\varphi} \approx 202$ nm to $l_\varphi \approx 104$ nm depending on the sheet density. The phase coherence length in Bi_2Se_3 films is known to scale with the thickness d as $l_\varphi \propto d^\zeta$ with $\zeta \approx 0.7$ [249], which means that microflake B with $d = (130 \pm 7)$ nm should have a higher phase coherence length than the above mentioned thin films with few QL thickness, especially at $T_{\mathrm{bath}} = 0.3$ K.

The prefactor $\tilde{\alpha}$ in Fig. 9.6 f) reduces from $\tilde{\alpha}(T_{\mathrm{bath}} = 0.3\ \mathrm{K}) \approx 0.49$ to $\tilde{\alpha}(T_{\mathrm{bath}} = 1.5\ \mathrm{K}) \approx 0.37$. The reduction of α with increasing T_{bath} is in accordance with previous findings in Bi_2Se_3 thin films [248]. The reduction of the prefactor $|\alpha| < 0.5$ is interpreted in terms of a reduced effective number of phase coherent channels [248].

In cooperation with Dr. Olivio Chiatti the microflakes C and D are investigated with respect to their $R(B)$ characteristics. An optical micrograph of microflake C is depicted in Fig. 9.7 a) with the measurement configuration. Since most of the Au contacts have a shortcut to another Au contact, a two-terminal setup is chosen, as depicted in Fig. 9.7 a). The $R(B)$ measurement in Fig. 9.7 b) shows a cusp that modifies the magnetoresistance R_{xx} to lower values and is therefore attributed to weak anti-localization. Due to a lack of Hall contacts, measurements of R_{xy} were not possible. Therefore the conductivity of microflake C is calculated by $\sigma_{xx} = 1/\rho_{xx} = l/wR_{xx}$ with the width $w = 9.0$ µm and the length $l = 4.9$ µm.

Since the contribution of ρ_{xy} to σ_{xx} was found to be only 1% for microflake B, this approximation is considered to be justifiable.

In a next step Eq. 9.6 is fitted to the measured σ_{xx}. Similar to microflake B the prefactor α is found to exceed the expected prefactor $\alpha_{WAL} = 0.5$ by two orders of magnitude. Taking the contribution of every second QL to σ_{xx} into account results in $\Delta\tilde{\sigma}_{xx} = \sigma_{xx}/100$ and $\tilde{\alpha} = \alpha/100$. The HLN fits are depicted in Fig. 9.7 c). The prefactor $\tilde{\alpha}$ and the phase coherence length l_φ are depicted in Fig. 9.7 d) and e). The phase coherence length l_φ is roughly in accord with the thickness $d = (200 \pm 10)$ nm of microflake C at $T_{bath} = 0.3$ K. As T_{bath} increases l_φ decreases by about a half at $T_{bath} = 1.9$ K. The effective prefactor adopts the value $\tilde{\alpha} = 0.25 \pm 0.02$ at $T_{bath} = 0.3$ K and decreases down to $\tilde{\alpha} = 0.17 \pm 0.1$ at $T_{bath} = 0.8$ K, but slightly increases again at $T_{bath} = 1.9$ K.

An optical micrograph of microflake D is depicted in Fig. 9.8 a) and also shows the measurement four-point configuration. The contact pattern of microflake D also allows Hall measurements that yield an electron density of $n = 1.2 \cdot 10^{17}$ cm^{-3} and an electron mobility of $\mu_e = 675$ cm^2/Vs [260], both strongly reduced compared to

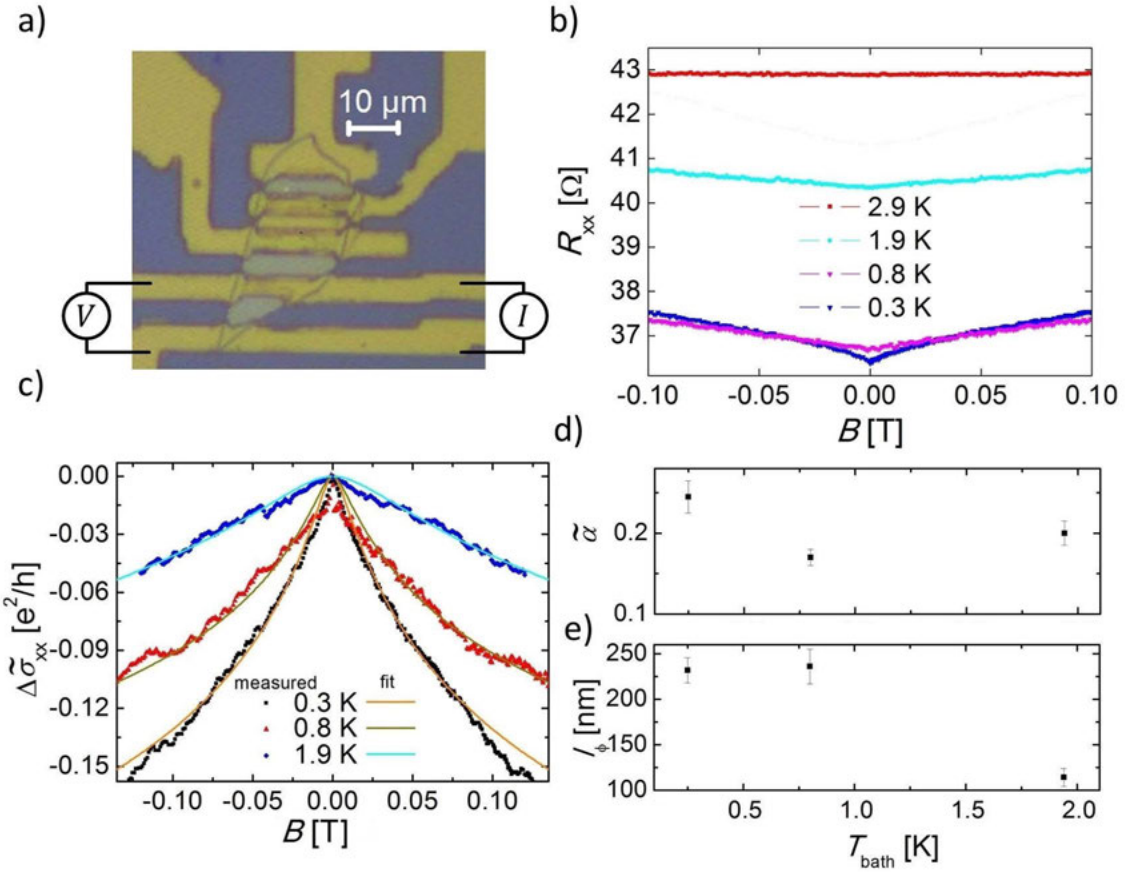

Figure 9.7: Magnetoresistance measurements of the Bi_2Se_3 microflake C. a) An optical micrograph of the microflake shows the measurement configuration. b) The magnetoresistance $R_{xx}(B)$ is depicted and shows a cusp around $B = 0$ T for $T_{bath} = 0.3$ K, 0.8 K and $T_{bath} = 1.9$ K. The cusp is not observed at $T_{bath} = 2.9$ K. c) The change of the conductivity $\Delta\tilde{\sigma}_{xx}(B) = \tilde{\sigma}_{xx}(B) - \tilde{\sigma}_{xx}(0)$ is shown (symbols). The solid lines represent the fit of the Hikami-Larkin-Nagaoka equation to the data. d) The prefactor $\tilde{\alpha}$ and e) the phase coherence length l_φ, derived from the HLN fit as free parameters, are presented.

those of the metallic microflakes A and B. The measured four-point longitudinal magnetoresistance R_{xx} in Fig. 9.8 b) shows cusps that are attributed to weak anti-localization. From the Hall measurements and R_{xx} the longitudinal conductance σ_{xx} is calculated and the HLN equation is fitted to $\Delta\sigma_{xx} = \sigma_{xx}(B) - \sigma_{xx}(0)$. The free parameters α and l_φ are depicted in Fig. 9.8 d). The phase coherence length l_φ is about 40 nm and remains relatively unchanged for all investigated T_{bath}. The prefactor is $\alpha = 0.50 \pm 0.03$ for $T_{bath} = 0.3$ K, as expected for WAL, and decreases down to $\alpha = 0.30 \pm 0.07$ at $T_{bath} = 1.9$ K.

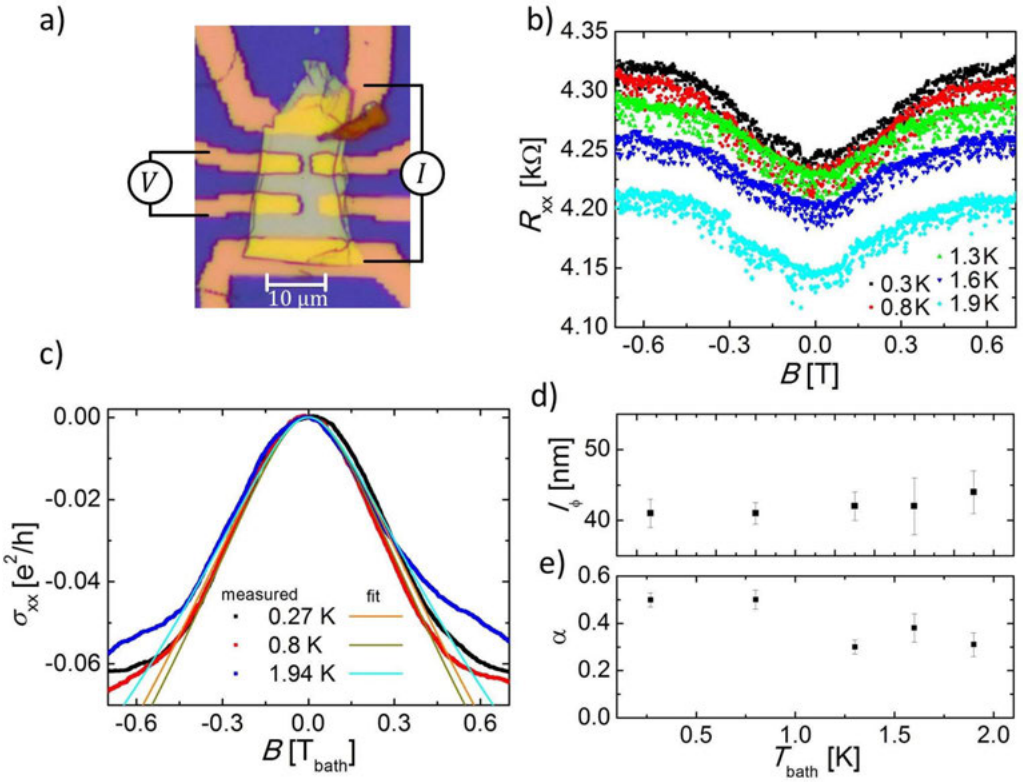

Figure 9.8: Magnetoresistance measurements of the Bi_2Se_3 microflake D. a) An optical micrograph of the microflake shows the four-point measurement configuration. b) The longitudinal four-point magnetoresistance $R_{xx}(B)$ is depicted and shows a cusp around $B = 0$ T for $T_{bath} = 0.3$ K, 0.8 K, 1.3 K, 1.6 K and $T_{bath} = 1.9$ K. c) The change of the conductivity $\Delta\sigma_{xx}(B) = \sigma_{xx}(B) - \sigma_{xx}(0)$ is shown (symbols). The solid lines represent the fit of the Hikami-Larkin-Nagaoka equation to the data. d) The prefactor α and e) the phase coherence length l_φ that are derived from the HLN fit as free parameters are presented.

9.4 Discussion of the layered 2D transport

In the last two sections four Bi_2Se_3 microflakes were investigated with respect to their $R(T_{\mathrm{bath}})$ and $R(B)$ characteristics. These microflakes were exfoliated from a bulk single crystal whose band structure is determined by ARPES measurements (see Appendix L). The ARPES measurements show a single Dirac cone in the Brillouin zone and reveal the nature of the topological surface states. The Bi_2Se_3 crystal is nominally undoped but Se vacancies typically lead to effective n-doping, which shifts the Fermi energy towards the bulk conduction band. This seems to be the case for the investigated Bi_2Se_3 crystals since the Fermi energy is located in the bulk conduction band and is considered to be the reason why the three microflakes A, B and C were found to have a metallic $R(T_{\mathrm{bath}})$ characteristic. A fit with the Bloch-Grüneisen equation yields a Debye temperature of $\Theta_{\mathrm{D}} = (345 \pm 3)$ K for microflake A, $\Theta_{\mathrm{D}} = (402 \pm 5)$ K for microflake B and $\Theta_{\mathrm{D}} = (420 \pm 10)$ K for microflake C. In literature the Debye temperature is rarely discussed for Bi_2Se_3. However, applying the Bloch-Grüneisen equation yields $\Theta_{\mathrm{D}} = (340 \pm 40)$ K for a 120 nm film of Bi_2Se_3 and $\Theta_{\mathrm{D}} = (370 \pm 10)$ K for a Bi_2Se_3 bulk crystal [242]. The residual resistance ratios of microflakes A, B and C ranging from $\rho_{300\mathrm{K}}/\rho_0 \approx 1.3$ to $\rho_{300\mathrm{K}}/\rho_0 \approx 1.8$ are all comparable to what is found in literature [241, 242]. Overall it can be said that the metallic $R(T_{\mathrm{bath}})$ characteristics that are measured for microflakes A, B and C are in fair agreement with what is found in literature.

Hall measurements yield electron densities of $n = (1.8 \pm 0.1) \cdot 10^{19}$ cm^{-3} for microflake A and $n = (1.28 \pm 0.03) \cdot 10^{19}$ cm^{-3} for microflake B. These electron densities are comparable to the electron density found for the bulk crystal, i.e. $n_{\mathrm{bulk}} = 1.9 \cdot 10^{19}$ cm^{-3}, by the group of Prof. Dr. Lada Yashina. The magnetoresistance $R(B)$ was modified by a cusp at $B = 0$ to lower values by about 7-10% for microflake B and C. The cusps are attributed to weak anti-localization. Fitting the HLN equation to the magnetoresistance suggests that multiple 2D layers, i.e. parallel conducting 2D systems, contribute to the measured electrical conductivity σ_{xx}. It is assumed that for microflakes B and C half of the QLs contribute to σ_{xx} since the prefactor α has to be divided by half the number of the flake's quintuple layers. Both the prefactor α and the phase coherence length l_φ tend to decrease as the bath temperature T_{bath} is increased for both microflakes.

For microflake D a semiconducting $R(T_{\mathrm{bath}})$ characteristic was found and a cusp at $B = 0$ in the $R(B)$ measurement was found to modify the resistance by about 1%. The cusp was fitted by the HLN equation and is attributed to weak anti-localization. In contrast to the metallic microflakes A, B and C for microflake D the prefactor α from the HLN equation is $\alpha = 0.50 \pm 0.03$ for $T_{\mathrm{bath}} = 0.3$ K, as expected for weak anti-localization without having to be divided by the number of QL. This suggests that the magnetotransport is dominated by the properties of the 2D surface states of microflake D. This picture fits well with the fact that microflake D is the only one that showed a semiconducting $R(T_{\mathrm{bath}})$ characteristic that is a hallmark for a topological insulator having its Fermi energy located in the gap. Similar to the previous investigations α decreases as T_{bath} increases until it reaches $\alpha = 0.31 \pm 0.05$ at $T_{\mathrm{bath}} = 1.9$ K. The fact that the semiconducting flake among the investigated microflakes is the only one that does show evidence for 2D single layer magnetotransport suggests that the additional 2D layers may be hosted by Se-depleted surface region. Microflake D is considered to be exfoliated from a bulk region of the Bi_2Se_3 where Se vacancies are by far less present than for microflakes

A, B and C.

Recent investigations [260] of the quantum Hall effect in a Bi_2Se_3 macroflake with thickness $d \approx 110$ µm at $T_{\mathrm{bath}} = 0.3$ K showed a Hall conductance σ_{xy} that aligns with multiples of e^2/h only if the σ_{xy} is divided by half the number of QL of the macroflake. The resulting conductance $\tilde{\sigma}_{\mathrm{xy}}$ is interpreted as the conductance per 2D layer. This result is similar to the result found by Cao *et. al.* [27] and similar to the results of the magnetoresistance measurements presented here.

Chapter 10

Summary

In the first part of this thesis $Al_xGa_{1-x}As/GaAs$ heterostructures are investigated with respect to their electrical transport properties and their noise spectra at temperatures of a few Kelvin. The $Al_xGa_{1-x}As/GaAs$ wafer were grown by the group of Prof. Dr. Andreas Wieck, whereas the structuring of the quantum devices was performed by Dr. Sven Buchholz, both at the Ruhr-University of Bochum. The investigations mainly aim to deduce information about the phase coherence of electrons in branched 1D waveguide networks that are formed to quantum rings. Preliminary investigations of the electrical transport and noise properties of non-branched 1D constrictions serve as reference for the more complicated quantum rings. Two of the quantum rings also host quantum point contacts (QPCs) for a better mode control. In addition, the heat flow of a quantum ring device in the presence of a temperature gradient is analyzed by means of thermal noise. The main results are listed in the following and will subsequently be described in more detail:

- **Effective mass:** Shubnikov-de Haas (SdH) measurements of a narrow heating structure yield an effective mass of $m_e^* = (0.057 \pm 0.005)m_0$ which is reduced compared to the GaAs bulk value $m_e^* = 0.067m_0$ [131].

- **Thermal subband spectroscopy:** A method is implemented that takes advantage of the shift of the threshold voltage V_{th} of a QPC when the bath temperature is increased. This shift allows to estimate the gate efficiency of a QPC's gate structure and therefore supports more traditional approaches of subband spectroscopy.

- **Excess noise:** In all investigated quantum ring devices the thermal noise exceeds the expectation value by up to 60 % at a bath temperature of $T_{bath} = 4.2$ K. This excess noise is reduced as the bath temperature is increased and is not observed anymore at $T_{bath} = 12$ K, as found for one quantum ring. Another quantum ring showed strongly reduced excess noise if either of the two arms is depleted by a top-gate. This excess noise is not observed in the 1D constrictions. A model is presented that attributes the excess noise to be a result of correlated noise sources, where each of the two ring arms represents one source of noise. In this model the correlation is considered to stem from phase coherent electrons.

- **Heat flow:** The measured noise spectra yield information about the increase of the electron temperature ΔT_e in the presence of a temperature gradient. The results indicate that ΔT_e is proportional to the square of the heating

current I_h and that electron-phonon coupling is not strong enough to mediate a measurable ΔT_e at $T_{bath} = 4.2$ K within the uncertainty of 0.2 K. The measurement of ΔT_e further indicates that the heat flow is linked to the electrical conductance, as stated by the Wiedemann-Franz relation. Wave packet simulations, performed by Dr. Tobias Kramer and Dr. Christoph Kreisbeck, support this picture and point to a potential asymmetry in the device that acts as switch for the electrical conductance and therefore for the heat flow.

- **Quantum interference:** Magnetoresistance oscillations are measured in quantum rings in the presence of a perpendicular magnetic field. From the period of these oscillations it is concluded that they can be explained in terms of the Aharonov-Bohm (AB) effect. The observability of the AB effect is found to strongly depend on the cooling process. Phase rigidity of the interfering electrons is found in an asymmetric quantum ring when a symmetric measurement setup is used.

In the second part of the thesis exfoliated Bi_2Se_3 microflakes are investigated with respect to their $R(T_{bath})$ and $R(B)$ characteristics. The crystal is grown by the group of Prof. Dr. Lada Yashina at the Moscow State University with the Bridgman technique. The main results are listed in the following:

- **Temperature dependence:** The $R(T_{bath})$ characteristics of three microflakes are found to be metallic which is attributed to Se vacancies in the material. In contrast, for one microflake the $R(T_{bath})$ characteristic is that of a semiconductor which is attributed to less Se vacancies in the material.

- **2D layered transport:** Microflakes with metallic $R(T_{bath})$ characteristics show cusps in their $R(B)$ characteristics that can be attributed to weak antilocalization (WAL). An evaluation with the Hikami-Larkin-Nagaoka model (HLN) suggests that the measured resistance is a result of parallel conduction of multiple 2D layers.

- **Semiconducting flake:** The microflake with the semiconducting $R(T_{bath})$ characteristics shows a WAL cusp in $R(B)$, which can be evaluated with the HLN model without assuming multiple 2D layers.

Electrical Characterization

Shubnikov-de Haas oscillations were measured in the narrow 2DEG of a quantum ring. A Dingle plot of the oscillation minima and maxima reveals a quantum lifetime of $\tau_q = 9.8 \cdot 10^{-13}$ s at $T_{bath} = 0.3$ K whose ratio to the elastic scattering time $\tau_e/\tau_q \approx 12$ suggests the dominant scattering mechanism to be long-range scattering from remote ionized impurities at $T_{bath} = 0.3$ K. This also holds at $T_{bath} = 4.2$ K with $\tau_q \approx 4.4 \cdot 10^{-13}$ s and $\tau_e/\tau_q \approx 27$ and is expected for modulation-doped $Al_xGa_{1-x}As/GaAs$ heterostructures at low temperatures [137]. The measured SdH oscillations yield an electron density of $n = (1.90 \pm 0.08) \cdot 10^{11}$ cm^{-2} at $T_{bath} = 4.2$ K and $n = (1.83 \pm 0.06) \cdot 10^{11}$ cm^{-2} at $T_{bath} = 0.3$ K which is both reduced compared to $n_{Wieck} = 2.07 \cdot 10^{11}$ cm^{-2}, measured by the group of Prof. Dr. Andreas Wieck at $T_{bath} = 4.2$ K. This deviation is attributed to the lateral confinement of 2 µm of the 2DEG. The effective mass is derived from the amplitude of the SdH oscillations at $T_{bath} = 0.3$ K and $T_{bath} = 4.2$ K and is found to be $m_e^* = (0.057 \pm 0.005)m_0$ which

is reduced compared to the GaAs bulk value $m^*_{\mathrm{e,\,GaAs}} = 0.067 m_0$ [131]. Studies of m^*_e in $\mathrm{Al_xGa_{1\text{-}x}As/GaAs}$ devices [133, 134] found a relation between m^*_e and the electron density n. Their studies indicate that $m^*_\mathrm{e} \approx 0.06\ m_0$ is to be expected for $n \approx 1.9 \cdot 10^{11}$ cm^{-2}, which fits $m^*_\mathrm{e} = (0.057 \pm 0.005) m_0$, measured in this thesis.

Measurements of the transconductance yield a gate efficiency of $\gamma = 11 \pm 3$ %, a subband spacing of $\hbar\omega_y = (11 \pm 2)$ meV as well as $\hbar\omega_x = (5 \pm 1)$ meV for the two subbands with the lowest energy for a single QPC with a width of $w \approx 100$ nm. Transconductance measurements of the QPCs with $w' \approx 170$ nm, incorporated in quantum rings, show a similar γ and $\hbar\omega_x$. The subband spacing of $\hbar\omega_y = (6.3 \pm 0.1)$ meV is reduced compared to the single QPC which is due to $w' > w$. In order to make the results from the subband spectroscopy more reliable, an additional approach to measure γ is chosen. This approach is based on the measurement of the threshold voltage V_th for various temperatures. The shift of V_th for a given thermal energy $k_\mathrm{B}T_\mathrm{bath}$ allows to estimate the gate efficiency γ when compared with the simulated $G(E_\mathrm{F}, T_\mathrm{bath})$. For the single QPC in the range 4.2 K $\leq T_\mathrm{bath} <$ 60 K this results in $\gamma = 16 \pm 3$ % and agrees with the result from the subband spectroscopy, i.e. $\gamma = 11 \pm 3$ %, within the measurement uncertainty. This method allows to measure with relatively low gate voltages, which is advantageous for devices that are susceptible to leakage currents. Furthermore, the gate efficiency can be deduced for devices with less pronounced conductance plateaus.

Measurements of the quantized conductance allowed to estimate the series resistance R_s of the 1D constrictions and the quantum rings. For the 1D constrictions the series resistance is found to be $R_\mathrm{s} = 142\ \Omega$ for the single QPC, $R_\mathrm{s} = 580\ \Omega$ for a bent 1D constriction and $R_\mathrm{s} = 710\ \Omega$ for a straight 1D constriction. For the quantum rings that host a QPC the series resistance is found to be $R_\mathrm{s} \approx 700\ \Omega$. In these cases the resistance of the waveguide structures dominates R_s which facilitates the evaluation of the noise spectra since the structures with higher resistances dominate the measured thermal noise.

Excess noise in quantum ring structures

Noise measurements were shown for all $\mathrm{Al_xGa_{1\text{-}x}As/GaAs}$-based 1D constrictions and quantum rings of this thesis at $T_\mathrm{bath} = 4.2$ K. The thermal noise $S_\mathrm{V,w}$, deduced from the measured noise spectra, is in accord with the calculated i.e. theoretically expected value $S_\mathrm{V,Th}$ for a single QPC, a straight 1D constriction and a bent 1D constriction. For the quantum ring devices the measured thermal noise $S_\mathrm{V,w}$ and the theoretically expected value $S_\mathrm{V,Th}$ did not agree with each other within the uncertainty limits at $T_\mathrm{bath} = 4.2$ K. The discrepancy $S_\mathrm{V,excess} = S_\mathrm{V,w} - S_\mathrm{V,Th}$ is referred to as 'excess noise' in this thesis and the relative excess noise is found to be $0 < S_\mathrm{V,excess}/S_\mathrm{V,Th} < 0.6$ for the investigated quantum rings. For one quantum ring finger gates allowed to deplete each of the two arms of the ring. If both arms are electrically conducting, the relative excess noise for this ring is found to be $0.3 < S_\mathrm{V,excess}/S_\mathrm{V,Th} < 0.6$. However, if either of the two arms of the ring is electrically non-conducting the relative excess noise is strongly reduced to $S_\mathrm{V,excess}/S_\mathrm{V,Th} = 0.1 \pm 0.1$. The assumption was made that the occurrence of the excess noise is linked to the interference of electrons in the quantum ring and should therefore be reduced at higher bath temperatures T_bath. The thermal noise $S_\mathrm{V,w}$ of a quantum ring was measured at $T_\mathrm{bath} > 4.2$ K. In this quantum ring it was possible to investigate an 1D constriction that is attached to the quantum ring. This 1D constriction

has the same width as the waveguides that form the quantum ring, but is not part of it. For this 1D waveguide no excess noise was observed. The excess noise of the quantum ring structure is measured for the temperatures 4.2 K $\leq T_{\mathrm{bath}} \leq$ 12 K and is found to decrease with increasing temperature. Noise measurements at $T_{\mathrm{bath}} = 12$ K, 20 K and $T_{\mathrm{bath}} = 30$ K did not show excess noise. The temperature dependence $S_{\mathrm{V,excess}}/S_{\mathrm{V,Th}}(T_{\mathrm{bath}})$ was compared to the ratio of the thermal length to the length of the quantum ring's longer arm $L_{\mathrm{T}}/L_{\mathrm{ring}}$ (T_{bath}). The thermal length serves as an upper limit for the phase coherence length since dephasing by electron-electron interaction is not taken into consideration. A distinction is made between the diffusive thermal length $L_{\mathrm{T,d}}$ and the ballistic thermal length $L_{\mathrm{T,b}}$. The excess noise is found to be $L_{\mathrm{T,b}}/L_{\mathrm{ring}} < S_{\mathrm{V,w}}/S_{\mathrm{V,Th}} < L_{\mathrm{T,d}}/L_{\mathrm{ring}}$ which is unexpected since the waveguides of this quantum ring are considered to be a ballistic system at $T_{\mathrm{bath}} = 4.2$ K. In an attempt to explain the occurrence of excess noise, the arms of the quantum ring are considered as correlated noise sources that are coupled to each other, whereas the coupling is mediated by phase coherent electrons. This would provide new possibilities to probe the phase coherence in a ring interferometer.

Heat flow in a quantum ring structure

The heat flow through a quantum ring device was studied out of thermal equilibrium. Along the quantum ring a temperature gradient was established by applying a heating current I_{h} in one part of the device while measuring the electron temperature T_{e} in another part of the device by means of thermal noise measurements. The measurements were performed at $T_{\mathrm{bath}} = 4.2$ K. Both parts of the device are connected by a waveguide that shows a quantization of the electrical conductance when sweeping the gate voltage V_{g}. The increase of the electron temperature ΔT_{e} was found to scale with I_{h}^2 for the gate voltages that showed the first three conductance plateaus of this waveguide, i.e. for $N = 1$, 2 and for $N = 3$. The relation $\Delta T_{\mathrm{e}} \propto \sqrt{N}$ was found which seems to contradict the results, obtained in a single 1D constriction where $\Delta T_{\mathrm{e,\,lit}} \propto N$ was observed [50, 161, 160]. Here, the measurement for $N = 0$ did not show an increase of T_{e}, which suggests that the electron-phonon interaction is not strong enough to mediate a direct exchange of heat between the electron reservoirs in this quantum ring device at $T_{\mathrm{bath}} = 4.2$ K. Further noise measurements in another part of the structure and the electrical conductance of the quantum ring's waveguides allowed to estimate qualitatively the rate of heat flow through the measurement device, when assuming the validity of the Wiedemann-Franz relation. This estimation and a wave packet analysis that is based on the Landauer-Büttiker approach, performed by Dr. Tobias Kramer and Dr. Christoph Kreisbeck, point towards a potential asymmetry in the quantum ring. This potential asymmetry reflects a portion of incoming electron waves and therefore acts as switch for the heat flow. This must not be confused with the intentional asymmetry of the quantum ring devices that is defined in the manufacturing. The additional, unintentional asymmetry qualitatively explains the deviation between the observed $T_{\mathrm{e}} \propto \sqrt{N}$ and $T_{\mathrm{e,\,lit}} \propto N$ that is observed in literature for single 1D constrictions.

Interference measurements in quantum rings

The magnetoresistance of multiple quantum ring devices was investigated in the presence of a magnetic field B in the range $-30\ \mathrm{mT} \leq B \leq 30\ \mathrm{mT}$. The magnetic field was applied perpendicularly to the 2DEG of each device. The measured four-point magnetoresistance oscillations at $T_{\mathrm{bath}} = 0.3$ K were identified to be Aharonov-Bohm oscillations due to the period of $\Delta B = 2$ mT that is in accord with the magnetic flux $\Phi_{\mathrm{m}} = h/e$, penetrating the enclosed area of the quantum rings. The visibility of the oscillations for the investigated devices is about 1 %, which is relatively low compared to the visibilities of about 3-5 % of etched quantum rings with similar size at $T_{\mathrm{bath}} = 0.3$ K [148] and comparable excitation current I_{Osc}. Etched two-terminal $\mathrm{Al_xGa_{1\text{-}x}As/GaAs}$-based quantum rings show visibilities of typically 10 % [146, 192] up to more than 50 % [210]. For one quantum ring device it was shown that the observability of the Aharonov-Bohm oscillations strongly depends on the cooling of the device. In addition, a modulation of the oscillation amplitude is observed. Whether this modulation can be described as beating, cannot be said without doubt since only two periods of this modulation appear in the chosen measurement range. Similar modulations are attributed to beating and are observed in electrostatically defined [215, 216] and in an etched [173] quantum ring made from a $\mathrm{Al_xGa_{1\text{-}x}As/GaAs}$ heterostructure. The beating can be interpreted in terms of different trajectories, resulting from multiple occupied conductor channels causing slightly different enclosed areas and thus different magnetic fluxes Φ_{m} [217]. The two-point differential conductance across a quantum ring with incorporated QPC shows fluctuations at $T_{\mathrm{bath}} = 0.3$ K when sweeping the gate voltage of a finger gate that covers the QPC. This makes the conductance plateaus of the QPC, observable at $T_{\mathrm{bath}} = 4.2$ K, hard to identify. These fluctuations are typically explained in terms of universal conductance fluctuations [146] or energy-dependent resonances [192, 138] in the quantum ring and are considered to be an indicator of phase coherent transport through the device. The magnetoresistance oscillations of this quantum ring were measured for seven gate voltages that correspond to the 1st and the 2nd conductance plateau of the QPC. When changing the gate voltage of the finger gate that covers the QPC, the magnetoresistance is found to change the electron phase either by 0 or by π. This is a typical hallmark of phase rigidity. The phase rigidity, observed in two- [187, 190, 191, 192] and four-terminal devices [148, 194], is accompanied by $R(B) = R(-B)$. Such a symmetry is roughly given around $B = 0$ for the observed magnetoresistance.

$R(T_{\mathrm{bath}})$ characteristic of $\mathrm{Bi_2Se_3}$ microflakes

Nominally undoped $\mathrm{Bi_2Se_3}$ microflakes were exfoliated and contacted with an Au contact pattern by means of optical lithography. ARPES measurements, performed by the group of Prof. Dr. Oliver Rader at BESSY II - Helmholtz-Zentrum Berlin, confirmed the existence of the topological edge states in the source crystal. However, the ARPES measurements also revealed that the Fermi energy is located inside the bulk conduction band. In a first step the $R(T_{\mathrm{bath}})$ measurement was presented and found to be metallic for the two microflakes A and B. A fit to the Bloch-Grüneisen relation yields a residual resistance ratio of $\rho_{300\mathrm{K}}/\rho_0 \approx 1.7$ for microflake A and $\rho_{300\mathrm{K}}/\rho_0 \approx 1.8$ for microflake B and a Debye temperature of $\Theta_{\mathrm{D}} = (345 \pm 3)$ K for microflake A and $\Theta_{\mathrm{D}} = (402 \pm 5)$ K for microflake B. The temperature coefficient is evaluated for the linear regime of T_{bath} and is $\alpha \approx 0.0018\ \mathrm{K}^{-1}$ at $T_{\mathrm{bath}} = 300$ K

for microflake A and B. This is comparable to what is found for Bi_2Se_3 thin films [242, 251, 253].

In cooperation with Dr. Olivio Chiatti two further microflakes, C and D, were investigated in the same manner. Microflake C has a metallic and microflake D has a semiconducting $R(T_{\mathrm{bath}})$ characteristic. A possible conclusion is that the Fermi energy of microflakes A, B and C is located in the bulk conduction band. In ARPES measurements, performed by the group of Prof. Dr. Oliver Rader, it can be seen that this is actually the case for the source crystal which is probably due to Se vacancies. It is assumed that the Se vacancies are less present in microflake D due to exfoliating from a bulk region of the source crystal that is relatively free from Se vacancies. A fit to the Bloch-Grüneisen relation allowed to find $\rho_{300\mathrm{K}}/\rho_0 \approx 1.2$ and $\Theta_{\mathrm{D}} = (420 \pm 10)$ K for microflake C. The residual resistance ratios and the Debye temperatures of the microflakes A, B and C are in fair agreement with what is found in literature for Bi_2Se_3 thin films and bulk [242, 241].

Magnetotransport properties of Bi_2Se_3 microflakes

The four-point measurement of the magnetoresistance at low magnetic fields, i.e. $-2\ \mathrm{T} < B < 2\ \mathrm{T}$, shows a cusp that modifies the magnetoresistance to negative values around $B = 0$ by about 10 % for microflake B which is interpreted as WAL by applying the HLN [66] equation. One of the two free parameters from the HLN fit is the prefactor α that is found to be about two orders of magnitude higher than expected for $\alpha_{\mathrm{WAL}} = 0.5$. Following the approach by Cao *et. al.* [27], the magnetoresistance is interpreted as the result of parallel 2D systems. In the case of microflake B every second quintuple layer (QL) is considered to be one of these 2D systems. A similar result is found for a macroflake with the thickness $d \approx 110\ \mu\mathrm{m}$ [260] where the conductivity matches multiples of e^2/h when every second QL is considered to be one of many parallel conducting 2D systems, i.e. when the conductivity is divided by half the number of the sample's QL. Hall measurements yield $n = (1.8 \pm 0.1) \cdot 10^{19}\ \mathrm{cm}^{-3}$ for microflake A and $n = (1.28 \pm 0.03) \cdot 10^{19}\ \mathrm{cm}^{-3}$ for microflake B at $T_{\mathrm{bath}} = 0.3$ K which is comparable to Bi_2Se_3 flakes [239] and bulk single crystals [256, 257, 238] with relatively high n-doping, probably due to Se vacancies. The measured electron mobility is found to be $\mu = (1050 \pm 70)\ \mathrm{cm}^2/\mathrm{Vs}$ for microflake A and $\mu_{\mathrm{e}} = (1660 \pm 80)\ \mathrm{cm}^2/\mathrm{Vs}$ for microflake B.

The microflakes C and D each show a cusp in the magnetoresistance that indicates WAL. Microflake C was found to show the same indications for 2D layered transport as microflake B where each second QL represents one 2D system. In contrast to microflakes B and C, the HLN fit to the cusp of the semiconducting microflake D yields a prefactor that matches $\alpha_{\mathrm{WAL}} = 0.5$, as expected for WAL.

The semiconducting $R(T_{\mathrm{bath}})$ characteristic and the fact that applying the HLN fit does not show indications of 2D layered transport supports the assumption that the Fermi energy is located between the bulk valence band and the bulk conduction band for microflake D. This causes the measured magnetoresistance to be dominated by the topological surface states of the Bi_2Se_3 microflake. As mentioned above, the ARPES measurements of the source crystal confirm the Fermi energy to be inside of the bulk conduction band, probably due to Se vacancies. The semiconducting microflake D however, is considered to be exfoliated from a bulk region of the source crystal where less Se vacancies are present and the Fermi energy is therefore lower.

For the microflakes B, C and D the prefactor α decreases as T_{bath} increases in

the range 0.3 K $\leq T_{\mathrm{bath}} <$ 2.0 K. The reduction of α with increasing T_{bath} is in accordance with previous findings in Bi_2Se_3 thin films [248] and is interpreted in terms of a reduced effective number of phase coherent channels [248].

The second free parameter from the HLN equation is the phase coherence length l_φ which is unaffected by applying the model of parallel conductance of layered 2D systems. For microflake C $l_\varphi \approx 230$ is in fair agreement with the flake's thickness $d = (200 \pm 10)$ nm and for the microflakes B $l_\varphi \approx 78$ nm is found to be about one half of the flake's thickness $d = (130 \pm 7)$ nm at $T_{\mathrm{bath}} = 0.3$ K. In the range 0.3 K $\leq T_{\mathrm{bath}} <$ 2.0 K l_φ is found to decrease as T_{bath} increases for microflakes B and C. For microflake D $l_\varphi \approx 40$ nm is found to be about one fifth of the flake's thickness $d = (220 \pm 10)$ nm at $T_{\mathrm{bath}} = 0.3$ K and appears to be constant in the range 0.3 K $\leq T_{\mathrm{bath}} <$ 2.0 K.

Chapter 11

Outlook

In the present thesis a ^{3}He cryostat was used for the measurements of the magnetoresistance of the Aharonov-Bohm effect at $T_{\mathrm{bath}} = 0.3$ K. A dilution refrigerator allows to reach temperatures of $T_{\mathrm{bath}} = 25$ mK and can increase the phase coherence length in the quantum rings. This enhances the visibility of the Aharonov-Bohm oscillations.

The quantum effects that were presented in this thesis are highly susceptible to external noise sources, such as the power grid. In order to further minimize the unwanted noise, an uninterruptible power supply (UPS) can be used to supply the measurement devices.

Excess noise in quantum rings can be further studied by using the schematic in Fig. 11.1. In contrast to the quantum ring devices used in this thesis, the two quantum rings have a difference in their circumferences. For this difference a factor of roughly two is proposed. The phase coherence length in the larger quantum ring is more likely to be too small to allow the observation of interference effects at a given bath temperature. If the excess noise in quantum rings is actually linked to the interference of electrons, the larger quantum ring should always show a smaller portion of excess noise than the smaller ring. Therefore, if the bath temperature is increased, the larger quantum ring should show no excess noise anymore at a certain bath temperature where the smaller ring still shows excess noise. Additional 1D waveguides act as leads to the quantum rings and also serve as reference system,

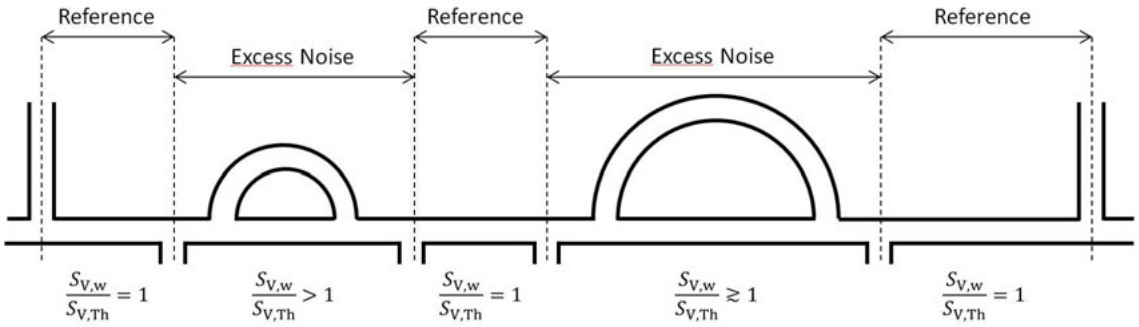

Figure 11.1: Schematic of a device that allows to further study excess noise in quantum rings. Two quantum rings with different circumferences are connected in series. Additional 1D waveguides act as leads and allow to study both quantum rings separately. If excess noise is linked to electron interference, it is expected to mainly occur in the smaller ring device.

i.e. no excess noise should occur there, as shown in this thesis. The device does not need a gate structure and should be kept as simple as possible to avoid additional noise from unknown sources.

The investigated Bi_2Se_3 microflakes were obtained by using exfoliation which only allows for a rough control of the obtained sample thickness. Since the thickness of the sample is a crucial parameter in the analysis of 2D layered transport, MBE-grown devices would be more suitable in the future.

References

[1] T. Young, "The Bakerian lecture: Experiments and calculations relative to physical optics", *Philosophical Transactions of the Royal Society of London*, vol. **94**, p. 1, 1804.

[2] E. Schrödinger, "Quantisierung als Eigenwertproblem", *Annalen der Physik*, vol. **385**, no. 13, p. 437, 1926.

[3] H. P. Stapp, "The Copenhagen interpretation", *American Journal of Physics*, vol. **40**, no. 8, p. 1098, 1972.

[4] F. Schwabl, *Quantenmechanik*. Springer-Verlag, 2013.

[5] G. Ludwig, *Die Grundlagen der Quantenmechanik*, vol. **70**. Springer-Verlag, 2013.

[6] Y. Aharonov and D. Bohm, "Significance of electromagnetic potentials in the quantum theory", *Physical Review*, vol. **115**, no. 3, p. 485, 1959.

[7] G. Bergmann, "Weak localization in thin films: a time-of-flight experiment with conduction electrons", *Physics Reports*, vol. **107**, no. 1, p. 1, 1984.

[8] E. Abrahams, P. W. Anderson, D. C. Licciardello, and T. V. Ramakrishnan, "Scaling theory of localization: Absence of quantum diffusion in two dimensions", *Physical Review Letters*, vol. **42**, no. 10, p. 673, 1979.

[9] G. Bergmann, "Weak anti-localization—an experimental proof for the destructive interference of rotated spin 1/2", *Solid State Communications*, vol. **42**, no. 11, p. 815, 1982.

[10] V. N. Lutskii, "Quantum size effect—present state and perspectives of experimental investigations", *physica status solidi (a)*, vol. **1**, no. 2, p. 199, 1970.

[11] B. J. van Wees, H. van Houten, C. W. J. Beenakker, *et al.*, "Quantized conductance of point contacts in a two-dimensional electron gas", *Physical Review Letters*, vol. **60**, no. 9, p. 848, 1988.

[12] D. A. Wharam, T. J. Thornton, R. Newbury, *et al.*, "One-dimensional transport and the quantisation of the ballistic resistance", *Journal of Physics C: Solid State Physics*, vol. **21**, no. 8, p. L209, 1988.

[13] A. Y. Cho, "Film deposition by molecular-beam techniques", *Journal of Vacuum Science & Technology*, vol. **8**, no. 5, p. S31, 1971.

[14] H. Kroemer, "Nobel lecture: Quasielectric fields and band offsets: Teaching electrons new tricks", *Reviews of Modern Physics*, vol. **73**, no. 3, p. 783, 2001.

[15] Z. I. Alferov, "Nobel lecture: The double heterostructure concept and its applications in physics, electronics, and technology", *Reviews of Modern Physics*, vol. **73**, no. 3, p. 767, 2001.

[16] L. Pfeiffer, K. W. West, H. L. Stormer, and K. W. l. Baldwin, "Electron mobilities exceeding 107 cm^2/Vs in modulation-doped GaAs", *Applied Physics Letters*, vol. **55**, no. 18, p. 1888, 1989.

[17] C. T. Foxon, J. J. Harris, D. Hilton, J. Hewett, and C. Roberts, "Optimisation of (Al, Ga) As/GaAs two-dimensional electron gas structures for low carrier densities and ultrahigh mobilities at low temperatures", *Semiconductor Science and Technology*, vol. **4**, no. 7, p. 582, 1989.

[18] K. v. Klitzing, G. Dorda, and M. Pepper, "New method for high-accuracy determination of the fine-structure constant based on quantized Hall resistance", *Physical Review Letters*, vol. **45**, no. 6, p. 494, 1980.

[19] J. E. Moore, "The birth of topological insulators", *Nature*, vol. **464**, no. 7286, p. 194, 2010.

[20] M. Z. Hasan and C. L. Kane, "Colloquium: topological insulators", *Reviews of Modern Physics*, vol. **82**, no. 4, p. 3045, 2010.

[21] F. D. M. Haldane, "Model for a quantum Hall effect without Landau levels: Condensed-matter realization of the "parity anomaly"", *Physical Review Letters*, vol. **61**, no. 18, p. 2015, 1988.

[22] D. J. Thouless, M. Kohmoto, M. P. Nightingale, and M. Den Nijs, "Quantized Hall conductance in a two-dimensional periodic potential", *Physical Review Letters*, vol. **49**, no. 6, p. 405, 1982.

[23] A. Y. Kitaev, "Fault-tolerant quantum computation by anyons", *Annals of Physics*, vol. **303**, no. 1, p. 2, 2003.

[24] A. Bertoni, P. Bordone, R. Brunetti, C. Jacoboni, and S. Reggiani, "Quantum logic gates based on coherent electron transport in quantum wires", *Physical Review Letters*, vol. **84**, no. 25, p. 5912, 2000.

[25] M. J. Gilbert, R. Akis, and D. K. Ferry, "Magnetically and electrically tunable semiconductor quantum waveguide inverter", *Applied Physics Letters*, vol. **81**, no. 22, p. 4284, 2002.

[26] T. A. Fulton and G. J. Dolan, "Observation of single-electron charging effects in small tunnel junctions", *Physical Review Letters*, vol. **59**, no. 1, p. 109, 1987.

[27] H. Cao, J. Tian, I. Miotkowski, *et al.*, "Quantized Hall effect and Shubnikov–de Haas oscillations in highly doped Bi_2Se_3: Evidence for layered transport of bulk carriers", *Physical Review Letters*, vol. **108**, no. 21, p. 216803, 2012.

[28] T. Ando, A. B. Fowler, and F. Stern, "Electronic properties of two-dimensional systems", *Reviews of Modern Physics*, vol. **54**, no. 2, p. 437, 1982.

[29] J. J. Harris, J. A. Pals, and R. Woltjer, "Electronic transport in low-dimensional structures", *Reports on Progress in Physics*, vol. **52**, no. 10, p. 1217, 1989.

[30] S. Datta, *Electronic transport in mesoscopic systems*. Cambridge University Press, 1997.

[31] D. Ferry and S. M. Goodnick, *Transport in Nanostructures*. No. 6, Cambridge University Press, 1997.

[32] J. H. Davies, *The Physics of Low-Dimensional Semiconductors: An Introduction*. Cambridge: Cambridge University Press, 1998.

[33] C. W. J. Beenakker and H. van Houten, "Quantum transport in semiconductor nanostructures", *Solid State Physics*, vol. **44**, p. 1, 1991.

[34] R. Landauer, "Spatial variation of currents and fields due to localized scatterers in metallic conduction", *IBM Journal of Research and Development*, vol. **1**, no. 3, p. 223, 1957.

[35] M. Büttiker, "Four-terminal phase-coherent conductance", *Physical Review Letters*, vol. **57**, no. 14, p. 1761, 1986.

[36] D. M. I., *Spin physics in semiconductors*. Berlin: Springer, 2008.

[37] P. A. Lee, A. D. Stone, and H. Fukuyama, "Universal conductance fluctuations in metals: Effects of finite temperature, interactions, and magnetic field", *Physical Review B*, vol. **35**, no. 3, p. 1039, 1987.

[38] R. Landauer, "Spatial variation of currents and fields due to localized scatterers in metallic conduction", *IBM Journal of Research and Development*, vol. **32**, p. 306, 1988.

[39] R. Landauer, "Electrical resistance of disordered one-dimensional lattices", *Philosophical Magazine*, vol. **21**, no. 172, p. 863, 1970.

[40] M. Büttiker, Y. Imry, R. Landauer, and S. Pinhas, "Generalized many-channel conductance formula with application to small rings", *Physical Review B*, vol. **31**, no. 10, p. 6207, 1985.

[41] R. de Picciotto, H. L. Stormer, L. N. Pfeiffer, K. W. Baldwin, and K. W. West, "Four-terminal resistance of a ballistic quantum wire", *Nature*, vol. **411**, no. 6833, p. 51, 2001.

[42] T. J. Thornton, M. Pepper, H. Ahmed, D. Andrews, and G. J. Davies, "One-dimensional conduction in the 2D electron gas of a GaAs-AlGaAs heterojunction", *Physical Review Letters*, vol. **56**, no. 11, p. 1198, 1986.

[43] A. D. Wieck and K. Ploog, "In-plane-gated quantum wire transistor fabricated with directly written focused ion beams", *Applied Physics Letters*, vol. **56**, no. 10, p. 928, 1990.

[44] P. E. Lindelof and M. Aagesen, "Measured deviations from the saddle potential description of clean quantum point contacts", *Journal of Physics: Condensed Matter*, vol. **20**, no. 16, p. 164207, 2008.

[45] L. I. Glazman, G. B. Lesovik, D. E. Khmel'Nitskii, and R. I. Shekhter, "Reflectionless quantum transport and fundamental ballistic-resistance steps in microscopic constrictions", *Soviet Journal of Experimental and Theoretical Physics Letters*, vol. **48**, p. 238, 1988.

[46] M. Büttiker, "Quantized transmission of a saddle-point constriction", *Physical Review B*, vol. **41**, no. 11, p. 7906, 1990.

[47] Y. M. Blanter and M. Büttiker, *Semiconductors and Semimetals*. Academic Press Inc, 2000.

[48] H. van Houten, C. W. J. Beenakker, and B. J. Van Wees, "Quantum point contacts", *Semiconductors and Semimetals*, vol. **35**, p. 9, 1992.

[49] P. N. Butcher, "Thermal and electrical transport formalism for electronic microstructures with many terminals", *Journal of Physics: Condensed Matter*, vol. **2**, no. 22, p. 4869, 1990.

[50] H. Van Houten, L. W. Molenkamp, C. W. J. Beenakker, and C. T. Foxon, "Thermo-electric properties of quantum point contacts", *Semiconductor Science and Technology*, vol. **7**, no. 3B, p. B215, 1992.

[51] G. L. Snider, M. S. Miller, M. J. Rooks, and E. L. Hu, "Quantized conductance in ballistic constrictions at 30 K", *Applied Physics Letters*, vol. **59**, no. 21, p. 2727, 1991.

[52] J. E. F. Frost, M. Y. Simmons, M. Pepper, *et al.*, "Temperature limits for ballistic quantization in a GaAs/AlGaAs one-dimensional constriction", *Journal of Physics: Condensed Matter*, vol. **5**, no. 44, p. L559, 1993.

[53] A. Kristensen, J. B. Jensen, M. Zaffalon, *et al.*, "Conductance quantization above 30 k in GaAlAs shallow-etched quantum point contacts smoothly joined to the background 2DEG", *Journal of Applied Physics*, vol. **83**, no. 1, p. 607, 1998.

[54] M. J. Kelly, "Transmission in one-dimensional channels in the heated electron regime", *Journal of Physics: Condensed Matter*, vol. **1**, no. 41, p. 7643, 1989.

[55] L. I. Glazman and A. V. Khaetskii, "Nonlinear quantum conductance of a point contact", *Journal of Experimental and Theoretical Physics Letters*, vol. **48**, p. 591, 1988.

[56] L. Martin-Moreno, J. T. Nicholls, N. K. Patel, and M. Pepper, "Non-linear conductance of a saddle-point constriction", *Journal of Physics: Condensed Matter*, vol. **4**, no. 5, p. 1323, 1992.

[57] N. K. Patel, J. T. Nicholls, L. Martn-Moreno, *et al.*, "Evolution of half plateaus as a function of electric field in a ballistic quasi-one-dimensional constriction", *Physical Review B*, vol. **44**, no. 24, p. 13549, 1991.

[58] K. J. Thomas, M. Y. Simmons, J. T. Nicholls, *et al.*, "Ballistic transport in one-dimensional constrictions formed in deep two-dimensional electron gases", *Applied Physics Letters*, vol. **67**, no. 1, p. 109, 1995.

[59] N. J. Curson, R. Nemutudi, N. J. Appleyard, *et al.*, "Ballistic transport in a $GaAs/Al_xGa_{1-x}As$ one-dimensional channel fabricated using an atomic force microscope", *Applied Physics Letters*, vol. **78**, no. 22, p. 3466, 2001.

[60] G. Apetrii, S. Fischer, U. Kunze, D. Reuter, and A. Wieck, "Influence of processing parameters on the transport properties of quantum point contacts fabricated with an atomic force microscope", *Semiconductor Science and Technology*, vol. **17**, no. 7, p. 735, 2002.

[61] H. Ibach and H. Lüth, *Festkörperphysik: Einführung in die Grundlagen.* Springer-Verlag, 2009.

[62] J. Chen, H. J. Qin, F. Yang, *et al.*, "Gate-voltage control of chemical potential and weak antilocalization in Bi_2Se_3", *Physical Review Letters*, vol. **105**, no. 17, p. 176602, 2010.

[63] L. Fu and C. L. Kane, "Topological insulators with inversion symmetry", *Physical Review B*, vol. **76**, no. 4, p. 045302, 2007.

[64] G. Matteucci and G. Pozzi, "New diffraction experiment on the electrostatic Aharonov-Bohm effect", *Physical Review Letters*, vol. **54**, no. 23, p. 2469, 1985.

[65] P. W. Anderson, "Absence of diffusion in certain random lattices", *Physical Review*, vol. **109**, no. 5, p. 1492, 1958.

[66] S. Hikami, A. I. Larkin, and Y. Nagoka, "Spin-orbit interaction and magnetoresistance in the two dimensional random system", *Progress of Theoretical Physics*, vol. **63**, no. 2, p. 707, 1980.

[67] J. B. Johnson, "Thermal agitation of electricity in conductors", *Physical Review*, vol. **32**, no. 1, p. 97, 1928.

[68] R. Kubo, "The fluctuation-dissipation theorem", *Reports on Progress in Physics*, vol. **29**, no. 1, p. 255, 1966.

[69] H. Nyquist, "Thermal agitation of electric charge in conductors", *Physical Review*, vol. **32**, no. 1, p. 110, 1928.

[70] C. Riha, P. Miechowski, S. S. Buchholz, *et al.*, "Mode-selected heat flow through a one-dimensional waveguide network", *Applied Physics Letters*, vol. **106**, no. 8, p. 083102, 2015.

[71] S. S. Buchholz, E. Sternemann, O. Chiatti, *et al.*, "Noise thermometry in narrow two-dimensional electron gas heat baths connected to a quasi-one-dimensional interferometer", *Physical Review B*, vol. **85**, no. 23, p. 235301, 2012.

[72] N. Wiener, "Generalized harmonic analysis", *Acta Mathematica*, vol. **55**, no. 1, p. 117, 1930.

[73] A. Khintchine, "Korrelationstheorie der stationären stochastischen prozesse", *Mathematische Annalen*, vol. **109**, no. 1, p. 604, 1934.

[74] Y. M. Blanter and M. Büttiker, "Shot noise in mesoscopic conductors", *Physics Reports*, vol. **336**, no. 1, p. 1, 2000.

[75] K. Hirakawa and H. Sakaki, "Energy relaxation of two-dimensional electrons and the deformation potential constant in selectively doped AlGaAs/GaAs heterojunctions", *Applied Physics Letters*, vol. **49**, no. 14, p. 889, 1986.

[76] Y. Y. Proskuryakov, J. T. Nicholls, D. I. Hadji-Ristic, A. Kristensen, and C. B. Sørensen, "Energy-loss rate of a two-dimensional electron gas measured using a mesoscopic thermometer", *Physical Review B*, vol. **75**, no. 4, p. 045308, 2007.

[77] J. P. Pekola, K. P. Hirvi, J. P. Kauppinen, and M. A. Paalanen, "Thermometry by arrays of tunnel junctions", *Physical Review Letters*, vol. **73**, no. 21, p. 2903, 1994.

[78] C. Kurdak, D. C. Tsui, S. Parihar, S. A. Lyon, and M. Shayegan, "Electron temperature in low-dimensional wires using thermal noise measurements", *Applied Physics Letters*, vol. **67**, no. 3, p. 386, 1995.

[79] F. N. Hooge, "1/f noise sources", *IEEE Transactions on Electron Devices*, vol. **41**, no. 11, p. 1926, 1994.

[80] A. Van der Ziel, *Noise in solid state devices and circuits.* Wiley-Interscience, 1986.

[81] C. D. Motchenbacher and J. A. Connelly, *Low noise electronic system design.* Wiley, 1993.

[82] W. Schottky, "Über spontane Stromschwankungen in verschiedenen Elektrizitätsleitern", *Annalen der Physik*, vol. **362**, no. 23, p. 541, 1918.

[83] V. P. Kunets, U. Müller, J. Dobbert, *et al.*, "Generation–recombination noise in doped-channel $Al_{0.3}Ga_{0.7}As/GaAs/In_{0.2}Ga_{0.8}As$ quantum well micro-Hall devices", *Journal of Applied Physics*, vol. **94**, no. 12, p. 7590, 2003.

[84] V. P. Kunets, W. Hoerstel, H. Kostial, *et al.*, "High electric field performance of $Al_{0.3}Ga_{0.7}As/GaAs$ and $Al_{0.3}Ga_{0.7}As/GaAs/In_{0.3}Ga_{0.7}As$ quantum well micro-Hall devices", *Sensors and Actuators A: Physical*, vol. **101**, no. 1, p. 62, 2002.

[85] P. M. Mooney, "Deep donor levels (DX centers) in III-V semiconductors", *Journal of Applied Physics*, vol. **67**, no. 3, p. R1, 1990.

[86] D. J. Chadi and K. J. Chang, "Theory of the atomic and electronic structure of DX centers in GaAs and $Al_xGa_{1-x}As$ alloys", *Physical Review Letters*, vol. **61**, no. 7, p. 873, 1988.

[87] D. Lang and R. Logan, "Large-lattice-relaxation model for persistent photoconductivity in compound semiconductors", *Physical Review Letters*, vol. **39**, no. 10, p. 635, 1977.

[88] K. S. Ralls, W. J. Skocpol, L. D. Jackel, *et al.*, "Discrete resistance switching in submicrometer silicon inversion layers: Individual interface traps and low-frequency (1/f?) noise", *Physical Review Letters*, vol. **52**, no. 3, p. 228, 1984.

[89] N. V. D'yakonova, M. E. Levinshtein, and S. L. Rumyantsev, "Nature of the bulk 1/f noise in GaAs and Si", *AIP Conference Proceedings*, vol. **285**, no. 1, p. 593, 1993.

[90] L. Ren and M. R. Leys, "1/f noise at room temperature in n-type GaAs grown by molecular beam epitaxy", *Physica B: Condensed Matter*, vol. **172**, no. 3, p. 319, 1991.

[91] M. Tacano, Y. Sugiyama, and H. Soga, "Device process dependence of low-frequency noise in GaAlAs/GaAs heterostructure", *Solid-State Electronics*, vol. **32**, no. 1, p. 49, 1989.

[92] S. Hashiguchi, N. Aoki, and H. Ohkubo, "Distribution of $1/f$ noise in an epitaxial GaAs mesfet", *Solid-State Electronics*, vol. **29**, no. 7, p. 745, 1986.

[93] P. Dutta and P. M. Horn, "Low-frequency fluctuations in solids: 1/f noise", *Reviews of Modern Physics*, vol. **53**, no. 3, p. 497, 1981.

[94] F. N. Hooge, "$1/f$ noise is no surface effect", *Physics Letters A*, vol. **29**, no. 3, p. 139, 1969.

[95] A. L. McWhorter, "1/f noise and germanium surface properties", *Semiconductor Surface Physics*, p. 207, 1957.

[96] G. Vasilescu, *Electronic noise and interfering signals: principles and applications*. Springer Science & Business Media, 2006.

[97] S. Adachi, *GaAs and related materials: bulk semiconducting and superlattice properties*. World Scientific, 1994.

[98] R. Dingle, H. L. Störmer, A. C. Gossard, and W. Wiegmann, "Electron mobilities in modulation-doped semiconductor heterojunction superlattices", *Applied Physics Letters*, vol. **33**, no. 7, p. 665, 1978.

[99] J. Whitaker, "Electrical properties of n-type aluminium arsenide", *Solid-State Electronics*, vol. **8**, no. 8, p. 649, 1965.

[100] M. E. Straumanis and C. D. Kim, "Phase extent of gallium arsenide determined by the lattice constant and density method", *Acta Crystallographica*, vol. **19**, no. 2, p. 256, 1965.

[101] M. J. Kelly, *Low-dimensional semiconductors: materials, physics, technology, devices*, vol. **3**. Clarendon Press, 1995.

[102] J. Fujita, Y. Ohnishi, Y. Ochiai, and S. Matsui, "Ultrahigh resolution of calixarene negative resist in electron beam lithography", *Applied Physics Letters*, vol. **68**, no. 9, p. 1297, 1996.

[103] H. Van Houten, B. J. Van Wees, M. G. J. Heijman, and J. P. Andre, "Submicron conducting channels defined by shallow mesa etch in GaAs-AlGaAs heterojunctions", *Applied Physics Letters*, vol. **49**, no. 26, p. 1781, 1986.

[104] C. L. Kane and E. J. Mele, "Quantum spin Hall effect in graphene", *Physical Review Letters*, vol. **95**, no. 22, p. 226801, 2005.

[105] C. L. Kane and E. J. Mele, "Z 2 topological order and the quantum spin Hall effect", *Physical Review Letters*, vol. **95**, no. 14, p. 146802, 2005.

[106] B. A. Bernevig, T. L. Hughes, and S.-C. Zhang, "Quantum spin Hall effect and topological phase transition in HgTe quantum wells", *Science*, vol. **314**, no. 5806, p. 1757, 2006.

[107] M. König, S. Wiedmann, C. Brüne, *et al.*, "Quantum spin Hall insulator state in HgTe quantum wells", *Science*, vol. **318**, no. 5851, p. 766, 2007.

[108] J. E. Moore and L. Balents, "Topological invariants of time-reversal-invariant band structures", *Physical Review B*, vol. **75**, no. 12, p. 121306, 2007.

[109] R. Roy, "Topological phases and the quantum spin Hall effect in three dimensions", *Physical Review B*, vol. **79**, no. 19, p. 195322, 2009.

[110] H. Zhang, C.-X. Liu, X.-L. Qi, *et al.*, "Topological insulators in Bi_2Se_3, Bi_2Te_3 and Sb_2Te_3 with a single Dirac cone on the surface", *Nature Physics*, vol. **5**, no. 6, p. 438, 2009.

[111] Y. Xia, D. Qian, D. Hsieh, *et al.*, "Observation of a large-gap topological-insulator class with a single Dirac cone on the surface", *Nature Physics*, vol. **5**, no. 6, p. 398, 2009.

[112] D. Hsieh, D. Qian, L. Wray, *et al.*, "A topological Dirac insulator in a quantum spin Hall phase", *Nature*, vol. **452**, no. 7190, p. 970, 2008.

[113] S. Nakajima, "The crystal structure of Bi_2Te_3- xSex", *Journal of Physics and Chemistry of Solids*, vol. **24**, no. 3, p. 479, 1963.

[114] J. Qi, X. Chen, W. Yu, *et al.*, "Ultrafast carrier and phonon dynamics in Bi_2Se_3 crystals", *Applied Physics Letters*, vol. **97**, no. 18, p. 182102, 2010.

[115] I. E. Abbott's, "Graphene: exploring carbon flatland", *Physics Today*, vol. **60**, no. 8, p. 35, 2007.

[116] M. C. Shaughnessy, N. C. Bartelt, J. A. Zimmerman, and J. D. Sugar, "Energetics and diffusion of gold in bismuth telluride-based thermoelectric compounds", *Journal of Applied Physics*, vol. **115**, no. 6, p. 063705, 2014.

[117] L. Duband, L. Clerc, E. Ercolani, L. Guillemet, and R. Vallcorba, "Herschel flight models sorption coolers", *Cryogenics*, vol. **48**, no. 3, p. 95, 2008.

[118] "From www.oxford-instruments.com downloaded on 28.04.2017",

[119] J. Pavelka, J. Sikula, M. Tacano, and M. Toita, "Activation energy of rts noise", *Radioengineering*, 2011.

[120] C. Dekker, A. J. Scholten, F. Liefrink, *et al.*, "Spontaneous resistance switching and low-frequency noise in quantum point contacts", *Physical Review Letters*, vol. **66**, no. 16, p. 2148, 1991.

[121] M. Sampietro, L. Fasoli, and G. Ferrari, "Spectrum analyzer with noise reduction by cross-correlation technique on two channels", *Review of Scientific Instruments*, vol. **70**, no. 5, p. 2520, 1999.

[122] M. Von Haartman and M. Östling, *Low-frequency noise in advanced MOS devices*. Springer Science & Business Media, 2007.

[123] C. Riha, "Thermisches rauschen in algaas/gaas nanostrukturen (master thesis)", 2013.

[124] L. W. Molenkamp, H. Van Houten, C. W. J. Beenakker, R. Eppenga, and C. T. Foxon, "Quantum oscillations in the transverse voltage of a channel in the nonlinear transport regime", *Physical Review Letters*, vol. **65**, no. 8, p. 1052, 1990.

[125] *Model SR830 DSP Lock-In Amplifier*.

[126] K. I. Inc., "Ac and dc current source 6221", 2015.

[127] K. I. Inc., "Nanovoltmeter 2182a", 2015.

[128] E. Sternemann, "Magnetotransportuntersuchungen an gaas/algaas-quantendrahtringstrukturen", 2010.

[129] L. Schubnikow and W. J. De Haas, "A new phenomenon in the change of resistance in a magnetic field of single crystals of bismuth.", *Nature*, vol. **126**, no. 3179, p. 500, 1930.

[130] R. W. Shaw and D. E. Hill, "Shubnikov-de Haas oscillations in n-type GaAs", *Physical Review B*, vol. **1**, no. 2, p. 658, 1970.

[131] S. M. Sze and K. K. Ng, *Physics of Semiconductor Devices*. John wiley & sons, 2006.

[132] A. T. Hatke, M. A. Zudov, J. D. Watson, *et al.*, "Evidence for effective mass reduction in GaAs/AlGaAs quantum wells", *Physical Review B*, vol. **87**, no. 16, p. 161307, 2013.

[133] P. T. Coleridge, M. Hayne, P. Zawadzki, and A. S. Sachrajda, "Effective masses in high-mobility 2d electron gas structures", *Surface Science*, vol. **361**, p. 560, 1996.

[134] Y.-W. Tan, J. Zhu, H. L. Stormer, *et al.*, "Measurements of the density-dependent many-body electron mass in two dimensional GaAs/AlGaAs heterostructures", *Physical Review Letters*, vol. **94**, no. 1, p. 016405, 2005.

[135] T. Ando, "Theory of quantum transport in a two-dimensional electron system under magnetic fields. iv. oscillatory conductivity", *Journal of the Physical Society of Japan*, vol. **37**, no. 5, p. 1233, 1974.

[136] J. P. Harrang, R. J. Higgins, R. K. Goodall, *et al.*, "Quantum and classical mobility determination of the dominant scattering mechanism in the two-dimensional electron gas of an AlGaAs/GaAs heterojunction", *Physical Review B*, vol. **32**, no. 12, p. 8126, 1985.

[137] C. Hamaguchi, *Basic semiconductor physics*. Springer Science & Business Media, 2009.

[138] S. S. Buchholz, "Kohärenter elektronentransport in eindimensionalen gaas/algaas nanostrukturen und quantenringen (dissertation)", 2011.

[139] J. B. Johnson, "The schottky effect in low frequency circuits", *Physical Review*, vol. **26**, no. 1, p. 71, 1925.

[140] M. B. Weissman, "1/f noise and other slow, nonexponential kinetics in condensed matter", *Reviews of Modern Physics*, vol. **60**, no. 2, p. 537, 1988.

[141] A. van der Ziel, X. Zhang, and A. H. Pawlikiewicz, "Location of 1/f noise sources in bjt's and hbjt's—i. theory", *IEEE Transactions on Electron Devices*, vol. **33**, no. 9, p. 1371, 1986.

[142] S. Jarrix, C. Delseny, F. Pascal, and G. Lecoy, "Noise correlation measurements in bipolar transistors. i. theoretical expressions and extracted current spectral densities", *Journal of Applied Physics*, vol. **81**, no. 6, p. 2651, 1997.

[143] X. N. Zhang and A. Van Der Ziel, "Correlation between thermoelectric $1f$ noise and current $1f$ noise in intrinsic germanium", *Physica B+ C*, vol. **124**, no. 1, p. 62, 1984.

[144] M. Reznikov, M. Heiblum, H. Shtrikman, and D. Mahalu, "Temporal correlation of electrons: Suppression of shot noise in a ballistic quantum point contact", *Physical Review Letters*, vol. **75**, no. 18, p. 3340, 1995.

[145] A. Kumar, L. Saminadayar, D. C. Glattli, Y. Jin, and B. Etienne, "Experimental test of the quantum shot noise reduction theory", *Physical Review Letters*, vol. **76**, no. 15, p. 2778, 1996.

[146] A. E. Hansen, A. Kristensen, S. Pedersen, C. B. Sørensen, and P. E. Lindelof, "Mesoscopic decoherence in Aharonov-Bohm rings", *Physical Review B*, vol. **64**, no. 4, p. 045327, 2001.

[147] K.-T. Lin, Y. Lin, C. C. Chi, *et al.*, "Temperature-and current-dependent dephasing in an Aharonov-Bohm ring", *Physical Review B*, vol. **81**, no. 3, p. 035312, 2010.

[148] S. S. Buchholz, S. F. Fischer, U. Kunze, *et al.*, "Control of the transmission phase in an asymmetric four-terminal Aharonov-Bohm interferometer", *Physical Review B*, vol. **82**, no. 4, p. 045432, 2010.

[149] B. J. LeRoy, A. C. Bleszynski, K. E. Aidala, *et al.*, "Imaging electron interferometer", *Physical Review Letters*, vol. **94**, no. 12, p. 126801, 2005.

[150] E. J. Heller, K. E. Aidala, B. J. LeRoy, *et al.*, "Thermal averages in a quantum point contact with a single coherent wave packet", *Nano Letters*, vol. **5**, no. 7, p. 1285, 2005.

[151] F. Carillo, G. Biasiol, D. Frustaglia, *et al.*, "$In_{0.75}Ga_{0.25}As$ on GaAs submicron rings and their application for coherent nanoelectronic devices", *Physica E: Low-dimensional Systems and Nanostructures*, vol. **32**, no. 1, p. 53, 2006.

[152] A. Yacoby, U. Sivan, C. P. Umbach, and J. M. Hong, "Interference and dephasing by electron-electron interaction on length scales shorter than the elastic mean free path", *Physical Review Letters*, vol. **66**, no. 14, p. 1938, 1991.

[153] A. Yacoby, M. Heiblum, H. Shtrikman, V. Umansky, and D. Mahalu, "Dephasing of ballistic electrons as a function of temperature and carrier density", *Semiconductor Science and Technology*, vol. **9**, no. 5S, p. 907, 1994.

[154] C. W. J. Beenakker, H. v. Houten, *et al.*, "Quantum point contacts", *Physics Today*, vol. **49**, no. 7, p. 22, 1996.

[155] K. K. Choi, D. C. Tsui, and K. Alavi, "Dephasing time and one-dimensional localization of two-dimensional electrons in $GaAs/Al_xGa_{1-x}As$ heterostructures", *Physical Review B*, vol. **36**, no. 14, p. 7751, 1987.

[156] T. Hiramoto, K. Hirakawa, Y. Iye, and T. Ikoma, "Phase coherence length of electron waves in narrow AlGaAs/GaAs quantum wires fabricated by focused ion beam implantation", *Applied Physics Letters*, vol. **54**, no. 21, p. 2103, 1989.

[157] M. Cassé, Z. D. Kvon, G. M. Gusev, *et al.*, "Temperature dependence of the Aharonov-Bohm oscillations and the energy spectrum in a single-mode ballistic ring", *Physical Review B*, vol. **62**, no. 4, p. 2624, 2000.

[158] B. L. Altshuler, A. G. Aronov, and D. E. Khmelnitsky, "Effects of electron-electron collisions with small energy transfers on quantum localisation", *Journal of Physics C: Solid State Physics*, vol. **15**, no. 36, p. 7367, 1982.

[159] G. Seelig and M. Büttiker, "Charge-fluctuation-induced dephasing in a gated mesoscopic interferometer", *Physical Review B*, vol. **64**, no. 24, p. 245313, 2001.

[160] S. Jezouin, F. D. Parmentier, A. Anthore, *et al.*, "Quantum limit of heat flow across a single electronic channel", *Science*, vol. **342**, no. 6158, p. 601, 2013.

[161] O. Chiatti, J. T. Nicholls, Y. Y. Proskuryakov, *et al.*, "Quantum thermal conductance of electrons in a one-dimensional wire", *Physical review letters*, vol. **97**, no. 5, p. 056601, 2006.

[162] U. Sivan and Y. Imry, "Multichannel Landauer formula for thermoelectric transport with application to thermopower near the mobility edge", *Physical Review B*, vol. **33**, no. 1, p. 551, 1986.

[163] C. Riha, O. Chiatti, S. S. Buchholz, *et al.*, "Heat flow, transport and fluctuations in etched semiconductor quantum wire structures", *physica status solidi (a)*, vol. **213**, no. 3, p. 571, 2016.

[164] J. R. Wendt, J. A. Simmons, J. S. Moon, *et al.*, "Dual-side electron beam lithography for independent submicron gating of double quantum well devices", *Semiconductor Science and Technology*, vol. **13**, no. 8A, p. A86, 1998.

[165] T. Kramer, C. Kreisbeck, C. Riha, *et al.*, "Thermal energy and charge currents in multi-terminal nanorings", *AIP Advances*, vol. **6**, no. 6, p. 065306, 2016.

[166] T. Kramer, C. Kreisbeck, and V. Krueckl, "Wave packet approach to transport in mesoscopic systems", *Physica Scripta*, vol. **82**, no. 3, p. 038101, 2010.

[167] J. B. Pendry, "Quantum limits to the flow of information and entropy", *Journal of Physics A: Mathematical and General*, vol. **16**, no. 10, p. 2161, 1983.

[168] C. R. Proetto, "Thermopower oscillations of a quantum-point contact", *Physical Review B*, vol. **44**, no. 16, p. 9096, 1991.

[169] F. N. Hooge, T. G. M. Kleinpenning, and L. K. J. Vandamme, "Experimental studies on 1/f noise", *Reports on Progress in Physics*, vol. **44**, no. 5, p. 479, 1981.

[170] R. G. Chambers, "Shift of an electron interference pattern by enclosed magnetic flux", *Physical Review Letters*, vol. **5**, no. 1, p. 3, 1960.

[171] R. A. Webb, S. Washburn, C. P. Umbach, and R. B. Laibowitz, "Observation of h/e Aharonov-Bohm oscillations in normal-metal rings", *Physical Review Letters*, vol. **54**, no. 25, p. 2696, 1985.

[172] S. Datta, M. R. Melloch, S. Bandyopadhyay, *et al.*, "Novel interference effects between parallel quantum wells", *Physical Review Letters*, vol. **55**, no. 21, p. 2344, 1985.

[173] G. Timp, A. M. Chang, J. E. Cunningham, *et al.*, "Observation of the Aharonov-Bohm effect for ω c $\tau >$ 1", *Physical Review Letters*, vol. **58**, no. 26, p. 2814, 1987.

[174] A. Bachtold, C. Strunk, J.-P. Salvetat, *et al.*, "Aharonov-Bohm oscillations in carbon nanotubes", *Nature*, vol. **397**, no. 6721, p. 673, 1999.

[175] S. Russo, J. B. Oostinga, D. Wehenkel, *et al.*, "Observation of Aharonov-Bohm conductance oscillations in a graphene ring", *Physical Review B*, vol. **77**, no. 8, p. 085413, 2008.

[176] H. Peng, K. Lai, D. Kong, *et al.*, "Aharonov-Bohm interference in topological insulator nanoribbons", *Nature Materials*, vol. **9**, no. 3, p. 225, 2010.

[177] C. Jönsson, "Elektroneninterferenzen an mehreren künstlich hergestellten feinspalten", *Zeitschrift für Physik*, vol. **161**, no. 4, p. 454, 1961.

[178] R. B. Leighton and M. L. Sands, *The Feynman Lectures on Physics: Quantum mechanics*, vol. **3**. Addison-Wesley Pub. Co., 1965.

[179] R. Bach, D. Pope, S.-H. Liou, and H. Batelaan, "Controlled double-slit electron diffraction", *New Journal of Physics*, vol. **15**, no. 3, p. 033018, 2013.

[180] L. Zehnder, "Ein neuer Interferenzrefraktor", *Zeitschrift für Instrumentenkunde*, vol. **11**, p. 275, 1891.

[181] L. Mach, "Über einen Interferenzrefraktor", *Zeitschrift für Instrumentenkunde*, vol. **12**, p. 89, 1892.

[182] J. C. Jamin, "Neuer Interferential-Refractor", *Annalen der Physik*, vol. **174**, no. 6, p. 345, 1856.

[183] Y. Ji, Y. Chung, D. Sprinzak, *et al.*, "An electronic Mach-Zehnder interferometer", *Nature*, vol. **422**, no. 6930, p. 415, 2003.

[184] E. Hecht and A. Zajac, "Optics, chap 3", 1987.

[185] W. Liang, M. Bockrath, D. Bozovic, *et al.*, "Fabry-Perot interference in a nanotube electron waveguide", *Nature*, vol. **411**, no. 6838, p. 665, 2001.

[186] P. A. Lee and A. D. Stone, "Universal conductance fluctuations in metals", *Physical Review Letters*, vol. **55**, no. 15, p. 1622, 1985.

[187] A. Yacoby, M. Heiblum, D. l. Mahalu, and H. Shtrikman, "Coherence and phase sensitive measurements in a quantum dot", *Physical Review Letters*, vol. **74**, no. 20, p. 4047, 1995.

[188] R. Schuster, E. Buks, M. Heiblum, *et al.*, "Phase measurement in a quantum dot via a double-slit interference experiment", *Nature*, vol. **385**, no. 6615, p. 417, 1997.

[189] S. Katsumoto, "Coherence and spin effects in quantum dots", *Journal of Physics: Condensed Matter*, vol. **19**, no. 23, p. 233201, 2007.

[190] M. Sigrist, T. Ihn, K. Ensslin, *et al.*, "Phase coherence in the inelastic cotunneling regime", *Physical Review Letters*, vol. **96**, no. 3, p. 036804, 2006.

[191] B. Grbić, R. Leturcq, T. Ihn, *et al.*, "Aharonov-Bohm oscillations in p-type GaAs quantum rings", *Physica E: Low-dimensional Systems and Nanostructures*, vol. **40**, no. 5, p. 1273, 2008.

[192] S. Pedersen, A. E. Hansen, A. Kristensen, C. B. Sørensen, and P. E. Lindelof, "Observation of quantum asymmetry in an Aharonov-Bohm ring", *Physical Review B*, vol. **61**, no. 8, p. 5457, 2000.

[193] L. Onsager, "Reciprocal relations in irreversible processes. II.", *Physical Review*, vol. **38**, no. 12, p. 2265, 1931.

[194] C. Kreisbeck, T. Kramer, S. S. Buchholz, *et al.*, "Phase shifts and phase π jumps in four-terminal waveguide Aharonov-Bohm interferometers", *Physical Review B*, vol. **82**, no. 16, p. 165329, 2010.

[195] M. Buttiker, "Symmetry of electrical conduction", *IBM Journal of Research and Development*, vol. **32**, no. 3, p. 317, 1988.

[196] G. F. Giuliani and J. J. Quinn, "Lifetime of a quasiparticle in a two-dimensional electron gas", *Physical Review B*, vol. **26**, no. 8, p. 4421, 1982.

[197] C. Hodges, H. Smith, and J. W. Wilkins, "Effect of Fermi surface geometry on electron-electron scattering", *Physical Review B*, vol. **4**, no. 2, p. 302, 1971.

[198] O. Chiatti, S. S. Buchholz, U. Kunze, *et al.*, "Electron waveguide interferometers for spin-dependent transport experiments", *physica status solidi (b)*, vol. **251**, no. 9, p. 1753, 2014.

[199] G. Hackenbroich and H. A. Weidenmüller, "Transmission through a quantum dot in an Aharonov-Bohm ring", *Physical Review Letters*, vol. **76**, no. 1, p. 110, 1996.

[200] D. Smirnov, J. C. Rode, and R. J. Haug, "Suppression of decoherence in a graphene monolayer ring", *Applied Physics Letters*, vol. **105**, no. 8, p. 082112, 2014.

[201] B. L. Al'tshuler, A. G. Aronov, and B. Z. Spivak, "The Aaronov-Bohm effect in disordered conductors", *JETP Letters*, vol. **33**, no. 2, p. 94, 1981.

[202] D. U. Sharvin and Y. U. V. Sharvin, "Magnetic flux quantization in a cylindrical film of a normal metal", *JETP Letters*, vol. **34**, no. 5, p. 272, 1981.

[203] G. J. Dolan, J. C. Licini, and D. J. Bishop, "Quantum interference effects in lithium ring arrays", *Physical Review Letters*, vol. **56**, no. 14, p. 1493, 1986.

[204] G. M. Gusev, Z. D. Kvon, L. V. Litvin, *et al.*, "Aharonov-Bohm oscillations in a 2D electron gas with a periodic lattice of scatterers", *JETP Letters*, vol. **55**, no. 2, p. 123, 1992.

[205] F. Nihey, S. W. Hwang, and K. Nakamura, "Observation of large h/2e oscillations in semiconductor antidot lattices", *Physical Review B*, vol. **51**, no. 7, p. 4649, 1995.

[206] K. Tsubaki, "Aharonov-Bohm oscillation in rings with permalloy", *Japanese Journal of Applied Physics*, vol. **40**, no. 3S, p. 1902, 2001.

[207] A. Yacoby, R. Schuster, and M. Heiblum, "Phase rigidity and h/2e oscillations in a single-ring Aharonov-Bohm experiment", *Physical Review B*, vol. **53**, no. 15, p. 9583, 1996.

[208] S. Washburn and R. A. Webb, "Aharonov-Bohm effect in normal metal quantum coherence and transport", *Advances in Physics*, vol. **35**, no. 4, p. 375, 1986.

[209] T. Ihn, "Topological insulators: Oscillations in the ribbons", *Nature Materials*, vol. **9**, no. 3, p. 187, 2010.

[210] U. F. Keyser, S. Borck, R. J. Haug, *et al.*, "Aharonov-Bohm oscillations of a tuneable quantum ring", *Semiconductor Science and Technology*, vol. **17**, no. 5, p. L22, 2002.

[211] M. Pioro-Ladriere, J. H. Davies, A. Long, *et al.*, "Origin of switching noise in GaAs/$Al_xGa_{1-x}As$ lateral gated devices", *Physical Review B*, vol. **72**, no. 11, p. 115331, 2005.

[212] J. R. Kirtley, T. N. Theis, P. M. Mooney, and S. L. Wright, "Noise spectroscopy of deep level (DX) centers in GaAs-$Al_xGa_{1-x}As$ heterostructures", *Journal of Applied Physics*, vol. **63**, no. 5, p. 1541, 1988.

[213] B. Grbić, R. Leturcq, T. Ihn, *et al.*, "Aharonov-Bohm oscillations in the presence of strong spin-orbit interactions", *Physical Review Letters*, vol. **99**, no. 17, p. 176803, 2007.

[214] M. J. Yang, C. H. Yang, and Y. B. Lyanda-Geller, "Quantum beating in ring conductance: Observation of spin chiral states and Berry's phase", *Europhysics Letters*, vol. **66**, no. 6, p. 826, 2004.

[215] C. J. B. Ford, T. J. Thornton, R. Newbury, *et al.*, "The Aharonov-Bohm effect in electrostatically defined heterojunction rings", *Journal of Physics C: Solid State Physics*, vol. **21**, no. 10, p. L325, 1988.

[216] V. A. Tkachenko, Z. D. Kvon, D. Sheglov, *et al.*, "Aharonov-Bohm oscillation amplitude in small ballistic interferometers", *JETP Letters*, vol. **79**, no. 3, p. 136, 2004.

[217] G. Metalidis and P. Bruno, "Inelastic scattering effects and the Hall resistance in a four-probe ring", *Physical Review B*, vol. **73**, no. 11, p. 113308, 2006.

[218] W.-C. Tan and J. Inkson, "Landau quantization and the Aharonov-Bohm effect in a two-dimensional ring", *Physical Review B*, vol. **53**, no. 11, p. 6947, 1996.

[219] J. Liu, W. Gao, K. Ismail, *et al.*, "Correlations between Aharonov-Bohm effects and one-dimensional subband populations in GaAs/$Al_xGa_{1-x}As$ rings", *Physical Review B*, vol. **48**, no. 20, p. 15148, 1993.

[220] X.-L. Qi and S.-C. Zhang, "Topological insulators and superconductors", *Reviews of Modern Physics*, vol. **83**, no. 4, p. 1057, 2011.

[221] Y. Ando, "Topological insulator materials", *Journal of the Physical Society of Japan*, vol. **82**, no. 10, p. 102001, 2013.

[222] S.-Q. Shen, *Topological insulators: Dirac equation in condensed matters*, vol. **174**. Springer Science & Business Media, 2013.

[223] R. Dornhaus and G. Nimtz, "The properties and applications of the $Hg_{1-x}Cd_xTe$ alloy system", in *Narrow-Gap Semiconductors*, p. 119, Springer, 1983.

[224] J. Moore, "Topological insulators: The next generation", *Nature Physics*, vol. **5**, no. 6, p. 378, 2009.

[225] Z. Ren, A. A. Taskin, S. Sasaki, K. Segawa, and Y. Ando, "Large bulk resistivity and surface quantum oscillations in the topological insulator Bi_2Te_2Se", *Physical Review B*, vol. **82**, no. 24, p. 241306, 2010.

[226] J. Xiong, A. C. Petersen, D. Qu, *et al.*, "Quantum oscillations in a topological insulator Bi_2Te_2Se with large bulk resistivity (6Ωcm)", *Physica E: Low-dimensional Systems and Nanostructures*, vol. **44**, no. 5, p. 917, 2012.

[227] Z. Ren, A. A. Taskin, S. Sasaki, K. Segawa, and Y. Ando, "Fermi level tuning and a large activation gap achieved in the topological insulator Bi_2Te_2Se by Sn doping", *Physical Review B*, vol. **85**, no. 15, p. 155301, 2012.

[228] Y. L. Chen, J. G. Analytis, J.-H. Chu, *et al.*, "Experimental realization of a three-dimensional topological insulator, Bi_2Te_3", *Science*, vol. **325**, no. 5937, p. 178, 2009.

[229] Z. Alpichshev, J. G. Analytis, J.-H. Chu, *et al.*, "STM imaging of electronic waves on the surface of Bi_2Te_3: topologically protected surface states and hexagonal warping effects", *Physical Review Letters*, vol. **104**, no. 1, p. 016401, 2010.

[230] Z.-H. Pan, E. Vescovo, A. V. Fedorov, *et al.*, "Electronic structure of the topological insulator Bi_2Se_3 using angle-resolved photoemission spectroscopy: evidence for a nearly full surface spin polarization", *Physical Review Letters*, vol. **106**, no. 25, p. 257004, 2011.

[231] L. Fu and C. L. Kane, "Superconducting proximity effect and Majorana fermions at the surface of a topological insulator", *Physical Review Letters*, vol. **100**, no. 9, p. 096407, 2008.

[232] L. Fu and C. L. Kane, "Probing neutral Majorana fermion edge modes with charge transport", *Physical Review Letters*, vol. **102**, no. 21, p. 216403, 2009.

[233] A. R. Akhmerov, J. Nilsson, and C. W. J. Beenakker, "Electrically detected interferometry of Majorana fermions in a topological insulator", *Physical Review Letters*, vol. **102**, no. 21, p. 216404, 2009.

[234] Y. G. Semenov, X. Duan, and K. W. Kim, "Electrically controlled magnetization in ferromagnet-topological insulator heterostructures", *Physical Review B*, vol. **86**, no. 16, p. 161406, 2012.

[235] M.-X. Wang, C. Liu, J.-P. Xu, *et al.*, "The coexistence of superconductivity and topological order in the Bi_2Se_3 thin films", *Science*, vol. **336**, no. 6077, p. 52, 2012.

[236] B. Yan, D. Zhang, and C. Felser, "Topological surface states of Bi_2Se_3 coexisting with Se vacancies", *physica status solidi (RRL)-Rapid Research Letters*, vol. **7**, no. 1-2, p. 148, 2013.

[237] J. Navratil, J. Horak, T. Plecháček, *et al.*, "Conduction band splitting and transport properties of Bi_2Se_3", *Journal of Solid State Chemistry*, vol. **177**, no. 4, p. 1704, 2004.

[238] J. G. Analytis, J.-H. Chu, Y. Chen, *et al.*, "Bulk Fermi surface coexistence with Dirac surface state in Bi_2Se_3: A comparison of photoemission and Shubnikov–de Haas measurements", *Physical Review B*, vol. **81**, no. 20, p. 205407, 2010.

[239] M. Petrushevsky, E. Lahoud, A. Ron, *et al.*, "Probing the surface states in Bi_2Se_3 using the Shubnikov–de Haas effect", *Physical Review B*, vol. **86**, no. 4, p. 045131, 2012.

[240] Y. Yan, L.-X. Wang, X. Ke, *et al.*, "High-mobility Bi_2Se_3 nanoplates manifesting quantum oscillations of surface states in the sidewalls", *Scientific reports*, vol. **4**, p. 3817, 2014.

[241] H. Cao, S. Xu, I. Miotkowski, *et al.*, "Structural and electronic properties of highly doped topological insulator Bi_2Se_3 crystals", *physica status solidi (RRL)-Rapid Research Letters*, vol. **7**, no. 1-2, p. 133, 2013.

[242] Y. Onose, R. Yoshimi, A. Tsukazaki, *et al.*, "Pulsed laser deposition and ionic liquid gate control of epitaxial Bi_2Se_3 thin films", *Applied Physics Express*, vol. **4**, no. 8, p. 083001, 2011.

[243] H. B. Zhang, H. L. Yu, D. H. Bao, *et al.*, "Weak localization bulk state in a topological insulator bi 2 te 3 film", *Physical Review B*, vol. **86**, no. 7, p. 075102, 2012.

[244] T. Ando, T. Nakanishi, and R. Saito, "Berry's phase and absence of back scattering in carbon nanotubes", *Journal of the Physical Society of Japan*, vol. **67**, no. 8, p. 2857, 1998.

[245] P. A. Lee and T. V. Ramakrishnan, "Disordered electronic systems", *Reviews of Modern Physics*, vol. **57**, no. 2, p. 287, 1985.

[246] A. A. Taskin, S. Sasaki, K. Segawa, and Y. Ando, "Manifestation of topological protection in transport properties of epitaxial Bi_2Se_3 thin films", *Physical Review Letters*, vol. **109**, no. 6, p. 066803, 2012.

[247] J. Chen, X. Y. He, K. H. Wu, *et al.*, "Tunable surface conductivity in Bi_2Se_3 revealed in diffusive electron transport", *Physical Review B*, vol. **83**, no. 24, p. 241304, 2011.

[248] H. Steinberg, J.-B. Laloë, V. Fatemi, J. S. Moodera, and P. Jarillo-Herrero, "Electrically tunable surface-to-bulk coherent coupling in topological insulator thin films", *Physical Review B*, vol. **84**, no. 23, p. 233101, 2011.

[249] Y. S. Kim, M. Brahlek, N. Bansal, *et al.*, "Thickness-dependent bulk properties and weak antilocalization effect in topological insulator Bi_2Se_3", *Physical Review B*, vol. **84**, no. 7, p. 073109, 2011.

[250] N. P. Butch, K. Kirshenbaum, P. Syers, *et al.*, "Strong surface scattering in ultrahigh-mobility Bi_2Se_3 topological insulator crystals", *Physical Review B*, vol. **81**, no. 24, p. 241301, 2010.

[251] N. Bansal, Y. S. Kim, M. Brahlek, E. Edrey, and S. Oh, "Thickness-independent transport channels in topological insulator Bi_2Se_3 thin films", *Physical Review Letters*, vol. **109**, no. 11, p. 116804, 2012.

[252] S. S. Hong, W. Kundhikanjana, J. J. Cha, *et al.*, "Ultrathin topological insulator Bi_2Se_3 nanoribbons exfoliated by atomic force microscopy", *Nano Letters*, vol. **10**, no. 8, p. 3118, 2010.

[253] J. Wang, A. M. DaSilva, C.-Z. Chang, *et al.*, "Evidence for electron-electron interaction in topological insulator thin films", *Physical Review B*, vol. **83**, no. 24, p. 245438, 2011.

[254] W. F. Leonard and R. L. Ramey, "Temperature coefficient of resistance in thin metal films", *Journal of Applied Physics*, vol. **37**, no. 9, p. 3634, 1966.

[255] W. T. Pawlewicz, J. A. Rayne, and R. W. Ure, "Resistivity of Bi_2Te_3 from 1.3 K to 300 K", *Physics Letters A*, vol. **48**, no. 5, p. 391, 1974.

[256] G. R. Hyde, H. A. Beale, I. L. Spain, and J. A. Woollam, "Electronic properties of Bi_2Se_3 crystals", *Journal of Physics and Chemistry of Solids*, vol. **35**, no. 12, p. 1719, 1974.

[257] H. Köhler and H. Fischer, "Investigation of the conduction band Fermi surface in Bi_2Se_3 at high electron concentrations", *physica status solidi (b)*, vol. **69**, no. 2, p. 349, 1975.

[258] H.-T. He, G. Wang, T. Zhang, *et al.*, "Impurity effect on weak antilocalization in the topological insulator Bi_2Te_3", *Physical Review Letters*, vol. **106**, no. 16, p. 166805, 2011.

[259] L. Zhang, M. Dolev, Q. I. Yang, *et al.*, "Weak localization effects as evidence for bulk quantization in Bi_2Se_3 thin films", *Physical Review B*, vol. **88**, no. 12, p. 121103, 2013.

[260] O. Chiatti, C. Riha, D. Lawrenz, *et al.*, "2D layered transport properties from topological insulator Bi_2Se_3 single crystals and micro flakes", *Scientific Reports*, vol. **6**, p. 27483, 2016.

[261] A. A. Taskin, S. Sasaki, K. Segawa, and Y. Ando, "Achieving surface quantum oscillations in topological insulator thin films of Bi_2Se_3", *Advanced Materials*, vol. **24**, no. 41, p. 5581, 2012.

Appendix A

In Fig. 11.2 the zincblende crystal structure of the binary compound semiconductors AlAs and GaAs is shown. The space group is F-43m (number 216) and the lattice parameters are $a_{\mathrm{AlAs}} = 5.661$ Å [99] and $a_{\mathrm{GaAs}} = 5.653$ Å [100].

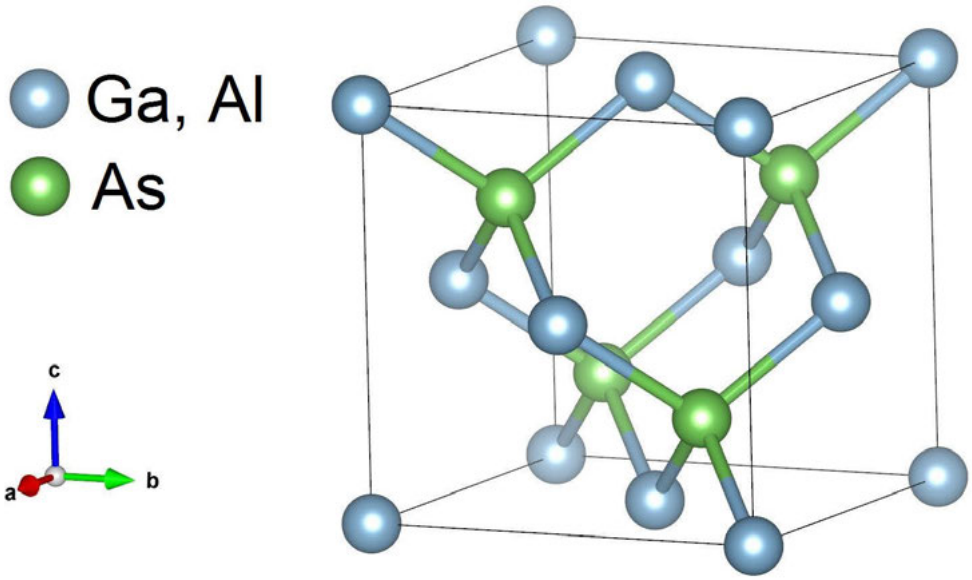

Figure 11.2: Schematic of the zincblende crystal structure. This is the crystal structure of the binary compound semiconductors AlAs and GaAs.

Appendix B

Material Parameters for the Wafer 11159

		$T = 300$ K	$T = 4.2$ K
illuminated	μ (cm^2/Vs)	5848	$3.04 \cdot 10^6$
	n (cm^{-2})	$-5.77 \cdot 10^{11}$	$-3.38 \cdot 10^{11}$
not illuminated	μ (cm^2/Vs)	5781	$2.43 \cdot 10^6$
	n (cm^{-2})	$-5.64 \cdot 10^{11}$	$-2.07 \cdot 10^{11}$

Layer sequence for the Wafer 11159

	Material	Layer thickness
10 x{	GaAs	50 nm
	GaAs	5 nm
	AlGaAs	5 nm
	GaAs	650 nm
	$Al_{0.34}Ga_{0.66}As$	55 nm
	$Al_{0.34}Ga_{0.66}As$:Si*	50 nm
	GaAs:Si*	5 nm

* Homogeneously doped with a concentration of $5.3 \cdot 10^{17}$ cm^{-3}

Material Parameters for the Wafer 12088

		$T = 4.2$ K
not illuminated	μ (cm^2/Vs)	$1.05 \cdot 10^6$
	n (cm^{-2})	$-3.1 \cdot 10^{11}$

Layer sequence for the Wafer 12088

	Material	Layer thickness
10 x{	GaAs	50 nm
	GaAs	5 nm
	AlGaAs	5 nm
	GaAs	650 nm
	$Al_{0.35}Ga_{0.65}As$	20 nm
	$Al_{0.35}Ga_{0.65}As$:Si**	30.3 nm
	GaAs:Si**	5 nm

** Homogeneously doped with a concentration of 1.0^{18} cm^{-3}

Appendix C

Sample preparation of the Bi_2Se_3 flakes

Material	Bi_2Se_3-002
Substrate	Si, boron-doped, 5×5 mm^2*
SiO_2 layer on top of Si substrate	300 nm
Sonication of the SiO_2-substrate	2 minutes
Drying	N_2 - pistol
Null-Exfoliation to remove oxidized layers	1 time
Exfoliation with adhesive tape	Folding and unfolding 3 times each
Sonication of substrate and sample	25 s*
Drying	N_2 - pistol
Examination of sample geometry	Sensofar Plμ Neox - Confocal
Cleaning substrate and sample	acetone, 80° for 5 minutes
Cleaning substrate and sample	ethanol, 80° for 5 minutes
Drying	N_2 - pistol
Prebaking of substrate and sample	120°, 5 min
Positive photoresist	ECI 3027
Developer	326 MIF
Spincoating of ECI 3027	90 rps for 40 s
Prebaking of photoresist	120° for 60 s
Laser diameter for macroscopic pattern	5 μm, 405 nm wavelength
Laser diameter for microscopic pattern	1 μm, 405 nm wavelength
Expose resist sensitivity	200 mJ/cm^2
Focus	about 700
Exposure to developer	17 s
Plasmacleaning with O_2	45 s, 90 W
Plasmacleaning with H_2	60 s, 90 W
Sputtering of titanium	5 nm (99,99 % purity)
Sputtering of gold	50 nm (99,9 % purity)
Solving resist in acetone	at least 30 min
Lift-Off	Pipetting with acetone
Gluing into chipcarrier	Silver paint
Examination of sample thickness	AFM
Bonding	Aluminium wire

* Sonication is performed in acetone

Appendix D

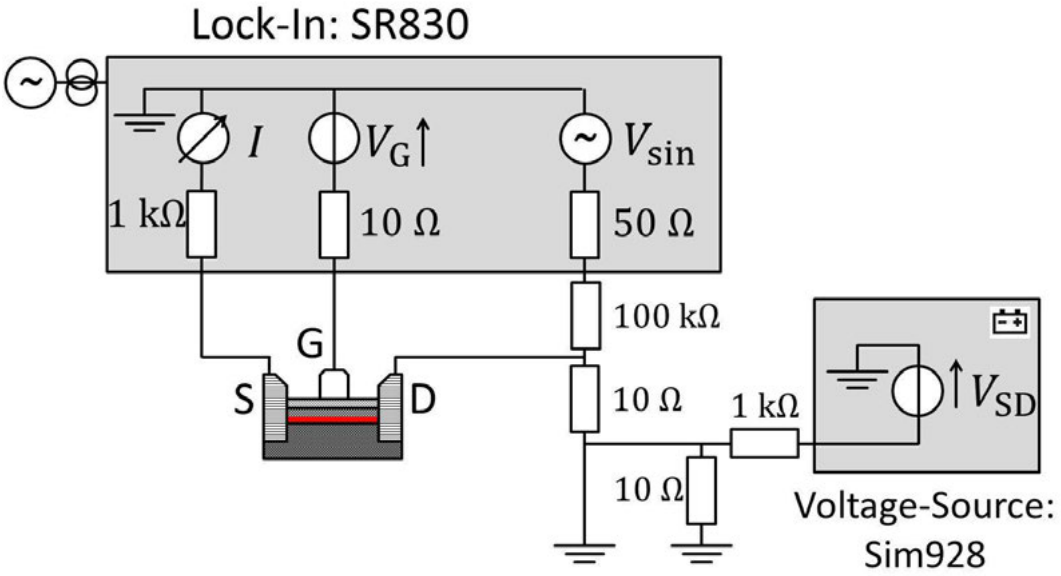

Figure 11.3: Alternative measurement setup for conductance measurements in the non-linear regime. The active voltage devider of the setup, presented in Fig. 4.2 b) is replaced by a passive voltage devider to reduce noise.

Appendix E

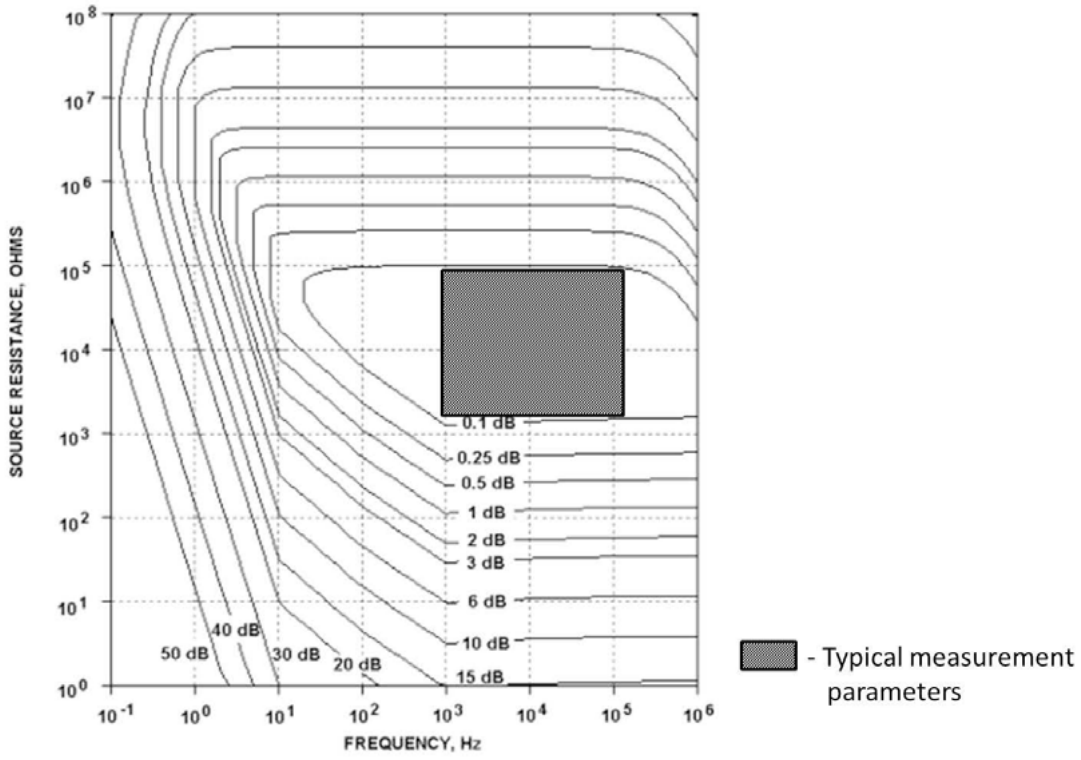

Figure 11.4: Noise Figure of the ultra low-noise voltage preamplifiers Model 5184 from System Recovery. The highlighted rectangle marks the measurement parameters that are typically used in this thesis.

Appendix F

QRA-asymmetric quantum ring
(Internal: 11159-S10-A)
The device includes 1D waveguides with a width of $w \approx 510$ nm and an 1D constriction in the straight arm with a width of $w_{\mathrm{QPC}} \approx 170$ nm. Both arms of the quantum rings are covered by finger gates. The ring has a mean radius of $r = (1.1 \pm 0.1)$ µm.

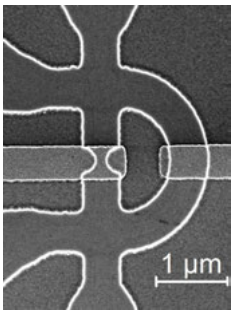

QRB-asymmetric quantum ring
(Internal: 11159-S10-B)
The device includes 1D waveguides with a width of $w \approx 510$ nm and an 1D constriction in the straight arm with a width of $w_{\mathrm{QPC}} \approx 170$ nm. The straight arm of the quantum rings is covered by a finger gate. The ring has a mean radius of $r = (1.1 \pm 0.1)$ µm.

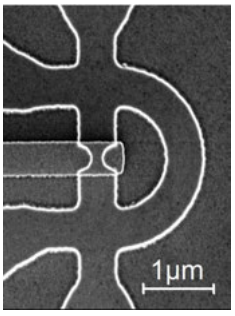

QRC-asymmetric quantum ring
(Internal: 11159-S11-B)
The device comprises 1D waveguides with a width of $w \approx 510$ nm that is connected by two narrow 2D heater structures. In this device no gate structure is available. The ring has a mean radius of $r = (1.1 \pm 0.1)$ µm.

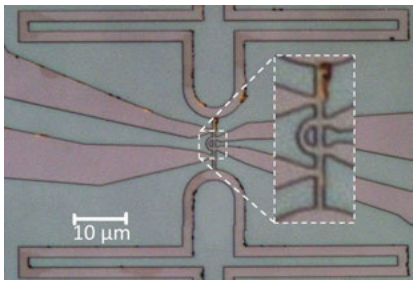

QRD-asymmetric quantum ring
(Internal: 11159-S10-F)
The device includes 1D waveguides with a width of $w \approx 170$ nm that act as 1D constrictions and lead to a quantized conductance in the upper crossing. A global top-gate allows to change the Fermi energy of the device. The ring has a mean radius of $r = (1.0 \pm 0.1)$ µm.

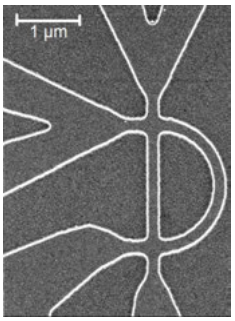

ConstrA-quantum point contact (Internal: 12088-S3-F)
The device consists of five quantum point contacts (QPCs) all of which have a comparable width of ≈ 100 nm. A global top-gate allows to change the Fermi energy of all QPCs at once. The scanning electron micrograph shows a QPC of the device 12088-S3 with similar width and length.

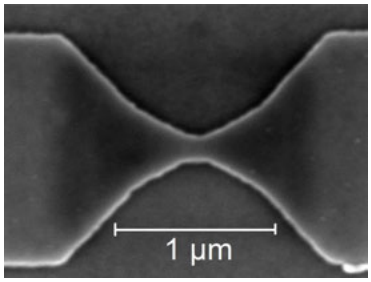

ConstrB-bent electron waveguide (Internal: 12088-S2-B_3-12)
The device consists of a bent 1D waveguide with a width of $w \approx 285$ nm and a length of $l \approx 3.7$ µm. The scanning electron micrograph shows a similar device with a width of $w \approx 160$ nm.

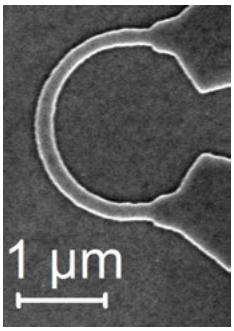

ConstrC-unbent electron waveguide (Internal: 12088-S2-B_4-11)
The device consists of an unbent 1D waveguide with a width of $w \approx 285$ nm and a length of $l \approx 2.8$ µm. The scanning electron micrograph shows a similar device with a width of $w \approx 160$ nm.

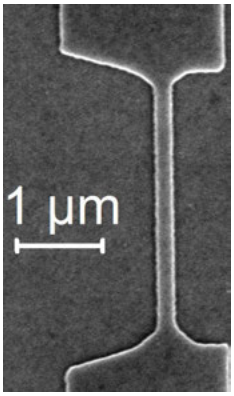

The images were taken in Bochum by Dr. Sven Buchholz

Appendix G

The leakage current is measured for all $Al_xGa_{1-x}As/GaAs$ devices that are used in this thesis. In Fig. 11.5 a) the leakage current is shown and is significant for three devices. Two of these devices comprise a global top-gate, which is the reason why the leakage current density in Fig. 11.5 b) is less significant for these structures.

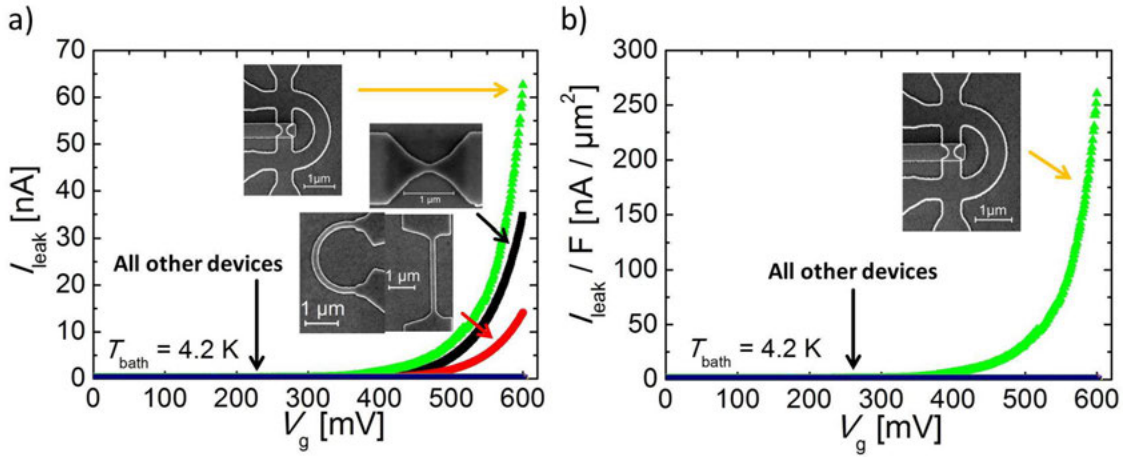

Figure 11.5: a) Leakage current and b) leakage current density of the $Al_xGa_{1-x}AS/GaAs$ heterostructures.

Appendix H

Here, the measured noise spectrum of two parallel circuits, consisting of two resistors R_1 and R_2 each, is depicted. The measurement is performed for the resistance combination $R_1 = 10$ kΩ, $R_2 = 10$ kΩ and the combination $R_1 = 10$ kΩ, $R_1 = 1$ kΩ. The corresponding expectation values are

$$S_{\mathrm{V,Th}} = 4k_{\mathrm{B}}RT_{\mathrm{e}} + 2 \cdot 4k_{\mathrm{B}} \cdot 300K \cdot \frac{R^2}{5\ \mathrm{M\Omega}} \tag{11.1}$$

with $R^{-1} = R_1^{-1} + R_2^{-1}$ and $T_{\mathrm{e}} = 300$ K. The measurement is depicted in Fig. 11.6 and shows that the measured white part of the spectrum $S_{\mathrm{V,w}}$ corresponds to its expectation value. The presented measurements aim to prove that the excess noise that is measured in quantum rings does not stem from the pure fact that the two ring arms are connected in parallel to each other.

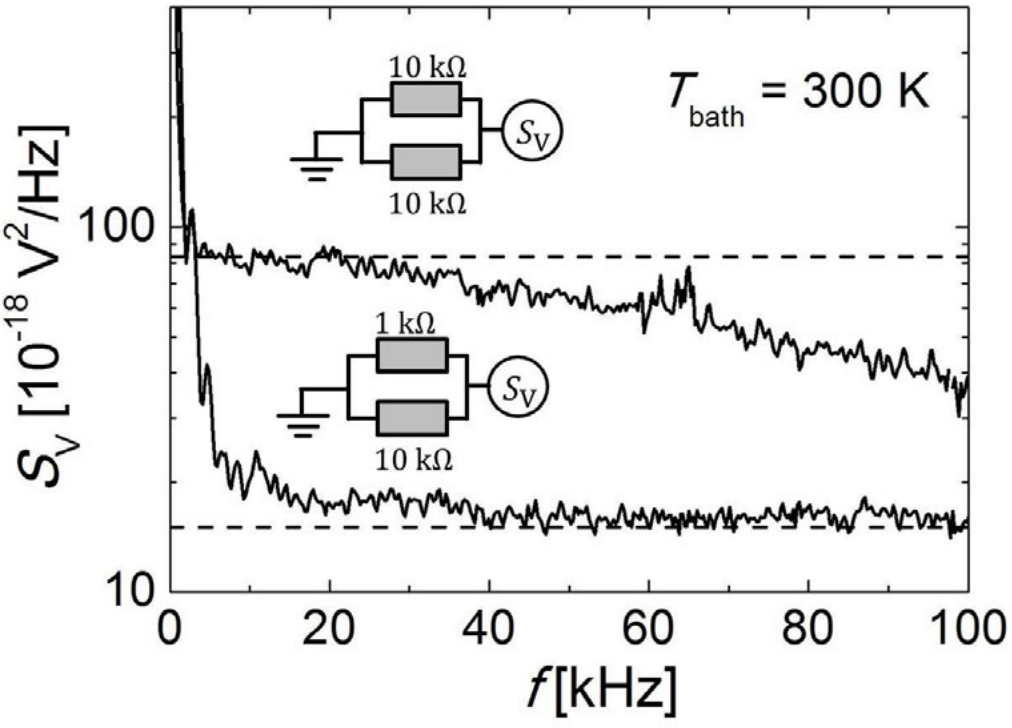

Figure 11.6: Measured noise spectra of two parallel macroscopic resistors at $T_{\mathrm{bath}} = 300$ K (solid line). The noise spectrum with the higher PSD is measured with two 10 kΩ resistors that are connected in parallel. The noise spectrum with the lower PSD is measured with a 10 kΩ resistor that is connected in parallel to a 1 kΩ resistor. The dashed line corresponds to the expected value $S_{\mathrm{V,Th}}$ of the setup that is calculated from the reciprocal addition of the two resistors.

Appendix I

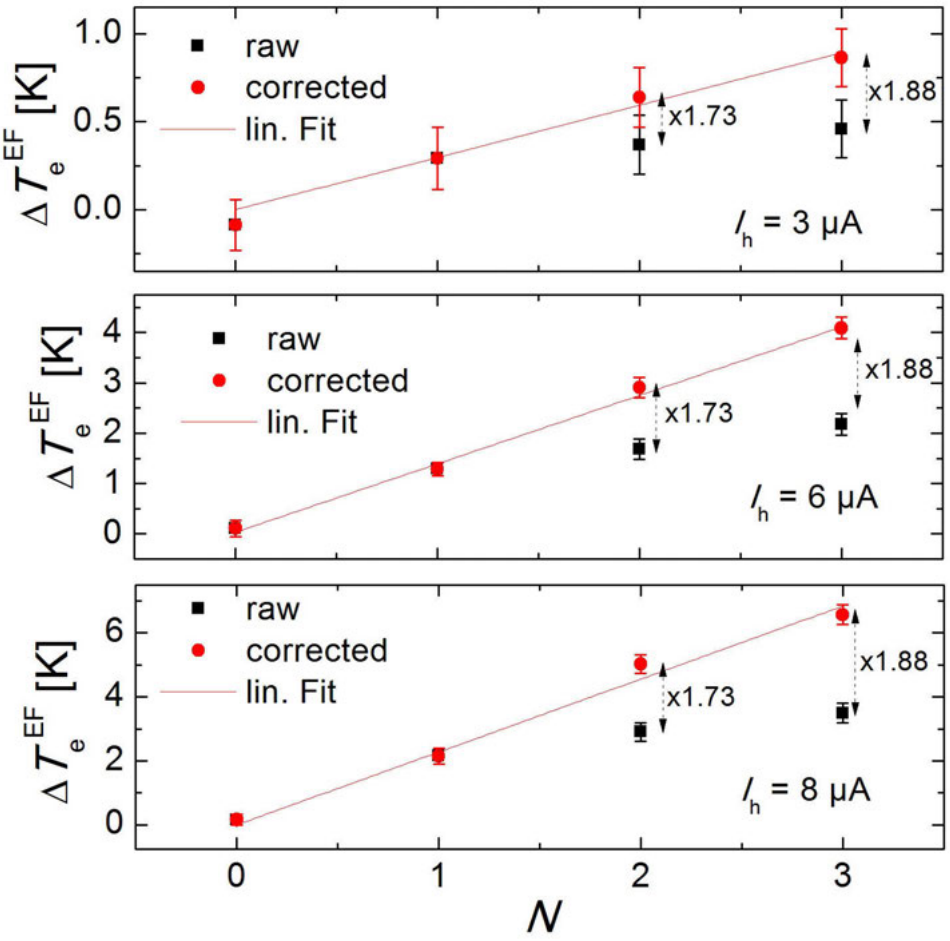

Figure 11.7: Increase of electron temperature in the device QRD in thermal non-equilibrium for the heating currents $I_\mathrm{h} = 3$ µm, 6 µm and $I_\mathrm{h} = 8$ µm. Black symbols refer to measurement values. Red symbols refer to the correction of the black symbols according to the heat branching model in Sec. 7.3

Appendix J

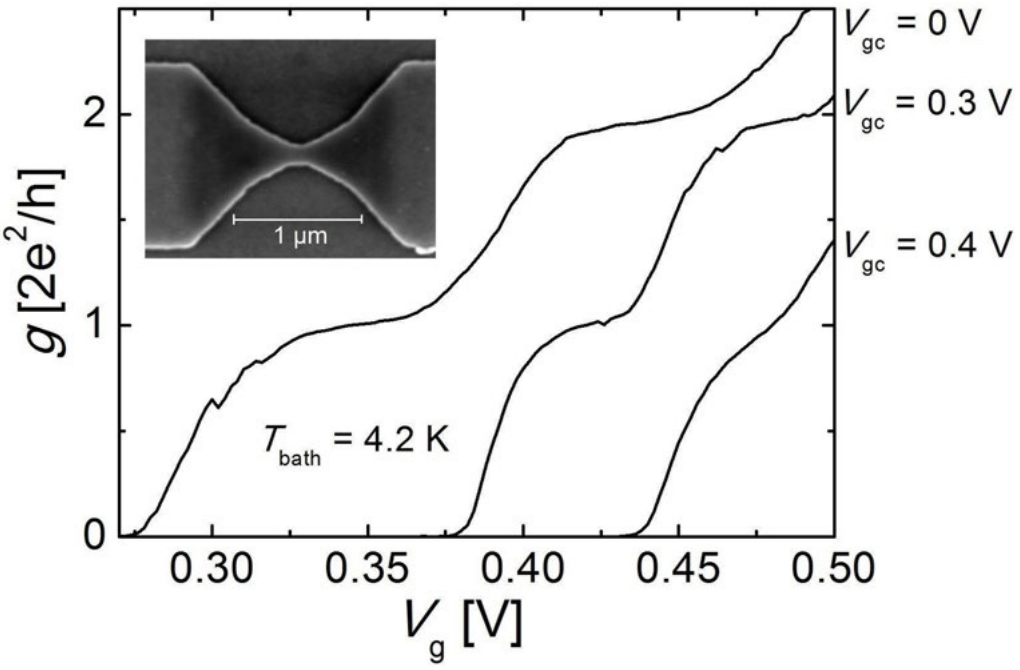

Figure 11.8: Differential conductance of the device ConstrA after bias cooling with gate voltage V_{gc}. The threshold voltage shifts to higher voltages for higher V_{gc}.

Appendix K

Microflake A
(Internal: Bi_2Se_3-002-003)
(Exfoliation: C. Riha; Measurements: C. Riha; HLN fits: C. Riha)
The microflake has a thickness of $d = (340 \pm 10)$ nm and a contact geometry that allows four-point measurements of R_{xx} and R_{xy}. The $R(T_{bath})$ characteristic is metallic.

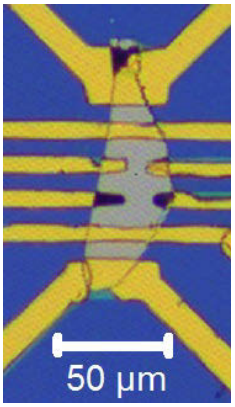

Microflake B
(Internal: Bi_2Se_3-002-001)
(Exfoliation: C. Riha; Measurements: C. Riha, D. Lawrenz, F. Herling; HLN fits: C. Riha)
The microflake has a thickness of $d = (130 \pm 7)$ nm and a contact geometry that allows four-point measurements of R_{xx} and R_{xy}. The $R(T_{bath})$ characteristic is metallic. The magnetoresistance at low magnetic fields shows a dip that can be attributed to WAL if layered 2D transport is considered.

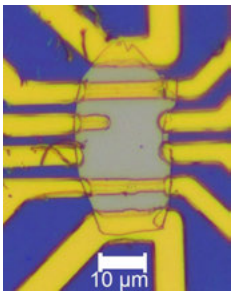

Microflake C
(Internal: Bi_2Se_3-002-009A)
(Exfoliation: S. Dusari; Measurements: O. Chiatti; HLN fits: C. Riha)
The microflake has a thickness of $d = (200 \pm 10)$ nm. Shortcuts in the contact circuit allow two-point measurements only. The $R(T_{bath})$ characteristic is metallic. The magnetoresistance at low magnetic fields shows a dip that can be attributed to WAL if layered 2D transport is considered.

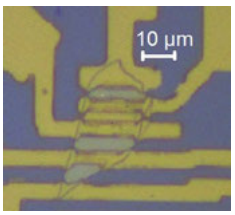

Microflake D
(Internal: Bi2Se3-200815-W9-S1)

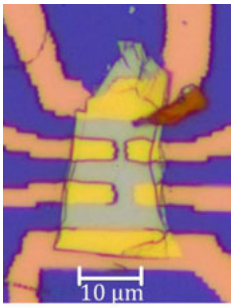

(Exfoliation: O. Chiatti; Measurements: O. Chiatti; HLN fits: C. Riha)
The microflake has a thickness of $d = (220 \pm 10)$ nm. The contact geometry allows four-point measurements. The $R(T_{\mathrm{bath}})$ characteristic is semiconducting. The magnetoresistance at low magnetic fields shows a dip that can be attributed to WAL. No layered 2D transport has to be considered.

Appendix L

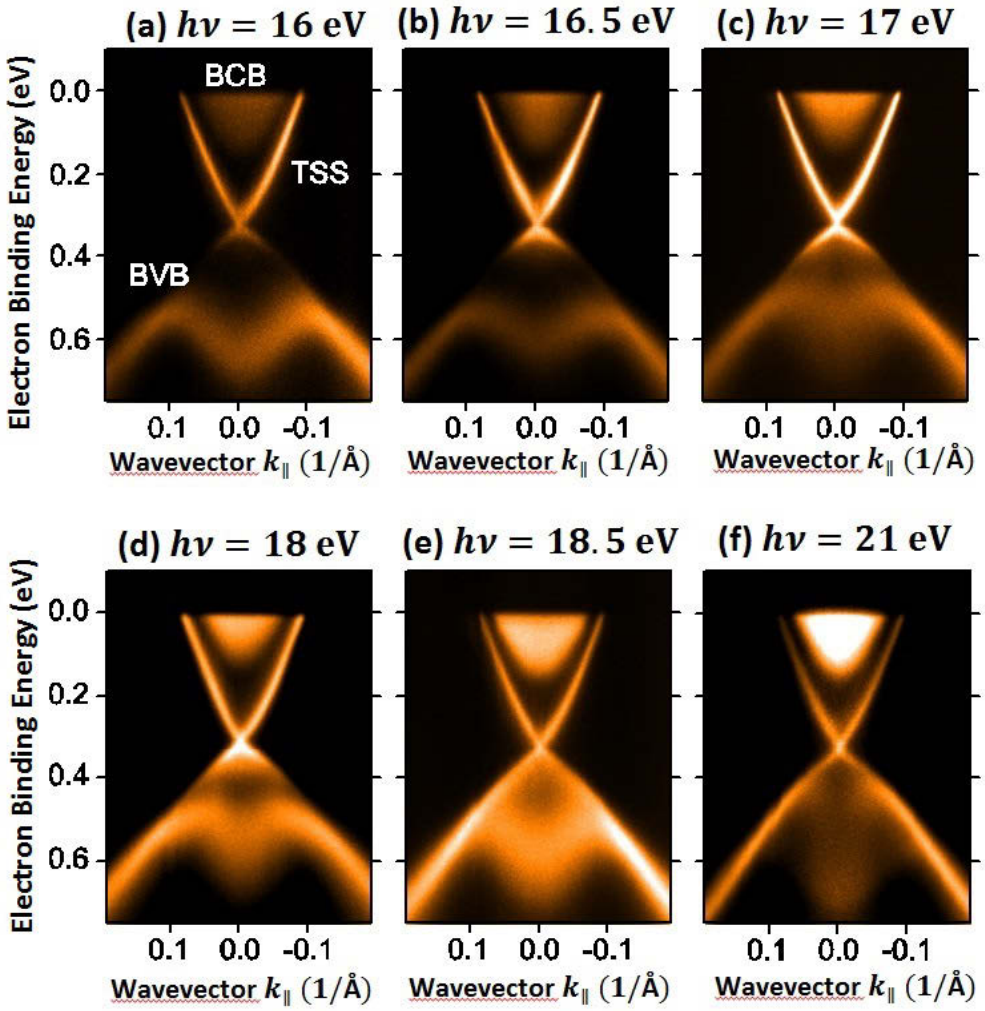

Figure 11.9: ARPES measurements of a Bi_2Se_3 bulk single crystal at photon energies a) 16 eV, b) 16.5 eV, c) 17 eV, d) 18 eV, e) 18.5 eV and f) 21 eV at 12 K that were performed by the group of Prof. Dr. Oliver Rader. The dispersion is measured as a function of the electron wave vector $k_{||}$ parallel to the surface. In a) the bulk valence band (BVB), the bulk conduction band (BCB) and the time-reversal symmetry protected surface states (TSS) are denoted. The dispersion of the TSS has no k_z dependence, as expected from the 2D surface states. In contrast, the dispersion of the BVB reaches its maximum intentsity at a photon energy of about $h\nu = 18$ eV and the BCB reaches its minimum at about $h\nu = 21$ eV. The flakes are stable to atmosphere and to the lithography process. The measurements were performed using soft x-rays of 400 eV photon energy and horizontal polarization. The PEEM field of view is 25 µm.

Appendix M

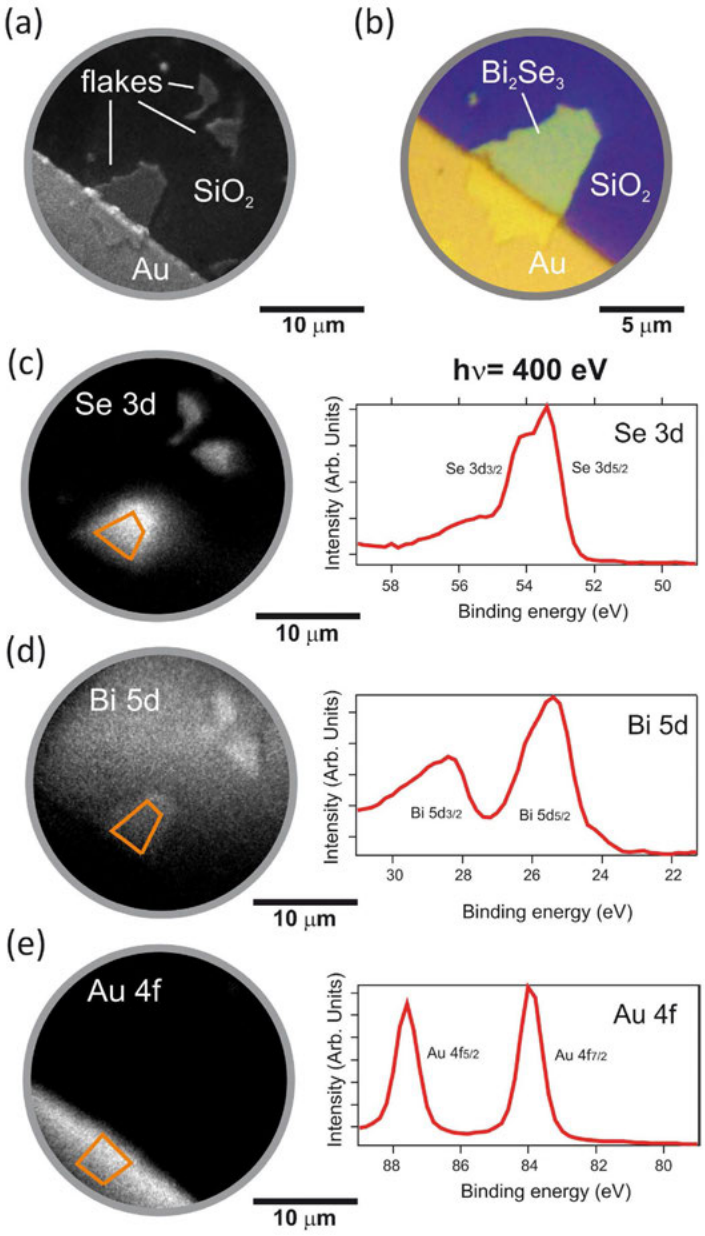

Figure 11.10: PEEM characterization of a contacted Bi_2Se_3 flake [260]. a) Overview image with vacuum UV light of the flake and Au contact area. b) Corresponding confocal microscopy image of the same flake revealing thickness homogeneity. c-e) Core-level spectromicroscopy of the flake area and of the Au contact area. On the left, spatially resolved images taken at the kinetic energies of the c) Se $3d_{5/2}$, d) Bi $5d_{5/2}$ and d) Se $4f_{5/2}$ core-levels. On the right, the corresponding core-level spectra are shown. The spectra are extracted from the small areas indicated in each PEEM image on the left with a kinetic energy resolution of about 0.2 eV.

Acknowledgement

First off all I would like to express my gratitude to Prof. Dr. Saskia Fischer for giving me the opportunity to participate in the study of the quantum phenomena in quantum rings and for her supervision that contributed to the success of this thesis to a great extend. This gratitude also refers to the supply of the measurement devices that are indispensable for the exciting work in this field.

I would like to offer my special thanks to Prof. Dr. Lada Yashina from the Moscow State University for providing the Bi_2Se_3 source material and to Prof. Dr. Oliver Rader from Bessy II in Berlin for sharing the results of the ARPES measurements of these crystals.

I am grateful to Dr. Tobias Kramer from the Konrad-Zuse-Zentrum für Informationstechnik Berlin and Dr. Christoph Kreisbeck from the Havard University, Cambridge for providing the wave packet simulations and for fruitful discussions.

I want to thank Dr. Olivio Chiatti for his expertise in the field of low-dimensional transport and Dr. Rüdiger Mitdank for competent advices.

I also want to thank Prof. Dr. Andreas Wieck and Prof. Dr. Dirk Reuter for manufacturing the $Al_xGa_{1-x}As$/GaAs wafer and Dr. Sven Buchholz for defining the quantum devices.

Moreover, I thank Dr. Fariba Hatami for sharing her knowledge of low noise phenomena in semiconductors with me.

Furthermore, I want to thank the whole group novel materials for the friendly atmosphere and for interesting discussions. Finally, I want to thank my family and Olga Strauch for their support and motivation.

List of Publications

- Christian Riha, Philipp Miechowski, Sven S. Buchholz, Olivio Chiatti, Andreas D. Wieck, Dirk Reuter and Saskia F. Fischer. Mode-selected heat flow through a one-dimensional waveguide network. *Applied Physics Letters* **106**(8), 083102, (2015).

- Christian Riha, Olivio Chiatti, Sven S. Buchholz, Dirk Reuter, Andreas D. Wieck and Saskia F. Fischer. Heat flow, transport and fluctuations in etched semiconductor quantum wire structures. *Physica status solidi (a)* **213**(3),571, (2016).

- Tobias Kramer, Christoph Kreisbeck, Christian Riha, Olivio Chiatti, Sven S. Buchholz, Andreas D. Wieck, Dirk Reuter and Saskia Fischer. Thermal energy and charge currents in multi-terminal nanorings. *AIP Advances* **6**(6), 065306, (2016).

- Olivio Chiatti, Christian Riha, Dominic Lawrenz, Marco Busch, Srujana Dusari, Jaime Sánchez-Barriga, Anna Mogilatenko, Lada V.Yashina, Sergio Valencia, Akin A. Ünal, Oliver Rader and Saskia F. Fischer. 2D layered transport properties from topological insulator Bi_2Se_3 single crystals and micro flakes. *Scientific Reports* **6**, 27483, (2016).

In preparation:

- Christian Riha, Philipp Miechowski, Sven S. Buchholz, Olivio Chiatti, Andreas D. Wieck, Dirk Reuter and Saskia F. Fischer. Excess noise in $Al_xGa_{1-x}As$/GaAs-based quantum rings. In preparation.

Statutory Declaration

I declare on oath that I completed this work on my own and that information which has been directly or indirectly taken from other sources has been noted as such. Neither this, nor a similar work, has been published or presented to an examination committee.

Christian Riha